Exploring Alien Skies

Detection and Characterisation of Exoplanetary Atmospheres with Ground-based Transmission Spectroscopy

vorgelegt von
Master of Science
Elyar Sedaghati
aus Teheran

Von der Fakultät II - Mathematik und Naturwissenschaften
der Technischen Universität Berlin
zur Erlangung des akademischen Grades
Doktor der Naturwissenschaften
Dr. rer. nat.

genehmigte Dissertation

Promotionsausschuss:
Vorsitzender: Prof. Dr. rer. nat. Mario Dähne
Gutachterin: Prof. Dr. rer. nat. Heike Rauer
Gutachter: Prof. Dr. rer. nat. Artie P. Hatzes
Gutachter: Dr. rer. nat. Henri M. J. Boffin
Tag der wissenschaftlichen Aussprache: 30.06.2017

Berlin 2017

Abstract

Characterisation of extra-solar planets is hot business. Since the first discoveries of these alien worlds merely a couple of decades ago, we have made huge progress in understanding and differentiating their physical properties. Of those aspects, the atmosphere has proved to be the most interesting characteristic. Not only does it lead to better understand the interior of a planet and its formation process and history, it also provides us with a channel through which possible signs of biological life on those worlds capable of harbouring them can be detected. This cumulative thesis highlights mainly results from three published first-author publications, as well as a further study currently under review, all of which are presented in peer-reviewed journals. The atmospheres of the three planets in the hot Jupiter regime, those the size of Jupiter and very close to their host stars, are studied with the technique of transmission spectroscopy.

Sedaghati et al. (2017) utilises the FORS2 instrument, at the VLT, data from ESO's archive to perform transmission spectroscopy in the presence of systematic effects introduced by the old, degraded prisms of the atmospheric dispersion corrector. Gaussian Process methods are used to model the correlated noise in the transit light curves of the exoplanet WASP-80b and estimate the contribution from various sources of *red* noise. From the obtained transmission spectrum, the presence of molecular species, that lead to enhanced absorption in the infra-red domain, is rejected. Additionally neutral, atomic potassium is detected from absorption both in the line cores and the pressure-broadened wing. Both of these conclusions are made at high statistical significance ($\gg 5\sigma$).

Sedaghati et al. (2015) is a letter which briefly presented the improvements made to transmission spectroscopic observations performed with FORS2 and provided the community with the impetus to once again return to this instrument for such observations. Since then, there has been an unprecedented number of publications announcing a variety of exo-atmospheric detections with this instrument. In a study currently under review, WASP-19b observations of this work are utilised together with two further observations of this target with near-UV and near-IR grisms of FOR2 to obtain a complete optical and high resolution transmission spectrum of this planet. With the aid of highly specialised observational and analysis techniques, as well

as atmospheric retrieval methods, this work makes the very first significant detection of a metal oxide (TiO) in the atmosphere of an exoplanet. This finding sheds new light on hot exo-atmosphere thermal inversion theories. Additionally, there is also significant detections of H_2O and strong scattering hazes.

Finally, Sedaghati et al. (2016) is the study of the atmosphere of WASP-17b, the exoplanet with one of the largest expected atmospheric signals in transmission. In this work, presence of potassium in the upper atmosphere is significantly detected from enhanced absorption in the pressure-broadened wings of the line core. Additionally, there is very marginal evidence for the presence of sodium in the atmosphere, which had previously been claimed to have been discovered.

The works presented here make valuable contributions to a very limited sample of exoplanetary atmosphere detections. Together they present a benchmark for an optimal approach to performing transmission spectroscopy from the ground and show the capabilities of the FORS2 instrument in performing such studies. The methodology provides a conservative, and subsequently realistic, approach to estimating the final parameter precisions and fully accounts for the contribution of systematic noise in a non-parametric manner. Hence, any atmospheric claim made in this work constitutes a robust statistical detection.

Zusammenfassung

Die Charakterisierung extrasolarer Planeten ist ein viel diskutiertes Thema. Seit der ersten Entdeckung dieser fremden Welten vor nur ein paar Jahrzehnten, gab es groβartige Fortschritte im Verstehen und Unterscheiden ihrer physikalischen Eigenschaften. Von all diesen ist die Atmosphäre die wahrscheinlich interessanteste. Wir erhalten nicht nur ein besseres Verständnis vom Inneren des Planeten, seiner Entstehungsprozesse und seiner Geschichte, sondern auch zusätzliche Informationen über mögliche Zeichen von biologischem Leben.

Die vorliegende kumulative Arbeit beleuchtet hauptsächlich die Resultate von drei bereits publizierten Erstautor Schriften, sowie einer, sich derzeit noch im Review Prozess befindlichen, weiteren Studie. Alle hier präsentierten Arbeiten beschäftigen sich mit den Atmosphären von drei Exoplaneten im sogenannten "hot Jupiter" Regime. Für ihre Analyse wurde das Transmission-Spektroskopie Verfahren verwendet.

In Sedaghati et al. (2017) wurden Transmission-Spektroskopie FORS2 Archivdaten aus der ESO Datenbank benutzt. Diese Daten beinhalten systematische Effekte die durch das Verwenden von älteren, degradierten Prismen des atmosphärischen Dispersion Korrektors entstehen. Mit der Gauβ-Prozess Methode wird korreliertes Rauschen in der Transit-Lichtkurve des Exoplaneten WASP-80b modelliert und der Beitrag der verschiedenen Quellen von rotem Rauschen abgeschätzt.

Die Präsenz von Molekülen führt zu gesteigerter Absorption im infraroten Bereich. Aus diesem Grund werden diese aus dem Transmission Spektrum herausgerechnet. Neutrales, atomares Kalium konnte sowohl im Spektrallinienkern als auch im druckverbreiterten Flügel nachgewiesen werden. Beide Ergebnisse sind statistisch signifikant ($\gg 5\sigma$).

In Sedaghati et al. (2015) werden die Fortschritte der Transmission-Spektroskopie mit dem FORS2 Instrument am VLT vorgestellt und damit neuer Antrieb für die Nutzung dieses Instruments für solche Beobachtungen geliefert. Seitdem gibt es eine beispiellose Anzahl an Publikationen, welche eine Vielzahl an exo-atmosphärischen Entdeckungen mit diesem Instrument melden.

In der Studie, welche momentan geprüft wird, werden WASP-19b Messungen aus den vorhergehenden Arbeiten benutzt und mit zwei weiteren

Messungen im nahen UV und IR Bereichs mit Gitterprismen des FOR2 Instruments gekoppelt. Damit entsteht ein vollständiges optisches und hoch aufgelöstes Transmissions Spektrum dieses Planeten. Mit Hilfe von spezialisierten Beobachtungs- und Analysetechniken, sowie atmosphärischen Wiedergewinnungsverfahren, ist dies die erste signifikante Beobachtung von Metalloxid (TiO) in der Atmosphäre von Exoplaneten. Dieser Fund wirft neues Licht auf "hot exo-atmosphere thermal inversion" Theorien. Zusätzlich können signifikante Mengen von H_2O und stark streuendem Dunst beobachtet werden.

In Sedaghati et al. (2016) wird eine ausführliche Studie der Atmosphäre von WASP-17b dargestellt. Von WASP-17b wird erwartet, dass er eines der größten atmosphärischen Signale in Transmission hat. In dieser Arbeit wird die Präsenz von Kalium in der oberen Atmosphäre signifikant nachgewiesen durch verstärkte Absorption im druckverbreiterten Linienflügel der Spektrallinie. Zusätzlich gibt es marginale Anzeichen für die Präsenz von Natrium in der Atmosphäre. Dies wurde bereits in einer anderen Studie festgestellt.

Die hier präsentierten Arbeiten liefern einen wertvollen Beitrag zu sehr eingeschränkten Proben von exoplanetaren Atmosphären. Sie sind ein Maßstab für einen optimalen Einsatz des bodengebundenen Transmission-Spektroskopie Verfahrens und beweisen das Potential des FORS2 Instruments am VLT für solche Studien. Diese Methode liefert einen konservativen, durchgehend realistischen Ansatz zur Abschätzung der Parameter Genauigkeit unter Berücksichtigung von systematischem Rauschen mit einer nicht-parametrisiertem Methode. Daraus folgt, dass jegliche These die in dieser Arbeit dargestellt wird eine statistisch robuste Entdeckung darstellt.

Acknowledgements

First and foremost I would like to thank Dr. Henri Boffin for all the help, support, advice and care throughout my entire PhD. Simply put, none of this work would be possible without his guidance. Having seen him at work has taught me what it means to be an astronomer and a scientist. Be it, comments on a paper on Christmas day from Patagonia while on holiday, or detailed and prompt analyses of my many poorly written ESO proposals, I never felt short of support. Following the four rules of a Boffin has been a life saver in every aspect. His push for tenacity will always ring in my ears.

I would also like to extend my gratitude to Prof. Heike Rauer for supporting me since the beginning of my Master's thesis all the way through to the end of my PhD. The hard work and dedication that she puts into the preparation for the PLATO space mission guarantees continued success for the future of exoplanetary community, from which I will benefit greatly. I will forever be indebted to her for the valuable advice and support throughout my time at the DLR.

I am also greatly thankful for all the discussions, advice and support from Dr. Juan Cabrera, Dr. Szilard Csizmadia, Dr. Anders Eriksson, Dr. Alexis Smith and Dr. Petr Kabath on my papers and this thesis, and to Dr. Claudia Dreyer for helping me with the German abstract. Special mention also goes to Prof. Artie Hatzes for an unending supply of support with recommendation letters and mesmerising talks.

At ESO, I would like to extend my appreciation to Dr. Claudio Melo for supporting me with a studentship in Santiago and all the great advice on science and career. The time in Chile would have been a whole lot different without Paul. Submitting proposals from Starbucks in Lima, in the morning hours before the deadline is one of many "fun" memories that I will never forget. Looking forward to making a few more back in Chile very soon. Same goes to Adrien and Ivan for my short time in Garching. Liz, Tomek, Jos, wee Catherine, Matt, big Giacomo, little Giacomo, Micha, Pablo and Luca, thank you all for making life so much fun in Santiago. It is truly sad that none of you will be there when I return.

This work is dedicated to Nina who has put up with me and stood by me through long periods of separation.

Contents

List of Figures

Abbreviations

ACS Advanced Camera for Surveys. 6

ADC Atmospheric Dispersion Corrector. 17

ADU Analogue-to-Digital Unit. 45, 57

ARIEL Atmospheric Remote-sensing Exoplanet Large-survey. 79

BIC Bayesian Information Criterion. 32, 33, 48, 56

CCD Charged-Coupled Device. 15, 22, 45, 57, 76

CRIRES CRyogenic high-resolution InfraRed Echelle Spectrograph. 81

ELT Extremely Large Telescope. 12, 80

EMM ESO Meteo Monitor. 50

ESA European Space Agency. 50, 79

ESO European Organisation for Astronomical Research in the Southern Hemisphere. 12, 21, 49, 73, 74, 81

ESPRESSO The Echelle SPectrograph for Rocky Exoplanet and Stable Spectroscopic Observations. 81

FIMS FORS Instrument Mask Simulator. 19

FORS2 FOcal Reducer and low dispersion Spectrograph 2. 8–13, 15–19, 21–23, 26, 36, 37, 39, 43–45, 47, 50, 51, 54–56, 68, 73–76, 80

FoV Field of View. 15, 16, 18, 19, 21, 22, 26, 45, 76

FWHM Full Width at Half Maximum. 29, 36, 50

GDAS Global Data Association System. 50

GMOS Gemini Multi-Object Spectrograph. 9, 80

GMT Giant Magellan Telescope. 80

GROND Gamma-ray Burst Optical/Near infra-red Detector. 40

HARPS High Accuracy Radial velocity Planet Searcher. 11

HAWK-I High Acuity Wide field K-band Imager. 10

HST Hubble Space Telescope. 4, 6, 7, 11, 31, 48, 63, 64, 68, 74, 77, 79

IAU International Astronomical Union. 1

IMACS Inamori Magellan Areal Camera and Spectrograph. 9

IR Infra-red. 7, 10, 12, 40, 41, 74, 79–81

IRAF Image Reduction and Analysis Facility. 21

JWST James Webb Space Telescope. 7, 12, 68, 77, 79, 80

LADC Longitudinal Atmospheric Dispersion Corrector. 17, 21–23, 25–29, 34, 36, 38, 43, 44, 47, 73–75

LBT Large Binocular Telescope. 9

MCMC Monte-Carlo Markov-Chains. 33–35, 61, 63

MIPAS Michelson Interferometer for Passive Atmospheric Sounding. 50

MIRI Mid Infra-Red Instrument (on-board the JWST). 79

MIT Massachusetts Institute of Technology. 15

MMIRS MMT and Magellan Infrared Spectrograph. 10

MODS Multi-Object Double Spectrograph. 9

MOS Multi-Object Spectroscopy. 15, 18

MXU Mask eXchange Unit. 15, 18, 22, 26, 54, 55, 75

NAOJ National Astronomical Observatory of Japan. 5

NASA National Aeronautics and Space Administration. 7, 12

NIR Near Infra-Red. 40

NIRSPEC the Near InfRared echelle SPECtrograph. 10

NIRSpec Near Infra-Red Spectrograph (on-board the JWST). 79

PI Principal Investigator. 21, 22

PSF Point Spread Function. 8, 29, 36, 54

rms Root mean square. 55

S/N Signal to Noise ratio. 30, 45–47, 54

STIS Space Telescope Imaging Spectrograph. 6, 11, 63, 64

STScI Space Telescope Science Institute. 21

TMT Thirty Meter Telescope. 80

UT Universal Time. 25

UT Unit Telescope. 15, 16, 22

UV Ultra Violet. 16

VLT Very Large Telescope. 9, 10, 15–17, 22, 68, 81

WASP Wide Angle Search for Planets. 11

Nomenclature & Constants

G Universal gravitational constant (6.674×10^{-11} $\mathrm{Nm^2kg^{-2}}$). 3

$\rho_{\mathbf{jup}}$ Jupiter's density (1.33 $\mathrm{gcm^{-3}}$). 11

σ Standard deviation. 8, 10, 11

c Speed of light in vacuum (2.9979×10^{-8} $\mathrm{ms^{-1}}$). 64

h Plank's constant (6.62607×10^{-34} $\mathrm{m^2kgs^{-1}}$). 64

k_B Boltzmann's constant (1.3806×10^{-23} $\mathrm{m^2kgs^{-2}K^{-1}}$). 2, 64

u Atomic mass unit (1.6605×10^{-27} kg). 2, 8, 48

Å Ångström (10^{-10} m). 6, 10, 11, 36–40, 48, 55, 74

′ Arcminutes. 15, 22

″ Arcseconds. 15, 22, 25, 46, 47, 54

AlO Aluminium Oxide. 67, 69, 70

bar metric unit of pressure (1×10^5 pascals). 3, 7, 11, 69–71

BJD Barycentric Julian Date. 35, 62

CaH Calcium Hydride. 67, 69–71

CH_4 Methane. 10, 39–41, 81

CO Carbon monoxide. 39–41, 81

CO_2 Carbon dioxide. 10

CrH Chromium Hydride. 67, 69, 70

exoplanet Extra-solar planet (one that orbits a star other than the Sun). 1

FeH Iron Hydride. 67, 69, 70

H Atomic Hydrogen. 10, 39, 48, 76

H Atmospheric scale height. 3, 4

H_2 Molecular Hydrogen. 48, 49, 52, 67, 69, 70, 72, 77

H_2O Water. 10, 39–41, 49, 67–69, 71, 72, 77, 81

He Helium. 10, 39, 48, 67, 69, 70, 72, 76

JD Julian Date. 35, 62

K Kelvin. 6, 11, 38–40, 64, 66, 68, 70, 77

K Potassium. 11, 38, 39, 48, 49, 67, 69–71, 74–76

$M_\oplus$ Earth's mass (5.9742×10^{24} kg). 9

M_{jup} Jupiter's mass (1.8987×10^{27} kg). 11, 22

MgF_2 Magnesium Fluoride. 17, 21, 43

MgH Magnesium Hydride. 67, 69, 70

Na Sodium. 2, 11, 39, 48, 49, 67, 69, 70, 75

NaH Sodium Hydride. 67, 69, 70

NH_3 Ammonia. 81

O_2 Molecular Oxygen. 48–50

ppb parts per billion (10^{-9}). 71

ppm parts per million (10^{-6}). 10, 11, 35, 62, 71

$R_\odot$ Sun's radius (6.9570×10^8 m). 69

$R_\oplus$ Earth's radius (6.3781×10^6 m). 9

R_{jup} Jupiter's radius (7.1492×10^7 m). 11, 22, 35, 69

ScH Scandium Hydride. 67, 69, 70

TiH Titanium Hydride. 67, 69, 70

TiO Titanium Oxide. 51, 52, 67–72, 77

VO Vanadium Oxide. 52, 67, 69, 70

Chapter 1

Introduction

Since the dawn of humanity, arriving at the unknown and setting foot upon strange shores has been second nature to us. Our ingenuity and curiosity about the cosmos have pushed those destinations beyond our own home planet and towards other celestial bodies. Ever since the two Voyager probes visited all outer planets in our Solar system[1], we have sent a whole host of probes to set foot on our nearest neighbours and do our bidding in exploring the universe beyond our home. Since the discovery of the first extra-solar planets (Latham et al., 1989; Wolszczan and Frail, 1992; Mayor and Queloz, 1995), those planets orbiting other stars beyond our own sun, our domain of exploration has taken on a different dimension.

With well more than 3000 planets discovered and confirmed to date[2], the field of exoplanetary research has moved far beyond discovery, and we have begun undertaking studies to understand physical properties of these alien worlds. At the forefront of such work has been the study of atmospheres around the exoplanets that was imagined as a means of detecting life before even the detection of first planet around a main sequence star (Leger et al., 1994), and further formalised after (Charbonneau et al., 2000). Seager and Sasselov (2000) showed that for a transiting planet, one that passes the disk of its host star from the point of view of an Earth-bound observer, one could infer the presence of an atmosphere from the imprint of absorption that is superimposed on the stellar flux passing through the planet atmosphere above the limb. The theory was motivated by transit observations of the hot Jupiter planet HD 209458 b (Henry et al., 2000), where increased absorption due to possible presence of alkali metals could lead to measurable variations in the transit depth. This has since evolved to a field of exoplanetary research known as *transmission spectroscopy* that is the core subject

[1] This statement is true now since Pluto is no longer defined as a planet, and instead a dwarf planet, after the resolution passed by the International Astronomical Union (IAU) general assembly in September 2006.

[2] There are 3608 confirmed planets as of the time of writing (1st of May 2017) from the `exoplanet.eu` data archive.

of this work.

Rauer et al. (2000a,b) were among the first to search for exospheric signatures in high resolution spectra of 51 Peg b, τ Boö b and HD 209458 b during their primary transits. And it was not long before the first detection was made, where significant photometric dimming difference for a band centred on the Na doublet as compared to adjacent bands, confirmed the presence of sodium in the upper atmosphere of HD 209458 b (Charbonneau et al., 2002). It must also be noted that apart from the technique discussed here and its subsequent results, other methods such the study of reflected and emitted light from a planet's day-side be it through orbital observations (e.g. Collier Cameron et al., 1999; Leigh et al., 2003; Snellen et al., 2010a,b; Birkby et al., 2017) or the observations of secondary eclipse depth variations (Snellen, 2005; Charbonneau et al., 2005; de Mooij et al., 2011) or spectroscopy of directly imaged planets (Barman et al., 2011; Currie et al., 2013; Lee et al., 2013), have also been very successful in characterising the atmospheres of their targets. All these techniques provide complementary results due to their respective wavelength domains and the pressure levels at which they probe an exo-atmosphere.

1.1 Transmission spectroscopy

Transmission spectroscopy, as employed in this work, is the measurement of minute variations in transit depth of a transiting exoplanet, that are due to an optically thick atmosphere. Assuming an ideal gas equation of state, the pressure in a planet's atmosphere is given as,

$$\mathrm{P} = \sum p_i = k_B \mathrm{T} \sum n_i \tag{1.1}$$

where p_i is the partial pressure due to individual species present in the atmosphere, k_B the Boltzmann's constant, T the equilibrium temperature and n_i the number densities of those species. Given that the atmospheric mass density ρ is written as $\rho = n\mu u$, with $n = \sum n_i$ and μ the **mean molecular mass** of the atmosphere given in units of atomic mass unit u, one rewrites equation 1.1 as,

$$P = \frac{\rho k_B \mathrm{T}}{\mu u} \tag{1.2}$$

For a given height z within the atmosphere, the infinitesimal change in pressure dP for a height deviation dz is due to the weight of the layer of atmosphere with thickness dz and thus,

$$\frac{dP}{dz} = -\rho g = -\frac{P\mu u}{k_B \mathrm{T}} g \tag{1.3}$$

with g (=GM_p/R_p^2) being the surface gravity. Assuming that g along with μ and T are constant for a given dz, one solves equation 1.3,

$$P = P_0 \exp\left(-\frac{z}{k_B \mathrm{T}/(\mu u g)}\right) = P_0 \exp\left(-\frac{z}{\mathrm{H}}\right) \tag{1.4}$$

where the **atmospheric scale height** H represents the height above the surface at which the pressure is reduced by a factor of e and it written explicitly as,

$$\mathrm{H} = \frac{k_B \mathrm{T}}{\mu_m g} \tag{1.5}$$

with $\mu_m (= \mu u)$ the mean molecular weight (referred to as μ from this point forward). Once this scale height is defined, it is then straightforward to estimate the incremental increase in the transit depth due to the presence of an optically thick atmosphere around a transiting exoplanet. This is a wavelength dependent effect, where the increase in the transit depth, $\Delta\delta$ is given by,

$$(\Delta\delta)_\lambda = \left(\frac{(R_p + N_\mathrm{H}\mathrm{H})^2}{R_\star^2} - \frac{R_p^2}{R_\star^2}\right)_\lambda \approx \left(2N_\mathrm{H}\mathrm{H}\frac{R_p}{R_\star^2}\right)_\lambda \tag{1.6}$$

Here δ represents the transit depth, R_p is the radius at which the planet is opaque at all wavelengths, $R_\star$ is the radius of the host star and N_H is the number of scale heights, the radial dimension of atmosphere annulus intercepted by the stellar radius. Its value is expected to be between 2 and 10, with the most likely value estimated as $\simeq 5$ (Seager et al., 2009). Additionally, this approximation can be made since $H \ll R_p$ for any planetary atmosphere.

In order to model the transmission of stellar flux, at a given wavelength, in terms of the composition of the exo-atmosphere, we first write the transit depth in terms of flux,

$$\delta_\lambda = 1 - \frac{F_\mathrm{in}}{F_\mathrm{out}} = \left(\frac{R_{p,\mathrm{atm}}}{R_\star}\right)_\lambda^2 - \left(\frac{F_\mathrm{atm}}{F_\star}\right)_\lambda \tag{1.7}$$

where F_in and F_out are the observed in-transit and out-of-transit fluxes, respectively, $R_{p,\mathrm{atm}}$ is the radius of the planet plus the portion of the atmosphere to be modelled[3], and $F_\star$ is flux of the host star. It must also be noted that the first term on the right hand side is only an estimate, since determination of flux ratios also depends on the limb darkening of the host star. F_atm is the additional flux that passes a planet's atmosphere, which is obtained by integrating each beam of light over the solid angle that is subtended by that atmosphere. This is achieved by solving the equation of

[3]This is typically extended from 1 bar to a pressure of 1 μbar in calculated temperature-pressure profiles.

radiative transfer, specifically and only for absorption of starlight passing through the atmosphere,

$$I(\lambda) = I_{0_\lambda} e^{-\tau_\lambda} \tag{1.8}$$

with I and I_0 being the emergent and incident stellar intensities, respectively, and τ_λ is the wavelength dependent, line of sight optical depth that is calculated according to,

$$\tau_\lambda = \int \kappa_\lambda d\ell \tag{1.9}$$

where κ_λ is the total opacity at a given wavelength λ and $d\ell$ is the differential path of a beam along the line of sight of the observer.

Three possible make-ups of planetary atmospheres are depicted in figure 1.1. The top panel highlights a clear and extended atmosphere, which is hydrogen-dominated. This type of exo-atmosphere is easiest to probe and currently within the detection capabilities of our telescopes and instruments. For such an atmosphere, a large portion of the blue end of the penetrating stellar light is scattered through elastic processes from the atmospheric particles, what is better known as *Rayleigh scattering*. This fact means that a transit light curve measured from a filter placed at the blue end of the spectrum would be deeper and therefore lead to a larger inferred planetary radius. An example of such observations is shown in figure 1.2, where two separate instruments on board the HST are used to obtain the complete optical transmission spectrum of the hot Jupiter planet HD 189733b. Here the signature of Rayleigh scattering in the clear atmosphere of this planet is significantly detected. From this measured slope, one obtains certain characteristics of the atmosphere using the description of Lecavelier Des Etangs et al. (2008), where the effective altitude z is given by,

$$z(\lambda) = \mathrm{H} \ln \left(\frac{\xi_{abs} P_{z=0} \sigma_{abs}(\lambda)}{\tau_{eq}} \sqrt{\frac{2\pi R_p}{k_B T \mu_m g}} \right) \tag{1.10}$$

with σ_{abs} and ξ_{abs} are the cross section and abundance of the dominant absorbing species. τ_{eq} is defined as the optical depth at an altitude z_{eq} such that a sharp occulting disk of radius $R_p + z_{eq}$ produces the same absorption depth as the planet with its translucent atmosphere[4]. Knowing this relation and having observed the variations of atmospheric altitude as a function of wavelength, one derives H and the equilibrium temperature of the atmosphere T from,

$$T = \frac{\mu_m g}{k_B} \left(\frac{d \ln \sigma}{d\lambda} \right)^{-1} \frac{dz(\lambda)}{d\lambda} \tag{1.11}$$

[4]In other words, τ_{eq} is defined by $R_p(\lambda) = R_p + z_{eq}$

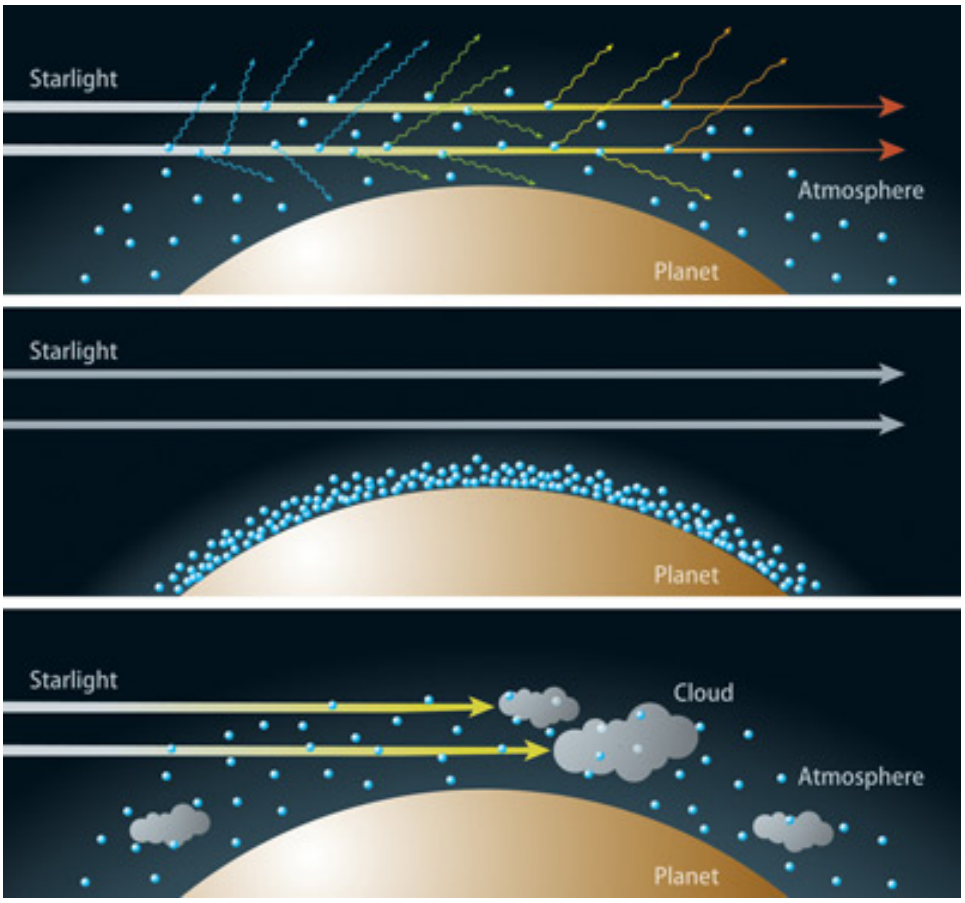

Figure 1.1: (*top*) A planet with a clear and extended atmosphere that is hydrogen-dominated. The elastic scattering, better known as Rayleigh scattering, disperses a large portion of the blue section of the stellar light passing through the atmosphere, while less of the red end of the light is dispersed, due to their longer wavelengths. As a result of this process, the transit of the exoplanet will appear deeper in photometry towards the blue end of a spectrum, as compared to the red edge.
(*middle*) If the sky has a less extended, water-rich atmosphere, the effect of the Rayleigh scattering is much weaker than in a hydrogen-dominated atmosphere. In this case, transits in all colors have almost the same transit depths.
(*bottom*) If the sky has extensive clouds, most of the light cannot be transmitted through the atmosphere, even though hydrogen dominates it. As a result, transits in all colors have almost the same depths. (Credit: National Astronomical Observatory of Japan (NAOJ))

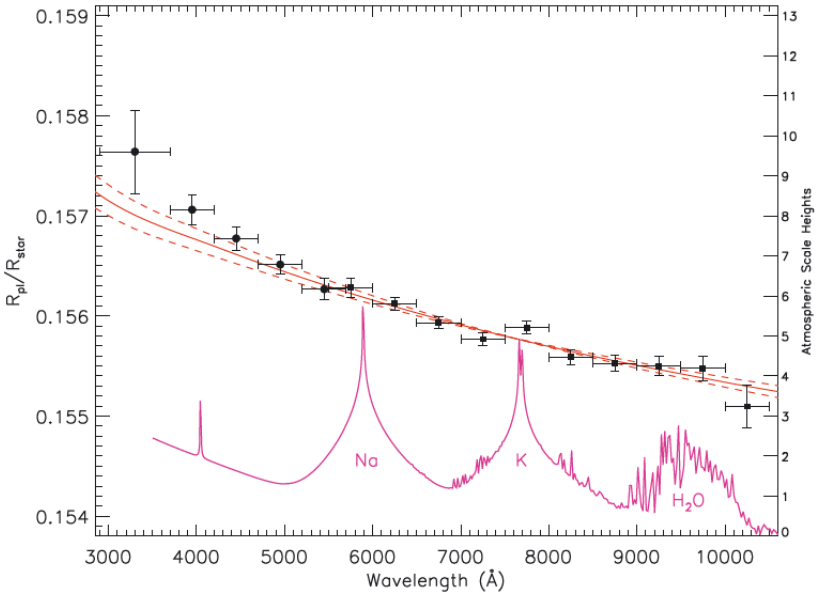

Figure 1.2: A complete optical transmission spectrum of the hot Jupiter planet HD 189733 b. This spectrum is obtained using two separate instruments on-board the Hubble Space Telescope (HST). The points blueward of 5600 Å are Space Telescope Imaging Spectrograph (STIS) G430L measurements (*circles*) of Sing et al. (2011) and those redward are from Advanced Camera for Surveys (ACS) from Pont et al. (2008) (*squares*). The secondary y-axis gives the planetary radius in units of atmospheric scale heights above the base of the atmosphere described in the text, calculated for an equilibrium temperature of 1340 K. The solid and dashed red lines represent the predictions, made only from the ACS data, for a Rayleigh scattering spectrum with $T = 1340 \pm 150$ K. The magenta line shows a haze-free model atmosphere for HD 189733b from Fortney et al. (2010) using a planet-wide average temperature-pressure profile.

From figure 1.2, if one makes the scaling assumption in the form of $\sigma = \sigma_0(\lambda/\lambda_0)^\alpha$, then the slope of the transmission spectrum is given by $dR_p/d\ln\lambda = dz/d\ln\lambda = \alpha \mathrm{H}$, and subsequently we have,

$$\alpha T = \frac{\mu_m g}{k_B} \frac{dR_p}{d\ln\lambda} \tag{1.12}$$

Making the assumption of $\alpha = -4$ for Rayleigh scattering, Lecavelier Des Etangs et al. (2008) measure a temperature of 1460 ± 130 K for HD 189733 b, consistent with estimates from other techniques (Deming et al., 2006; Knutson et al., 2007).

It is also of note to define where the planetary radius R_p, used up to now, is measured at. The limb of a planet is usually defined either at the

cloud tops, or at the 1-bar level (Atreya, 1986). Typically in transmission spectroscopy, the planet limb is defined as the boundary, the cloud tops for instance, above which a planet's atmosphere is transparent to the continuum of stellar radiation piercing through it. The clouds are assumed to be 1 pressure scale height above the cloud base, which is expected to be substantially above the 1 bar level (Seager, 1999). Therefore, it is only for the atmospheric layer above this cloud top where transmission spectroscopy method is applicable and it accounts for its probing domain.

1.2 Targets & atmospheric detections

As we have seen from the previous section, referring to equation 1.6, those transiting planets with clear atmospheres and large scale heights are ideal for transmission spectroscopy observations. A detection parameter space for the known transiting exoplanets is shown in figure 1.3 using this calculation, where the signal is plotted as a function of the host star apparent magnitude. This is because it is the magnitude of the host star that puts limitations upon the cadence and subsequently the time resolution of the observations. This has a direct impact upon the precision with which the transit depth is measured. These observations can be performed both from space-borne observatories and ground-based facilities. Each of these approaches has its own unique advantages, as well as their shortcomings. Space observatories have the advantage of not being affected by atmospheric extinction, contamination and turbulence and therefore benefit from having the entire electromagnetic range as probing domain. Transmission spectra of a variety of transiting exoplanets have already been obtained using space facilities such as the HST or *Spitzer space telescope* (e.g. Ehrenreich et al., 2007; Sing et al., 2011, 2016; Deming et al., 2013; Wakeford et al., 2013; Knutson et al., 2014). In the near future, National Aeronautics and Space Administration (NASA)'s James Webb Space Telescope (JWST; Gardner et al., 2006) will probe exo-atmospheres in the Infra-red (IR), where transmission spectroscopy from the ground is not possible due to lack of transmission in the Earth's atmosphere there. This the domain where plenty of molecular absorptions are present. However a major issue with the light curves obtained with the HST for instance is the temporal coverage, which is due to its low earth orbit and the subsequent earth occultations. This fact means that individual exoplanetary transit light curves observed with the HST are always partial. The Spitzer space telescope on the other hand only allows for photometric observations in the IR, where only two channels at 3.6 and 4.5 μm are still operational.

Ground-based observations, on the other hand, benefit from telescopes that have large primary mirrors, allowing for great collecting areas for the stellar light. Since transmission spectroscopy requires spectroscopic mea-

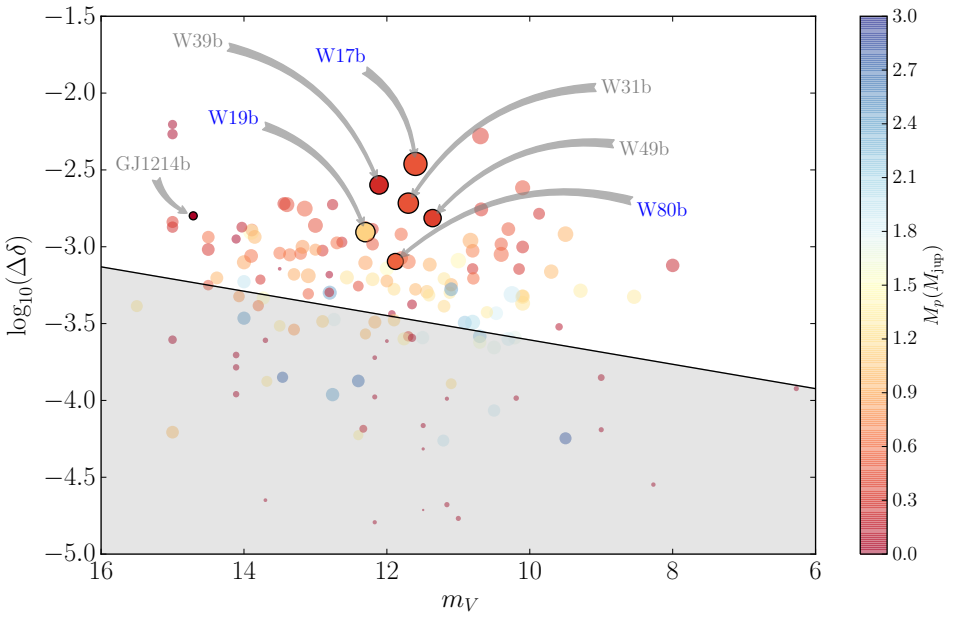

Figure 1.3: Transmission spectrum signal (the expected variation in transit depth) as a function of host star magnitude, calculated for number scale height, $N_{\rm H}$, equal to 3 in equation 1.6. Only planets with estimated temperatures are plotted. The sizes of the circles linearly correlated to the planetary radii and colours to the masses, the scale for which is given in the colour bar on the right hand side. Those planets studied through transmission spectroscopy with the FOcal Reducer and low dispersion Spectrograph 2 (FORS2) instrument have been highlighted with solid borders and annotated (those studied in the this work in blue and other studies in grey). A tentative and conservative estimate of the detection space for this instrument is shown where the exo-atmospheres in the white region should be detectable with a single transit observation with 3σ confidence. Planet parameters are based on data downloaded from `exoplanet.eu` and the scale heights are calculated assuming a mean molecular mass μ_m of 2 u.

surements at high time resolution, this is a huge asset to such facilities. To overcome the issue of telluric contamination and extinction, one has to obtain simultaneous spectra of the target star with the transiting planet and several other reference stars in the field of view. Hence, through differential spectrophotometric techniques, one removes the effects of the atmosphere to a first order. Therefore, multi-object spectroscopy is a basic necessity for performing transmission spectroscopy from the ground. One way to achieve this, is to put multiple stars in a long slit that is wide enough to encompass the entire Point Spread Function (PSF) of the stars. However, this has obvious geometrical limitations and a better way is to use

Table 1.1: Observations

Instrument	Telescope	Target	λ-range (nm)	Bin size (nm)	Reference
FORS2	VLT	GJ 1214	780–1 000	20	Bean et al. (2010)
		GJ 1214 b	610–850	10,20	Bean et al. (2011)
		WASP-19b	560–820	16–22.5	Sedaghati et al. (2015)
		WASP-17b	570–825	5–20	Sedaghati et al. (2016)
		WASP-49b	730–1 000	10	Lendl et al. (2016)
		WASP-39b	411–810	10	Nikolov et al. (2016)
		WASP-31b	400–840	15	Gibson et al. (2017)
GMOS (N/S)	Gemini	HAT-P-32b	520–930	14	Gibson et al. (2013a)
		WASP-29b	515–720	15	Gibson et al. (2013b)
		WASP-12b	720–1 010	15	Stevenson et al. (2014)
OSIRIS	GTC	HAT-P-19b	560–770	5–20	Mallonn et al. (2015)
		WASP-43b	540–920	10,25	Murgas et al. (2014)
		HAT-P-32b	518–918	20	Nortmann et al. (2016)
		TrES-3b	530–930	25	Parviainen et al. (2016)
IMACS	Magellan	WASP-6b	480–860	20	Jordán et al. (2013)
MMIRS	Magellan	WASP-19b	1 250–2 350	100	Bean et al. (2013)
DOLORES	TNG	HAT-P-1b	525–760	60	Montalto et al. (2015)
LDSS-3C	Magellan	HAT-P-26b	720–1 000	12.5	Stevenson et al. (2016)
MODS	LBT	HAT-P-32b	330–1 000	110	Mallonn and Strassmeier (2016)
MOSFIRE	Keck	GJ 3470 b	1 960–2 390	40	Crossfield et al. (2013)

designated multi-object spectrographs. There are only a handful of telescope/instrument combinations that are capable of performing such studies, most productive of which are Gemini/GMOS (Hook et al., 2004), Magellan/IMACS (Bigelow et al., 1998), LBT/MODS (Rothberg et al., 2016) and VLT/FORS2 (Appenzeller et al., 1998). The work presented in this thesis has been performed exclusively using data taken with the FORS2 instrument, and therefore transmission spectroscopy results only with this instrument will now be highlighted. However, the reader is encouraged to also refer to what has been obtained using the other ground-based facilities, a complete list of which is given in table 1.1.

GJ 1214 b

GJ 1214 b (Charbonneau et al., 2009) is a planet in the mini-Neptune regime, orbiting the M4.5, 14.71V magnitude star Gliese 1214, discovered by the MEarth project (Berta et al., 2012). It has a mass of 6.46 ± 0.99 $M_\oplus$ and a radius of 2.67 ± 0.12 $R_\oplus$. Rogers and Seager (2010) originally postulated that this planet almost certainly has a significant gas component due to

its low density ($\rho_p = 1870 \pm 400$ kg m^{-3}). Following on, Miller-Ricci and Fortney (2010) showed that structural models predict a H-He envelope of at least 0.05% the total mass of the planet, with a small possibility remaining for atmospheric compositions that include heavier atoms and/or molecules (eg. pure CO_2 or water steam). Subsequently, they calculated theoretical transmission spectra for such atmospheres and showed that for those scenarios where the atmosphere has a low mean molecular mass, the expected signal would be of the order of 0.3% (cf. figure 1.3).

The first atmospheric observations of this planet were then performed by Bean et al. (2010) using the FORS2 instrument at the VLT. They obtained a transmission spectrum for this planet at 200 Å resolution in the region of $0.78 - 1.00$ μm. They obtained a featureless spectrum in this domain, ruling out a cloud-free hydrogen-dominated atmosphere at 4.9σ confidence. Crossfield et al. (2011) observed a transit of this planet using the Near-IR high resolution spectrograph NIRSPEC on Keck II telescope. Through cross-correlation of spectral changes throughout the transit with a host of theoretical atmospheric models, they searched for planetary radius variations associated with absorption in the atmosphere. They rule out wavelength dependent transit depth variations of $\gtrsim 500$ ppm over the covered domain of $2.1 - 2.4$ μm. Subsequently, a suit of plausible atmospheres, including a gaseous hydrogen-dominated atmosphere in chemical equilibrium, are significantly discarded. Finally, they suggest that their observations point to an atmosphere that is H and He dominated but is devoid of CH_4. If this depletion would be the result of photochemical processes, the produced hazes suppress features in the optical, a fact that has been observed, as mentioned previously (Bean et al., 2010). Bean et al. (2011) performed further multi-object spectroscopic observations of this planet using again the FORS2 instrument but utilising a grism centred more towards the blue end of the visible spectrum, as well as the MMIRS instrument on the Magellan telescope covering the J, H and K atmospheric window bands. Additionally they performed photometric observations with the VLT's HAWK-I instrument using a narrow-band filter at 2.09 μm. They conclude that the data are consistent with a featureless spectrum and disagreement with the features detected by Croll et al. (2011) in the K band. Therefore the conclusion is that this planet's atmosphere must either consist of at least 70% H_2O by mass or optically thick high altitude clouds and hazes to produce the observed spectrum.

WASP-39 b

Another exoplanet whose atmosphere has been probed with the FORS2 instrument is the cool Saturn WASP-39 b (Faedi et al., 2011), annotated in

figure 1.3, from the SuperWASP[5] survey. It is a highly inflated planet orbiting a G-type dwarf, with a mass of 0.28 ± 0.03 M_{jup} and a radius of 1.27 ± 0.04 R_{jup}. Due to its very low density (0.14 ± 0.02 ρ_{jup}) and relatively high equilibrium temperature (1116 ± 33 K), it is a suitable candidate for transmission spectroscopy, a fact that is also highlighted in figure 1.3. Nikolov et al. (2016) performed such studies with the FORS2 instrument for this planet using a grism covering mid-optical range of $0.411 - 0.810$ μm. They obtained a transmission spectrum at 100 Å resolution, with spectral light curve precisions of ~ 240 ppm, rivalling the quality achieved with the HST. They detect the presence of Na in the clear atmosphere of this planet at 3.2σ confidence, as well as some evidence for K. These results are highly consistent with the spectrum observed with the HST (Fischer et al., 2016) and demonstrate the great potentials of the FORS2 spectrograph for optical transmission spectroscopy.

Others

In addition to those targets described so far, there have also been results published on two further exoplanets using FORS2 observations, besides the results the make up the core of this thesis. Those are WASP-31 b (Anderson et al., 2011) and WASP-49 b (Lendl et al., 2012), again annotated in figure 1.3. Gibson et al. (2017) obtained the transmission spectrum of WASP-31 b in the range of $0.40 - 0.84$ μm, where they detect a cloud-deck as well as a Rayleigh scattering slope. However, they rule out the large potassium feature that was previously reported using HST/STIS data (Sing et al., 2015). They hypothesise that the reason for such discrepancy is either telluric contamination of the ground-based observations, a point that will be discussed in chapter 4, or an underestimation of the uncertainties when using linear basis models to account for the systematics in the HST/STIS analysis of Sing et al. (2015).

Finally, Lendl et al. (2016) observed the exoplanet WASP-49 b using this instrument with a grism centred towards the red end of the visible domain, and therefore obtaining its transmission spectrum between 0.73 and 1.02 μm. They observed the target in three separate epochs with the same set up, and obtained a spectrum consistent with an atmosphere with high altitude clouds at the 1 mbar or lower pressure levels. More recent results, using the HARPS spectrograph have detected significant presence of Na in its atmosphere, from high resolution spectroscopy of the sodium D doublet lines (Wyttenbach et al., 2017). Their results point to a cloud free atmosphere for this planet, exhibiting an enhanced signature. This is a discrepancy that is most likely due to the significant systematic trends introduced to the light curves by the degraded atmospheric dispersion corrector of FORS2,

[5] http://www.superwasp.org/

whose characteristics are discussed in chapter 2 and its effects on differential photometric observations in chapter 3.

1.3 Aims & outline

It has been established that detection and characterisation of exoplanetary atmospheres are essential to understanding the formation mechanisms, as well as evolutionary paths of planets. Additionally, they also give us clues about the interior structures of planets (Dorn et al., 2015) and in the not-too-distant future will provide an avenue to detecting possible indications of biological processes on these alien worlds. NASA's JWST and ESO's ELT will take the next significant steps towards achieving those goals. Since the former will observe targets only in the IR domain, ground-based facilities will play an essential role in complementing its results and help to distinguish between competing atmospheric models describing them. Therefore, it is essential for us to understand and solve the challenges currently facing us in performing the precision observations required for this science goal and interpreting their results in a statistically unbiased manner. Currently being the leading instrument to perform transmission spectroscopy from the ground, FORS2 has provided the community with an invaluable outlet to embark on studying exoplanetary atmospheres. This fact has been specially true since the upgrade that this instrument went through in November 2014, which is described in detail in chapter 4. This work will look to answer these important questions:

- How and to what extent was the degraded atmospheric dispersion corrector of the FORS2 instrument responsible for introduction of systematic trends into transit light curves?
- What were the improvements made to transmission spectroscopy observations with FORS2 after the upgrade of the dispersion corrector prisms?
- What is the optimum observational strategy and instrumental set up for such observations with this instrument?
- Is the instrument capable of detecting the presence of the main optical absorbers in the atmospheres of exoplanets?
- How far can we push the instrument in detecting the finer details of exo-atmosphere through multi-channel, multi-epoch and optimised observations, in synergy with highly specialised systematic noise modelling techniques?
- How is the presence of various optical absorbers coupled with one another?

- Are metal oxides, that have been proposed as the source of temperature inversion in atmospheres of hot Jupiters, truly present and detectable in exo-atmospheres? In other words, is the TiO/VO hypothesis true?

This cumulative thesis gives a summary of works published in Sedaghati et al. (2015), Sedaghati et al. (2016) and Sedaghati et al. (2017) focusing on performing transmission spectroscopy observations with the FORS2 instrument for the purpose of detecting exoplanetary atmospheres. Sedaghati et al. (2017) presents WASP-80b observations that were performed prior to the upgrade of the instrument, highlights the systematic trends introduced by the degraded atmospheric dispersion corrector and presents a method for modelling such effects. Sedaghati et al. (2015) gives the results of the initial observations performed for testing the improvements made to the systematic trends in differential, transit light curves, via transmission spectroscopy of WASP-19b. Sedaghati et al. (2016) gives the results of improved observations with optimised observational strategy and the detection of potassium in the atmosphere of the exoplanet WASP-17b.

Additionally, results from this work have been used in publications by Boffin et al. (2015), Boffin et al. (2016b) and Csizmadia et al. (2016). A complete list of all publications is given before the Appendix.

This thesis is structured, not in the chronological order of the presented published work, but rather in the logical order of the science content of those publications. Initially, a brief introduction to the instrument used for all the observations in this work (FORS2) is presented in chapter 2, and in chapter 3 transmission spectroscopy of WASP-80b, a rare giant orbiting a cool dwarf, is done to highlight the problems associated with the prisms of the old atmospheric dispersion corrector, since the dataset was taken prior to their upgrade. Chapter 4 presents the process of the instrument upgrade and the results from the initial technical run testing the improvements made to transmission spectroscopy observations. Furthermore, it highlights results from a single observational campaign of WASP-17b, and multi-epoch observations of WASP-19b, both performed after the upgrade. Finally, chapter 5 gives a summary of all the publications that form the basis of this thesis and looks at what is to be expected from this science case in the near future.

Chapter 2

The FORS2 instrument

The FOcal Reducer and low dispersion Spectrograph (FORS2; Appenzeller et al., 1998) is the second of two almost identical multi-purpose, first generation instruments at the UT1 of the VLT. It is mounted at the Cassegrain focus[1], shown in figure 2.1. It is an all-dioptric instrument that covers roughly the entire visible wavelength domain ($\sim 0.33 - 1.10$ μm) and provides an image scale of $0.25''$ pixel^{-1} at the standard readout mode, which bins the data by 2 pixels along both axes of the CCD. It is equipped with 2 different sets of detectors, the default red-optimised MIT CCDs, and the blue-optimised E2V set taken from the decommissioned FORS1 instrument. What sets this instrument apart from others at the VLT is its multi-mode functionality. Those include,

- multi-object spectroscopy with movable arms (MOS)
- multi-object spectroscopy with exchangeable masks (MXU)
- long-slit spectroscopy
- imaging- and spectro-polarimetry
- high time-resolution imaging and spectroscopy

of which we will focus on the first two modes, MOS and MXU, as those are the ones used for work done in this thesis and transmission spectroscopy in general.

With the standard resolution collimator, the Field of View (FoV) of the instrument is $6.8' \times 6.8'$, which makes it suitable for transmission spectroscopy as it enables selection of multiple comparison stars. In the MOS mode, up to 19 pairs of arms can be moved into the focal plane to define slitlets at user-defined widths. Alternatively, in the MXU mode, the instrument also offers the possibility of inserting a custom designed mask in the

[1] This is the focal point of the secondary mirror (M2) of the telescope, situated directly below the large primary mirror (M1).

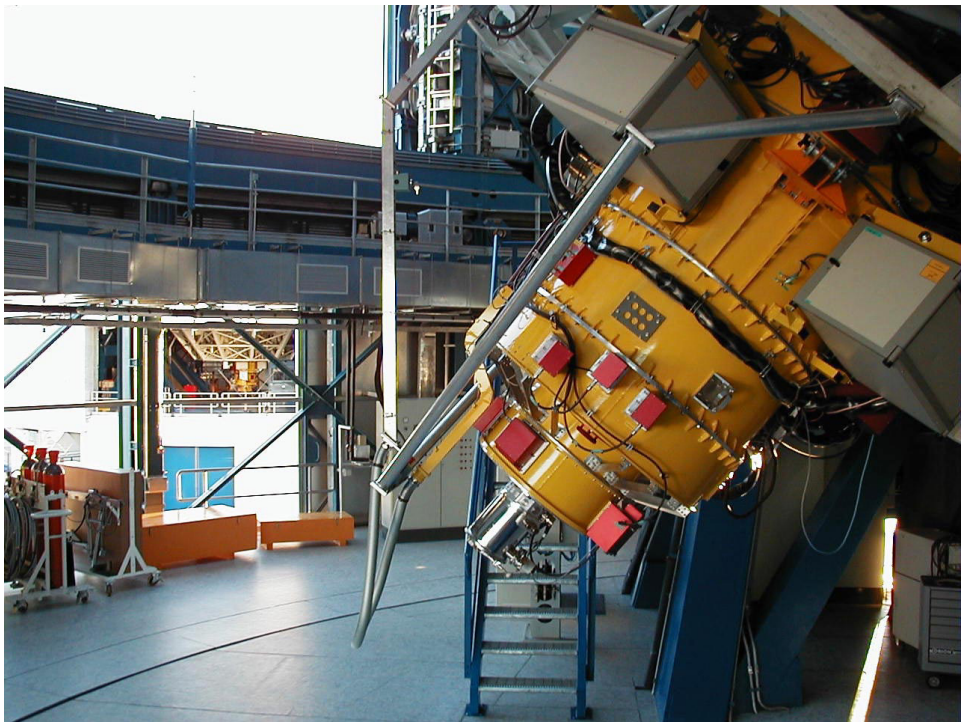

Figure 2.1: The twin FORS instruments. FORS2 is shown in the foreground at the Cassegrain focus of UT2, and the now decommissioned FORS1 instrument is visible in the background, at the same focus of UT1. In 2009 FORS1 was decommissioned to make room for the first of the second generation instruments at the VLT, namely X-shooter, where FORS2 was then moved to its current location. © ESO

focal plane, where up to 470 slits of differing length, width and shape can be cut using the dedicated laser machine. This is generally the preferred method for transmission spectroscopy, as it allows for better selection of the areas of the FoV to be passed to the dispersing grisms. The instrument comes equipped with many standard and holographic grisms of differing native resolutions and wavelength coverages[2].

2.1 Dispersion correction

In order to correct for the chromatic dispersion at high airmass that particularly affects images from large telescopes at blue/UV wavelengths, the

[2] A comprehensive list of all the available grisms, along with their specifications, can be found at www.eso.org/sci/facilities/paranal/instruments/fors/inst/grisms.html

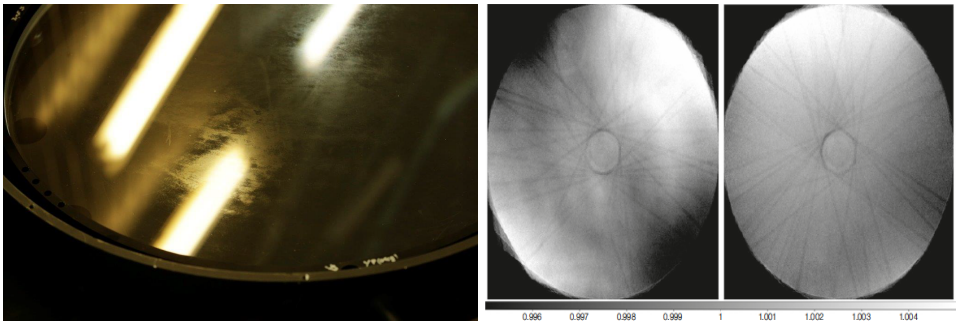

(a) (b)

Figure 2.2: (a) Image of the old LADC prism showing the degradation of the anti-reflective coating. (b) Stacked flat-field images taken with the R_Special filter before (*left*) and after (*right*) the upgrade of the instrument in 2014. The scale represents artefacts in range of ±0.5% from unity. [*(a) credit* Boffin et al. (2015) and *(b) credit* Boffin et al. (2016a).]

FORS2 instrument includes an Atmospheric Dispersion Corrector (ADC)[3]. An alternative design to the single or zero-deviation ADC was proposed by Avila et al. (1997), which is known as the Longitudinal Atmospheric Dispersion Corrector (LADC)[4] and has been part of the telescope since the operation of the instrument. It consists of two prisms of opposite orientation which are moved linearly in the vertical sense with respect to each other. The forward prism is the one that corrects the dispersion, while the second prism essentially corrects the pupil tilt.

The two prisms of the LADC have MgF_2 anti-reflective coating that in principle improves the transmission of light through them, by reducing the amount of reflection from them. However, this coating has been known to degrade with time (figure 2.2a), which leads to differential transmission of light through the unit and causes inhomogeneous artefacts in images, highlighted by flatfield images shown in figure 2.2b. This inhomogeneity is of critical importance when performing differential photometry, the consequences of which are discussed in detail in chapter 3. Since the VLT is an alt-azimuthal telescope and transit observations entail sequences spanning a few hours throughout the night, various targets are expected to pass through large paths across the LADC prisms. This is due to the field rotation and the fact that the LADC is rotationally fixed.

This thesis will look at the systematic effects introduced to transit light curves, by this differential transmission, the process of upgrading the LADC prisms and the improved transmission spectroscopic observations with the

[3]Strictly speaking this is a component of the telescope, and not the instrument since it is placed outside of it, in the M3 tower.

[4]Alternatively known as the Linear Atmospheric Dispersion Corrector.

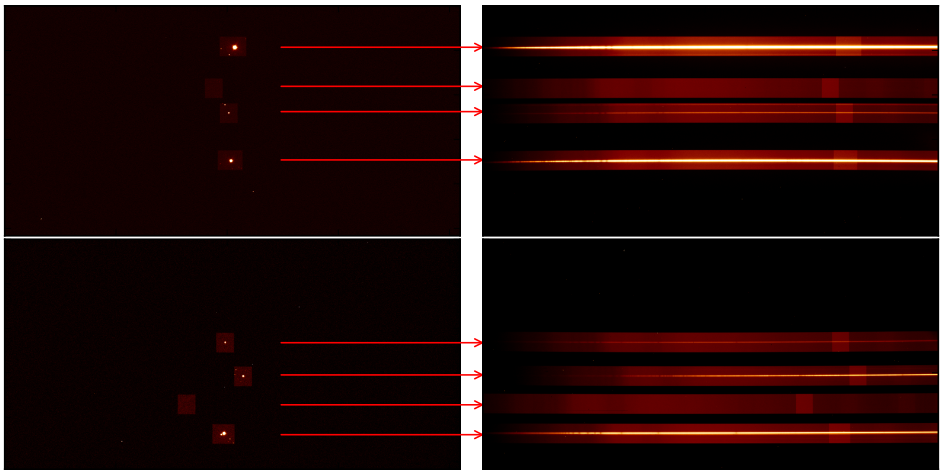

Figure 2.3: MXU observations of WASP-19 and several comparison stars with FORS2. The top panels represent chip 1 and the bottom ones chip 2 of the detector mosaic. The left panels show the MXU design and the right ones the recorded spectra after the dispersing grism has been placed in the light path.

FORS2 instrument, including various, high significance exo-atmospheric detections.

2.2 Multi-object spectroscopy

The FORS2 instrument performs multi-object spectroscopy in two modes, namely MOS and MXU. This is an essential capability of a spectrograph that is to perform observations leading to transmission spectroscopy of an exoplanetary atmosphere. MOS mode allows for simultaneous observations of up to 19 targets within the FoV with the use of pairs of arms that are individually driven by motors. This set up allows for slit widths larger than $0.3''$and slit lengths of $22.5''$, while lengths that are integer multiples of this value are also possible by stacking the slits above one another. However, this fact presents a disadvantage for this mode, as slit widths quite often have to be fine-tuned for precise inclusion of a target coupled with insertion of sky regions and exclusion of background stars in the slit. One benefit of this mode is its ability to adjust slit configuration *in situ*, which is not of concern in the science case of transmission spectroscopy.

Therefore, to overcome the aforementioned disadvantage, FORS2 also offers the MXU mode for performing multi-object spectroscopy. For this set up, one prepares a custom-designed mask with slits of arbitrary length,

width and shape[5] cut into it with a laser cutting machine situated on-site, an example of which is shown in the left panel of figure 2.3. This set up naturally allows for greater flexibility in the selection of comparison stars, which is essential in performing transmission spectroscopy. Once this mask is placed in the light path, the light from each slit is then passed through a dispersing element, a grism in this case, and the individual stellar spectra are recorded on the CCD, as shown in the right panel of figure 2.3.

2.3 Transmission spectroscopy observations

To obtain the wavelength-dependent variations of planetary radius, related to transit depth measurements given in equation 1.7, one performs differential spectrophotometric observations. This is the reason why those instruments that offer multi-object spectroscopy, are such a vital tool in exoplanet atmospheric detections. There are two prerequisite conditions that have to be met, if a viable transmission spectrum is to be obtained. Firstly, one requires high precision transit light curves, a fact that is dictated by the brightness of the target and the comparison star/s, as well as the stability and precision of the instrument, its detectors and their readout circuits. Second requirement is the necessity for high temporal observations in order to have plenty of data points throughout the transit. This is essential for determination of various parameters. For instance, plenty of points during ingress and egress are required to better determine the limb darkening of the host star, which is highly correlated with the transit depth measurements. It is therefore rather obvious the need for a telescope with a large collecting area (primary mirror), as well as an instrument with a large FoV for greater flexibility in selection of suitable comparison stars. The need for fast sampling also means that the instrument used should provide dispersing elements capable of recording low to mid-resolution stellar spectra. FORS2 ticks all the boxes above.

In preparation of such observations, great care has to be taken in selection of comparison stars and subsequently the design of the observing mask, an example of which is shown in figure 4.3 in an upcoming chapter. This mask, together with the appropriately chosen grism, will be used to record stellar spectra for a duration of time that spans at a minimum 1 hour either side of the first and the last transit contact points. The recorded, two-dimensional spectra are then to be reduced following standard astronomical data reduction procedures, such as bias and flatfield correction, sky background and cosmic ray removal, as well as a careful extraction to one-dimensional spectra, which are subsequently wavelength-calibrated us-

[5]It must be noted that there are limitations imposed on the dimensions based on the stability and robustness of the mask, which is defined with the FORS Instrument Mask Simulator (FIMS) software.

ing arc-lamp frames provided as part of the standard calibration frames. The dispersion solutions of spectra for each star are further corrected by comparing them with each other and finally a cross correction is applied across various stars. Such discrepancies among the various recoded spectra arise from seeing variations moving the centroid of each star relative to its respective, very wide slit.

Once these final, corrected spectra are obtained, one integrates them for their largest possible common wavelength domain, whose variations as a function of time result in raw photometry of the individual stars, also referred to as *light curves*. Differential transit light curves are then obtained through dividing the light curve of the star with a transiting planet by the individual comparison stars, as well as all of their possible combinations, which are then normalised to their respective out of transit flux levels. Through a statistical analysis of these light curves the final reference star/s is chosen. The integration of the target and the chosen comparison star/s is repeated for their largest wavelength domain to obtain the final broadband transit light curve. This is to be modelled for an analytical transit function, as well as a noise model, both to be introduced in the following chapter. From this modelling process, one obtains the wavelength-independent parameters of the transit, which are then used as strict priors in modelling the spectral (narrowband) light curves. These so-called *spectrophotometric* light curves are obtained by integrating the target and comparison stars within narrow integration bins, values of which are determined by an statistical analysis of light curve precision as a function of bin size across the entire wavelength domain. An example of such analysis is shown in figure 6 of Sedaghati et al. (2016), attached at the end of this thesis. The values of planetary radii determined from modelling these light curves, as a function of bin centre, gives the final *transmission spectrum*, which is used to probe the atmospheric characteristics of the planet being observed indirectly.

Chapter 3

LADC systematics

As mentioned in the previous chapter, the atmospheric dispersion corrector, better known as the LADC, of the FORS2 instrument had in the past suffered from degradation. Namely the MgF_2 anti-reflective coating had been corroded in a non-uniform manner. This fact caused differential transmission of light through the telescope optics, depending on the exact location of a star in the FoV. This effect was demonstrated in figure 2.2b of the previous chapter. The project to address this problem will be described in the following chapter. In this chapter, I will present results from the analysis of data taken prior to this upgrade, i.e. with the old, degraded LADC. Initially all data taken during this period were rendered useless due to those aforementioned systematic trends, and subsequently those datasets were not looked at by their respective PI's. As part of my work, I analysed all those datasets using my semi-automated reduction and analysis pipeline used for all the data presented in this thesis. In this chapter I present detailed analysis of one of those datasets, showing how with careful consideration of the systematic noise sources one is able to extract valuable results even from those datasets taken prior to the instrument upgrade.

3.1 FORS2 archival studies

As part of the project analysing the systematic trends in FORS2 exoplanet transit light curves, all publicly available transit sperctrophotometric observations were downloaded from the ESO archive services[1]. All these datasets were run through the automated reduction and analysis `PyRAF`[2] pipeline, which is described in more detail in section 3.2. A summary of all the datasets analysed is given in table 3.1, with the differential transit light

[1] `http://archive.eso.org/eso/eso_archive_main.html`

[2] `PyRAF` is a command language for running IRAF tasks that is based on the `Python` scripting language, and is a product of the Science Software Branch at the Space Telescope Science Institute (STScI).

curves plotted in figure 3.1. An initial analysis of these light curves concluded that exoplanet transit light curves obtained with the FORS2 instrument were generally, severely affected by the degraded LADC unit. This conclusion can be made in most cases, where differential light curves relative various reference stars show significantly differing systematic trends, owing to the individual path taken by the light of each individual star, through the prisms of the LADC. Of all the datasets analysed, transit observations of WASP-80b (091.C-0377(C) given in table 3.1) were chosen for detailed analysis of transmission spectroscopy in the presence of LADC systematics. This analysis is presented in the following section. However, as a future project, all the remaining datasets will be analysed, to try to extract all the information possible from them.

3.2 WASP-80b observations & data reduction

WASP-80b is a gas giant transiting a cool, possibly late K-type 11.88V magnitude dwarf, with a mass of 0.554 $\pm$ 0.035 M_{jup} and radius of 0.952 $\pm$ 0.026 R_{jup}, orbiting its host star with a 3.068 day period (Triaud et al., 2013). It is one of only a handful of gas giants orbiting a late-type dwarf host (e.g. WASP-43b, Kepler-45b, HAT-P-54b, HATS-6b; Hellier et al., 2011; Johnson et al., 2012; Bakos et al., 2015; Hartman et al., 2015) and has a day-side temperature within the T-dwarf range (Triaud et al., 2015). These authors also found a transmission spectrum indistinguishable from a flat line and no evidence of active region crossing by the planet (Triaud et al., 2013; Mancini et al., 2014), despite the stellar spectral analysis indicating high levels of activity (Mancini et al., 2014).

A single transit of WASP-80b was observed using Antu, the 8.2m UT1 of the VLT with the FORS2 instrument on the 16th of June 2013, with the data taken as part of the programme 091.C-0377(C) (PI: Gillon), before the LADC upgrade. The programme itself comprised of four transit observations, two of which were not performed due to bad weather, while the light curves from the fourth transit suffered from severe systematic effects and are subsequently not used for the analysis in this work, previously presented in figure 3.1. The instrument has a $6.8' \times 6.8'$ FoV and is equipped with two detectors, where the red-optimised MIT set was utilised for the observations. The instrument was used in the MXU mode, which means that a custom designed mask with $10''$-wide slits positioned on the target and comparison stars, was placed in the light path. This essentially acts as a blocking mask to free the CCD for recording of the simultaneous spectra. The 600z grism (with the order sorter filter OG590) was used as the dispersing element, yielding a spectral range of $\sim 0.73 - 1.05$ μm, although the exact wavelength coverage for each target is dependent on the horizontal location of its slit on the CCD.

Table 3.1: Summary of the FORS2 exoplanet transmission spectroscopy archival data analysis. The datasets in gray have not been presented in figure 3.1 due to lack of data or their uselessness.

Programme ID	Run	Target	Grism	Remarks
087.C-0225	C	WASP-17b	600z	Observations affected by LADC deficiencies.
	D	WASP-17b	600z	The slit was misplaced by the observers and the main target was therefore not observed.
	E	WASP-15b	600z	Observations significantly affected by LADC deficiencies.
	F	CoRoT-2b	600z	No arc frames taken, therefore wavelength calibration not possible. Data useless. Also only 37 images taken due to bad weather.
087.C-0409	A	WASP-4b	600z	Lost to bad weather.
	B	WASP-4b	600z	Light curve affected by severe LADC systematics.
088.C-0776	A	WASP-19b	600z	All but one diff. LC compromised by systematic trends.
	B	WASP-31b	600z	Severe systematic trends. Impossible to analyse.
	C	WASP-39b	600z	Not enough observations made. Most of transit missed due to bad weather.
090.C-0758[a]	B	WASP-49b	600z	Observations fine. LCs affected by clouds post transit.
	C	WASP-49b	600z	Diff. LCs affected by LADC systematics. Partial solution through specific combination of ref. stars.
	D	WASP-49b	600z	presence of correlated noise is quite evident.
091.C-0222	A	GJ 436 b	1028z	Minimal systematic effects present, but observations quite noisy.
091.C-0377	C[b]	WASP-80b	600z	Systematic noise originating from LADC present, but light curves extremely precise.
	E	WAPS-80b	600z	Severe systematic effects present during the second half transit. Most likely originating from the electronics.

[a] Data published in Lendl et al. (2016).

[b] Data published in Sedaghati et al. (2017).

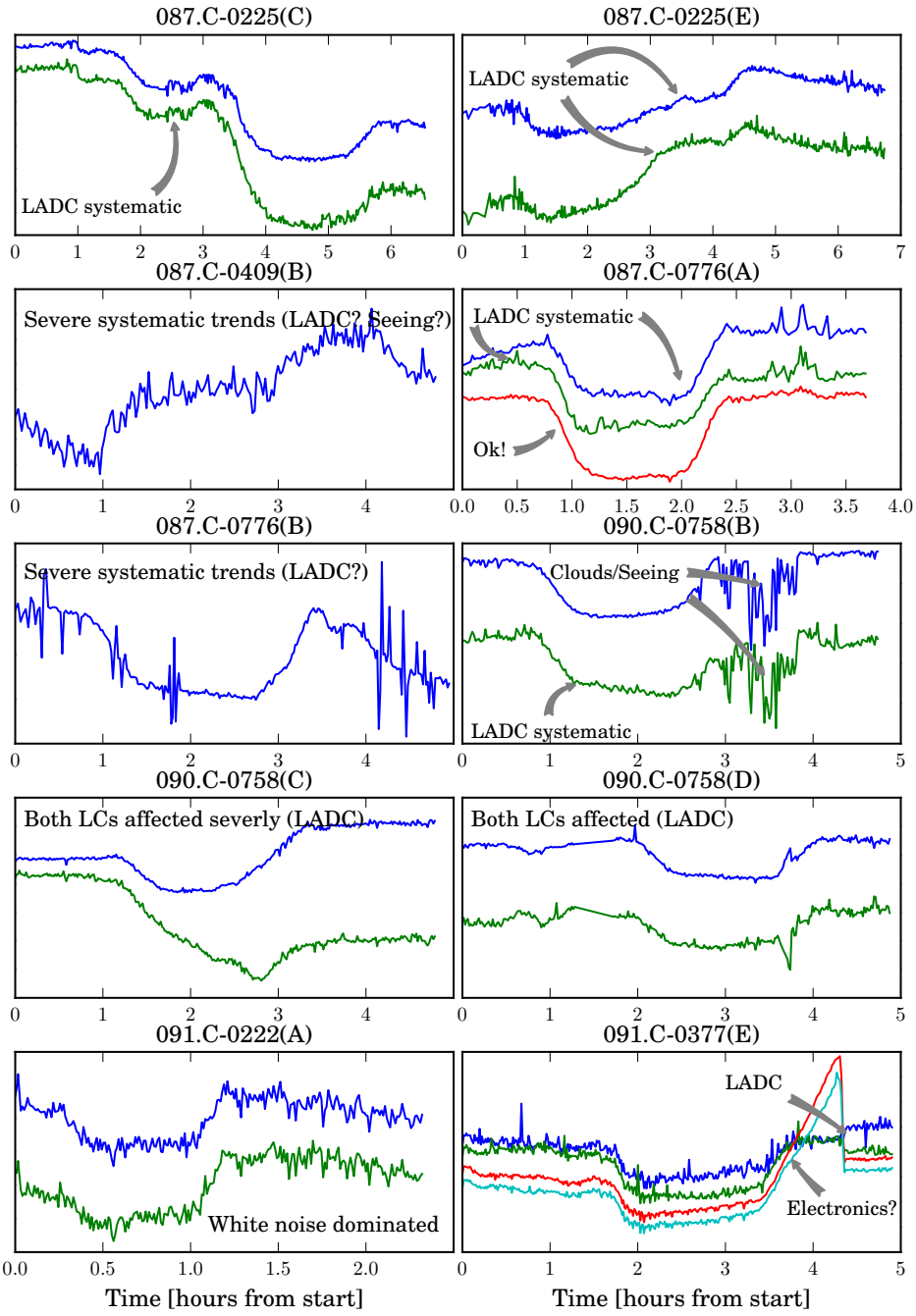

Figure 3.1: Differential broadband transit light curves for the archival datasets analysed, details of which are given in table 3.1. Different colours represent various reference stars used, that have been shifted vertically for clarity. Various systematic trends have been annotated for each plot.

The entire science observational sequence lasted ∼4.87 hours, with the first frame taken at 05:17 UT and the last taken at 10:04 UT. The complete transit lasted ∼2.26 hours, with first contact at 06:17 UT and the last one at 8:32 UT. The LADC was left in park position during the observing sequence, with the two prisms fixed at their minimal separation distance of 30 mm. The standard 100 kHz readout mode was used, which together with exposure time of 25 s (apart from the first seven frames where adjustments were made in order to reach the optimal value), yielded 277 exposures, 130 of which were during the transit. The conditions were clear throughout the night and the seeing varied between 0.97″ and 2.35″. The field started at airmass of 1.24, rose to 1.08 and the last frame was taken at airmass 1.45. A copy of the mask was created for the purpose of wavelength calibration, with narrow 1″-slits centred on the science slits. Bias, flatfield and arc-lamp (for the purpose of wavelength calibration) images were taken, as part of the routine daytime calibration sequences, before and after the observations.

A reduction pipeline based on `PyRAF`, which is optimised to the science goals of transmission spectroscopy, was used for the purpose of data reduction and analysis (Sedaghati et al., 2016). In addition to the standard steps of overscan and bias shape subtraction, spectral flat-fielding and wavelength calibration, sky background subtraction and cosmic ray contamination removal, the pipeline also includes steps for optimizing the size of the extraction box used to obtain the one-dimensional stellar spectra, performed independently for each star. We also experiment with the optimal extraction algorithm (Horne, 1986) and check to see if this in any way improves the quality of the extracted spectra, which was not the case. Once the wavelength calibrated spectra are obtained, the pipeline makes corrections to the dispersion solution calculated for each target. This is first done for all the spectra of each star through optimisation of the cross correlation function, and then the spectra of the stars are further corrected with respect to each other to ensure a consistent solution across all apertures. This is a necessary and important step due to the low resolution of the spectra. An example set of these wavelength calibrated and corrected spectra is shown in figure 3.2.

Broadband light curves

To obtain the broadband light curves, we integrate the series of spectra for each star within the largest possible common domain (shown as the grey area in figure 3.2), which are shown in figure 3.3(a). At first glance, we observe an airmass-dependent trend for all the targets, as well as the clear transit signal of WASP-80b. Initially we correct all the light curves for both of these factors, the results of which are shown in figure 3.3(b). These values are later on used to search for possible physical variants responsible for some of the systematic trends in the final differential transit light curve. We also

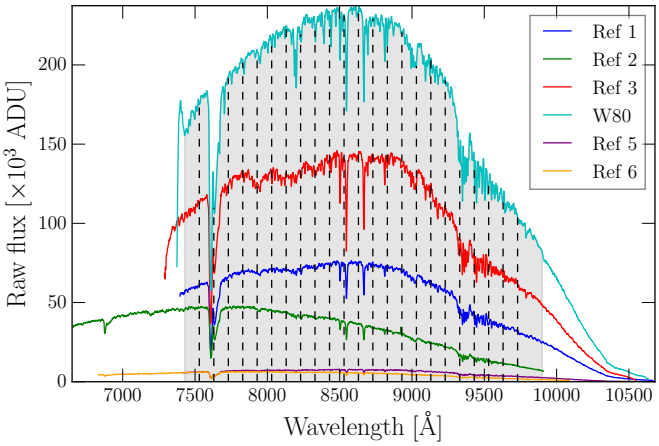

Figure 3.2: Wavelength calibrated and corrected spectra of all the stars observed with the MXU. The grey area shows the wavelength domain used to obtain all the broadband light curves. The dashed lines show the boundaries of the spectrophotometric channels, used for integration of WASP-80 and reference stars. Figure adopted from Sedaghati et al. (2017).

produce differential transit light curves of WASP-80 with respect to all the observed comparison stars, shown in Figure 3.3(c). This shows a transit light curve that is very precise and its deviations from a transit model are mostly due to systematic trends. Most significantly, we observe an almost V-shape transit, which could be interpreted as crossing of a stellar spot by the exoplanet, as was observed for WASP-52b (Kirk et al., 2016). However, this claim cannot be made until all possible sources of correlated noise in the data have been considered.

Instrumental effects

The aforementioned inhomogeneities in the degraded anti-reflective coating of the old LADC were causing differential transmission through the telescope optics, which would then manifest itself as systematic flux variations in the differential light curves. I now take a closer look at this effect.

Boffin et al. (2016a) presented the improvement in the transmission of light through the optical elements of FORS2 by comparing a stack of flat-field images from before and after the LADC exchange (figure 2.2b). For our analysis of the systematic trends attributed to the old degraded LADC (used for the observations here), I use their stacked flatfield image taken with the R_SPECIAL+76 filter, shown in figure 3.4a. The individual twi-light flatfields used to construct this frame were taken approximately a year after the observations. To this effect, the exact initial position of the FoV relative to the LADC configuration, inferred through observation of flatfield

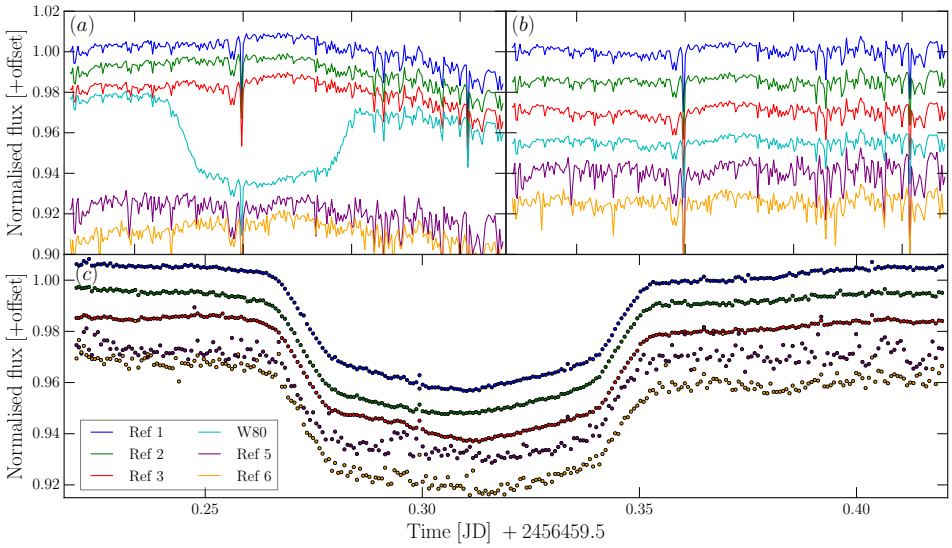

Figure 3.3: (*a*) Raw broadband light curves, normalised to out of transit level and shifted for visual aid. (*b*) Broadband light curves corrected for airmass. The transit has been removed from the WASP-80 data. This data is used to check for correlations with other physical parameters, besides the airmass. (*c*) Differential transit light curves, again normalised to the out of transit flux level and shifted for clarity. The colours correspond to the raw light curves. These data are not corrected for the airmass dependent variations, as this will be part of the analytical transit model. Figure adopted from Sedaghati et al. (2017).

inhomogeneities, is not precisely known. Therefore, one can only try to estimate this position from possible trends in the light curves. In figure 3.4a I plot the observed stars at this estimated starting position and trace the path of each star through the entire observing sequence, where every 10th exposure is shown with a dot.

To obtain the possible starting point of the field of view relative to the LADC setup, I rotate the configuration shown in figure 3.4a for 360° at 1° steps to cover all possible initial positions. If the LADC deficiencies are the cause of systematic trends in the light curve, then at the true path of the field there will be a spike in the calculated correlation between the light curve of each star (the ones that are corrected for airmass and transit, ref. figure 3.3(b)) and the flatfield value along the path taken by the star, shown in 3.4a and read in 3.5(a,b). This calculated correlation as a function of field rotation angle is shown in figure 3.4b, where the indicated peak at 86° starting angle could point to a possible relative orientation of the LADC

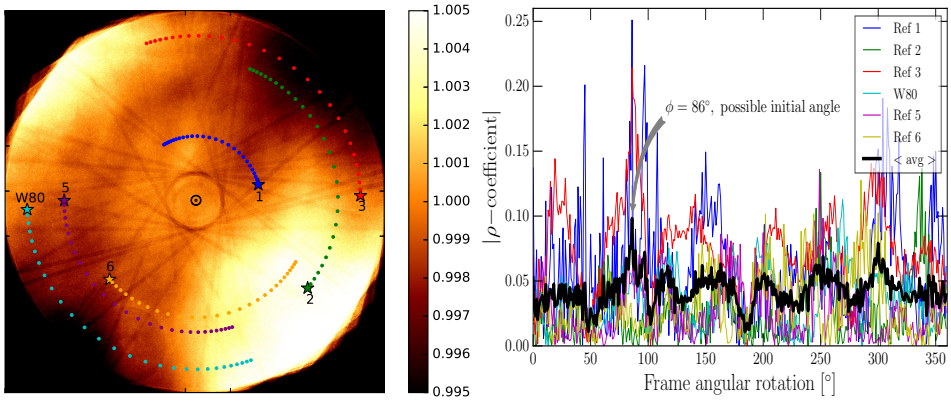

(a) (b)

Figure 3.4: (a) Studying the systematic effects due to the old degraded LADC prisms from the stacked flat-field image. The colour bar on the right shows the scale of the effect (i.e. between -0.5% and $+0.5\%$). The plotted stars are the 6 observed targets at the starting position that optimises the correlation with the light curve residuals, calculated from the adjacent plot. The dots represent the position of the star in every 10th frame. The colours are consistent with all the light curve plots and additionally each star has been labelled corresponding to the aperture number, used consistently throughout the chapter. (b) Determination of LADC deficiencies and light curve systematic trends. The initial setup is rotated, and the correlation between the flatfield value along each path, with the corresponding light curve is calculated. The thick black line represents the mean correlation value for all the stars. A lack of strong correlation indicates that the degraded LADC is not a significant cause of systematic trends in the light curves. Figures adopted from Sedaghati et al. (2017).

at the beginning of the observing sequence[3]. As a measure of correlation, I simply choose the *Pearson's correlation coefficient*, ρ, defined as the ratio of the covariance of the two variables ($\mathrm{cov}(x, y)$) to the product of their respective standard deviations (σ_x, σ_y).

In order to study the impact of the LADC inhomogeneities on the measured light curves, I read the normalised flatfield value along the path of each star, for this given starting position, which is shown in figure 3.5(a). I use the normalised flatfield, as its variations are a direct indication of the problems caused by the degraded LADC coating. Additionally, since we are also interested in the correction of the differential transit light curves, as a second order correction, I also calculate the ratio of these readings to

[3]It must be noted that this value is 3° offset from what is calculated based on the orientation of the stacked flatfield image.

the values read along the path of WASP-80. This is shown in figure 3.5(b). The calculated correlation between the light curve residuals and the flatfield variations due to the degraded LADC is rather weak, which means that the LADC is not a major contributor to the systematic trends. However, it must be noted that the flatfield images used to construct the composite image in figure 3.4a were taken more than a year after the epoch of the observations analysed in this work. Therefore, the conclusion about the impact of the LADC deformities is rather tentative.

A further possible cause of correlated noise is the spatial stability of the instrument. I characterise the positioning of stellar spectra on the detectors along two axes, spatial and spectral (Δy & Δx). The former variation is measured by taking the mean of the mid-points of several fitted Gaussian profiles to the two-dimensional images across the entire frame in the spatial direction, which are plotted relative to the initial frame in figure 3.5(e). The latter is measured in a similar way, but instead several telluric absorption features are fitted in the one-dimensional spectra, shown in figure 3.5(c). Studying the relations between both of these variables indicated no significant correlation with the flux variations, which is perhaps due to the stability of the instrument and the data reduction procedure accounting for any remaining residual effects.

Telluric effects

In addition to the instrumental effects mentioned previously, telluric conditions also play a significant role in introducing time-correlated noise into the measured time-series data. Namely, variations in the measure of atmospheric seeing, due to turbulence, cause changes in the stellar PSF along both the dispersion and the physical axes. The former is measured as the FWHM of Gaussian profile fits to several telluric absorption lines in the one dimensional spectra, variations of which are shown in figure 3.5(d) and denoted as "<sky> fwhm". This is essentially the convolution of the instrumental profile and the true stellar profile, and therefore a measure of variations in the stellar psf given the instrument response is constant. The FWHM of the PSF along the physical axis is also measured through recording the characteristics of several Gaussian function fits to various columns (orthogonal to the dispersion axis) of the two dimensional spectra. These are shown in figure 3.5(f), as "psf fwhm" in units of arcseconds, which is another approach to measuring the seeing variations.

I compare the variations of seeing measured separately for each star (from the PSF FWHM) to the normalised flux after the correction for the airmass trend. For WASP-80, additionally, the transit feature is also removed for these calculations, in order to maintain a constant degree of freedom in all correlation calculations. For the measure of correlation, I again use Pearson's parameter described briefly earlier. The levels of correlation between

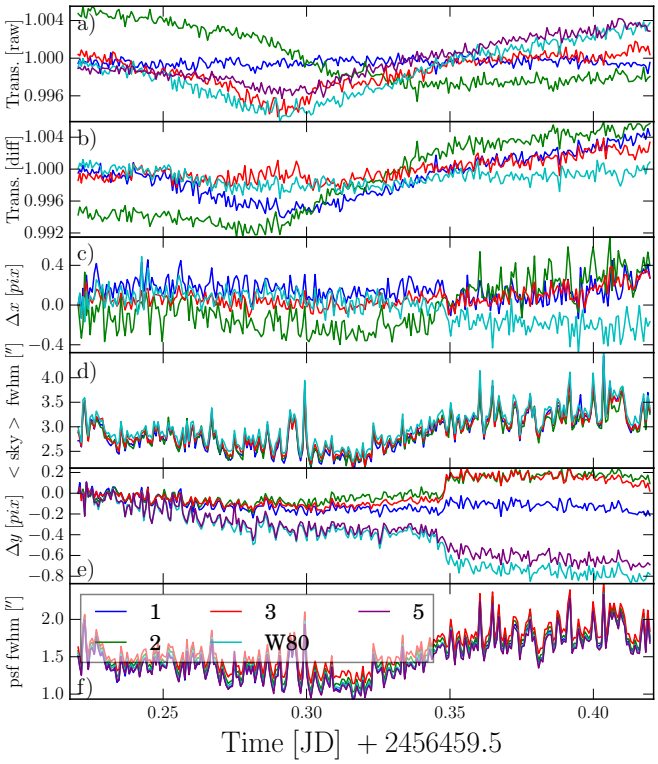

Figure 3.5: Measurement of physical variants that could possibly introduce systematic trends in the light curves. (a) Shows the measurement of normalised flatfield flux along the (most likely) path of the individual stars, and (b) represents the same measurements but relative to the values of WASP-80's path. (c) Shows the measurement of spectral shift in the dispersion direction relative to the first observation calculated by measuring the centres of multiple telluric absorption features across the entire spectrum, and (d) is the average FWHM values of those fitted gaussian profiles, which is dependent on seeing conditions. (e) Indicates the drift of spectra along the physical axis relative to the first frame, calculated by again fitting multiple gaussian functions along the physical axis of the two dimensional spectra, and (f) shows the variations of FWHM values of those fitted profiles. These variations are identical in shape to what was measured along the dispersion axis as expected, and are used as a direct measure of seeing condition variations. These parameters have not been calculated for reference star 6 due to its very low spectral S/N. Figure adopted from Sedaghati et al. (2017).

individual flux variations and atmospheric seeing are consistent across all the stars and point to a *moderate* association between the two parameters. The relation between each pair of parameters is calculated using an *orthogonal least squares* approach (Isobe et al., 1990), using the `odr` package from `python`'s `scipy` (Jones et al., 2001). This is preferred to the standard linear regression approach due to the present uncertainties in determining "psf fwhm". I use the gradients of these relationships to transform the measured seeing values to flux variations for each star, which in turn will be used as an input of the systematic model, to be described shortly. I choose this approach instead of constructing a correction model to avoid the introduction of biases in parameter determination and error estimation.

3.3 WASP-80b transit light curve model

Transit light curves are modelled with the implementation of the analytic solution of Mandel and Agol (2002) as the mean function. Additionally, the correlated noise is estimated as a Gaussian Process (GP), which provides a model-independent stochastic method for the inclusion of the systematic component into the model (Rasmussen and Williams, 2006). The application of GPs to modelling exoplanet transit light curves and transmission spectroscopy was introduced by Gibson et al. (2012b). The strength of this approach in accounting for systematic trends was highlighted in the detection of hazes in the atmosphere of the exoplanet HD 189733 b, where auxiliary information from the HST were used to train the GP model (Gibson et al., 2012a). Subsequently, I use their `GeaPea` and `Infer` modules[4] for the definition of the GP and the implementation of Bayesian inference.

In the Bayesian framework, the likelihood function, $\mathcal{L}$, is written as a matrix equation in order to introduce off-diagonal elements to the covariance,

$$\log \mathcal{L}\left(\boldsymbol{r}|\mathbf{X},\theta,\phi\right) = -\frac{1}{2}\left(\boldsymbol{r}^T\boldsymbol{\Sigma}^{-1}\boldsymbol{r} + \log|\boldsymbol{\Sigma}| + N\log 2\pi\right) \tag{3.1}$$

where $\boldsymbol{r}(= f_i - M_i)$ is the residual vector with M being the transit model, $\mathbf{X}$ is the $N \times K$ input parameter matrix (K being the number of inputs and N being the number of data points or flux measurements), θ and ϕ are collections of noise and transit model parameters respectively, and $\boldsymbol{\Sigma}$ represents the covariance matrix. Ideally one would like to make every element of the covariance matrix a free parameter in the model, but the size of the matrix ($N \times N$) makes this rather impractical. Hence one "models" those elements using a covariance function, more commonly referred to as the *kernel*. With the aid of this kernel, the covariance matrix is written as $\Sigma_{ij} = k(x_i, x_j, \theta) + \delta_{ij}\sigma^2$, x being an input of the kernel, δ the Kronecker

[4]Written in `Python` programming language and available freely from the following repository: `https://github.com/nealegibson`

delta and σ^2 the variance term, the last two of which ensure the addition of Poisson or white noise to the diagonal of the covariance matrix.

For the kernel, I use the Squared Exponential (SE)[5] kernel, which for a multi-dimensional parameter space (K), in its additive form, is written as,

$$k_{SE}(x_i, x_j, \theta) = \zeta \exp\left[-\sum_{\alpha=1}^{K} \eta_\alpha \left(x_{\alpha,i} - x_{\alpha,j}\right)^2\right] \tag{3.2}$$

where ζ is the maximum covariance and η_α are inverse scale parameters for all the input vectors $\mathbf{x}$ (essentially the columns of the $\mathbf{X}$ matrix). This parameter determines the length of the "wiggles" in the function. I choose this form for the kernel as it is the de-facto default form for GPs as it is infinitely differentiable and easy to integrate against most functions. Other choices of kernels will be discussed later on in this thesis.

Finally, in the definition of the analytical transit function, I use the quadratic limb-darkening (Kopal, 1950) law to describe the centre to limb variations of brightness across the stellar disk. I made this choice after the comparison of the Bayesian Information Criterion (BIC) (Schwarz, 1978) values for models of higher complexity, such as the three parameter (Sing, 2010) or the non-linear Claret (2000) laws.

I model the best two broadband differential transit light curves shown in figure 3.3(c), which are produced by using the comparison stars 1 and 2 (top two), as the other light curves are either too noisy or suffer from large systematic effects. These light curves are obtained by the integration of the relevant spectra within the domain that is shaded in grey in figure 3.2. In addition to the transit function, we also include a quadratic term in the description of the analytical transit model, to account for the colour-dependent, second-order airmass effect in the differential light curves.

To find the maximum posterior solution, $\mathcal{P}$, one needs to optimise the Bayesian relation,

$$\log \mathcal{P}\left(\theta, \phi | \boldsymbol{f}, \mathbf{X}\right) = \log \mathcal{L}\left(\boldsymbol{r} | \mathbf{X}, \theta, \phi\right) + \log \mathrm{P}\left(\theta, \phi\right) \tag{3.3}$$

which is true up to a constant term, where the final term on the right hand side of the equation is the prior probability assumed for the parameters of the complete model. I generally use uninformative priors for the transit parameters, with the exception of the linear and quadratic limb darkening coefficients ($c_{1,2}$), the orbital period, P, and the eccentricity, e, according to:

$$\mathrm{P}(\phi) = \begin{cases} \mathcal{N}(3.06785234, 10^{-10}) & \text{for } \phi \in [\mathrm{P}], \\ \mathcal{N}(0, 10^{-10}) & \text{for } \phi \in [e], \\ 0 & \text{if } c_1 + c_2 > 1, \\ 1 & \text{otherwise.} \end{cases} \tag{3.4}$$

[5] Also known as the Radial Basis Function

which fixes the period and eccentricity of the orbit to what has previously been determined by Triaud et al. (2013), and also ensures positive brightness across the stellar disk. For the noise model parameters, we set the following prior probability distributions,

$$\mathrm{P}(\theta) = \begin{cases} \Gamma(1,1) & \text{for } \theta \in [\zeta, (\eta_1, ..., \eta_K)]\,, \\ 0 & \text{if } \sigma_w < 0, \\ 1 & \text{otherwise.} \end{cases} \tag{3.5}$$

to ensure positive values for all the parameters, as well as using a gamma distribution[6] with shape and scale parameters both set to unity, $\Gamma(1,1)$, to encourage their values towards zero if the inputs that they represent are truly irrelevant in explaining the data (Gibson et al., 2012b).

For the starting values of the fitted parameters, I use the Nelder-Mead simplex algorithm (Nelder and Mead, 1965) to find an initial set of optimal solutions for the transit and noise parameters. To find the maximum posterior solution, I optimise the log posterior given in equation 3.3. These parameter posterior distributions are obtained by using the Monte-Carlo Markov-Chains (MCMC) method to explore the joint posterior probability distribution of our multivariate models (Collier Cameron et al., 2007; Winn et al., 2008; Gibson et al., 2012b). I run four independent MCMC simulations with 100 walkers, of 100,000 iterations each. Once the chains are computed, I extract the marginalised posteriors for the free parameters to check for mutual convergence and for possible correlations among any pairs of parameters. The transit parameters that are fitted for are mid-transit time (T_0), scaled semi-major axis ($a/R_\star$), relative planetary radius ($R_p/R_\star$), impact parameter (b), limb-darkening coefficients (c_1 & c_2), the three coefficients of the baseline model. This model is a second order polynomial of the parallactic angle $p^2(q)$, whose complexity is chosen using again the BIC selection rule. This baseline model was initially chosen as a quadratic in time, which would describe low frequency variations due to the colour difference between the target and the comparison star. However, this approach results in out of transit flux fit that is worse than using the parallactic angle, and additionally leads to an overestimation of planetary radius as compared to previous results from photometry in our wavelength region. In addition to these, we also fit for the noise model parameters (ζ, $[\eta_1, ..., \eta_K]$, σ^2).

In order to decide what input parameters to include in the description of the GP model, as well as which of the two final broadband light curves suffer less from systematic effects, I model both of these broadband data series with the previously described model using up to three input parameters for the kernel. I did not find any evidence of correlation with any other optical state parameters, to justify their initial inclusion into our model. To compare the

[6]The probability density function for a gamma $\Gamma(k,\theta)$ distribution of a variable x is given by $f(x,k,\theta) = x^{k-1}\exp(-x/\theta)/\theta^k$.

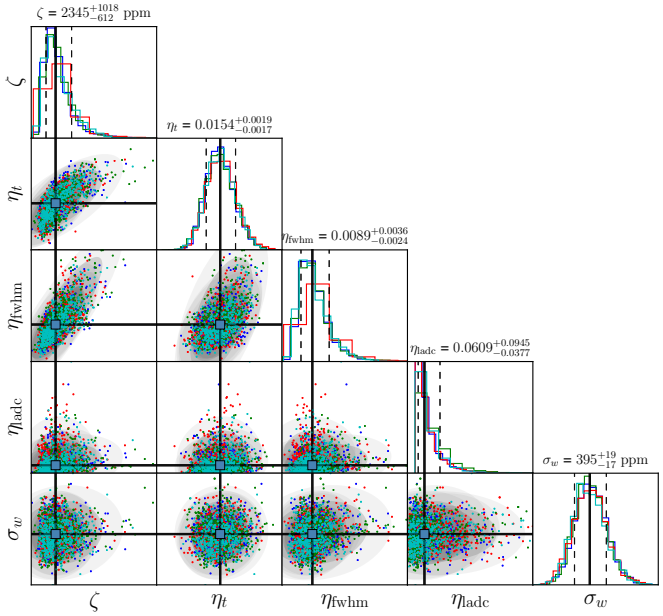

Figure 3.6: Correlation plots for the noise model parameters, as well as their posterior distributions, shown for the broadband transit light of WASP-80b obtained relative to reference star 1. The four colours correspond to the 4 independent MCMC simulations, each of 100,000 length. For the scatter plots, I choose a random subset from each chain. The final quoted parameter values are plotted as blue squares and their values, together with their associated errors, are given on top of each relevant posterior plot. Figure adopted from Sedaghati et al. (2017).

fitted models, I calculate their BIC values, which include a penalty term for addition of complexity to a model. This analysis indicates that the systematic model is best able to describe the broadband light curve relative to the comparison star 1, when *time*, *seeing* and the *ladc inhomogeneity* are all used to model the covariance matrix. However, it must be noted that there is some evidence against this model relative to the case that does not include the LADC variations (ΔBIC$\leq$6), but I choose to include this final parameter due to the small increase in the reduced chi-squared statistic (χ^2_ν). The correlations and posterior distributions of the parameters of this noise model are given in figure 3.6. From these posterior probability distributions I infer that the noise model input parameters are significantly relevant in describing the data, as the inverse length scale values, η_i, for all the inputs are $> 3\sigma$ away from 0, with the exception of $\eta_{\rm ladc}$ ($\sim 2\sigma$).

The best fit noise model, as well as the corresponding transit function are given in figure 3.7 (as red and blue lines respectively), for the broadband light curve obtained relative to reference star 1, as discussed previously. The

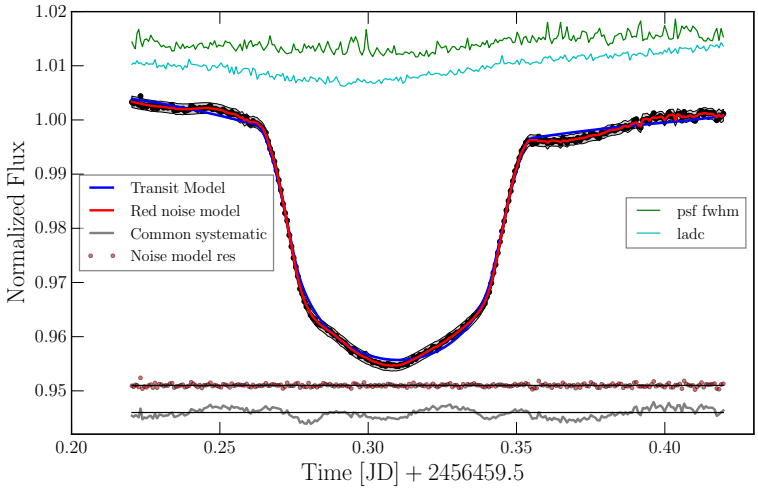

Figure 3.7: Broadband transit light curve of WASP-80b. The dark blue line is the best fit transit model and the red line is our systematic model with three inputs and the dark and grey areas are the 1- and 3-σ confidences of that model, respectively. The residuals of this model are shown as red dots below the light curve, shifted for clarity. The grey line represents the common mode correction, which is essentially the residuals of the transit model alone (with the systematic noise model). The green and cyan lines at the top of the plot are the inputs of the covariance kernel, i.e. the PSF FWHM and the differential LADC discrepancy, respectively.

inferred transit and noise model parameters from this fit are given in table 3.2, together with their 1-σ uncertainties. The inferred transit parameters are in statistical agreement with those values reported by previous studies, covering a similar wavelength domain as the FORS2 observations (Triaud et al., 2013, 2015; Mancini et al., 2014; Fukui et al., 2014). I particularly use those values obtained by Mancini et al. (2014) as a benchmark due to their high precision light curves and the common wavelength coverage of their observations, namely in Sloan i' and z' filters.

3.4 WASP-80b transmission spectrum

To obtain the wavelength dependent variations of the planetary radius, i.e. the transmission spectrum, the spectra are integrated within smaller, 100 Å bins, that are shown as dashed lines in figure 3.2. This bandwidth determines the resolution of the final transmission spectrum and is chosen through a statistical analysis of stellar spectra (Sedaghati et al., 2016). This bandwidth is similar to most previous transmission spectroscopy studies performed with the FORS2 instrument (Bean et al., 2011; Lendl et al., 2016;

Table 3.2: The inferred transit parameters of WASP-80b from the analysis of MCMC simulations.

Transit Parameter	Value
Mid-Transit, T_0, [JD] +2456459	$0.80879 \pm 7.3\times10^{-5}$
Barycentric corrected T_0 [BJD_{TDB}]	2456459.809578
Scaled semi-major axis, $a/R_\star$	12.0647 ± 0.0099
Relative planetary radius, $R_p/R_\star$	0.17386 ± 0.00030
Impact parameter, b	0.2325 ± 0.0087
Linear LD coefficient, c_1	0.491 ± 0.238
Quadratic LD coefficient, c_2	0.485 ± 0.198
Noise Parameter	
Maximum covariance, ζ [ppm]	2345^{+1018}_{-612}
Time inverse scale parameter, η_t	0.0140 ± 0.0018
fwhm inverse scale parameter, $\eta_{\rm fwhm}$	$0.0089^{+0.0036}_{-0.0024}$
ladc inverse scale parameter, $\eta_{\rm ladc}$	$0.0609^{+0.0945}_{-0.0377}$
White noise, σ [ppm]	395 ± 18
Derived parameter	
Planet radius, R_p [R_{jup}]	$0.99^a \pm 0.03$
Orbital inclination, i [°]	88.90 ± 0.06

[a] Calculated using the stellar radius of $0.586 \pm 0.018 R_\odot$ from Triaud et al. (2015).

Sedaghati et al., 2016; Gibson et al., 2017) and those initial raw so-called spectrophotometric light curves are shown in the left panel of figure 3.8. As one looks for relative variations of transit depth in transmission spectroscopy, these spectral light curves are corrected for the common mode systematics that are present across all the channels (e.g. Lendl et al., 2016; Nikolov et al., 2016; Gibson et al., 2017). The common mode systematic correction is obtained through the division of broadband or white light curve by the analytical transit model that includes the baseline model as a quadratic function of the parallactic angle and no correlated noise component. This correction sequence is shown as the grey line at the bottom of figure 3.7. Subsequently, the spectral light curves are divided by this common correction term and modelled with the same systematic noise model as was done for the white light curve. The corrected spectral light curves, together with the associated correlated noise models, are shown in the right panel of figure 3.8.

It must also be noted that the impact of the presence of unocculted spots on the stellar surface is estimated, which is wavelength domain of the observations causes insignificant relative variations in the inferred relative planetary radius values. More details are given in the manuscript of the publication related to this chapter (Sedaghati et al., 2017).

In modelling the spectral channels I set strict, informative priors on the values of model parameters that are wavelength independent (T_0, $a/R_\star$, b). Since the limb darkening of the star is a chromatic aspect, the two coefficients of the law describing the centre to limb intensity variations are taken as free parameters in modelling the narrow-band light curves, with prior probabilities same as the broadband case. One would also expect that seeing- and LADC-dependent systematics to be wavelength independent, which are removed by the common mode correction approach. To confirm this, I allow their respective inverse scale parameters ($\eta_{\rm fwhm}$ and $\eta_{\rm ladc}$) to be free in our analysis, and check whether their posterior distributions approach zero for each channels, which in fact was the case for all light curves. This procedure also ensures that uncertainties from any residual systematics are fully accounted for and their contributions to the final parameter error estimation are correctly propagated. The transmission spectrum, obtained from this modelling process is given together with results from previous studies (Mancini et al., 2014; Fukui et al., 2014; Triaud et al., 2015) in panel *(a)* of figure 3.9, and separately in panel *(b)*.

Additionally light curves from very narrow (30 Å) integration bins around the potassium doublet absorption region (0.766 & 0.770 μm) are produced for possible detection of K. We modelled these light curves with the same approach as was done for the 100 Å spectroscopic light curves, the results from which are shown in figure 3.9c.

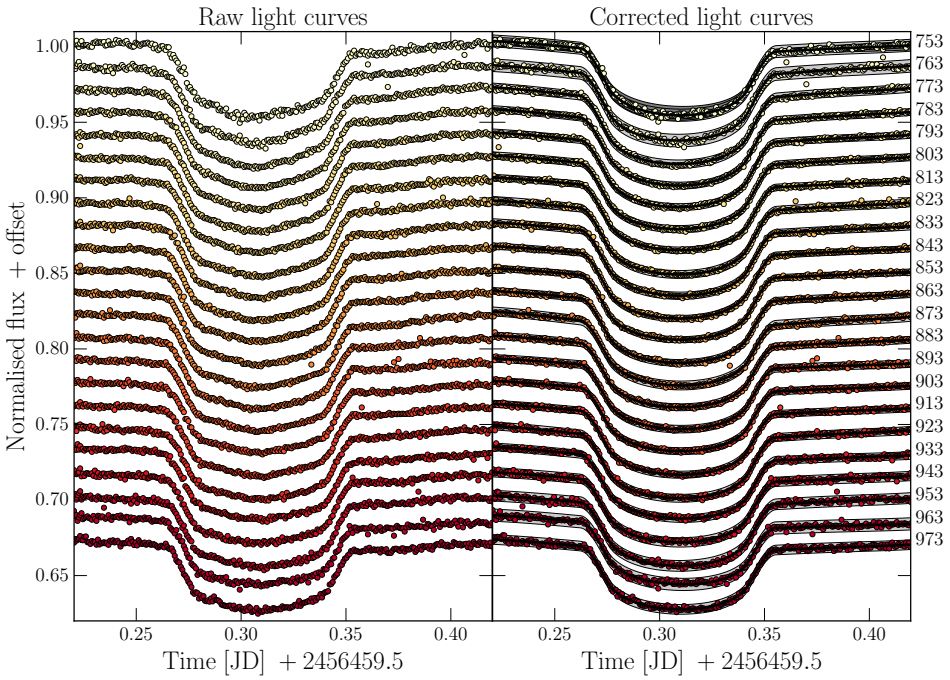

Figure 3.8: Spectrophometric light curves of WASP-80b transit, obtained through narrowband integration of spectra from the FORS2+600z grism, normalised to out of transit flux and shifted for clarity. The left panel shows the raw differential light curves, and the right panel presents the same light curves corrected for the common mode of systematics. The central wavelength of each channel is given to the right of each light curve, with bin size of 100 Å. The best fit transit model for each channel is given as a solid black line, with the 3σ confidence of each fit shaded as light grey. Figure adopted from Sedaghati et al. (2017).

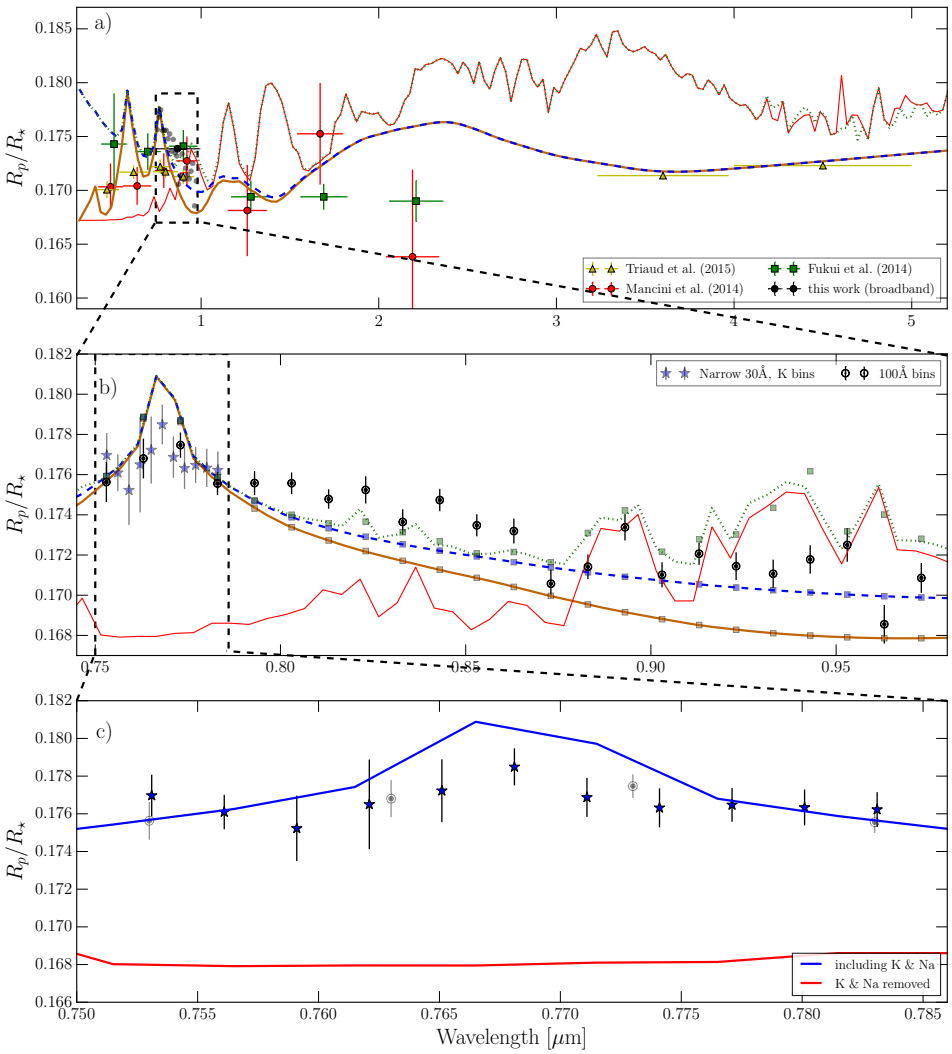

Figure 3.9: *(a)* Broadband transmission spectrum of WASP-80b stitched together from previous studies of this planet, as well as the broadband and spectroscopic points form our analysis. The three overplotted atmospheric models are produced with the `Exo-Transmit` code, at 800 K equilibrium temperature, 0.1× solar metallicity. The black dotted model includes the three molecules, H_2O, CO and CH_4, as well as H, He, Na and K. The blue dashed and brown solid lines are the same as the previous model, but with the molecular species removed, where in the brown model Rayleigh scattering has additionally been switched off. *(b)* A zoom into the region, where our transmission spectrum of WASP-80b is obtained with the 600z grism of FORS2, produced with bins of 100 Å width. The plotted models are the same as above. *(c)* A further zoom into the region of absorption from the potassium line core and the wings. The presence of potassium in the upper atmosphere is detected using the results from very narrow (30Å) bins, where confirmation is made through a comparison with models that include potassium (*solid blue, same as the dashed blue in the above plots*) and one that excludes it (*solid red*). Figure adopted from Sedaghati et al. (2017).

3.5 Discussion

To interpret the observational results, I compare the transmission spectrum from the previous section to a variety of forward atmospheric models that explore a wide range of the parameter space, limited by abundance files provided by the atmospheric modelling code. For this purpose, I use the open source, publicly available `Exo-Transmit`[7] code (Kempton et al., 2017) to model the planet size variations as a function of wavelength, using the opacity information provided (Freedman et al., 2008, 2014; Lupu et al., 2014). It must be stressed that I do not fit these spectra to the data and simply over-plot them for comparison. Triaud et al. (2015) measured the brightness temperature of WASP-80b as $\sim$ 900 K from *Spitzer* photometry of occultations, with the equilibrium temperature calculated as 825 ± 19 K. Consequently, I calculated theoretical spectra for 700 K, 800 K and 900 K equilibrium temperature T-P profiles, where a comparison of the reduced chi-squared statistic, χ^2_ν, as measured with the combined transmission spectrum (c.f. figure 3.9a), suggests a significantly better fit for equilibrium temperature of 800 K as compared to 700 K, and marginally better with respect to the 900 K models. This result is in agreement with the estimated equilibrium temperature of the exo-atmosphere. Therefore, from here on, I only plot models calculated with the 800 K equilibrium temperature T-P profile, and quote statistics based on this assumption.

Comparison to theoretically calculated models indicates a solar or sub-solar (1 or 0.1) metallicity for the atmospheric composition of this planet, with larger values ($5-1000\times$) yielding significantly larger χ^2_ν statistics. Furthermore, for all the models evaluated, we consider the case where condensation and rain out of molecules occurs. Again the comparison significantly suggests no evidence for rain out and therefore we compute the spectra with only gas phase chemistry accounted for. The complete transmission spectrum (Figure 3.9a) rules out the presence of absorption from H_2O, CO or CH_4 in the atmosphere, all of which have been included in the *dashed* model, and removed from the other two. I rule out their presence at $\gg 5\sigma$ significance, calculated through the bootstrap of transmission spectrum values and their associated errors (the estimated χ^2_r distributions are shown in the left panel of figure 3.10). This result is achieved mainly through the precise photometry of *spitzer* in the IR and GROND in the NIR. Additionally, the analysis gives marginal preference to models without a Rayleigh scattering signature, although this conclusion is not statistically significant ($\sim 2\sigma$). As mentioned earlier, the results also point to an atmosphere with sub-solar metallicity, although the exact level of it would need to be determined more precisely with retrieval models, once more spectroscopic data

[7] Available at the following repository: https://github.com/elizakempton/Exo_Transmit

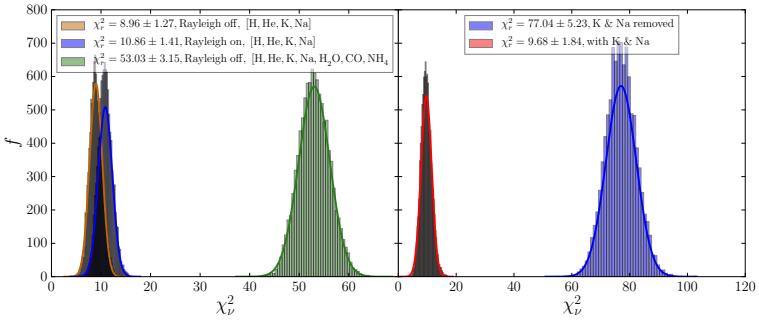

Figure 3.10: *(left)* χ^2_r distributions for the three atmospheric models shown in figure 3.9a, measured together with the data from broadband photometry. This analysis significantly rules out additional absorption in the IR due to molecular species such as H_2O, CO or CH_4, gives marginal preference to those that do not include a Rayleigh scattering signature. (*right*) same analysis, but performed for the two atmospheric models in figure 3.9c, where we significantly ($\gg 5\sigma$) detect the presence of potassium in the atmosphere of WASP-80b. Figure adopted from Sedaghati et al. (2017).

has been obtained over a larger wavelength range range – a work that is outside the scope of this analysis. It is noted that Triaud et al. (2015) find a metallicity for WASP-80b's atmosphere of $-0.13^{+0.15}_{-0.17}$, definitively leaving the possibility of sub-solar metallicity.

The bluest part of the transmission spectrum is clearly dominated by the wings of the potassium line. To investigate this further, narrow 30 Å bin light curves around the strong potassium doublet at ~ 0.786 μm are modelled. Those results are given in figure 3.9c, where comparison to atmospheric models with and without potassium included, confirms the presence of this alkali metal at very high significance ($\gg 5\sigma$), in the upper atmosphere of WASP-80b. This detection is again made through an estimation of the χ^2_r statistics from the bootstrap of the residuals, the results for which are shown in the right panel of figure 3.10. High resolution spectroscopy of this target during and out of transit (e.g. Wyttenbach et al., 2015) will provide an alternative method for validation of this detection.

Chapter 4

Atmospheric detections

Sections of this chapter are adopted from Sedaghati et al. (2015) (10.1051/0004-6361/201525822) and Sedaghati et al. (2016) (10.1051/0004-6361/201629090), reproduced with permission from Astronomy & Astrophysics, ©ESO.

4.1 The LADC upgrade

In order to ratify the systematic problems introduced by the degraded LADC anti-reflective coating, whose implications were discussed in detail in chapter 3, a project was proposed at Paranal observatory. As mentioned previously, this project involved the removal of the MgF_2 anti-reflective coating from the LADC unit of the decommissioned FORS1 instrument, and upgrading the FORS2 instrument with it. The exact details and the subsequent battery of tests analysing the performance of the upgraded instrument, are given in detail by Boffin et al. (2015). Those tests concluded that the upgrade of the prisms did not affect the image quality of the instrument and that the LADC was still efficient in correcting the atmospheric dispersion up to airmass of 1.6. Additionally, the uncoated prisms led to an increase in the dispersion through the optics and therefore the measured zero points across all filters, with gains of up to 0.12 magnitude in throughput.

In addition to those initial tests, the performance of the instrument in obtaining exoplanetary transmission spectra was checked through multi-object spectroscopic observations of WASP-19, host to one of the most highly irradiated gas giant exoplanets (Hebb et al., 2010). A single transit of this planet was observed on the 16th of November 2014 under thin cirrus during technical time. The results from the analysis of the subsequent data were published in Sedaghati et al. (2015) given in the Appendix at the end of this thesis. It is concluded that the upgrade of the instrument resulted in an improvement to the level of systematic trends present in the differential transit light curves, most likely associated with the more homogeneous

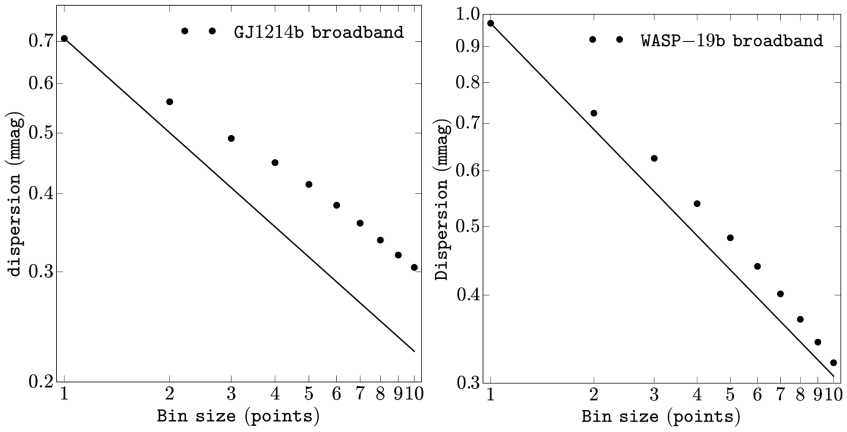

Figure 4.1: Improvement to the level of systematic noise present in the FORS2 transit light curves. *Left* panel shows the relation between the dispersion of the light curve residuals for a transit of GJ 1214 b observed prior to the LADC upgrade, the results from which were presented by Bean et al. (2011). *Right* panel shows the same relation from the transit light curve of WASP-19b obtained during the testing procedure of the instrument upgrade (Sedaghati et al., 2015). If only Gaussian noise is present, the dispersion of the residuals decreases according to the relation indicated by the solid black lines. Deviation from this relation is indicative of the presence of correlated or red noise in the data. The improvement to the instrument from the upgrade of the LADC unit is clearly evident.

transmission of light through the optics, from the target and comparison stars. This improvement is estimated through the analysis of the dispersion dependency upon binning of the light curve points. Such comparison, made between observations performed prior to the upgrade (GJ 1214 b) and our initial test after the upgrade (WASP-19b), is shown in figure 4.1. Namely, the deviation from the Gaussian noise relation, which highlights the presence of correlated noise, clearly shows that the instrument upgrade had a significant effect in improving the quality of the transit light curves obtained by the FORS2 instrument.

Although, the WASP-19b observations suffered from the presence of sporadic cirrus through the night, as well as far from ideal seeing conditions, the spectrophotometric analysis of the data still revealed a precise transmission spectrum of this planet in the visible ($\sim 0.5 - 0.8$ μm) domain using the 600RI grism; a testament to the improvements made to the instrument. However, since this dataset is re-analysed together with two further FORS2 observations as part of a multi-epoch, multi-grism observational campaign, the conclusions made from it will be presented together with those observations later in this chapter.

Following the publication of the initial results and preliminary analysis of various data taken afetr the instrument upgrade, some recommendations were subsequently made in Boffin et al. (2016b) based on my work, regarding observational and data analysis strategies for the entire community to follow in order to maximise the scientific output of transmission spectroscopy observations with FORS2. Those important points include:

- The target and comparison stars should be placed as close to the middle of the dispersion axis of the CCD as possible. This of course is limited by the availability of suitable reference stars within in the FoV of the instrument. This is because the exact wavelength coverage depends on the horizontal position of a slit on the CCD. This mentioned strategy guarantees the widest possible wavelength overlap between the difference spectra and maximises the coverage of the transmission spectrum. This is easily done if there is only one reference star, by changing the position angle on sky. This fact should actually dictate, among others mentioned below, which reference stars are taken.

- For the choices of references, stars of similar magnitude should be selected, which allows for a better comparison without the loss of S/N. This also ensures that the exposure time is not driven by one of the stars only, and therefore also guarantees that the flux of all stars will be similar. This is critical to mitigate any possible non-linearity effects of the CCD.

- Stars of similar colours should be utilised as comparison, so as to have similar spectra to compare to, especially for the broad-band light curve. It is therefore useful to do pre-imaging of the field through several filters to establish the best possible comparison stars (this would also make sure that any high proper-motion of the target is correctly handled when making the masks), unless the colours of all stars are already available in catalogues.

- The maximum pixel intensity of the brightest object should have at least 40 000 ADUs. The FORS2 CCDs are linear up to the saturation limit, 65 000 ADUs, but it is safer not to go too close to this limit.

- The counts of each exposure should constantly be checked throughout the observing sequence and the exposure times adjusted to maintain a constant flux level. This should ensure that any unknown sub-percentage non-linearity of the CCD does not introduce any false-positive signals into the eventual light curves. However, this approach

does lead to a slightly uneven sampling[1].

- A very long out-of-transit baseline should be obtained, before and after the transit, and if possible simultaneous photometric observations performed to monitor any stellar activity and the presence of stellar spots – preferably in a filter matching the wavelength range of the spectroscopic observations.

- If possible (that is, from a scheduling point of view and if the transit is short enough), observing through the meridian should be avoided, i.e. observe the full sequence before or after the meridian crossing. Going through the meridian implies the largest field rotation and this seems to lead to additional systematics in some cases. If the transit is too long, an epoch should be picked where the meridian crossing occurs out of transit.

- The `200 kHz`, `2×2`, `low` read-out mode should be used, as this will shorten the read-out time, and thanks to the low gain, allows increasing the exposure time before reaching the saturation limit. This thus helps to reduce the overheads and increase the time resolution of the observations, as well as increase the S/N obtained on a single spectrum.

- Observations should be done under clear conditions. If the atmosphere is not very stable, with thin (or thick!) clouds passing, it may be better to abort the observations and give back the telescope than to waste valuable telescope time for useless data. A good parameter to check for this is the value of the coherence time, as it is indicative of the stability of seeing conditions.

- Although this has not been characterised yet when used for transmission spectroscopy, for very bright targets it can be useful to consider using the "Virtual Slit", which uses the active optics of the telescope to spread the light in the y-direction (i.e. perpendicular to the wavelength dispersion) onto up to 6″ (that is, up to 24 binned pixels). This allows for longer integration times – allowing to observe bright targets without too much dead-time, and is the almost equivalent to defocusing (but not similar, and in one direction only) that is used in photometry.

- Very wide slits should be designed, i.e. equal or larger than 20″. This ensures that there are no slit losses, but also that in case there is a faint

[1] Some observers are less keen to adjust the exposure time during the whole sequence, in order to have a homogeneous sampling. This, however, requires estimating carefully how the flux will change with airmass and should allow for improvement in image quality, without saturating the spectra.

companion to your target or comparison stars, it also always stays in the slit. Obviously, this implies that the spectral resolution will then be determined by the image quality, typically 0.8–1″.

- Similarly, long enough slits should be designed to ensure enough sky is included to correct the spectra for telluric contamination, but it is advisable to also put one or two slits on empty regions (on both chips), to have a good estimate of the sky variations throughout the observing sequence. This should also be as aligned as possible to the science targets.

- The LADC should be placed in park position (30 mm) and in simulation during the whole observation. This allows minimising any systematics coming from the LADC, i.e. any additional moving parts. This means, however, that the differential refraction is not corrected for, but as the slits are long and wide, this should not imply slit losses.

- It should be ensured that a mask with narrow slits (0.4–1″) is designed, to be used for taking wavelength calibrations, as those done with the wide slits will be useless (e.g., won't be accepted by the FORS2 pipeline). More than a single calibration image should be requested to ensure maximum possible number of lines to determine the dispersion solution (3 or 5). These individual frames should be combined in a modal manner to maximise the number of lines from the calibration lamp in the final arc frame.

- Enough spectroscopic flats should be taken (7 is the standard number from the calibration plan, but you may wish to ask for 20 or more) with both masks, if possible before and after the observations to increase the S/N of the master flat frame.

- The data should be assessed in real time to check the quality of the differential broadband light curves as the observations progress[2]. This would give a clear indication if something needs to be changed in the experimental set up. For this to be possible, the user needs to write an automated combined reduction and analysis pipeline, for *in situ* monitoring of the data.

- The variations in the atmospheric coherence time should be monitored, as this parameter is indicative of the atmospheric stability. Ideally, one would like long coherence time, which translates to stable seeing conditions. Sudden changes in seeing are known to be directly correlated with the precision of differential light curves.

[2]This requires that the user request calibrations to be done prior to observations, which may not always be possible.

4.2 Potassium in the atmosphere of WASP-17b

Following the successful commission of the upgraded LADC unit of the FORS2 instrument, a transit of the exoplanet WASP-17b was observed, using the 600RI grism. This target was chosen due to its large expected atmospheric signal, as evident in figure 1.3. The exact details of the observations and data analysis have been presented in Sedaghati et al. (2016), which is included at the end of this thesis in the Appendix.

The analysis performed is similar to what was previously presented in the case of WASP-80b in chapter 3 (Sedaghati et al., 2017). Additionally, experiments were performed to correct for telluric contamination of the observed stellar spectra.

Potassium detection

The obtained transmission spectrum of WASP-17b, from modelling the common-mode-corrected spectrophotometric light curves, shown in figure 10 of Sedaghati et al. (2016), was subsequently compared to synthetically produced atmospheric models. Initially a flat spectrum is ruled out significantly ($> 3\sigma$). This is done by the comparison of fit statistics of a flat spectrum with a 1-σ tolerance to clear atmosphere models, which resulted in ΔBIC $\gg 10$, which provides a *very strong* evidence against the flat spectrum. Using a weighted least squares fit of a Rayleigh scattering slope to the transmission spectrum, a mean molecular weight, μ_g, of 2.05 ± 0.79 u for Bond albedo of 0, and 1.88 ± 0.73 u for 0.3, is obtained. These findings are consistent with upper limits determined for atmospheres of hot gas giants (Spiegel et al., 2010; Esteves et al., 2013). They point to an atmosphere dominated by H_2, but owing to the large uncertainties in determination of the Rayleigh slope, they could also point to the presence of H or He. However, a distinct lack of H-α absorption in transmission somewhat rules out the former.

In addition to the broadband transmission spectrum, absorption in the cores of both Na and K was probed using narrow 50 Å bin integrated transit light curves. No significant extended absorption in the Na was found, contrary to HST observations of Sing et al. (2016). Similarly potassium absorption in the atmosphere of WASP-17b was also searched for, again obtaining and analyzing light curves using 50 Å integration bins. Unfortunately, the majority of the potassium doublet core falls on top of the telluric O_2 (A) absorption lines, as shown in the right column of figure 11 of Sedaghati et al. (2016), which introduce large systematics for light curves obtained in this region. Hence, production and analysis transit light curves in this domain, where the signal is diminished by the Earth's atmosphere, is avoided. However, since the potassium core falls close to the red edge of the telluric forbidden region, one is able to probe and detect the red wing of

the pressure-broadened line (as it was done for the blue wing in WASP-80b observations). Using the data points redwards of the telluric absorption, there is a 3-σ improvement to the fit when a flat spectrum is compared to the atmospheric models including potassium. To date only one previous work has looked at this domain of the spectrum (Sing et al., 2016), where the narrow bin placed at the core of the potassium line is inconclusive in determining its presence or absence.

Charbonneau et al. (2002) first report detection of Na in the atmosphere of HD 209458 b. Subsequent studies suggested that the Na absorption was weaker than estimated by theory (Seager and Sasselov, 2000) and that the potassium signal was lacking (Snellen et al., 2008) for this planet. Four factors have been suggested that could influence the spectral bands of the alkali metals, Na and K: (i) an elemental abundance different from the commonly assumed solar value, (ii) masking by atmospheric hazes, (iii) in situ photochemical reactions, and/or (iv) condensation, e.g. on the planetary night side.

Lavvas et al. (2014) review processes affecting Na and K signals in hot Jupiter atmospheres and apply a photochemical model including in situ Na and K reactions. Regarding the effect of elemental abundances, they suggested values up to 6× lower than the solar one for Na and K, e.g. for HD 209458, based on stellar metallicity measurements. Regarding the masking of spectral bands, they note that it is difficult to mask only the sodium line (and not the potassium) since sodium is a strong absorber; this could however be achieved in the presence of certain hazes although the size distribution of the haze particles would have to be consistent with the observed Rayleigh slope. With regards to in situ photochemistry, two important species that are formed are: XH (formed via: X+H_2) and XOH (formed via X+H_2O) (where X=Na, K). Both XH and XOH can then undergo thermal decomposition to regenerate the alkali metal atoms. Uncertainties in the photochemistry include, for instance, reactions of potassium (e.g. here the three-body combination rates are not well known and one usually assumes the same coefficients as for sodium); also at hot-Jupiter temperatures, excited states could become important, the photochemical responses of which are not well-defined. Lavvas et al. (2014) conclude that the uncertainties in photochemistry however, are small compared with the potential effect of masking by hazes. Regarding condensation of alkali metals on the nightside, more work is required on, for example, the 3D transport mechanisms across the terminator.

Telluric correction experiment with `molecfit`

In order to correct for the telluric absorption in the individual stellar spectra ESO's `molecfit`[3] tool (Smette et al., 2015; Kausch et al., 2015), designed for this specific purpose and based on fitting synthetic transmission spectra to astronomical data. It also has the ability to estimate molecular abundances in the Earth's atmosphere, which was used as an optical state parameter of the GP systematics model. H_2O and O_2 were included in the modelling approach, fixing the value of oxygen and fitting for the water vapour content along the line of sight. Cross reference with the broadband transit light curve indicated moderate correlation between the slight differential variations in column density from the two stars and systematic noise in the time-series data. Therefore these variations were used to correct for such systematic trends in the light curves. As one would like to measure atmospheric variations on time scales comparable to the cadence of the observations, absorption models were found for each individual spectrum independently, while utilising the in-situ temperature and pressure profiles as a function of geoelevation. The sources of input are: the standard profile (produced by the Michelson Interferometer for Passive Atmospheric Sounding (MIPAS) on-board the ENVISAT[4] satellite), the Global Data Association System (GDAS) profile, and ESO Meteo Monitor (EMM) data, as well as instrumental and ambient parameters such as time, airmass, local pressure and temperature taken from the fits headers. In addition to the removal of telluric absorption features from the spectrum, the tool also allows for a further correction of the wavelength solution of the spectra based on the telluric lines. This dispersion solution correction was applied to all the spectra using a third order polynomial in wavelength to correct for any residual discrepancies. To find the telluric absorption models, first the areas of the spectrum containing extinction features were used. This solution is then used to obtain the telluric corrected spectra. An example of this complete procedure for spectra of WASP-17 and one reference star is shown in figure 4.2. The resolution of the spectra were fit using a Gaussian convolution filter, with the size of kernel set to 10 FWHM's in pixels, a value that was optimised for the best fit to the data.

Subsequently, these corrected spectra were used to produce the transmission spectrum with the same procedure as is standard. The statistical analysis of the resultant light curves were reproduced, as was done in figure 7 of Sedaghati et al. (2016), to check for any significant improvements to the quality of the time-series data extracted. It turns out that the overall quality of the light curves only improved marginally. This is due to the fact that `molecfit` was used in a way to only fit the broad telluric absorption features while keeping the narrower features intact. The difficulty in obtain-

[3] `http://eso.org/sci/software/pipelines/skytools/molecfit`
[4] ESA's environmental satellite.

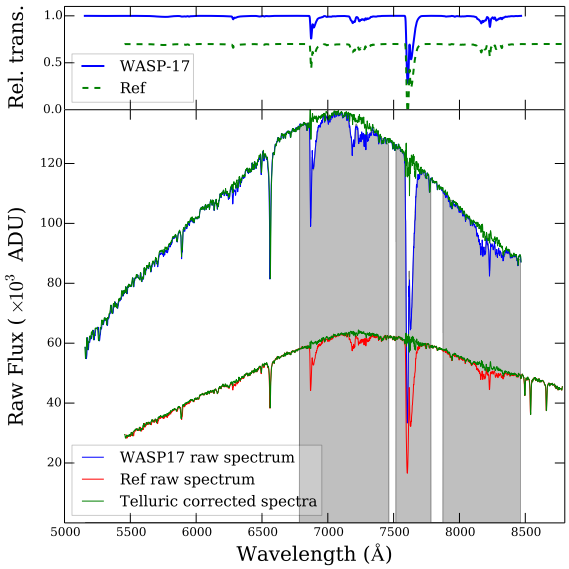

Figure 4.2: The process of telluric absorption line removal from the spectra. (*Top*) The derived sky transmission models for these particular spectra of WASP-17 (*blue solid*) and reference star (*green dashed, shifted for clarity*). (*Bottom*) An example of WASP-17 and the reference star spectra before (*blue & red*) and after (*green*) the removal of telluric absorption lines, respectively. The grey areas indicate the regions of the spectrum used to determine the sky absorption model.

ing a fit to the smaller features of the telluric absorption lines comes from the low resolution of FORS2 spectra.

After great debate and plenty of experiments, it was concluded that the spectral fit from `molecfit` was too dependent on the chosen initial parameters and the software was not able to fully fit the resolution of the input spectra. Consequently, the corrected spectra were either over- or under-fit in the regions of strong telluric absorption, such as the O_2 double feature around 0.77 μm. This fact is of acute concern as it would introduce unwanted signals in the final transmission spectrum. Therefore, the transmission spectrum obtained from the telluric corrected spectra were excluded from the final published worked. However, in principle, this approach should be able to improve the quality of the extracted transit light curves, given the problem of the spectral fitting of low resolution spectra is solved. Therefore, the application of telluric correction procedures in the production of exoplanet transmission spectra will be investigated in future work.

4.3 TiO, water & haze in the atmosphere of WASP-19b

Complementing the initial technical run testing the improvements to transmission spectroscopy observations with FORS2, two further observing runs of WASP-19b were performed with the blue and red grisms (600B and 600z, respectively). The programme was designed with the goal of obtaining a complete optical transmission spectrum of this planet, at unprecedented resolution and precision.

Numerous studies in the past decade have searched for TiO in hot Jupiter atmospheres with limited success. Hot H_2-rich atmospheres are expected to host metal oxides, such as TiO, in gaseous phase as observed in the atmospheres of hot brown dwarfs, or L Dwarfs. TiO has strong absorption features in the visible spectral range. Therefore, the presence of TiO in hot Jupiter atmospheres can strongly absorb incoming starlight and cause thermal inversions ('stratospheres') in the dayside atmospheres (Hubeny et al., 2003; Fortney et al., 2008). This phenomenon is analogous to ozone in the Earth's atmosphere intercepting incoming solar radiation to cause the Earth's stratosphere. Therefore, highly irradiated hot Jupiters have been predicted to host thermal inversions in their dayside atmospheres leading to thermal emission features in infrared spectra. However, despite extensive searches there has been no definitive detection of TiO or any other inversion-causing molecule in exoplanetary atmospheres to date. Recently, however, a tentative evidence for TiO was hypothesized by Evans et al. (2016) in the hot Jupiter WASP-121b based on a marginally excess absorption (by $\sim 2\sigma$) in a single photometric band at 0.6 μm. While this evidence is marginal and potentially degenerate with various other sources of opacity in the same band, there is now a rejuvenated search for robust spectroscopic signatures of TiO and other metal oxides in hot Jupiters atmospheres. The present work marks the first success in this direction with a conclusive spectroscopic detection of TiO in the Hot Jupiter WASP-19b.

WASP-19b is to date the shortest period hot-Jupiter discovered, orbiting very close to the Roche limit of its host star. This is the limit beyond which the tidal forces of the star will overcome the planet's own gravitational attraction, which causes the planet to disintegrate. It has a radius of approximately 40% larger than that of Jupiter's and mass that is 11% in excess of the Jovian value, putting it in a category of bloated gas giants. This is due to the excessive amount of radiation its dayside receives, given its proximity to its host. Subsequently, this leads to an effective temperature value in excess of 2000K, from planet's secondary eclipse depth measurements (Wong et al., 2016). Such so-called highly irradiated hot Jupiters have been predicted to include temperature inversions due to presence of metal oxides (Fortney et al., 2008), which is known as the TiO/VO hypothesis. Our work

provides the first concrete evidence for such theories.

Observations & data reduction

Multiple transits of WASP-19b (Hebb et al., 2009), a hot-Jupiter in an extremely tight orbit around its host star, were observed. The planet revolves around the 12.3 V_{mag}, G8V star on a 0.789 d orbit, making it one of the most highly irradiated hot Jupiters. The data were obtained over a 2-year period. The details of the three observing campaigns are given in table 4.1. The red-optimized MIT chip was used for the Green and Red data sets and the blue-optimized E2V chip set for Blue data.

For all sets of observations the instrument's atmospheric dispersion corrector was left in park position throughout the entire observing sequence, with its two prisms kept at minimal separation of 30 mm. For the two most recent sets of observations it was chosen to observe with the non-standard 200 kHz readout. This strategy allowed to spend more time on the target for a given cadence due to the reduced readout time, subsequently increasing the signal to noise ratio (S/N) of the spectra, as was prescribed in earlier in the chapter. For observations performed in MXU mode, custom designed masks with typically 30″ wide slitlets were created and placed on top of the target star, as well as a number of reference stars and the sky for monitoring variations in the sky background contamination level. As part of a routine calibration sequence, bias, flat-field and arc images were also taken. The arc frames were taken with the same slit configuration as the science sequences but with the slitlets' widths set to 1″ for increased resolution. Best effort was made in placing all the observed stars as much in the middle of the detector set as possible, in order to ensure maximal wavelength overlap between the targets. An example of a mask created for observations in the MXU mode is shown in figure 4.3. This is all in keeping with the optimal observation strategy with FORS2 for multi-object spectroscopy. The observational conditions for all sets of observations were generally clear but not photometric. Some sporadic cirrus affected the raw light curves in the Blue campaign, towards the ends of the observing sequence, which are mostly corrected for by differential photometry technique, although some residual effects still remain. These effects are however well modelled by the GP model. It must also be noted that the results from the Green data set are a reanalysis of the published resutlts in Sedaghati et al. (2015). This was done for two particular reasons; firstly, to have a homogeneous analysis of all three data sets, and secondly, Turner et al. (2016) have highlighted the shortcomings of the modelling algorithm used to model the transit light curves in that initial analysis, which was the `TAP` (Gazak et al., 2012) routine.

For the purpose of data reduction, a specialised `Pyraf` pipeline was written used also for the previous work presented in this thesis (Sedaghati et al., 2016, 2017), which included 1) overscan and bias-shape subtraction, 2) spec-

Table 4.1: Observational information of the three sets of the observational campaigns.

Dataset	Date	Programme ID	Mode	Airmass	Seeing ($''$)	Grism	λ (μm)	Readout mode	Exposures (in-transit)
Blue	30-01-16	096.C-0465(C)	MXU	$1.20 \rightarrow 1.07 \rightarrow 1.42$	1.49	600B	0.33 – 0.62	200kHz	150 (43)
Green	15-11-14	060.A-9203(F)	MXU	$2.57 \rightarrow 1.19$	1.13	600RI	0.536 – 0.853	100kHz	180 (88)
Red	29-02-16	096.C-0465(A)	MXU	$1.15 \rightarrow 1.07 \rightarrow 1.47$	1.18	600z	0.74 – 1.051	200kHz	212 (86)

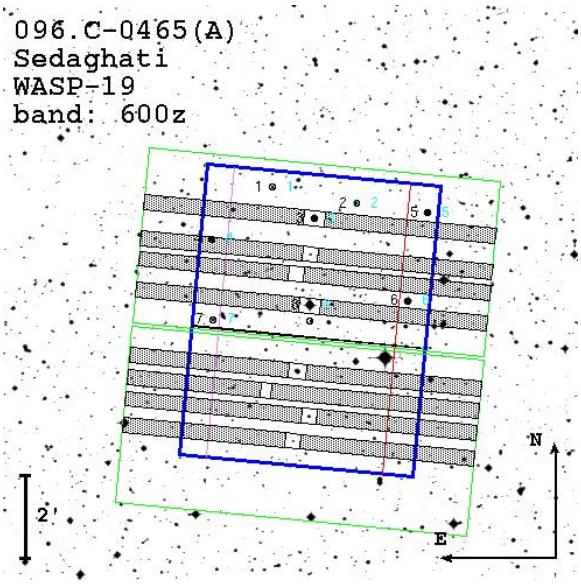

Figure 4.3: An example of a mask design used for MXU observations. Field of view of FORS2 is shown in green, with the blue lines indicating the two-chip detector mosaic. The gray shaded regions show the areas of the detectors used for recording the stellar spectra. In this instant, WASP-19 is the star in the upper-most slit.

troscopic flat-fielding, 3) spectral extraction, and 4) wavelength calibration. For the extraction of one-dimensional spectra from the two-dimensional science frames the optimal extraction algorithm of Horne (1986) is implemented. The size of the extraction box used for each star was varied and chosen through the analysis of dispersion in the subsequent light curves, an example of which is shown in figure 4.4. Namely, the width of the extraction box is selected once the gradient of the light curve dispersion relation to the extraction width is below 10^{-4} pix^{-1}, for the frame with the largest PSF in the spatial direction. This value is then used for all the frames in the corresponding dataset. In the example shown, 30 binned pixels were used for both the target and the comparison star. However, this extraction size varied from star to star, as well as night to night, due to variation of brightness and seeing conditions. Examples of such extracted spectra of the target and the comparison stars, for each data set, are shown in the top row of figure 4.5. To obtain the dispersion solutions, a Chebyshev function fit of order 4 was utilised using the one-dimensional extracted arc frames, that provided results with rms of 0.06 Å or better after deleting a few outlying features.

Once extracted, the series of the stellar spectra are integrated, initially within the largest common wavelength domain of all the targets. Their vari-

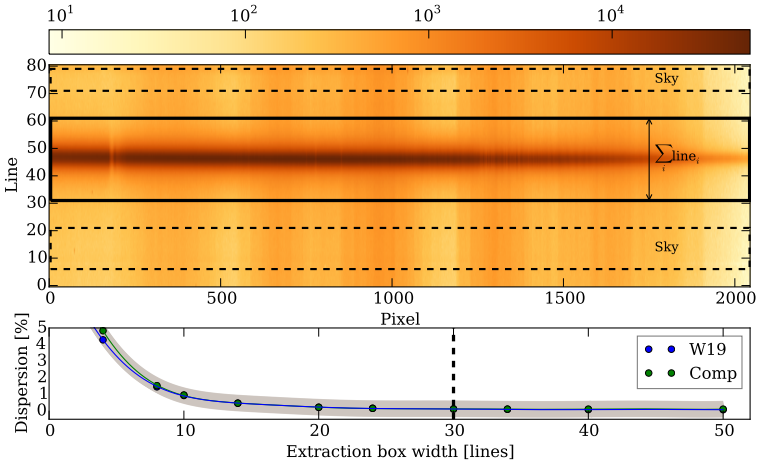

Figure 4.4: An example of a two-dimensional spectrum, from the Red data set, taken with the FORS2 instrument. The final size of the extraction box, as well as the regions used for sky subtraction have also been shown as boxes. (*bottom*) The process of choosing the extraction box width, where the final value is shown as a dashed line. The exemplar frame is selected at large seeing.

ations as a function of time result in the raw light curves. I then produce differential transit light curves by dividing the target light curve (that of WASP-19) by all the observed comparison stars, as well as all their possible combinations. The final comparison star is chosen as the one that produces the cleanest transit light curve (i.e. the light curve with the lowest residuals relative to a transit model). Once chosen, I reintegrate the target and the chosen comparison star for their largest common wavelength overlap. Examples of these final raw and differential light curves are given in the middle and bottom rows of figure 4.5, respectively, for the observing campaigns.

The spectrophotometric or narrow-band transit light curves are produced in an identical manner, but using integration bins of 10nm. This value is chosen through a statistical analysis of all three datasets, where the final decision is dictated by the least precise set (Sedaghati et al., 2016). All these light curves, used to produce the transmission spectrum, are shown in the left panels of figures 4.6, 4.7 and 4.8 for the Blue, Green and Red datasets respectively. For these light curves, they are further corrected by division through the residuals of the analytical model to the broadband light curve. This is known as the common mode systematic correction (Lendl et al., 2016; Nikolov et al., 2016; Gibson et al., 2017) and removes the wavelength-independent component of the systematic noise from the spectral light curves. These corrected light curves are again shown in the right panels of figures 4.6, 4.7 and 4.8, together with the GP models to be

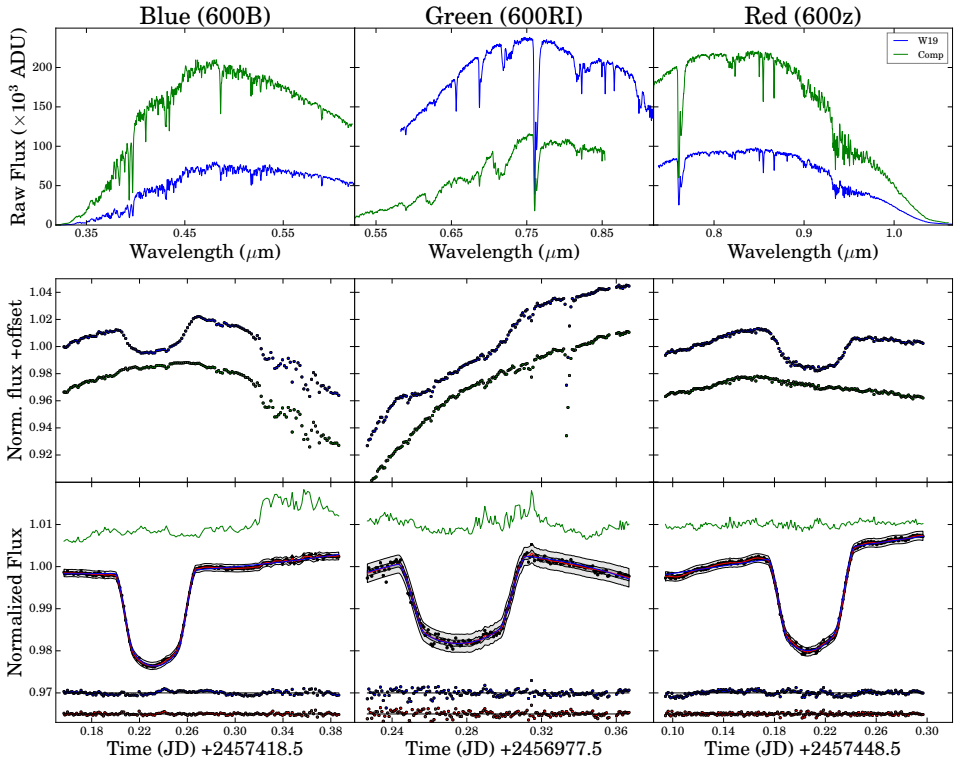

Figure 4.5: *Top* row represents an example set of spectra for the target (WASP-19) and the chosen comparison star, for each observing run denoted on top the respective columns. The counts are given in ADUs, read directly from the sum of values of CCD pixels. *Middle* row shows the light curves of the target and the comparison stars for each data set, that are obtained through broadband integration of the series of spectra. The colours are consistent with those used in the top row, and the values are normalised to the mean of the out of transit fluxes and shifted for clarity. The transit imprint from WASP-19b is clearly evident even in these raw light curves. *Bottom* row presents the differential, broadband light curves obtained simply through the division of the two light curves in the middle row. Additionally, I show the fitted transit model in blue, the Gaussian Process (GP) systematic noise model in red and its 1- and 3-σ confidence levels in dark and light gray shaded regions, respectively. The points below are the residuals of the two models, where the colours correspond to the fit that they represent. Finally, the green line is the flux variations due to changes in seeing conditions, that is used as an input of our GP model.

described in the following section.

Data analysis

The analyses and modelling of all transit light curves, both broadband and spectrophotometric, are identical to what was done for WASP-80b, presented previously in section 3.3. In the description of the analytical transit model, the quadratic limb darkening law (Kopal, 1950) is used to describe the centre to limb intensity variations across the stellar disk. This selection was made through a comparison of various alternative laws, using the ΔBIC formalism (Schwarz, 1978). Finally, I generally assume uninformative, flat prior assumptions about the searched parameters, represented as $\mathrm{P}(\theta, \phi)$ in equation 3.3, with the following exceptions,

$$\ln P(\boldsymbol{\theta}, \boldsymbol{\phi}) = \begin{cases} \ln \mathcal{N}(0.78884, 10^{-10}) & \text{for } \phi \in [\mathrm{P}], \\ \ln \mathcal{N}(0, 10^{-10}) & \text{for } \phi \in [e], \\ -\infty & \text{if } (c_1 + c_2 > 1), \\ \ln \mathcal{N}(\mu_i, 9\sigma_i^2) & \text{for } \phi \in [c_1, c_2], \\ \ln \Gamma(1, 1) & \text{if } \theta \in [\zeta, \eta_\alpha], \\ -\infty & \text{if } \sigma < 0 \end{cases} \tag{4.1}$$

What these prior assumptions essentially mean is that I fix the period and eccentricity of the transit to previously determined values and set prior gaussian distributions upon the values of the two limb darkening coefficients based on theoretically calculated values from `PHOENIX` models (Claret et al., 2013), with a width three times larger than the uncertainty in the theoretical model values for a greater flexibility in the search space. A gamma function, Γ, is chosen as the prior for the parameters of the kernel in order to encourage their values towards 0 if they are truly irrelevant in describing the correlated noise in the data (Gibson et al., 2012b).

The initial values for the free parameters are obtained using the Nelder-Mead simplex algorithm (Nelder and Mead, 1965), and then find the maximum posterior solution by optimising the log posterior given in equation 3.3. I obtain the posterior probability distribution functions by using the adaptive Markov Chain Monte Carlo (MCMC) method, which explores the joint probability for our multivariate models. For each light curve analysed for this work, I ran four independent MCMC simulations of length 100 000 iterations each and checked their mutual convergence using the Gelman-Rubin (Gelman et al., 2014) diagnostic. Example sets of samples drawn from such chains are given in figure 4.9 for a broadband and a spectral light curve fit. It must be noted that in addition to the analytical transit model, I also include a baseline function that is a quadratic polynomial of the parallactic angle throughout the observations that accounts for modulations introduced to the light curves by the rotation of the telescope, as well as the second-order,

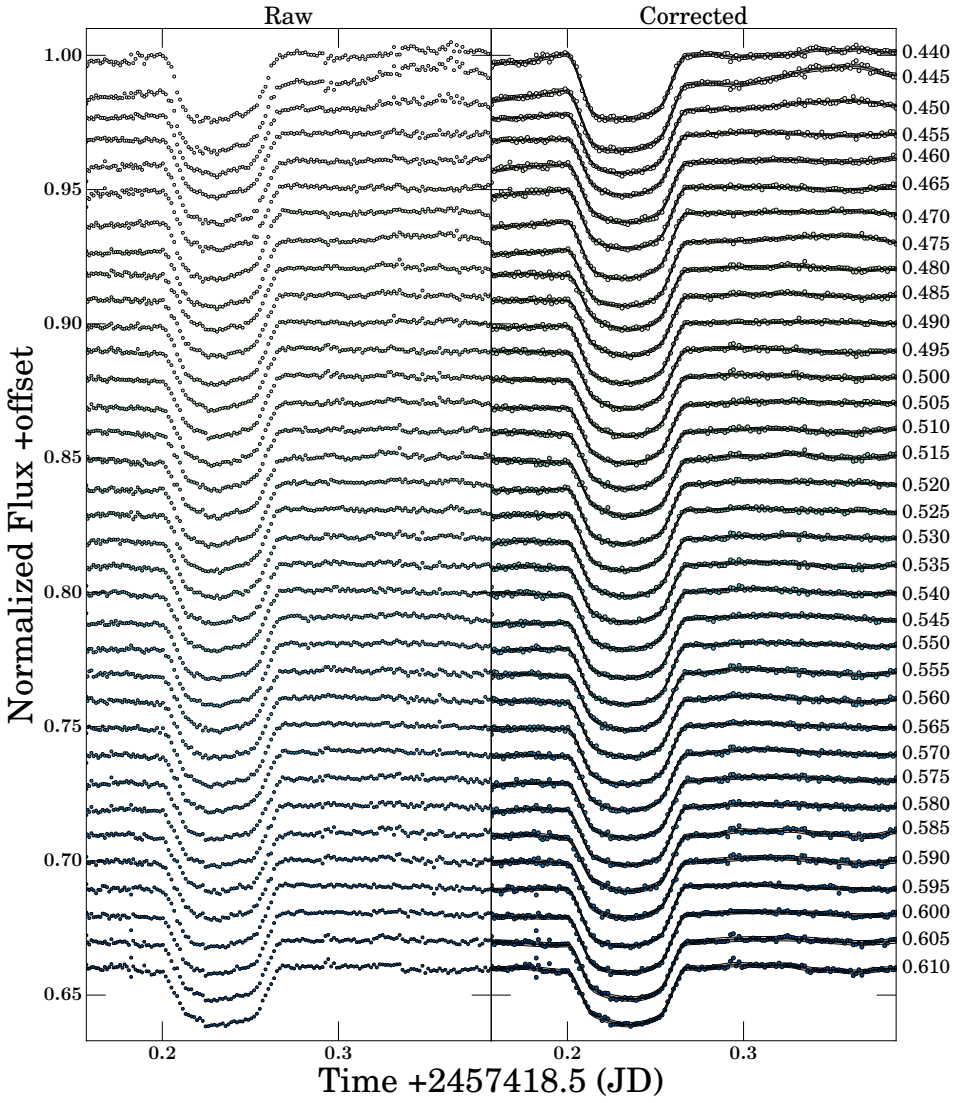

Figure 4.6: *Left* panel shows the raw light curves produced from each of the narrow-band channels in the Blue dataset. The *right* panel shows those light curves that have been corrected for the common mode systematics. The best fit GP systematic noise models are shown as solid black lines, with the centre of the integration bin for each light curve given to the right of it in microns. All light curves have been shifted vertically for clarity.

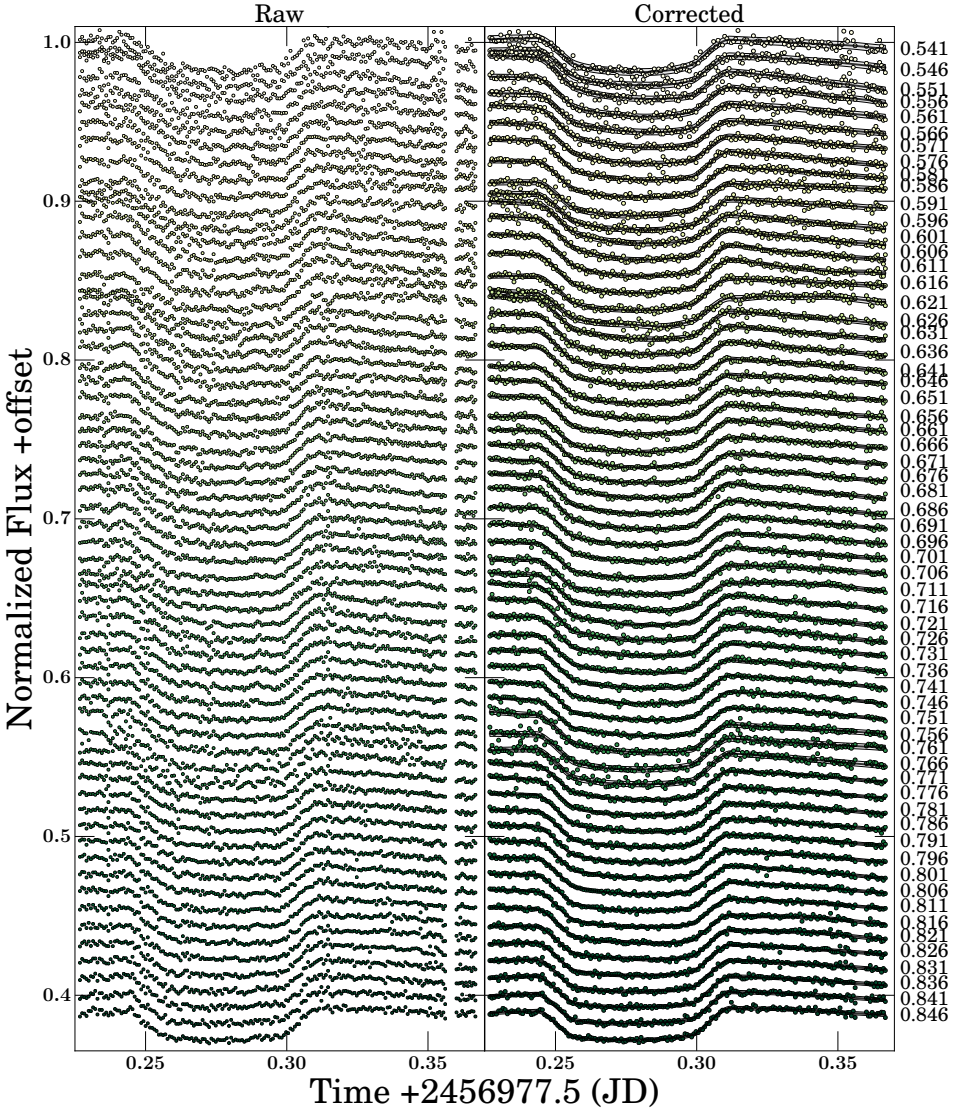

Figure 4.7: Same plot as figure 4.6 but produced for the Green dataset. All other details are identical.

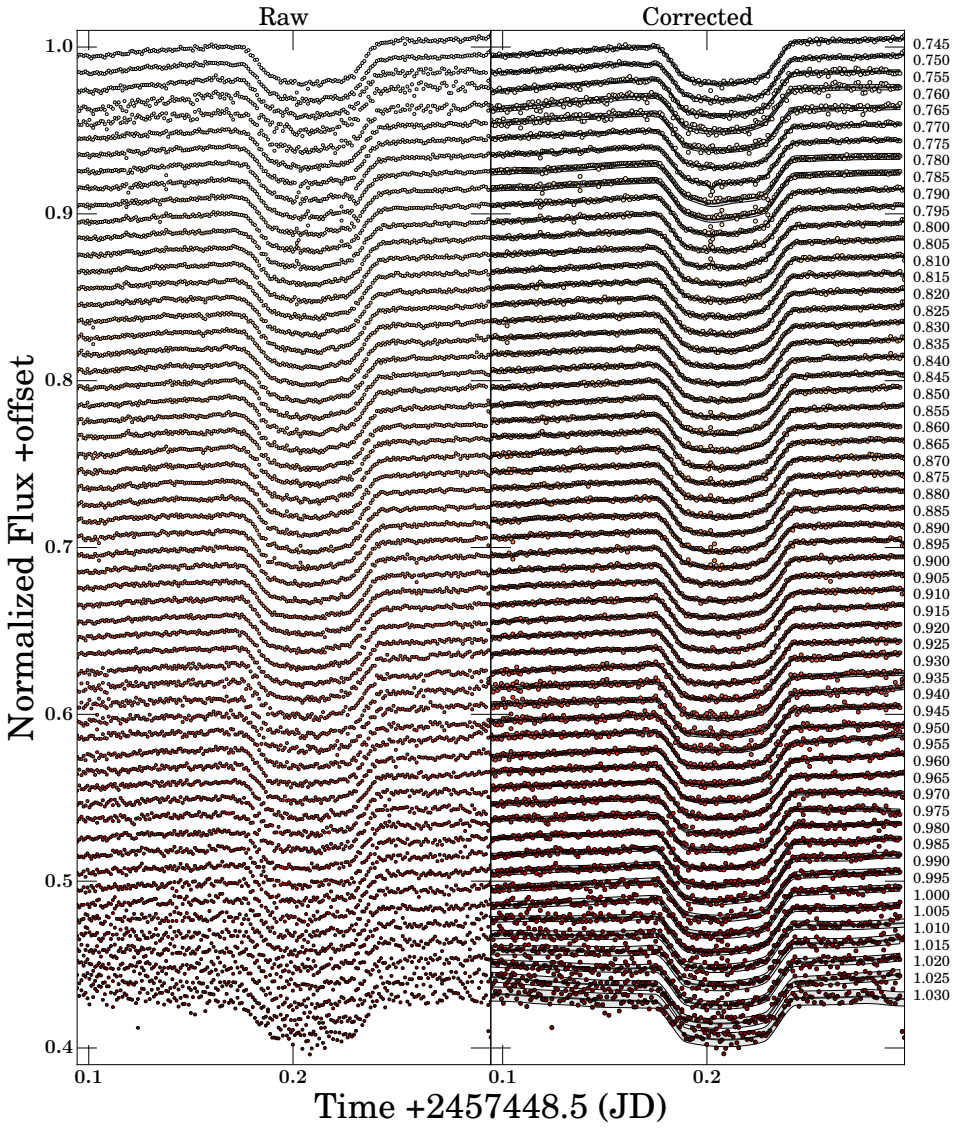

Figure 4.8: Same plot as figures 4.6 and 4.7 but produced for the Red dataset. All other details are identical.

colour-dependent extinction of the stars. This last fact is the reason why I fit for the parameters of this baseline model for all the spectrophotometric light curves.

I infer best fit parameter solutions from the analysis of those derived posterior distributions from all the MCMC simulations. Since all fitted parameters have a guassian posterior distribution, the results for the mean, mode and median of each parameter are statistically identical, with the exception of those noise parameters with gamma distribution prior functions. In those cases, I quote the median of the distribution as the solution, all of which are given in table 4.2.

Spot analysis

It has previously been shown that the transit light curves for WASP-19b towards the blue edge of the visible domain suffered significantly from presence of stellar spots (Huitson et al., 2013). Subsequently, it was not possible to produce the transmission spectrum from HST observations performed with the G430L grism of STIS due to the planet crossing such spot anomalies whose temperature difference to the surrounding stellar photosphere is larger towards shorter wavelengths. Therefore, I assume that the observations here could possibly be affected by stellar activity, although not to the same extent as the HST results since the wavelength coverage from the Blue dataset here starts at 0.44 μm as compared to 0.29 μm from STIS. There are two avenues through which presence of stellar spots can influence the transmission spectrum, namely *occulted* and *unocculted* spots.

Occulted spots: There is marginal evidence for a spot crossing event in the Blue dataset post mid-transit. To calculate the impact of this anomaly I model the light curves from the Blue dataset with a single spot crossing event included as part of the analytical model. This approach means the addition of four fitted parameters to the light curves describing the physical properties of the spot anomaly: two positional variables (parallel and perpendicular to the transit chord), angular size ($R_\bullet$) and the contrast ratio ($r_\bullet$). I first model the broadband light curve from the Blue dataset with the same procedure as was done previously, with the inclusion of four additional free parameters for the spot. This transit model including a spot crossing event is shown in figure 4.10, quoting the derived spot parameters and the relative planetary radius and the limb darkening coefficients. A large spot anomaly is detected overlapping with the transit chord, with a spectral radiance value very close to the surrounding photosphere, i.e. contrast ratio of 95%. In order to obtain the spot temperature, I model all the spectrophotometric light curves of the Blue dataset with a spot model, only fitting for the contrast ratio, as this is the only wavelength dependent aspect of the spot, the relation for which is

Table 4.2: Transit parameters from the broadband analysis of all three datasets. For each dataset the band centre and bandwidths (in brackets) are given at the top of each corresponding column. The rows with a single value are those wavelength-independent properties, common to all datasets.

Parameter (inferred)	Blue 4865 (2530) Å	Green 6941.5 (3172) Å	Red 8951.5 (3111) Å
Mid-Transit, T_c (JD) +2400000	57418.73368 ± 0.00010	56977.77754 ± 0.00019	57448.70885 ± 0.00020
T_c, Barycentric corrected (BJD_{TDB})	57418.73688	56977.77653	57448.71294
Period, P (days) [fixed]		0.78884	
Eccentricity, e [fixed]		0.0	
Scaled semi-major axis, $a/R_\star$		3.5875 ± 0.0574	
Impact parameter, b		0.6525 ± 0.0233	
Relative planetary radius, $R_p/R_\star$	0.14440 ± 0.00151	0.14366 ± 0.00181	0.14060 ± 0.00148
Linear LD coefficient, c_1	0.6709 ± 0.0616	0.5045 ± 0.1037	0.3152 ± 0.1195
Quadratic LD coefficient, c_2	0.0599 ± 0.0866	0.1361 ± 0.0934	0.1673 ± 0.1074
GP output scale, ζ (ppm)	748^{+418}_{-220}	650^{+1723}_{-218}	644^{+308}_{-181}
GP inverse length scale for t, η_t	$0.028^{+0.010}_{-0.009}$	$0.027^{+0.093}_{-0.015}$	$0.008^{+0.002}_{-0.001}$
GP inverse length scale for *seeing*, $\eta_{\rm fwhm}$	$0.006^{+0.004}_{-0.002}$	$0.010^{+0.018}_{-0.003}$	$0.006^{+0.013}_{-0.002}$
Poisson noise, σ_w (ppm)	276 ± 19	729 ± 71	318 ± 20
Parameter (derived)			
Semi-major axis, a (AU)		0.01651 ± 0.00064	
Orbital inclination, i (°)		$79.52^{+0.54}_{-0.56}$	
Planet radius, R_p ($R_{\rm jup}$)	1.3907 ± 0.0426	1.3836 ± 0.0454	1.3541 ± 0.0416

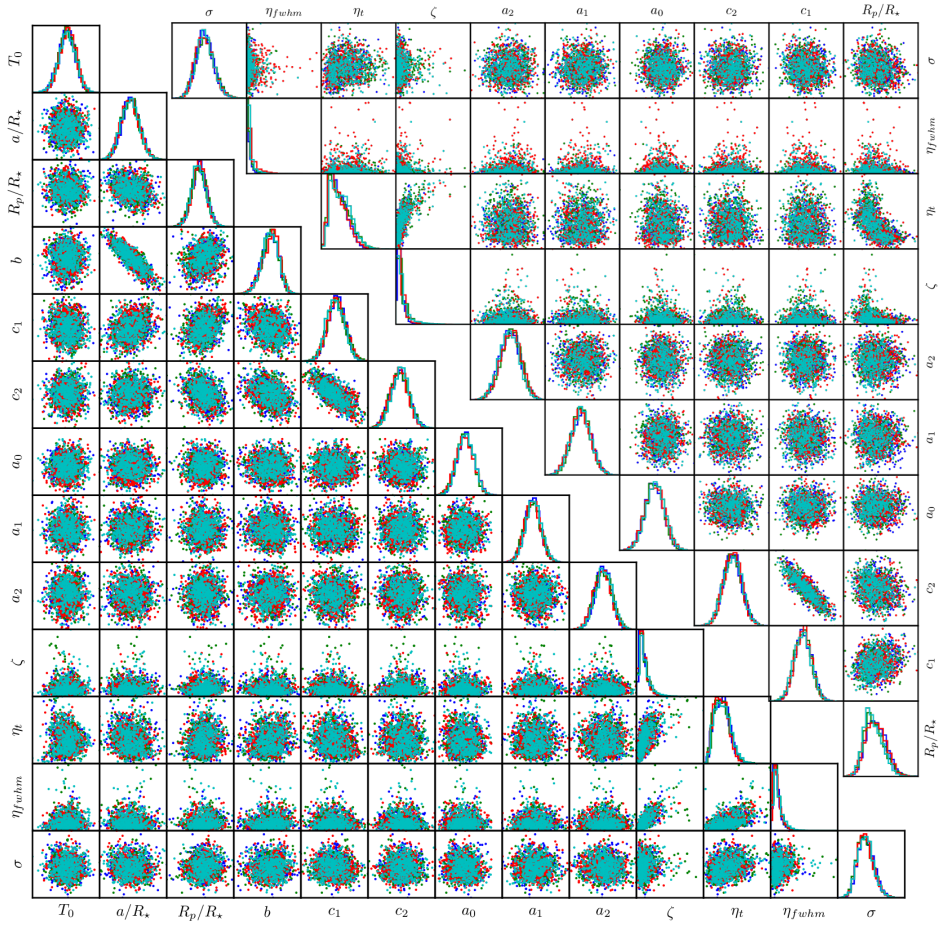

Figure 4.9: Random samples drawn from the four MCMC simulations, for all the fitted parameters, in modelling a broadband light curve (*bottom*) and a spectroscopic light curve (*top*). Both examples are from the Blue dataset. Mutual convergence of all independent chains is evident, as well as the well-documented degeneracies between the impact parameter (b) and the scaled semi-major axis ($a/R_\star$), and the two coefficients of the limb darkening law (c_1 & c_2).

given by a differential application of Planck's law,

$$r_\bullet \equiv \frac{B_\bullet(\lambda, T)}{B_\star(\lambda, T)} = \frac{e^{hc/(\lambda k_B T_\star)} - 1}{e^{hc/(\lambda k_B T_\bullet)} - 1} \tag{4.2}$$

where B is the spectral radiance of the spot ($\bullet$) or the star ($\star$), h is Plank's constant, c is the speed of light, k_B is the Boltzmann's constant, λ is the wavelength at which the flux is measured and T is the temperature of the spot or stellar photosphere.

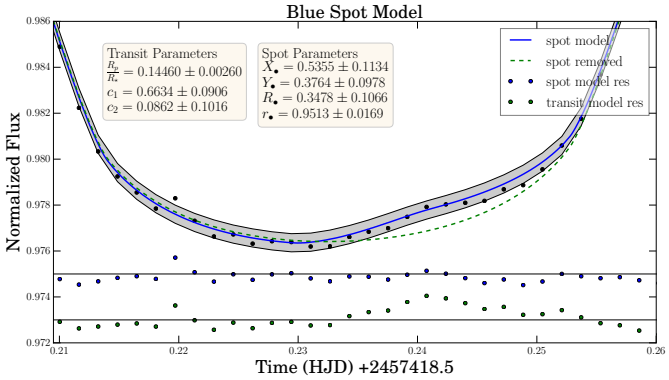

Figure 4.10: Broadband light curve of the Blue dataset, modelled using an analytical model that includes a spot crossing event by the planet. The new inferred planetary radius and the limb darkening coefficients are given in the box to the left, where the offset to the previous results is significantly lower than the derived precision. This is due to the fact that the systematic model accounts well for this anomaly. The inferred spot parameters are given in the middle top box.

The stellar photospheric temperature is 5568 ± 71 K, obtained through precise spectroscopic measurements Torres et al. (2012). From fitting the spectral channels for a spot model the wavelength dependence of the contrast ratio is obtained, shown in figure 4.11. This relation is governed by Equation 4.2 and through a least-squares minimisation approach we obtain a value of 5530 ± 5.6 K for the spot temperature, 38 K cooler than the surrounding photosphere. Furthermore, we compare the initial transmission spectrum in the blue to the one obtained from modelling the light curves with a spot model. These two sets of results are highly consistent, without any change to the obtained slope towards the shorter wavelengths, as is shown in figure 4.12. This consistency highlights the strength of the Gaussian Process red noise model in accounting for any systematic deviation from a transit function. It must be noted that the error bars for the set that include a spot crossing component are underestimated, since here no systematic noise model has been included. This is done to fully capture the impact of spot crossing upon the differential light curves.

Unocculted spots: WASP-19 is an active late G-star with spot anomalies on its surface detected by numerous previous studies (Mancini et al., 2013; Mandell et al., 2013; Tregloan-Reed et al., 2013). Consequently one has to assume that in addition to the occulted spot detected here, there are spots on the stellar surface that are not occulted by the planetary transit chord. Presence of these unocculted spots can lead to an overestimation of the integrated flux from the stellar disk and therefore the planetary relative radius, which is a chromatic effect. To estimate the impact of such unocculted spots

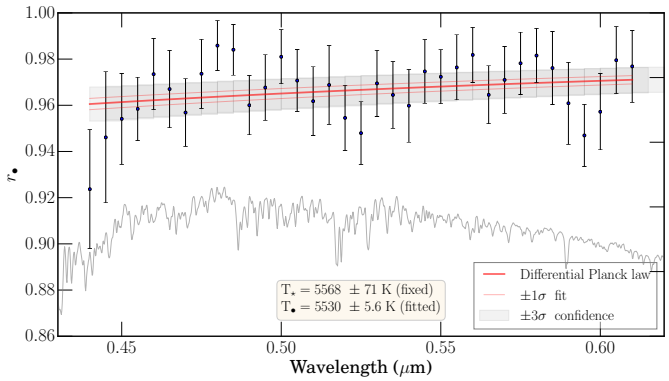

Figure 4.11: Dependence of spot contrast ratio on the wavelength, from which the spot temperature is determined, using Plank's law. For reference, a spectrum of WASP-19 is plotted in light gray. The prior stellar photospheric temperature ($T_\star$) and the fitted spot temperature ($T_\bullet$) are also given.

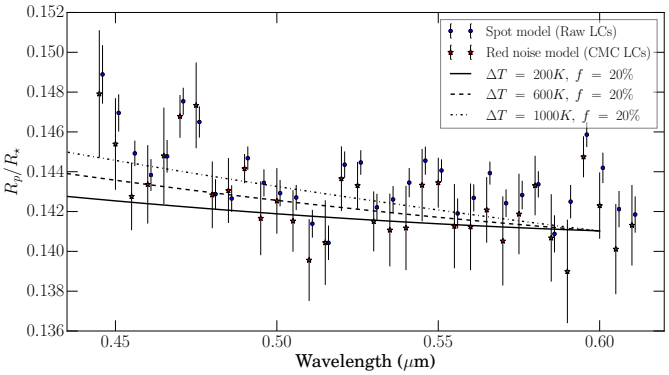

Figure 4.12: Comparison of transmission spectra in the blue, from red noise analysis and the spot modelling. The spot analysis results (*blue points*) have been shifted by +0.01 μm to better distinguish between the two sets of results.

on the transmission spectrum in the blue end of the spectrum and therefore their contribution to the observed slope, transit light curves for WASP-19b are simulated over a rotating spotted star. For information minimisation all possible spots are combined into a single spot with a 20% filling factor, based on previous spot detections in transit light curves of this planet. To estimate the maximum impact of this unocculted spot on the transit depth measurements, the longitude of this combined spot is selected at the center of the stellar disk, since this setup maximises the rotational modulations introduced into the photometry. The spot contrast is calculated via Planck's law, with its temperature 200, 600 and 1000 K below the surrounding pho-

tospheric temperature of 5568 K. Transit light curves are then simulated for each of the wavelength bins in the Blue dataset, at each given spot temperature, adapting those limb darkening coefficient values used as priors in modelling the spectral channels. These light curves are then modeled in a similar manner to the spectrophotometric time series of the observed data and the inferred relative radii as a function of wavelength are compared to the observational results, for each given spot temperature, shown in figure 4.12. The observed slope is partially explained by the possible presence of unocculted spots on the stellar disk, given large spot temperature differences of beyond 1000 K. Spot temperate difference of ∼500 K for an occulted spot has previously been reported (Tregloan-Reed et al., 2013), and together with the much lower temperature measurement here, it is concluded that the observed slope towards the blue end of the spectrum cannot alone be explained by the presence of unocculted spots on the surface. However, any atmospheric conclusions made from measurements of this slope will have to consider the contribution of stellar activity. McCullough et al. (2014) performed a similar analysis in determination of unocculted spot impact upon transmission spectroscopy of HD 189733 b, ruling out this effect as the cause of the observed transmission spectral signals (i.e. confirming their atmospheric nature).

Detailed atmospheric characterisation of WASP-19b[5]

The wavelength dependent radius variations, or the transmission spectrum, is shown in figure 4.13, where the combination of results from the three observing campaigns constructs a broadband spectrum with high precision. It is this precision that facilitates the detection of features originating from the exoplanetary atmosphere. The interpretation of this transmission spectrum is done through fitting theoretical atmospheric models to the data, a process that explores a wide range of the atmospheric parameter space.

The atmospheric properties of WASP-19b at the day-night boundary, probed by the transmission spectrum, are inferred using the atmospheric retrieval algorithm `POSEIDON` (MacDonald and Madhusudhan, 2017). This algorithm explores many millions of transmission spectra – spanning a wide range of chemical compositions, temperatures and cloud/haze properties – in order to identify the range of atmospheres consistent with the spectrum. In addition to the standard optical absorbers expected in hot Jupiter atmospheres (Madhusudhan et al., 2016) (H_2, He, Na, K and H_2O), a wide range of metal oxides and hydrides are considered: TiO, VO, AlO, TiH, NaH, MgH, CrH, CaH, ScH and FeH. The models spanned the continuum

[5]It must be noted that the atmospheric characterisation and analysis from the transmission spectrum is exclusively performed by Nikku Madhusudhan's group at the IoA, Cambridge University, UK. This section shows results from their study and reproduced with their permission.

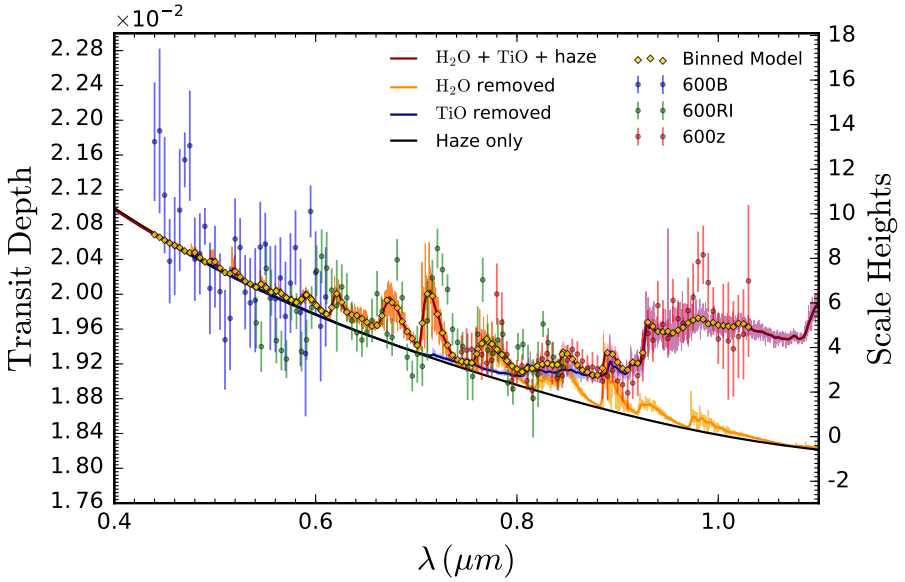

Figure 4.13: The blue, green, and red data points correspond to VLT FORS2 observations using the 600B, 600RI and 600z grisms, respectively. The overall best-fitting spectrum, including opacity due to H_2O, TiO and a global haze, is shown in red at a representative resolution of $R \approx 3000$. The orange spectrum demonstrates the effect of removing H_2O from the best-fit model, whilst the blue spectrum demonstrates the effect of removing TiO. The dark red and blue curves are Gaussian smoothed representations of these two spectra. The black curve shows the underlying haze slope, when H_2O and TiO have been removed.

from clear to cloudy atmospheres, both with and without scattering hazes, including 2D models with inhomogeneous cloud coverage.

We report robust detections of H_2O (6.9σ), TiO (5.3σ) and a strongly scattering haze (7.1σ) enveloping the planet. Constraints on the volume mixing ratios and haze properties are given in figure 4.14. The quantity of water is consistent with expectations for a solar composition atmosphere in thermochemical equilibrium (Madhusudhan, 2012), whilst the TiO abundance is sub-solar. Despite suggestions of substructure in the blue region of the spectrum, which could be explained by metal hydrides, the Bayesian model comparison concludes that a haze alone optimally explains the observations without the need to invoke other chemical species. The haze detected is $\sim 100\times$ stronger than Rayleigh scattering from H_2 alone, follows a power-law with an exponent around -10, and is consistent with 100% coverage across the terminator. An opaque cloud deck is not detected. Finally, the temperature in the line-of-sight photosphere is constrained to 2580^{+340}_{-280}

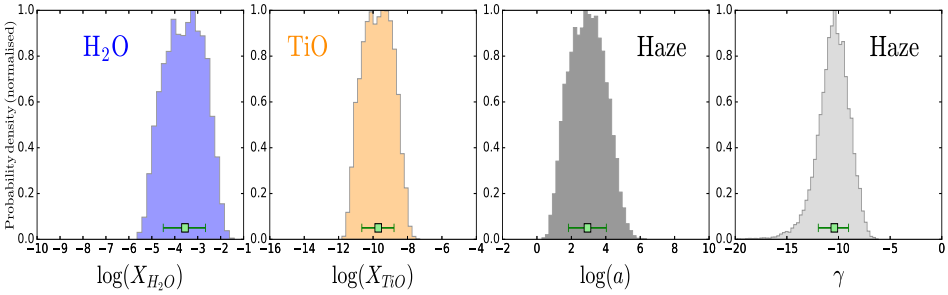

Figure 4.14: The two leftmost histograms show the marginalized posterior probability densities of the H_2O and TiO volume mixing ratios at WASP-19b's day-night terminator. The histograms on the right show the marginalized posterior probability densities of the haze Rayleigh enhancement factor and scattering slope.

K.

The robust detection of TiO in the atmosphere is consistent with expectations for the high temperatures ($\gtrsim$ 2000 K) in the atmosphere (Fortney et al., 2008). The finding marks the first spectroscopic detection of a refractory metal oxide in an exoplanetary atmosphere and demonstrates the importance of visible opacity in transmission spectra. The strong visible opacity contributed due to TiO can have substantial effects on the atmospheric temperature structure and circulation in the planet. If present in large enough quantities on the dayside, the TiO may cause a thermal inversion in the dayside atmosphere (Hubeny et al., 2003; Fortney et al., 2008) which could be observable using high-precision thermal emission spectra with HST and JWST in the future. This could also lead to strong day-night temperature gradients in the planetary atmosphere due to the increased opacity (Showman et al., 2009). Our results demonstrate the capability of ground-based transmission spectroscopy to pursue detailed molecular spectroscopy of exoplanetary atmospheres in the optical.

Retrieval analysis

Atmospheric models. WASP-19b's atmosphere is modelled at the day-night terminator via 100 axially-symmetric layers uniformly spaced in log-pressure between 10^{-6} and 10^{2} bar. It is assumed that $R_p = 1.31$ R_{jup}, $R_\star = 0.993$ $R_\odot$ and the surface gravity is taken as $g = 14.3$ ms^{-1}. Hydrostatic equilibrium is assumed, along with terminator-averaged temperature structure (Madhusudhan and Seager, 2009) and chemistry, with each species distributed uniformly with altitude. Clouds are parametrized by an opaque cloud deck, below which no electromagnetic radiation may pass. Hazes are included via a two-parameter power law Lecavelier Des Etangs

et al. (2008): $a\,\sigma_0(\lambda/\lambda_0)^\gamma$, where λ_0 is a reference wavelength (0.35 μm) and σ_0 is the H_2-Rayleigh scattering cross section at the reference wavelength ($5.31 \times 10^{-31}\,m^2$). Inhomogeneous cloud and haze distributions across the terminator are considered, parameterised by a cloud-coverage factor.

The chemical composition of the atmosphere is modelled as H_2-He dominated, with a fixed H_2/He ratio of 0.17. This background gas is considered to contain a mixture of trace molecular and atomic species, each with parameterised mixing ratios ranging between 10^{-16} and 10^{-2} of the total atmospheric content. A wide range of chemical species possessing prominent absorption features at visible wavelengths is considered, namely: H_2O, Na, K, TiO, VO, AlO, TiH, NaH, MgH, CrH, CaH, ScH and FeH. The molecular line list for H_2O was obtained from the `HITEMP` (Rothman et al., 2010) database, whilst those for the metal oxides and hydrides originated from the `ExoMol` project (Tennyson and Yurchenko, 2012). For each molecular species, cross-sections were pre-computed line-by-line (Hedges and Madhusudhan, 2016) and binned to a resolution of 1 cm^{-1} on a grid of temperatures and pressures spanning the range $10^{-4} - 10^{2}$ bar and $300 - 3500$ K. The Na and K cross sections were based on semi-analytic Lorentzian line profiles (Christiansen et al., 2010). H_2-H_2 and H_2-He collisionally-induced absorption is included from the `HITRAN` database (Richard et al., 2012).

The transmission spectrum of a given model atmosphere is computed by integrating the stellar intensity, exponentially-attenuated by the slant optical depth, over successive annuli for both cloud-free and uniformly-cloudy terminator regions (MacDonald and Madhusudhan, 2017). The two resulting spectra are then linearly-superimposed, weighted by the terminator cloud-coverage factor. The stellar intensities during and outside transit are integrated over the solar angle subtended at the observer to obtain their respective fluxes, with the transit depth given by the fractional stellar flux difference induced as the planet transits its host star. For the visible wavelength spectrum of WASP-19b, the transit depth is computed at 2,000 wavelength points uniformly spaced between $0.4 - 1.1$ μm. The spectrum is then convolved with the instrument point spread functions and integrated over the grism response curves to produce binned model points corresponding to the Blue, Green and Red datasets.

Retrieval methodology. The range of atmospheric properties consistent with the observed transmission spectrum is explored using the `POSEIDON` (MacDonald and Madhusudhan, 2017) atmospheric retrieval algorithm. This algorithm generates many millions of model transmission spectra, mapping the high-dimensional parameter space via the `MultiNest` (Feroz and Hobson, 2008; Feroz et al., 2009, 2013) multimodal nested sampling algorithm

(implemented by the python wrapper `PyMultiNest`[6] (Buchner et al., 2014)). This allows statistical estimation of the underlying atmospheric parameters, in addition to establishing detection significances for model features (e.g. chemical species, clouds/hazes) via nested Bayesian model comparison (Trotta, 2008).

Each model atmosphere is parameterised by a 6 parameter pressure-temperature profile (Madhusudhan and Seager, 2009), 4 parameter inhomogeneous cloud/haze prescription (MacDonald and Madhusudhan, 2017), the *a priori* unknown pressure at R_p, and independent parameters for the volume mixing ratios of a subset of the chemical species {Na, K, TiO, VO, AlO, TiH, NaH, MgH, CrH, CaH, ScH and FeH}. This results in a maximum parameter space dimensionality of 24. Priors for each parameter are taken as either uniform (e.g. top-of-atmosphere temperature) or uniform-in-the-logarithm (e.g. mixing ratios) – depending on whether the prior range is less than or more than two orders of magnitude, respectively.

Initial plausibility of each chemical species is established by computing a full 24-dimensional retrieval with 2,000 `MultiNest` live points. Flat posteriors were observed (no evidence, beyond an upper bound) for all chemical species except K, H_2O, TiO and CaH. The terminator cloud fraction sharply sloped towards the upper edge of the prior (100% cloud/haze coverage). With respect to this reference model, two identical retrievals were run: one with the cloud deck removed and one with the haze removed. Removing the haze incurred a substantial penalty to the Bayesian evidence ($\ln \mathcal{L} = 970.6 \rightarrow 953.6$) – corresponding to a Bayes factor of 1.4×10^7 – equivalent to a 6.1σ detection of a uniform haze across the terminator (with respect to the full chemistry model). The Bayesian evidence was unchanged within the error bars ($\sim$0.1) when the cloud deck was removed, indicating that the data does not support the presence of such a deck.

A second round of retrievals was conducted to assess the potential presence of K, H_2O, TiO and CaH. Given the strong evidence for uniform hazes from the first round, the cloud fraction was fixed to 100% for these runs, leading to a dimensionality of 14 for the reference model. A nested Bayesian model comparison was conducted by removing individual chemical species from the reference model, running a new retrieval for each, and computing the change in the Bayesian evidence. Little change, or a very slight increase, was observed when K and/or CaH were removed, indicating that they are not detected and their presence is only marginally suggested by the data. However, changes in $\ln \mathcal{L} > 10$ were observed when H_2O and/or TiO were removed, indicating strong support for their presence.

A final round of nested retrievals was conducted under the minimal refer-

[6]The multimodal nested sampling algorithm MultiNest, and its python wrapper PyMultiNest, are freely available from `https://ccpforge.cse.rl.ac.uk/gf/project/multinest/` and `https://github.com/JohannesBuchner/PyMultiNest`.

Table 4.3: Bayesian model comparison detections of WASP19b's terminator chemistry and cloud properties.

Model	Evidence $\ln(\mathcal{L}_i)$	Best-fit $\chi^2_{r,\min}$	Bayes Factor $\mathcal{B}_{0i}$	Detection of Ref.
Reference	974.37	1.89	Ref.	Ref.
No Haze	951.05	2.18	1.3×10^{10}	**7.1σ**
No H_2O	952.60	2.15	2.9×10^{9}	**6.9σ**
No TiO	962.06	2.10	2.2×10^{5}	**5.3σ**

Notes: The 'reference' model includes opacity due to H_2, He, H_2O and TiO, along with a parameterized cloud and haze description. An $n\sigma$ detection ($n \geq 3$) indicates the degree of preference for the reference model over the alternative model.

ence model containing just H_2O, TiO, haze and a cloud deck – corresponding to 12 free parameters. This simple reference model has a Bayesian evidence of $\ln \mathcal{L} = 974.37$, a notable increase over the initial reference model, further reaffirming that the additional model complexity incurred by the large collection of other metal oxides/hydrides is not justified in light of the data. The results of the Bayesian model comparison conducted on the basis of these retrievals, minimum best-fit reduced chi-squares, and detection significances for TiO, H_2O and the terminator-spanning haze, with respect to this reference model, are given in Table 4.3. The overall best-fitting transmission spectrum, drawn from the posterior of the reference model (shown in red in figure 4.13), has H_2O and TiO volume mixing ratios of 660 ppm and 0.41 ppb, respectively, with haze parameters a = 342, γ = -7.7 and a reference pressure of 0.2 bar.

Chapter 5

Summary & Outlook

5.1 Summary

This cumulative thesis consists of the following published and in preparation publications:

Sedaghati, E., Boffin, H. M. J., Delrez, L., Gillon, M., Csizmadia, Sz., Smith, A. and Rauer, H. (2017) ***Probing the atmosphere of a sub-Jovian planet orbiting a cool dwarf.*** **Monthly Notices of the Royal Astronomical Society, 468:3123-3134.**

Aim: The impact of the old, degraded LADC prisms, as well as other so-called optical state parameters, on differential spectrophotometric observations with the FORS2 instrument are studied. Such physical variants introduce what is known as *correlated* or *red noise* into exoplanetary transit light curves, due to their differential effects upon the light observed from the various stars. This work aims to quantify such effects using archival data from ESO's services, as well as provide benchmarks for correctly estimating their impact on the determination of precision in the inferred transit parameter values.

Methods: Differential spectrophotometry techniques are used to obtained transit light curves of the hot Jupiter WASP-80b using the 600z grism of the FORS2 instrument, which covers the optical domain towards the red end of the spectrum. Variations in the raw photometry are studied relative to a variety of physical variants that could be possible causes of correlated noise in the time series data. Specifically, the stellar positions relative to the LADC orientation as a function of time are analysed in depth. Those optical state parameters are used to train the Gaussian Process model for fully capturing the systematic noise in the light curves, paramount in inferring the correct precision for the estimated transit parameters. The obtained transmission spectrum is subsequently used together with synthetically produced atmospheric models of arbitrary composition to rule out or detect specific atomic/molecular species, as well as other atmospheric characteristics.

Results: The detailed analysis of the physical variants introducing systematic variations in the light curves was done through the calculation of the various correlation indicators between the flux variations and those parameters. This resulted in the atmospheric seeing and LADC variations (measured through reading the normalised flat-field values along the path of each star) being chosen as initial inputs for "modelling" the elements of the covariance matrix. Gamma prior functions were used for the corresponding length scale parameter of each input and their final inclusion was decided after the analysis of their posterior probability distribution functions. Namely, an input is included if and only if the median of its posterior distribution was more than 3σ away from 0. From modelling the broadband transit light curve, the wavelength independent parameters of the system were determined. Those values were then subsequently used as strict priors in modelling the spectrophotometric light curves, obtained from narrowband (100Å) integration bins. Determination of the relative planetary radius as a function of bin centre resulted in the *transmission spectrum* of this planet. Through comparison with synthetically produced theoretical atmospheric models, initially we rule out the presence of any molecular absorption in the upper atmosphere leading to increased radius in the IR. This conclusion was reached when our results were used together with those previous values obtained from HST spectroscopy. Our results, additionally, point to enhanced absorption in the pressure-broadened wing of K doublet falling within the wavelength domain of the grism employed. To investigate this further very narrowband (30Å) bins were used to obtain relative radius values around the core of the K doublet. Through comparison of these results with models with and without K included, resulted in the significant detection of neutral K in the upper atmosphere of WASP-80b, a rare giant orbiting a cool dwarf.

Sedaghati, E., Boffin, H. M. J., Csizmadia, S., Gibson, N., Kabath, P., Mallonn, M. and Van den Ancker, M. E. (2015) ***Regaining the FORS: optical ground-based transmission spectroscopy of the exoplanet WASP-19b with VLT+ FORS2.*** **Astronomy & Astrophysics, 576, L11.**

Aim: This work aimed at an initial analysis of the improvements made to transmission spectroscopy observations with the FORS2 instrument, following the LADC upgrade in November 2014. The publication of this letter led to this instrument again being considered for exoplanetary atmospheric detections, as it was previously determined that it was not suitable for such science case due to the LADC deficiencies. This work is based on data taken during a technical night that was afforded by ESO, following the upgrade of the prisms in the atmospheric dispersion corrector unit. WASP-19b was chosen for this work, primarily because it had an observable and suitable transit during the technical night, 14th of November 2014. Additionally, this target

had previously been observed using FORS2 in MXU mode. This allowed us to make a direct comparison with data taken with the old LADC unit and make a quantitative assessment of the improvements made to exoplanet transmission spectroscopy observations with this instrument.

Methods: Differential spectrophotometric techniques were used to observe a single transit of WASP-19b in the visible domain (0.54 – 0.85 μm) using the 600RI grism. Through modelling the narrowband spectral transit light curves, the spectrum of planetary radius as the function of wavelength was derived. A frequentist approach, as opposed to a Bayesian one, was used in determination of the best fit parameter values and their associated uncertainties.

Results: The analysis and comparison of the fit residuals for data from before and after the LADC upgrade, indicated a marginally significant reduction in the level of systematic noise present in FORS2 transit light curves. This was the main message of this work that gave the impetus to the wider community to resume transmission spectroscopy observations with this instrument. Additionally, our transmission spectrum of WASP-19b showed clear and significant agreement with previous results for the same planet and highlighted the reliability of the instrument. We generally observed a relatively flat spectrum devoid of any optical absorption from atomic species in the upper atmosphere, such as Na or K, both of which have strong absorption bands within our observation domain. However, due to the lack of precision, we were not able to distinguish atmospheric models including or lacking metal oxides, a fact that was improved upon in future studies.

Sedaghati, E., Boffin, H. M. J., Jeřabková, T., Muñoz, A. G., Grenfell, J. L., Smette, A., Ivanov, V. D., Csizmadia, S., Cabrera, J., Kabath, P. and Rocchetto, M. (2016) ***Potassium detection in the clear atmosphere of a hot-Jupiter-FORS2 transmission spectroscopy of WASP-17b.*** **Astronomy & Astrophysics, 596, A47.**

Aim: As part of a successful observing proposal, the exoplanet WASP-17b was observed using the 600RI grism of the FORS2 instrument. The aim of this project was to investigate atmospheric characteristics of the so-called bloated hot Jupiters. These are the planets that due to their proximity to their host stars, and subsequently immense amount of insolation they receive, have very extended atmospheres, which also leads to very low values of calculated densities. Such planets, due to their extensive atmospheres, and subsequently large atmospheric scale heights, present perfect opportunities to advance our understanding of exoplanetary atmospheres.

Methods: The observational and data reduction techniques here are similar to what was presented in previous publications. For the analysis of transit light curves, we used a Bayesian approach, where the systematic noise was modelled as a Gaussian Process. In this framework, the covariance matrix

in the description of the likelihood function was "modelled" with the aid of a carefully selected *kernel*, which allowed the introduction of off-diagonal elements to that matrix. Namely, this meant that the systematic noise was modelled in a non-parametric way and therefore no assumption is made about the form of the correlated noise. Also great effort was made in trying to remove the telluric absorption signatures upon the observed spectra. This was done using the `molecfit` routine, that utilises meteorological data from various satellites and stations.

Results: We created numerous synthetic atmospheric models exploring a limited domain in the atmospheric parameter space. Comparison to such models yielded the significant detection of neutral K via absorption in the pressure-broadened wing of the line core at ~ 0.768 μm. Additionally, via measurements of the Rayleigh scattering slope, we detect a H/He dominated atmosphere, through the estimation of the atmospheric mean molecular mass, μ_m. Unfortunately, the experiment of telluric absorption correction was not successful in improving the precision of transit light curves, most likely caused by the low resolution of FORS2 spectra.

Sedaghati, E., Boffin, H. M. J., MacDonald, R. J., Gandhi, S., Madhusudhan, N., Gibson, N. P., Oshagh, M., Claret, A. and Rauer, H. (2017) *TiO in the atmosphere of a hot Jupiter*. Nature, accepted.

Aim: Following single epoch/grism observations of previous studies, a programme was proposed to build upon the already existing data for the exoplanet WASP-19b. Namely, the proposed work consisted of transit observations of the same target with the 600B and the 600z grisms leading to a complete optical coverage of the transmission spectrum ($0.44 - 1.03$ μm). This broadband coverage, coupled with the high spectral precision expected from FORS2, would lead to a transmission spectrum that ticks all the boxes for probing the spectrum with atmospheric retrieval routines.

Methods: The observational strategies for the multi-epoch observations of this work followed the recommendations that we made in another work (Boffin et al., 2016b) for optimal scientific yield. This included a careful selection of comparison stars within the FoV and the design of the observing masks, as well as the use of non-standard CCD readout modes. Optimal extraction methods were tested and a highly specialised, automated analysis pipeline was developed that allowed for testing and optimising every step in the reduction and analysis approaches. The light curves were analysed using the previously mentioned Gaussian Process model with multiple optical state inputs in the calculation of the covariance matrix via the *kernel*. Additionally and importantly, the impact of occulted and unocculted spots were estimated through writing a new analytical model including spot crossing events and the simulations of transit with a spotted star, respectively. The

broadband transmission spectrum was subsequently analysed using retrieval methods that employs the specialised algorithm, `POSEIDON`, which explored many transmission spectra spanning a very wide range of the atmospheric parameter space. In addition to the standard optical absorbers expected in the atmosphere of a hot Jupiter, a wide range of metal oxides and hydrides were also considered. A continuum from clear to cloudy atmospheres, both with and without scattering hazes, including 2D models with inhomogeneous cloud coverage was considered.

Results: Our analysis of stellar activity and its impact on the final transmission spectrum concluded that the occulted spots were well accounted for by the Gaussian Process systematic model and the unocculted spots could not alone be responsible for the large observed slope towards the blue end of the spectrum. From the retrieval analysis, we report significant detections of H_2O (6.9σ), TiO (5.3σ) and a strongly scattering haze (7.1σ). The detection of water is consistent with expectation, since it was previously discovered in this planet using HST observations and acts as a sanity check of our results. The molecular quantities are consistent with expectations for a solar composition atmosphere in thermochemical equilibrium, whilst the TiO abundance is sub-solar. The detected haze is $\sim 100\times$ stronger than Rayleigh scattering from H_2 alone. We measure the line of sight temperature of the photosphere as 2580^{+340}_{-280} K. Detection of TiO in the atmosphere of WASP-19b marks the first spectroscopic detection of a refractory metal oxide in an exoplanetary atmosphere and demonstrates the importance of visible opacity in transmission spectra. If TiO is present in large enough quantities on the dayside, it may cause thermal inversion in the dayside atmosphere which could be observable using high precision thermal emission spectra with the HST and JWST. This could additionally lead to strong day-night temperature gradients in the planetary atmosphere due to the increased opacity.

All publications are printed in the Appendix at the end of this thesis. Results and data from this work have also been used in the following publications and reports:

Boffin, H. M. J., Blanchard, G., Gonzalez, O., Moehler, S., Sedaghati, E., Gibson, N., van den Ancker, M. E., Smoker, J., Anderson, J., Hummel, C., Dobrzycka, D., Smette, A., Rupprecht, G. (2015) ***Making FORS2 Fit for Exoplanet Observations (again).*** **The Messenger, 159, 6-9.**

Boffin, H. M. J., Sedaghati, E., Blanchard, G., Gonzalez, O., Moehler, S., Gibson, N., van den Ancker, M. E., Smoker, J., Anderson, J., Hummel, C. and Dobrzycka, D. (2016) ***Regaining the FORS: making optical ground-based transmission spectroscopy of exoplanets with VLT+ FORS2 possible again.*** **SPIE Astronomical Telescopes+ Instrumentation (pp. 99082B-99082B).**

Csizmadia, Sz., Sedaghati, E., Boffin, H. M. J. (2016) ***Discovery of a new δ Scuti-type variable in the FORS2 FoV, found during transit observations of WASP-19b. IBVS*****, 6200, t22-t23.**

Dehghan Firoozabadi, A., Diaz, A., Rojo, P., Soto, I., Mahu, R., Becerra Yoma, N., Sedaghati, E. (2017) ***Unsupervised method for correlated noise removal for multi-wavelength exo-planet transit observations.*** **Publications of the Astronomical Society of the Pacific. In press.**

The complete list of publications is summarised in the proceeding chapter.

5.2 Outlook

Currently, transmission spectroscopy provides the most promising avenue for probing atmospheres of exoplanets. One distant goal of this science case is to detect and characterise the atmospheres of those rocky exoplanets orbiting in the habitable zone of their host stars (Kasting, 1997; Kopparapu et al., 2013). Those targets are still beyond the reach of the direct imaging technique, that thus far has been successful only in probing a handful of giant planets on very wide orbits (e.g. Marois et al., 2008; Lagrange et al., 2009; Currie et al., 2012; Janson et al., 2013). Therefore, transmission spectroscopy currently offers the best hope for detection of any possible biosignatures (Snellen et al., 2013), indicative of biological processes producing them. Even at the time of writing, there are efforts being undertaken in detecting and characterising such planets, namely one of the planets in the newly discovered TRAPPIST-1 system (Gillon et al., 2016, 2017).

Space observatories

With the launch of the JWST, the successor to the HST, we will for the first time be able to probe atmospheres of exoplanets down to those rocky worlds in their respective habitable zones, in the IR domain at high resolution (Belu et al., 2011). This is the domain of the electromagnetic radiation where possible imprints from biomarkers (Segura et al., 2005; Kiang et al., 2007a,b) will be present in transmission spectra. This is due to the fact that this space telescope is designed for operation in this wavelength regime. NIRSpec (Birkmann et al., 2014) and MIRI (Wright et al., 2004) on-board the JWST will cover wavelengths up to far-IR. Shabram et al. (2011) have already shown, through simulations, the capabilities of those instruments in detection of the atmosphere of the Neptune-sized planet GJ 436 b.

In addition to those general purpose telescopes and instruments, there are currently a number of proposals being considered for dedicated space missions to perform exoplanet planets transmission spectroscopy. One of those is the Atmospheric Remote-sensing Exoplanet Large-survey (ARIEL; Puig et al., 2016; Tinetti et al., 2016), which is one of the three candidate missions selected by the ESA for its next medium-class science mission due for launch in 2026. Its objective is to study several hundred exoplanetary atmospheres, ranging from hot Jupiters all the way down to Earth-sized planets, in the visible to mid-IR ($0.5-7.8\ \mu$m). Given its success in selection, this mission will provide the community with an unprecedented sample of exoplanetary atmospheres that will facilitate a viable statistical study.

Ground-based facilities

Complementing those results from space-based observations, ground-based facilities will play a key role in obtaining broadband transmission spectra. For instance, the JWST transmission spectra will have a cut off wavelength in the near-IR regime as a lower limit. Therefore, it will be essential that those results are complemented with transmission spectra in the optical domain, obtained from ground-based facilities, including FORS2, GMOS or similar instruments capable of performing the demanding multi-object, high temporal, spectroscopic observations.

The new generation of Extremely Large Telescopes will allow us to probe exoplanets orbiting much fainter stars, as compared to the current limitations, through their enormous light collecting areas. Telescopes such as the ELT, TMT or GMT not only will probe planets around fainter targets and hence provide us with much larger sample of planets to choose from, they will also be able to probe the atmospheres of terrestrial planets. Those are currently beyond reach, since their atmospheric signals are too small for detection with the current facilities. Coupled with the large collecting areas of their primary mirrors, improved instrumentation (ELT-MOS for instance) and advances in adaptive optics technology (e.g. deformable secondary mirrors or multi-guide star systems), will facilitate derivation of much more precise transit light curves, which in turn translates to much improved precision in the determination of planetary radius. All these factors together will enable us to probe atmospheres of terrestrial planets with much smaller scale heights, as compared to those hot Jupiters currently being studied, including this work.

In this context, the methodology employed throughout this thesis provides a starting point and a benchmark, when we finally come to data obtained with those future facilities. Certainly, those telescopes and instruments will provide us with new challenges in correctly interpreting results leading to exoplanet atmospheric detections. How much caution and scepticism is placed upon capturing the extent to which those data are compromised by systematic effects, be it instrumental or stellar, will provide a measure of how much any conclusions and detections is to be trusted.

In addition to the method of transmission spectroscopy employed throughout this entire thesis, there is also very bright outlook for other, complementary methods of detecting exoplanetary atmospheres. For instance, another approach to performing transmission spectroscopy, is to zoom into the regions of interest, where any optical absorbers might be present. To do this, one takes very high resolution spectra in-transit, as well as just before and after. A comparison between the flux levels obtained from these two sets of spectra allows us to very precisely determine the presence of atomic species.

This type of study has already been performed with instruments such as HARPS at ESO's La Silla observatory. As part of my future research at ESO, I will be using current and future facilities like ESPRESSO to detect essential atmospheric signals with very high precision. While transmission spectroscopy probes the upper atmosphere, observing the **reflected and emitted light** from a planet's day-side allows us to probe deeper into the lower regions of the atmosphere and detect heavier species that due to their higher molecular weights are not present in the upper regions. This technique was successfully employed at the VLT using the CRIRES instrument on multiple instances to detect CO and H_2O (Birkby et al., 2013). The upgraded version of this instrument, CRIRES+ (Dorn et al., 2014), is planned for installation at the Nasmyth focus of UT3, some time in 2018. Being at ESO when this takes place, I will have the chance to work closely with this instrument and understand and improve the exo-atmospheric observations to be made with it. In addition to detecting the reflected light, the reach of this instrument into the near-IR will also allow for in-transit high resolution spectroscopy, giving us access to absorption regions for important molecular gases such as CO, NH_3, CH_4, and more.

Publications by E. Sedaghati

Sedaghati, E., Boffin, H. M. J., Csizmadia, Sz., Gibson, N., Kabath, P., Mallonn, M. and Van den Ancker, M. E., 2015. Regaining the FORS: optical ground-based transmission spectroscopy of the exoplanet WASP-19b with VLT+ FORS2. *Astron. & Astrophys*, 576, L11. DOI: 10.1051/0004-6361/201525822

Boffin, H. M. J., Blanchard, G., Gonzalez, O., Moehler, S., **Sedaghati, E.**, Gibson, N., van den Ancker, M. E., Smoker, J., Anderson, J., Hummel, C., Dobrzycka, D., Smette, A., Rupprecht, G., 2015. Making FORS2 Fit for Exoplanet Observations (again), *The Messenger*, 159, 6-9. 2015Msngr.159....6B

Sedaghati, E. and Boffin, H., 2015. Report on the "Chilean Exoplanet Meeting". *The Messenger*, 161, 49-51. 2015Msngr.161...49S

Sedaghati, E., Boffin, H. M. J., Jeřabková, T., Muñoz, A. G., Grenfell, J. L., Smette, A., Ivanov, V. D., Csizmadia, Sz., Cabrera, J., Kabath, P. and Rocchetto, M., 2016. Potassium detection in the clear atmosphere of a hot-Jupiter-FORS2 transmission spectroscopy of WASP-17b. *Astron. & Astrophys*, 596, A47. DOI: 10.1051/0004-6361/201629090

Boffin, H. M. J., **Sedaghati, E.**, Blanchard, G., Gonzalez, O., Moehler, S., Gibson, N., van den Ancker, M. E., Smoker, J., Anderson, J., Hummel, C. and Dobrzycka, D., 2016. Regaining the FORS: making optical ground-based transmission spectroscopy of exoplanets with VLT+ FORS2 possible again. *SPIE Astronomical Telescopes+ Instrumentation* (pp. 99082B-99082B). DOI: 10.1117/12.2232094

Csizmadia, Sz., **Sedaghati, E.**, Boffin, H. M. J., 2016. Discovery of a new δ Scuti-type variable in the FORS2 FoV, found during transit observations of WASP-19b. *IBVS*, 6200, t22-t23. 2016IBVS.6200...12C

Sedaghati, E., Boffin, H. M. J., Delrez, L., Gillon, M., Csizmadia, Sz., Smith, A. and Rauer, H., 2017. Probing the atmosphere of a sub-Jovian planet orbiting a cool dwarf. *Monthly Notices of the Royal Astronomical Society*, 468, 3123-3134. DOI: 10.1093/mnras/stx646

Dehghan Firoozabadi, A., Diaz, A., Rojo, P., Soto, I., Mahu, R., Becerra Yoma, N., **Sedaghati, E.**, 2017. Unsupervised method for correlated noise removal for multi-wavelength exo-planet transit observations. *Publications of the Astronomical Society of the Pacific*. In press.

Sedaghati, E., Boffin, H. M. J., MacDonald, R. J., Gandhi, S., Madhusudhan, N., Gibson, N. P., Oshagh, M., Claret, A. and Rauer, H., 2017. Detection of TiO in a hot Jupiter atmosphere. *Nature*, accepted.

Bibliography

Anderson, D. R., A. Collier Cameron, C. Hellier, M. Lendl, T. A. Lister, P. F. L. Maxted, D. Queloz, B. Smalley, A. M. S. Smith, A. H. M. J. Triaud, R. G. West, D. J. A. Brown, M. Gillon, F. Pepe, D. Pollacco, D. Ségransan, R. A. Street, and S. Udry
2011. WASP-31b: a low-density planet transiting a metal-poor, late-F-type dwarf star. A&A, 531:A60.

Appenzeller, I., K. Fricke, W. Fürtig, W. Gässler, R. Häfner, R. Harke, H.-J. Hess, W. Hummel, P. Jürgens, R.-P. Kudritzki, K.-H. Mantel, W. Meisl, B. Muschielok, H. Nicklas, G. Rupprecht, W. Seifert, O. Stahl, T. Szeifert, and K. Tarantik
1998. Successful commissioning of FORS1 - the first optical instrument on the VLT. *The Messenger*, 94:1.

Atreya, S. K.
1986. Atmospheres and Ionospheres of the Outer Planets and Their Satellites. *Physics and Chemistry in Space*, 15.

Avila, G., G. Rupprecht, and J. M. Beckers
1997. Atmospheric dispersion correction for the FORS Focal Reducers at the ESO VLT. In *Optical Telescopes of Today and Tomorrow*, A. L. Ardeberg, ed., volume 2871 of Proc. SPIE, Pp. 1135–1143.

Bakos, G. Á., J. D. Hartman, W. Bhatti, A. Bieryla, M. de Val-Borro, D. W. Latham, L. A. Buchhave, Z. Csubry, K. Penev, G. Kovács, B. Béky, E. Falco, T. Kovács, A. W. Howard, J. A. Johnson, H. Isaacson, G. W. Marcy, G. Torres, R. W. Noyes, P. Berlind, M. L. Calkins, G. A. Esquerdo, J. Lázár, I. Papp, and P. Sári
2015. HAT-P-54b: A Hot Jupiter Transiting a 0.6 $M_{\odot}$ Star in Field 0 of the K2 Mission. AJ, 149:149.

Barman, T. S., B. Macintosh, Q. M. Konopacky, and C. Marois
2011. Clouds and Chemistry in the Atmosphere of Extrasolar Planet HR8799b. ApJ, 733:65.

Bean, J. L., J.-M. Désert, P. Kabath, B. Stalder, S. Seager, E. Miller-Ricci Kempton, Z. K. Berta, D. Homeier, S. Walsh, and A. Seifahrt
2011. The Optical and Near-infrared Transmission Spectrum of the Super-Earth GJ 1214b: Further Evidence for a Metal-rich Atmosphere. ApJ, 743:92.

Bean, J. L., J.-M. Désert, A. Seifahrt, N. Madhusudhan, I. Chilingarian, D. Homeier, and A. Szentgyorgyi
2013. Ground-based Transit Spectroscopy of the Hot-Jupiter WASP-19b in the Near-infrared. ApJ, 771:108.

Bean, J. L., E. Miller-Ricci Kempton, and D. Homeier
2010. A ground-based transmission spectrum of the super-Earth exoplanet GJ 1214b. Nature, 468:669–672.

Belu, A. R., F. Selsis, J.-C. Morales, I. Ribas, C. Cossou, and H. Rauer
2011. Primary and secondary eclipse spectroscopy with JWST: exploring the exoplanet parameter space. A&A, 525:A83.

Berta, Z. K., J. Irwin, D. Charbonneau, C. J. Burke, and E. E. Falco
2012. Transit Detection in the MEarth Survey of Nearby M Dwarfs: Bridging the Clean-first, Search-later Divide. AJ, 144:145.

Bigelow, B. C., A. M. Dressler, S. A. Shectman, and H. W. Epps
1998. IMACS: the multiobject spectrograph and imager for the Magellan I telescope. In *Optical Astronomical Instrumentation*, S. D'Odorico, ed., volume 3355 of Proc. SPIE, Pp. 225–231.

Birkby, J. L., R. J. de Kok, M. Brogi, E. J. W. de Mooij, H. Schwarz, S. Albrecht, and I. A. G. Snellen
2013. Detection of water absorption in the day side atmosphere of HD 189733 b using ground-based high-resolution spectroscopy at 3.2 μm. MNRAS, 436:L35–L39.

Birkby, J. L., R. J. de Kok, M. Brogi, H. Schwarz, and I. A. G. Snellen
2017. Discovery of Water at High Spectral Resolution in the Atmosphere of 51 Peg b. AJ, 153:138.

Birkmann, S. M., P. Ferruit, C. Alves de Oliveira, T. Böker, G. De Marchi, G. Giardino, M. Sirianni, M. Stuhlinger, P. Jensen, P. Rumler, M. Falcolini, M. B. J. te Plate, G. Cresci, B. Dorner, R. Ehrenwinkler, X. Gnata, and T. Wettemann
2014. Status of the JWST/NIRSpec instrument. In *Space Telescopes and Instrumentation 2014: Optical, Infrared, and Millimeter Wave*, volume 9143 of Proc. SPIE, P. 914308.

Boffin, H., G. Blanchard, O. Gonzalez, S. Moehler, E. Sedaghati, N. Gibson, M. van den Ancker, J. Smoker, J. Anderson, C. Hummel, D. Dobrzycka, A. Smette, and G. Rupprecht
2015. Making FORS2 Fit for Exoplanet Observations (again). *The Messenger*, 159:6–9.

Boffin, H., S. Moehler, and W. Freudling
2016a. FORS2 Rotating Flat Field Systematics Fixed − Recent Exchange of FORS LADC Prisms Improves the Long-known Flat-fielding Problem. *The Messenger*, 163:10–11.

Boffin, H. M. J., E. Sedaghati, G. Blanchard, O. Gonzalez, S. Moehler, N. Gibson, M. van den Ancker, J. Smoker, J. Anderson, C. Hummel, D. Dobrzycka, A. Smette, and G. Rupprecht
2016b. Regaining the FORS: making optical ground-based transmission spectroscopy of exoplanets with VLT+FORS2 possible again. volume 9908 of Proc. SPIE, P. 99082B.

Buchner, J., A. Georgakakis, K. Nandra, L. Hsu, C. Rangel, M. Brightman, A. Merloni, M. Salvato, J. Donley, and D. Kocevski
2014. X-ray spectral modelling of the AGN obscuring region in the CDFS: Bayesian model selection and catalogue. A&A, 564:A125.

Charbonneau, D., L. E. Allen, S. T. Megeath, G. Torres, R. Alonso, T. M. Brown, R. L. Gilliland, D. W. Latham, G. Mandushev, F. T. O'Donovan, and A. Sozzetti
2005. Detection of Thermal Emission from an Extrasolar Planet. ApJ, 626:523–529.

Charbonneau, D., Z. K. Berta, J. Irwin, C. J. Burke, P. Nutzman, L. A. Buchhave, C. Lovis, X. Bonfils, D. W. Latham, S. Udry, R. A. Murray-Clay, M. J. Holman, E. E. Falco, J. N. Winn, D. Queloz, F. Pepe, M. Mayor, X. Delfosse, and T. Forveille
2009. A super-Earth transiting a nearby low-mass star. Nature, 462:891–894.

Charbonneau, D., T. M. Brown, D. W. Latham, and M. Mayor
2000. Detection of Planetary Transits Across a Sun-like Star. ApJ, 529:L45–L48.

Charbonneau, D., T. M. Brown, R. W. Noyes, and R. L. Gilliland
2002. Detection of an Extrasolar Planet Atmosphere. ApJ, 568:377–384.

Christiansen, J. L., S. Ballard, D. Charbonneau, N. Madhusudhan, S. Seager, M. J. Holman, D. D. Wellnitz, D. Deming, M. F. A'Hearn, and EPOXI

Team
2010. Studying the Atmosphere of the Exoplanet HAT-P-7b Via Secondary Eclipse Measurements with EPOXI, Spitzer, and Kepler. ApJ, 710:97–104.

Claret, A.
2000. A new non-linear limb-darkening law for LTE stellar atmosphere models. Calculations for -5.0 < log[M/H] < +1, 2000 K < T_{eff} < 50000 K at several surface gravities. A&A, 363:1081–1190.

Claret, A., P. H. Hauschildt, and S. Witte
2013. New limb-darkening coefficients for Phoenix/1d model atmospheres. II. Calculations for 5000 K ≤ T_{eff} ≤ 10 000 K Kepler, CoRot, Spitzer, uvby, UBVRIJHK, Sloan, and 2MASS photometric systems. A&A, 552:A16.

Collier Cameron, A., K. Horne, A. Penny, and D. James
1999. Probable detection of starlight reflected from the giant planet orbiting τ Boötis. Nature, 402:751–755.

Collier Cameron, A., D. M. Wilson, R. G. West, L. Hebb, X.-B. Wang, S. Aigrain, F. Bouchy, D. J. Christian, W. I. Clarkson, B. Enoch, M. Esposito, E. Guenther, C. A. Haswell, G. Hébrard, C. Hellier, K. Horne, J. Irwin, S. R. Kane, B. Loeillet, T. A. Lister, P. Maxted, M. Mayor, C. Moutou, N. Parley, D. Pollacco, F. Pont, D. Queloz, R. Ryans, I. Skillen, R. A. Street, S. Udry, and P. J. Wheatley
2007. Efficient identification of exoplanetary transit candidates from SuperWASP light curves. MNRAS, 380:1230–1244.

Croll, B., L. Albert, R. Jayawardhana, E. Miller-Ricci Kempton, J. J. Fortney, N. Murray, and H. Neilson
2011. Broadband Transmission Spectroscopy of the Super-Earth GJ 1214b Suggests a Low Mean Molecular Weight Atmosphere. ApJ, 736:78.

Crossfield, I. J. M., T. Barman, and B. M. S. Hansen
2011. High-resolution, Differential, Near-infrared Transmission Spectroscopy of GJ 1214b. ApJ, 736:132.

Crossfield, I. J. M., T. Barman, B. M. S. Hansen, and A. W. Howard
2013. Warm ice giant GJ 3470b. I. A flat transmission spectrum indicates a hazy, low-methane, and/or metal-rich atmosphere. A&A, 559:A33.

Csizmadia, S., E. Sedaghati, and H. M. J. Boffin
2016. A new variable star in the FoV of WASP-19 from VLT/FORS2 observations. *Information Bulletin on Variable Stars*, 6200.

Currie, T., A. Burrows, N. Madhusudhan, M. Fukagawa, J. H. Girard, R. Dawson, R. Murray-Clay, S. Kenyon, M. Kuchner, S. Matsumura, R. Jayawardhana, J. Chambers, and B. Bromley
2013. A Combined Very Large Telescope and Gemini Study of the Atmosphere of the Directly Imaged Planet, β Pictoris b. ApJ, 776:15.

Currie, T., J. Debes, T. J. Rodigas, A. Burrows, Y. Itoh, M. Fukagawa, S. J. Kenyon, M. Kuchner, and S. Matsumura
2012. Direct Imaging Confirmation and Characterization of a Dust-enshrouded Candidate Exoplanet Orbiting Fomalhaut. ApJ, 760:L32.

de Mooij, E. J. W., R. J. de Kok, S. V. Nefs, and I. A. G. Snellen
2011. The GROUSE project. II. Detection of the K_s-band secondary eclipse of exoplanet HAT-P-1b. A&A, 528:A49.

Deming, D., J. Harrington, S. Seager, and L. J. Richardson
2006. Strong Infrared Emission from the Extrasolar Planet HD 189733b. ApJ, 644:560–564.

Deming, D., A. Wilkins, P. McCullough, A. Burrows, J. J. Fortney, E. Agol, I. Dobbs-Dixon, N. Madhusudhan, N. Crouzet, J.-M. Desert, R. L. Gilliland, K. Haynes, H. A. Knutson, M. Line, Z. Magic, A. M. Mandell, S. Ranjan, D. Charbonneau, M. Clampin, S. Seager, and A. P. Showman
2013. Infrared Transmission Spectroscopy of the Exoplanets HD 209458b and XO-1b Using the Wide Field Camera-3 on the Hubble Space Telescope. ApJ, 774:95.

Dorn, C., A. Khan, K. Heng, J. A. D. Connolly, Y. Alibert, W. Benz, and P. Tackley
2015. Can we constrain the interior structure of rocky exoplanets from mass and radius measurements? A&A, 577:A83.

Dorn, R. J., G. Anglada-Escude, D. Baade, P. Bristow, R. Follert, D. Gojak, J. Grunhut, A. Hatzes, U. Heiter, M. Hilker, D. J. Ives, Y. Jung, H.-U. Käufl, F. Kerber, B. Klein, J.-L. Lizon, M. Lockhart, T. Löwinger, T. Marquart, E. Oliva, L. Origlia, L. Pasquini, J. Paufique, N. Piskunov, E. Pozna, A. Reiners, A. Smette, J. Smoker, U. Seemann, E. Stempels, and E. Valenti
2014. CRIRES+: Exploring the Cold Universe at High Spectral Resolution. *The Messenger*, 156:7–11.

Ehrenreich, D., G. Hébrard, A. Lecavelier des Etangs, D. K. Sing, J.-M. Désert, F. Bouchy, R. Ferlet, and A. Vidal-Madjar
2007. A Spitzer Search for Water in the Transiting Exoplanet HD 189733b. ApJ, 668:L179–L182.

Esteves, L. J., E. J. W. De Mooij, and R. Jayawardhana
2013. Optical Phase Curves of Kepler Exoplanets. ApJ, 772:51.

Evans, T. M., D. K. Sing, H. R. Wakeford, N. Nikolov, G. E. Ballester, B. Drummond, T. Kataria, N. P. Gibson, D. S. Amundsen, and J. Spake
2016. Detection of H_2O and Evidence for TiO/VO in an Ultra-hot Exoplanet Atmosphere. ApJ, 822:L4.

Faedi, F., S. C. C. Barros, D. R. Anderson, D. J. A. Brown, A. Collier Cameron, D. Pollacco, I. Boisse, G. Hébrard, M. Lendl, T. A. Lister, B. Smalley, R. A. Street, A. H. M. J. Triaud, J. Bento, F. Bouchy, O. W. Butters, B. Enoch, C. A. Haswell, C. Hellier, F. P. Keenan, G. R. M. Miller, V. Moulds, C. Moutou, A. J. Norton, D. Queloz, A. Santerne, E. K. Simpson, I. Skillen, A. M. S. Smith, S. Udry, C. A. Watson, R. G. West, and P. J. Wheatley
2011. WASP-39b: a highly inflated Saturn-mass planet orbiting a late G-type star. A&A, 531:A40.

Feroz, F. and M. P. Hobson
2008. Multimodal nested sampling: an efficient and robust alternative to Markov Chain Monte Carlo methods for astronomical data analyses. MNRAS, 384:449–463.

Feroz, F., M. P. Hobson, and M. Bridges
2009. MULTINEST: an efficient and robust Bayesian inference tool for cosmology and particle physics. MNRAS, 398:1601–1614.

Feroz, F., M. P. Hobson, E. Cameron, and A. N. Pettitt
2013. Importance Nested Sampling and the MultiNest Algorithm. *ArXiv e-prints*, 1306:2144.

Fischer, P. D., H. A. Knutson, D. K. Sing, G. W. Henry, M. W. Williamson, J. J. Fortney, A. S. Burrows, T. Kataria, N. Nikolov, A. P. Showman, G. E. Ballester, J.-M. Désert, S. Aigrain, D. Deming, A. Lecavelier des Etangs, and A. Vidal-Madjar
2016. HST Hot-Jupiter Transmission Spectral Survey: Clear Skies for Cool Saturn WASP-39b. ApJ, 827:19.

Fortney, J. J., K. Lodders, M. S. Marley, and R. S. Freedman
2008. A Unified Theory for the Atmospheres of the Hot and Very Hot Jupiters: Two Classes of Irradiated Atmospheres. ApJ, 678:1419–1435.

Fortney, J. J., M. Shabram, A. P. Showman, Y. Lian, R. S. Freedman, M. S. Marley, and N. K. Lewis
2010. Transmission Spectra of Three-Dimensional Hot Jupiter Model Atmospheres. ApJ, 709:1396–1406.

Freedman, R. S., J. Lustig-Yaeger, J. J. Fortney, R. E. Lupu, M. S. Marley, and K. Lodders
2014. Gaseous Mean Opacities for Giant Planet and Ultracool Dwarf Atmospheres over a Range of Metallicities and Temperatures. ApJS, 214:25.

Freedman, R. S., M. S. Marley, and K. Lodders
2008. Line and Mean Opacities for Ultracool Dwarfs and Extrasolar Planets. ApJS, 174:504–513.

Fukui, A., Y. Kawashima, M. Ikoma, N. Narita, M. Onitsuka, Y. Ita, H. Onozato, S. Nishiyama, H. Baba, T. Ryu, T. Hirano, Y. Hori, K. Kurosaki, K. Kawauchi, Y. H. Takahashi, T. Nagayama, M. Tamura, N. Kawai, D. Kuroda, S. Nagayama, K. Ohta, Y. Shimizu, K. Yanagisawa, M. Yoshida, and H. Izumiura
2014. Multi-band, Multi-epoch Observations of the Transiting Warm Jupiter WASP-80b. ApJ, 790:108.

Gardner, J. P., J. C. Mather, M. Clampin, R. Doyon, M. A. Greenhouse, H. B. Hammel, J. B. Hutchings, P. Jakobsen, S. J. Lilly, K. S. Long, J. I. Lunine, M. J. McCaughrean, M. Mountain, J. Nella, G. H. Rieke, M. J. Rieke, H.-W. Rix, E. P. Smith, G. Sonneborn, M. Stiavelli, H. S. Stockman, R. A. Windhorst, and G. S. Wright
2006. The James Webb Space Telescope. Space Sci. Rev., 123:485–606.

Gazak, J. Z., J. A. Johnson, J. Tonry, D. Dragomir, J. Eastman, A. W. Mann, and E. Agol
2012. Transit Analysis Package: An IDL Graphical User Interface for Exoplanet Transit Photometry. *Advances in Astronomy*, 2012:697967.

Gelman, A., J. B. Carlin, H. S. Stern, and D. B. Rubin
2014. *Bayesian data analysis*, volume 2. Chapman and Hall CRC Boca Raton, FL, USA.

Gibson, N. P., S. Aigrain, J. K. Barstow, T. M. Evans, L. N. Fletcher, and P. G. J. Irwin
2013a. A Gemini ground-based transmission spectrum of WASP-29b: a featureless spectrum from 515 to 720 nm. MNRAS, 428:3680–3692.

Gibson, N. P., S. Aigrain, J. K. Barstow, T. M. Evans, L. N. Fletcher, and P. G. J. Irwin
2013b. A Gemini ground-based transmission spectrum of WASP-29b: a featureless spectrum from 515 to 720 nm. MNRAS, 428:3680–3692.

Gibson, N. P., S. Aigrain, F. Pont, D. K. Sing, J.-M. Désert, T. M. Evans, G. Henry, N. Husnoo, and H. Knutson
2012a. Probing the haze in the atmosphere of HD 189733b with Hubble

Space Telescope/WFC3 transmission spectroscopy. MNRAS, 422:753–760.

Gibson, N. P., S. Aigrain, S. Roberts, T. M. Evans, M. Osborne, and F. Pont
2012b. A Gaussian process framework for modelling instrumental systematics: application to transmission spectroscopy. MNRAS, 419:2683–2694.

Gibson, N. P., N. Nikolov, D. K. Sing, J. K. Barstow, T. M. Evans, T. Kataria, and P. A. Wilson
2017. VLT/FORS2 comparative transmission spectroscopy II: Confirmation of a cloud deck and Rayleigh scattering in WASP-31b, but no potassium? MNRAS, 467:4591–4605.

Gillon, M., E. Jehin, S. M. Lederer, L. Delrez, J. de Wit, A. Burdanov, V. Van Grootel, A. J. Burgasser, A. H. M. J. Triaud, C. Opitom, B.-O. Demory, D. K. Sahu, D. Bardalez Gagliuffi, P. Magain, and D. Queloz
2016. Temperate Earth-sized planets transiting a nearby ultracool dwarf star. Nature, 533:221–224.

Gillon, M., A. H. M. J. Triaud, B.-O. Demory, E. Jehin, E. Agol, K. M. Deck, S. M. Lederer, J. de Wit, A. Burdanov, J. G. Ingalls, E. Bolmont, J. Leconte, S. N. Raymond, F. Selsis, M. Turbet, K. Barkaoui, A. Burgasser, M. R. Burleigh, S. J. Carey, A. Chaushev, C. M. Copperwheat, L. Delrez, C. S. Fernandes, D. L. Holdsworth, E. J. Kotze, V. Van Grootel, Y. Almleaky, Z. Benkhaldoun, P. Magain, and D. Queloz
2017. Seven temperate terrestrial planets around the nearby ultracool dwarf star TRAPPIST-1. Nature, 542:456–460.

Hartman, J. D., D. Bayliss, R. Brahm, G. Á. Bakos, L. Mancini, A. Jordán, K. Penev, M. Rabus, G. Zhou, R. P. Butler, N. Espinoza, M. de Val-Borro, W. Bhatti, Z. Csubry, S. Ciceri, T. Henning, B. Schmidt, P. Arriagada, S. Shectman, J. Crane, I. Thompson, V. Suc, B. Csák, T. G. Tan, R. W. Noyes, J. Lázár, I. Papp, and P. Sári
2015. HATS-6b: A Warm Saturn Transiting an Early M Dwarf Star, and a Set of Empirical Relations for Characterizing K and M Dwarf Planet Hosts. AJ, 149:166.

Hebb, L., A. Collier-Cameron, B. Loeillet, D. Pollacco, G. Hébrard, R. A. Street, F. Bouchy, H. C. Stempels, C. Moutou, E. Simpson, S. Udry, Y. C. Joshi, R. G. West, I. Skillen, D. M. Wilson, I. McDonald, N. P. Gibson, S. Aigrain, D. R. Anderson, C. R. Benn, D. J. Christian, B. Enoch, C. A. Haswell, C. Hellier, K. Horne, J. Irwin, T. A. Lister, P. Maxted, M. Mayor, A. J. Norton, N. Parley, F. Pont, D. Queloz, B. Smalley, and P. J. Wheatley
2009. WASP-12b: The Hottest Transiting Extrasolar Planet Yet Discovered. ApJ, 693:1920–1928.

Hebb, L., A. Collier-Cameron, A. H. M. J. Triaud, T. A. Lister, B. Smalley, P. F. L. Maxted, C. Hellier, D. R. Anderson, D. Pollacco, M. Gillon, D. Queloz, R. G. West, S. Bentley, B. Enoch, C. A. Haswell, K. Horne, M. Mayor, F. Pepe, D. Segransan, I. Skillen, S. Udry, and P. J. Wheatley
2010. WASP-19b: The Shortest Period Transiting Exoplanet Yet Discovered. ApJ, 708:224–231.

Hedges, C. and N. Madhusudhan
2016. Effect of pressure broadening on molecular absorption cross sections in exoplanetary atmospheres. MNRAS, 458:1427–1449.

Hellier, C., D. R. Anderson, A. Collier Cameron, M. Gillon, E. Jehin, M. Lendl, P. F. L. Maxted, F. Pepe, D. Pollacco, D. Queloz, D. Ségransan, B. Smalley, A. M. S. Smith, J. Southworth, A. H. M. J. Triaud, S. Udry, and R. G. West
2011. WASP-43b: the closest-orbiting hot Jupiter. A&A, 535:L7.

Henry, G. W., G. W. Marcy, R. P. Butler, and S. S. Vogt
2000. A Transiting "51 Peg-like" Planet. ApJ, 529:L41–L44.

Hook, I. M., I. Jørgensen, J. R. Allington-Smith, R. L. Davies, N. Metcalfe, R. G. Murowinski, and D. Crampton
2004. The Gemini-North Multi-Object Spectrograph: Performance in Imaging, Long-Slit, and Multi-Object Spectroscopic Modes. PASP, 116:425–440.

Horne, K.
1986. An optimal extraction algorithm for CCD spectroscopy. PASP, 98:609–617.

Hubeny, I., A. Burrows, and D. Sudarsky
2003. A Possible Bifurcation in Atmospheres of Strongly Irradiated Stars and Planets. ApJ, 594:1011–1018.

Huitson, C. M., D. K. Sing, F. Pont, J. J. Fortney, A. S. Burrows, P. A. Wilson, G. E. Ballester, N. Nikolov, N. P. Gibson, D. Deming, S. Aigrain, T. M. Evans, G. W. Henry, A. Lecavelier des Etangs, A. P. Showman, A. Vidal-Madjar, and K. Zahnle
2013. An HST optical-to-near-IR transmission spectrum of the hot Jupiter WASP-19b: detection of atmospheric water and likely absence of TiO. MNRAS, 434:3252–3274.

Isobe, T., E. D. Feigelson, M. G. Akritas, and G. J. Babu
1990. Linear regression in astronomy. ApJ, 364:104–113.

Janson, M., T. D. Brandt, M. Kuzuhara, D. S. Spiegel, C. Thalmann, T. Currie, M. Bonnefoy, N. Zimmerman, S. Sorahana, T. Kotani,

J. Schlieder, J. Hashimoto, T. Kudo, N. Kusakabe, L. Abe, W. Brandner, J. C. Carson, S. Egner, M. Feldt, M. Goto, C. A. Grady, O. Guyon, Y. Hayano, M. Hayashi, S. Hayashi, T. Henning, K. W. Hodapp, M. Ishii, M. Iye, R. Kandori, G. R. Knapp, J. Kwon, T. Matsuo, M. W. McElwain, K. Mede, S. Miyama, J.-I. Morino, A. Moro-Martín, T. Nakagawa, T. Nishimura, T.-S. Pyo, E. Serabyn, T. Suenaga, H. Suto, R. Suzuki, Y. Takahashi, M. Takami, N. Takato, H. Terada, D. Tomono, E. L. Turner, M. Watanabe, J. Wisniewski, T. Yamada, H. Takami, T. Usuda, and M. Tamura
2013. Direct Imaging Detection of Methane in the Atmosphere of GJ 504 b. ApJ, 778:L4.

Johnson, J. A., J. Z. Gazak, K. Apps, P. S. Muirhead, J. R. Crepp, I. J. M. Crossfield, T. Boyajian, K. von Braun, B. Rojas-Ayala, A. W. Howard, K. R. Covey, E. Schlawin, K. Hamren, T. D. Morton, G. W. Marcy, and J. P. Lloyd
2012. Characterizing the Cool KOIs. II. The M Dwarf KOI-254 and Its Hot Jupiter. AJ, 143:111.

Jones, E., T. Oliphant, P. Peterson, et al.
2001. SciPy: Open source scientific tools for Python. http://www.scipy.org/.

Jordán, A., N. Espinoza, M. Rabus, S. Eyheramendy, D. K. Sing, J.-M. Désert, G. Á. Bakos, J. J. Fortney, M. López-Morales, P. F. L. Maxted, A. H. M. J. Triaud, and A. Szentgyorgyi
2013. A Ground-based Optical Transmission Spectrum of WASP-6b. ApJ, 778:184.

Kasting, J. F.
1997. Habitable Zones around Low Mass Stars and the Search For Extraterrestrial Life. *Origins of Life and Evolution of the Biosphere*, 27:291–3107.

Kausch, W., S. Noll, A. Smette, S. Kimeswenger, M. Barden, C. Szyszka, A. M. Jones, H. Sana, H. Horst, and F. Kerber
2015. Molecfit: A general tool for telluric absorption correction. II. Quantitative evaluation on ESO-VLT/X-Shooterspectra. A&A, 576:A78.

Kempton, E. M.-R., R. Lupu, A. Owusu-Asare, P. Slough, and B. Cale
2017. Exo-Transmit: An Open-Source Code for Calculating Transmission Spectra for Exoplanet Atmospheres of Varied Composition. PASP, 129(4):044402.

Kiang, N. Y., A. Segura, G. Tinetti, Govindjee, R. E. Blankenship, M. Cohen, J. Siefert, D. Crisp, and V. S. Meadows
2007a. Spectral Signatures of Photosynthesis. II. Coevolution with Other

Stars And The Atmosphere on Extrasolar Worlds. *Astrobiology*, 7:252–274.

Kiang, N. Y., J. Siefert, Govindjee, and R. E. Blankenship
2007b. Spectral Signatures of Photosynthesis. I. Review of Earth Organisms. *Astrobiology*, 7:222–251.

Kirk, J., P. J. Wheatley, T. Louden, S. P. Littlefair, C. M. Copperwheat, D. J. Armstrong, T. R. Marsh, and V. S. Dhillon
2016. Transmission spectroscopy of the inflated exoplanet WASP-52b, and evidence for a bright region on the stellar surface. MNRAS, 463:2922–2931.

Knutson, H. A., D. Charbonneau, L. E. Allen, J. J. Fortney, E. Agol, N. B. Cowan, A. P. Showman, C. S. Cooper, and S. T. Megeath
2007. A map of the day-night contrast of the extrasolar planet HD 189733b. Nature, 447:183–186.

Knutson, H. A., D. Dragomir, L. Kreidberg, E. M.-R. Kempton, P. R. McCullough, J. J. Fortney, J. L. Bean, M. Gillon, D. Homeier, and A. W. Howard
2014. Hubble Space Telescope Near-IR Transmission Spectroscopy of the Super-Earth HD 97658b. ApJ, 794:155.

Kopal, Z.
1950. Detailed effects of limb darkening upon light and velocity curves of close binary systems. *Harvard College Observatory Circular*, 454:1–12.

Kopparapu, R. K., R. Ramirez, J. F. Kasting, V. Eymet, T. D. Robinson, S. Mahadevan, R. C. Terrien, S. Domagal-Goldman, V. Meadows, and R. Deshpande
2013. Habitable Zones around Main-sequence Stars: New Estimates. ApJ, 765:131.

Lagrange, A.-M., D. Gratadour, G. Chauvin, T. Fusco, D. Ehrenreich, D. Mouillet, G. Rousset, D. Rouan, F. Allard, É. Gendron, J. Charton, L. Mugnier, P. Rabou, J. Montri, and F. Lacombe
2009. A probable giant planet imaged in the β Pictoris disk. VLT/NaCo deep L'-band imaging. A&A, 493:L21–L25.

Latham, D. W., R. P. Stefanik, T. Mazeh, M. Mayor, and G. Burki
1989. The unseen companion of HD114762 - A probable brown dwarf. Nature, 339:38–40.

Lavvas, P., T. Koskinen, and R. V. Yelle
2014. Electron Densities and Alkali Atoms in Exoplanet Atmospheres. ApJ, 796:15.

Lecavelier Des Etangs, A., F. Pont, A. Vidal-Madjar, and D. Sing
2008. Rayleigh scattering in the transit spectrum of HD 189733b. A&A, 481:L83–L86.

Lee, J.-M., K. Heng, and P. G. J. Irwin
2013. Atmospheric Retrieval Analysis of the Directly Imaged Exoplanet HR 8799b. ApJ, 778:97.

Leger, A., M. Pirre, and F. J. Marceau
1994. How to evidence life on a distant planet. Ap&SS, 212:327–333.

Leigh, C., A. Collier Cameron, S. Udry, J.-F. Donati, K. Horne, D. James, and A. Penny
2003. A search for starlight reflected from HD 75289b. MNRAS, 346:L16–L20.

Lendl, M., D. R. Anderson, A. Collier-Cameron, A. P. Doyle, M. Gillon, C. Hellier, E. Jehin, T. A. Lister, P. F. L. Maxted, F. Pepe, D. Pollacco, D. Queloz, B. Smalley, D. Ségransan, A. M. S. Smith, A. H. M. J. Triaud, S. Udry, R. G. West, and P. J. Wheatley
2012. WASP-42 b and WASP-49 b: two new transiting sub-Jupiters. A&A, 544:A72.

Lendl, M., L. Delrez, M. Gillon, N. Madhusudhan, E. Jehin, D. Queloz, D. R. Anderson, B.-O. Demory, and C. Hellier
2016. FORS2 observes a multi-epoch transmission spectrum of the hot Saturn-mass exoplanet WASP-49b. A&A, 587:A67.

Lupu, R. E., K. Zahnle, M. S. Marley, L. Schaefer, B. Fegley, C. Morley, K. Cahoy, R. Freedman, and J. J. Fortney
2014. The Atmospheres of Earthlike Planets after Giant Impact Events. ApJ, 784:27.

MacDonald, R. J. and N. Madhusudhan
2017. HD 209458b in New Light: Detection of Nitrogen Chemistry, Patchy Clouds and Sub-Solar Water. *ArXiv e-prints*, 1710:01113.

Madhusudhan, N.
2012. C/O Ratio as a Dimension for Characterizing Exoplanetary Atmospheres. ApJ, 758:36.

Madhusudhan, N., M. Agúndez, J. I. Moses, and Y. Hu
2016. Exoplanetary Atmospheres – Chemistry, Formation Conditions, and Habitability. Space Sci. Rev., 205:285–348.

Madhusudhan, N. and S. Seager
2009. A Temperature and Abundance Retrieval Method for Exoplanet Atmospheres. ApJ, 707:24–39.

Mallonn, M. and K. G. Strassmeier
2016. Transmission spectroscopy of HAT-P-32b with the LBT: confirmation of clouds/hazes in the planetary atmosphere. A&A, 590:A100.

Mallonn, M., C. von Essen, J. Weingrill, K. G. Strassmeier, I. Ribas, T. A. Carroll, E. Herrero, T. Granzer, A. Claret, and A. Schwope
2015. Transmission spectroscopy of the inflated exo-Saturn HAT-P-19b. A&A, 580:A60.

Mancini, L., S. Ciceri, G. Chen, J. Tregloan-Reed, J. J. Fortney, J. Southworth, T. G. Tan, M. Burgdorf, S. Calchi Novati, M. Dominik, X.-S. Fang, F. Finet, T. Gerner, S. Hardis, T. C. Hinse, U. G. Jørgensen, C. Liebig, N. Nikolov, D. Ricci, S. Schäfer, F. Schönebeck, J. Skottfelt, O. Wertz, K. A. Alsubai, V. Bozza, P. Browne, P. Dodds, S.-H. Gu, K. Harpsøe, T. Henning, M. Hundertmark, J. Jessen-Hansen, N. Kains, E. Kerins, H. Kjeldsen, M. N. Lund, M. Lundkvist, N. Madhusudhan, M. Mathiasen, M. T. Penny, S. Prof, S. Rahvar, K. Sahu, G. Scarpetta, C. Snodgrass, and J. Surdej
2013. Physical properties, transmission and emission spectra of the WASP-19 planetary system from multi-colour photometry. MNRAS, 436:2–18.

Mancini, L., J. Southworth, S. Ciceri, M. Dominik, T. Henning, U. G. Jørgensen, A. F. Lanza, M. Rabus, C. Snodgrass, C. Vilela, K. A. Alsubai, V. Bozza, D. M. Bramich, S. Calchi Novati, G. D'Ago, R. Figuera Jaimes, P. Galianni, S.-H. Gu, K. Harpsøe, T. Hinse, M. Hundertmark, D. Juncher, N. Kains, H. Korhonen, A. Popovas, S. Rahvar, J. Skottfelt, R. Street, J. Surdej, Y. Tsapras, X.-B. Wang, and O. Wertz
2014. Physical properties and transmission spectrum of the WASP-80 planetary system from multi-colour photometry. A&A, 562:A126.

Mandel, K. and E. Agol
2002. Analytic Light Curves for Planetary Transit Searches. ApJ, 580:L171–L175.

Mandell, A. M., K. Haynes, E. Sinukoff, N. Madhusudhan, A. Burrows, and D. Deming
2013. Exoplanet Transit Spectroscopy Using WFC3: WASP-12 b, WASP-17 b, and WASP-19 b. ApJ, 779:128.

Marois, C., B. Macintosh, T. Barman, B. Zuckerman, I. Song, J. Patience, D. Lafrenière, and R. Doyon
2008. Direct Imaging of Multiple Planets Orbiting the Star HR 8799. *Science*, 322:1348.

Mayor, M. and D. Queloz
1995. A Jupiter-mass companion to a solar-type star. Nature, 378:355–359.

McCullough, P. R., N. Crouzet, D. Deming, and N. Madhusudhan
2014. Water Vapor in the Spectrum of the Extrasolar Planet HD 189733b. I. The Transit. ApJ, 791:55.

Miller-Ricci, E. and J. J. Fortney
2010. The Nature of the Atmosphere of the Transiting Super-Earth GJ 1214b. ApJ, 716:L74–L79.

Montalto, M., N. Iro, N. C. Santos, S. Desidera, J. H. C. Martins, P. Figueira, and R. Alonso
2015. Further Constraints on the Optical Transmission Spectrum of HAT-P-1b. ApJ, 811:55.

Murgas, F., E. Pallé, M. R. Zapatero Osorio, L. Nortmann, S. Hoyer, and A. Cabrera-Lavers
2014. The GTC exoplanet transit spectroscopy survey . I. OSIRIS transmission spectroscopy of the short period planet WASP-43b. A&A, 563:A41.

Nelder, J. A. and R. Mead
1965. A simplex method for function minimization. *The computer journal*, 7(4):308–313.

Nikolov, N., D. K. Sing, N. P. Gibson, J. J. Fortney, T. M. Evans, J. K. Barstow, T. Kataria, and P. A. Wilson
2016. VLT FORS2 Comparative Transmission Spectroscopy: Detection of Na in the Atmosphere of WASP-39b from the Ground. ApJ, 832:191.

Nortmann, L., E. Pallé, F. Murgas, S. Dreizler, N. Iro, and A. Cabrera-Lavers
2016. The GTC exoplanet transit spectroscopy survey. IV. Confirmation of the flat transmission spectrum of HAT-P-32b. A&A, 594:A65.

Parviainen, H., E. Pallé, L. Nortmann, G. Nowak, N. Iro, F. Murgas, and S. Aigrain
2016. The GTC exoplanet transit spectroscopy survey. II. An overly large Rayleigh-like feature for exoplanet TrES-3b. A&A, 585:A114.

Pont, F., H. Knutson, R. L. Gilliland, C. Moutou, and D. Charbonneau
2008. Detection of atmospheric haze on an extrasolar planet: the 0.55-1.05 μm transmission spectrum of HD 189733b with the Hubble Space Telescope. MNRAS, 385:109–118.

Puig, L., G. L. Pilbratt, A. Heske, I. Escudero Sanz, and P.-E. Crouzet
2016. ARIEL: an ESA M4 mission candidate. In *Space Telescopes and Instrumentation 2016: Optical, Infrared, and Millimeter Wave*, volume 9904 of Proc. SPIE, P. 99041W.

Rasmussen, C. E. and C. K. Williams
2006. Gaussian processes for machine learning. 2006. *The MIT Press, Cambridge, MA, USA*, 38:715–719.

Rauer, H., D. Bockelée-Morvan, A. Coustenis, T. Guillot, and J. Schneider
2000a. Search for an exosphere around 51 Pegasi B with ISO. A&A, 355:573–580.

Rauer, H., A. Harris, A. Collier Cameron, and Export-Team
2000b. Spectroscopic Search for Atmospheric Signatures of Extrasolar Planets. In *Astronomische Gesellschaft Meeting Abstracts*, R. E. Schielicke, ed., volume 17.

Richard, C., I. E. Gordon, L. S. Rothman, M. Abel, L. Frommhold, M. Gustafsson, J.-M. Hartmann, C. Hermans, W. J. Lafferty, G. S. Orton, K. M. Smith, and H. Tran
2012. New section of the HITRAN database: Collision-induced absorption (CIA). *Journal of Quantitative Spectroscopy and Radiative Transfer*, 113:1276–1285.

Rogers, L. A. and S. Seager
2010. Three Possible Origins for the Gas Layer on GJ 1214b. ApJ, 716:1208–1216.

Rothberg, B., O. Kuhn, M. L. Edwards, J. M. Hill, D. Thompson, C. Veillet, and R. M. Wagner
2016. Current status of the facility instrumentation suite at the Large Binocular Telescope Observatory. In *Society of Photo-Optical Instrumentation Engineers (SPIE) Conference Series*, volume 9906 of Proc. SPIE, P. 990622.

Rothman, L. S., I. E. Gordon, R. J. Barber, H. Dothe, R. R. Gamache, A. Goldman, V. I. Perevalov, S. A. Tashkun, and J. Tennyson
2010. HITEMP, the high-temperature molecular spectroscopic database. *Journal of Quantitative Spectroscopy and Radiative Transfer*, 111:2139–2150.

Schwarz, G.
1978. Estimating the dimension of a model. *The annals of statistics*, 6(2):461–464.

Seager, S.
1999. *Extrasolar giant planets under strong stellar irradiation.* PhD thesis, Harvard University.

Seager, S., D. Deming, and J. A. Valenti
2009. Transiting Exoplanets with JWST. *Astrophysics and Space Science Proceedings*, 10:123.

Seager, S. and D. D. Sasselov
2000. Theoretical Transmission Spectra during Extrasolar Giant Planet Transits. ApJ, 537:916–921.

Sedaghati, E., H. M. J. Boffin, S. Csizmadia, N. Gibson, P. Kabath, M. Mallonn, and M. E. Van den Ancker
2015. Regaining the FORS: optical ground-based transmission spectroscopy of the exoplanet WASP-19b with VLT+FORS2. A&A, 576:L11.

Sedaghati, E., H. M. J. Boffin, L. Delrez, M. Gillon, S. Csizmadia, A. M. S. Smith, and H. Rauer
2017. Probing the atmosphere of a sub-Jovian planet orbiting a cool dwarf. MNRAS, 468:3123–3134.

Sedaghati, E., H. M. J. Boffin, T. Jeřabková, A. García Muñoz, J. L. Grenfell, A. Smette, V. D. Ivanov, S. Csizmadia, J. Cabrera, P. Kabath, M. Rocchetto, and H. Rauer
2016. Potassium detection in the clear atmosphere of a hot-Jupiter. FORS2 transmission spectroscopy of WASP-17b. A&A, 596:A47.

Segura, A., J. F. Kasting, V. Meadows, M. Cohen, J. Scalo, D. Crisp, R. A. H. Butler, and G. Tinetti
2005. Biosignatures from Earth-Like Planets Around M Dwarfs. *Astrobiology*, 5:706–725.

Shabram, M., J. J. Fortney, T. P. Greene, and R. S. Freedman
2011. Transmission Spectra of Transiting Planet Atmospheres: Model Validation and Simulations of the Hot Neptune GJ 436b for the James Webb Space Telescope. ApJ, 727:65.

Showman, A. P., J. J. Fortney, Y. Lian, M. S. Marley, R. S. Freedman, H. A. Knutson, and D. Charbonneau
2009. Atmospheric Circulation of Hot Jupiters: Coupled Radiative-Dynamical General Circulation Model Simulations of HD 189733b and HD 209458b. ApJ, 699:564–584.

Sing, D. K.
2010. Stellar limb-darkening coefficients for CoRot and Kepler. A&A, 510:A21.

Sing, D. K., J. J. Fortney, N. Nikolov, H. R. Wakeford, T. Kataria, T. M. Evans, S. Aigrain, G. E. Ballester, A. S. Burrows, D. Deming, J.-M. Désert, N. P. Gibson, G. W. Henry, C. M. Huitson, H. A. Knutson, A. Lecavelier Des Etangs, F. Pont, A. P. Showman, A. Vidal-Madjar, M. H. Williamson, and P. A. Wilson
2016. A continuum from clear to cloudy hot-Jupiter exoplanets without primordial water depletion. Nature, 529:59–62.

Sing, D. K., F. Pont, S. Aigrain, D. Charbonneau, J.-M. Désert, N. Gibson, R. Gilliland, W. Hayek, G. Henry, H. Knutson, A. Lecavelier Des Etangs, T. Mazeh, and A. Shporer
2011. Hubble Space Telescope transmission spectroscopy of the exoplanet HD 189733b: high-altitude atmospheric haze in the optical and near-ultraviolet with STIS. MNRAS, 416:1443–1455.

Sing, D. K., H. R. Wakeford, A. P. Showman, N. Nikolov, J. J. Fortney, A. S. Burrows, G. E. Ballester, D. Deming, S. Aigrain, J.-M. Désert, N. P. Gibson, G. W. Henry, H. Knutson, A. Lecavelier des Etangs, F. Pont, A. Vidal-Madjar, M. W. Williamson, and P. A. Wilson
2015. HST hot-Jupiter transmission spectral survey: detection of potassium in WASP-31b along with a cloud deck and Rayleigh scattering. MNRAS, 446:2428–2443.

Smette, A., H. Sana, S. Noll, H. Horst, W. Kausch, S. Kimeswenger, M. Barden, C. Szyszka, A. M. Jones, A. Gallenne, J. Vinther, P. Ballester, and J. Taylor
2015. Molecfit: A general tool for telluric absorption correction. I. Method and application to ESO instruments. A&A, 576:A77.

Snellen, I. A. G.
2005. High-precision K-band photometry of the secondary eclipse of HD 209458. MNRAS, 363:211–215.

Snellen, I. A. G., S. Albrecht, E. J. W. de Mooij, and R. S. Le Poole
2008. Ground-based detection of sodium in the transmission spectrum of exoplanet HD 209458b. A&A, 487:357–362.

Snellen, I. A. G., R. J. de Kok, E. J. W. de Mooij, and S. Albrecht
2010a. The orbital motion, absolute mass and high-altitude winds of exoplanet HD209458b. Nature, 465:1049–1051.

Snellen, I. A. G., R. J. de Kok, R. le Poole, M. Brogi, and J. Birkby
2013. Finding Extraterrestrial Life Using Ground-based High-dispersion Spectroscopy. ApJ, 764:182.

Snellen, I. A. G., E. J. W. de Mooij, and A. Burrows
2010b. Bright optical day-side emission from extrasolar planet CoRoT-2b. A&A, 513:A76.

Spiegel, D. S., A. Burrows, L. Ibgui, I. Hubeny, and J. A. Milsom
2010. Models of Neptune-Mass Exoplanets: Emergent Fluxes and Albedos. ApJ, 709:149–158.

Stevenson, K. B., J. L. Bean, A. Seifahrt, J.-M. Désert, N. Madhusudhan, M. Bergmann, L. Kreidberg, and D. Homeier
2014. Transmission Spectroscopy of the Hot Jupiter WASP-12b from 0.7 to 5 μm. AJ, 147:161.

Stevenson, K. B., J. L. Bean, A. Seifahrt, G. J. Gilbert, M. R. Line, J.-M. Désert, and J. J. Fortney
2016. A Search for Water in the Atmosphere of HAT-P-26b Using LDSS-3C. ApJ, 817:141.

Tennyson, J. and S. N. Yurchenko
2012. ExoMol: molecular line lists for exoplanet and other atmospheres. MNRAS, 425:21–33.

Tinetti, G., P. Drossart, P. Eccleston, P. Hartogh, A. Heske, J. Leconte, G. Micela, M. Ollivier, G. Pilbratt, L. Puig, D. Turrini, B. Vandenbussche, P. Wolkenberg, E. Pascale, J.-P. Beaulieu, M. Güdel, M. Min, M. Rataj, T. Ray, I. Ribas, J. Barstow, N. Bowles, A. Coustenis, V. Coudé du Foresto, L. Decin, T. Encrenaz, F. Forget, M. Friswell, M. Griffin, P. O. Lagage, P. Malaguti, A. Moneti, J. C. Morales, E. Pace, M. Rocchetto, S. Sarkar, F. Selsis, W. Taylor, J. Tennyson, O. Venot, I. P. Waldmann, G. Wright, T. Zingales, and M. R. Zapatero-Osorio
2016. The science of ARIEL (Atmospheric Remote-sensing Infrared Exoplanet Large-survey). In *Space Telescopes and Instrumentation 2016: Optical, Infrared, and Millimeter Wave*, volume 9904 of Proc. SPIE, P. 99041X.

Torres, G., D. A. Fischer, A. Sozzetti, L. A. Buchhave, J. N. Winn, M. J. Holman, and J. A. Carter
2012. Improved Spectroscopic Parameters for Transiting Planet Hosts. ApJ, 757:161.

Tregloan-Reed, J., J. Southworth, and C. Tappert
2013. Transits and starspots in the WASP-19 planetary system. MNRAS, 428:3671–3679.

Triaud, A. H. M. J., D. R. Anderson, A. Collier Cameron, A. P. Doyle, A. Fumel, M. Gillon, C. Hellier, E. Jehin, M. Lendl, C. Lovis, P. F. L. Maxted, F. Pepe, D. Pollacco, D. Queloz, D. Ségransan, B. Smalley,

A. M. S. Smith, S. Udry, R. G. West, and P. J. Wheatley
2013. WASP-80b: a gas giant transiting a cool dwarf. A&A, 551:A80.

Triaud, A. H. M. J., M. Gillon, D. Ehrenreich, E. Herrero, M. Lendl, D. R. Anderson, A. Collier Cameron, L. Delrez, B.-O. Demory, C. Hellier, K. Heng, E. Jehin, P. F. L. Maxted, D. Pollacco, D. Queloz, I. Ribas, B. Smalley, A. M. S. Smith, and S. Udry
2015. WASP-80b has a dayside within the T-dwarf range. MNRAS, 450:2279–2290.

Trotta, R.
2008. Bayes in the sky: Bayesian inference and model selection in cosmology. *Contemporary Physics*, 49:71–104.

Turner, J. D., K. A. Pearson, L. I. Biddle, B. M. Smart, R. T. Zellem, J. K. Teske, K. K. Hardegree-Ullman, C. C. Griffith, R. M. Leiter, I. T. Cates, M. N. Nieberding, C.-T. W. Smith, R. M. Thompson, R. Hofmann, M. P. Berube, C. H. Nguyen, L. C. Small, B. C. Guvenen, L. Richardson, A. McGraw, B. Raphael, B. E. Crawford, A. N. Robertson, R. Tombleson, T. M. Carleton, A. P. M. Towner, A. M. Walker-LaFollette, J. R. Hume, Z. T. Watson, C. K. Jones, M. J. Lichtenberger, S. R. Hoglund, K. L. Cook, C. A. Crossen, C. R. Jorgensen, J. M. Romine, A. R. Thompson, C. F. Villegas, A. A. Wilson, B. Sanford, J. M. Taylor, and T. N. Henz
2016. Ground-based near-UV observations of 15 transiting exoplanets: constraints on their atmospheres and no evidence for asymmetrical transits. MNRAS, 459:789–819.

Wakeford, H. R., D. K. Sing, D. Deming, N. P. Gibson, J. J. Fortney, A. S. Burrows, G. Ballester, N. Nikolov, S. Aigrain, G. Henry, H. Knutson, A. Lecavelier des Etangs, F. Pont, A. P. Showman, A. Vidal-Madjar, and K. Zahnle
2013. HST hot Jupiter transmission spectral survey: detection of water in HAT-P-1b from WFC3 near-IR spatial scan observations. MNRAS, 435:3481–3493.

Winn, J. N., M. J. Holman, G. Torres, P. McCullough, C. Johns-Krull, D. W. Latham, A. Shporer, T. Mazeh, E. Garcia-Melendo, C. Foote, G. Esquerdo, and M. Everett
2008. The Transit Light Curve Project. IX. Evidence for a Smaller Radius of the Exoplanet XO-3b. ApJ, 683:1076–1084.

Wolszczan, A. and D. A. Frail
1992. A planetary system around the millisecond pulsar PSR1257 + 12. Nature, 355:145–147.

Wong, I., H. A. Knutson, T. Kataria, N. K. Lewis, A. Burrows, J. J. Fortney, J. Schwartz, A. Shporer, E. Agol, N. B. Cowan, D. Deming, J.-M. Désert,

B. J. Fulton, A. W. Howard, J. Langton, G. Laughlin, A. P. Showman, and K. Todorov
2016. 3.6 and 4.5 μm Spitzer Phase Curves of the Highly Irradiated Hot Jupiters WASP-19b and HAT-P-7b. ApJ, 823:122.

Wright, G. S., G. H. Rieke, L. Colina, E. van Dishoeck, G. Goodson, T. Greene, P.-O. Lagage, A. Karnik, S. D. Lambros, D. Lemke, M. Meixner, H.-U. Norgaard, G. Oloffson, T. Ray, M. Ressler, C. Waelkens, D. Wright, and A. Zhender
2004. The JWST MIRI instrument concept. In *Optical, Infrared, and Millimeter Space Telescopes*, J. C. Mather, ed., volume 5487 of Proc. SPIE, Pp. 653–663.

Wyttenbach, A., D. Ehrenreich, C. Lovis, S. Udry, and F. Pepe
2015. Spectrally resolved detection of sodium in the atmosphere of HD 189733b with the HARPS spectrograph. A&A, 577:A62.

Wyttenbach, A., C. Lovis, D. Ehrenreich, V. Bourrier, L. Pino, R. Allart, N. Astudillo-Defru, H. M. Cegla, K. Heng, B. Lavie, C. Melo, F. Murgas, A. Santerne, D. Ségransan, S. Udry, and F. Pepe
2017. Hot Exoplanet Atmospheres Resolved with Transit Spectroscopy (HEARTS) I. Detection of hot neutral sodium at high altitudes on WASP-49b. *ArXiv e-prints*, 1702:00448.

Appendix

The following appendix includes the published works that form the basis of this thesis.

Monthly Notices of the ROYAL ASTRONOMICAL SOCIETY

MNRAS **468,** 3123–3134 (2017) doi:10.1093/mnras/stx646
Advance Access publication 2017 March 15

Probing the atmosphere of a sub-Jovian planet orbiting a cool dwarf

Elyar Sedaghati,[1,2,3★] Henri M. J. Boffin,[3★] Laetitia Delrez,[4,5★] Michaël Gillon,[5] Szilard Csizmadia,[1] Alexis M. S. Smith[1] and Heike Rauer[1,2]

[1] *Institut für Planetenforschung, Deutsches Zentrum für Luft- und Raumfahrt, Rutherfordstr. 2, D-12489 Berlin, Germany*
[2] *Zentrum für Astronomie und Astrophysik, TU Berlin, Hardenbergstr. 36, D-10623 Berlin, Germany*
[3] *European Southern Observatory, Karl-Schwarzschild-Straße 2, D-85748 Garching bei München, Germany*
[4] *Battcock Centre for Experimental Astrophysics, Cavendish Laboratory, J J Thomson Avenue, Cambridge CB3 0HE, UK*
[5] *Institut d'Astrophysique et de Géophysique, Université de Liége, Allée du 6 Août 19C, B-4000 Liége, Belgium*

Accepted 2017 March 10. Received 2017 March 7; in original form 2017 February 13

ABSTRACT

We derive the 0.01-μm binned transmission spectrum, between 0.74 and 1.0 μm, of WASP-80b from low-resolution spectra obtained with the Focal Reducer and low-dispersion Spectrograph 2 instrument attached to ESO's Very Large Telescope. The combination of the fact that WASP-80 is an active star, together with instrumental and telluric factors, introduces correlated noise in the observed transit light curves, which we treat quantitatively using Gaussian processes. Comparison of our results together with those from previous studies to theoretically calculated models reveals an equilibrium temperature in agreement with the previously measured value of 825 K, and a subsolar metallicity, as well as an atmosphere depleted of molecular species with absorption bands in the infrared ($\gg 5\sigma$). Our transmission spectrum alone shows evidence for additional absorption from the potassium core and wing, whereby its presence is detected from analysis of narrow 0.003 μm bin light curves ($\gg 5\sigma$). Further observations with visible and near-ultraviolet filters will be required to expand this spectrum and provide more in-depth knowledge of the atmosphere. These detections are only made possible through an instrument-dependent baseline model and a careful analysis of systematics in the data.

Key words: instrumentation: spectrographs – techniques: spectroscopic – planets and satellites: atmospheres – planets and satellites: individual: WASP-80b – planetary systems.

1 INTRODUCTION

The remarkable progress made to date in detecting and characterizing extrasolar planets has been made possible through dedicated space- and ground-based facilities. In a mere couple of decades, we have gone from discovering the first of these so-called exoplanets (Campbell, Walker & Yang 1988; Wolszczan & Frail 1992; Mayor & Queloz 1995) to characterizing their physical properties, the most fascinating of which has been the detection of their atmospheres. This is particularly an intriguing feature of these alien worlds, as it provides the means for understanding the mechanisms involved in formation and evolution of planets (Mordasini et al. 2012a,b; Dorn et al. 2015), as well as presenting the opportunity for detection of biomarkers (Kaltenegger & Traub 2009; Benneke & Seager 2012; Snellen et al. 2013), pointing to perhaps biological processes on those planets capable of harbouring life-forms producing them.

One method through which the atmospheric envelope around a transiting exoplanet is detected is *transmission spectroscopy*, where minute, wavelength-dependent variations of the transit depth are measured from modelling the spectrophotometric transit light curves (Seager & Sasselov 2000). This method generally probes the upper layers of the atmosphere, where lower pressure levels together with shorter optical paths lead to transmission of stellar radiation through the exo-atmosphere. This process leaves distinct spectral imprints on the observed radiation, one consequence of which is wavelength-dependent relative planetary radius (obtained from measuring the transit depth).

Such studies are performed with observations either from space (Ehrenreich et al. 2007; Sing et al. 2011, 2016; Deming et al. 2013; Wakeford et al. 2013; Knutson et al. 2014) or with ground-based facilities (Narita et al. 2005; Gibson et al. 2013; Stevenson et al. 2014; Sedaghati et al. 2015, 2016; Lendl et al. 2016; Mallonn & Strassmeier 2016), both of which have their own advantages. Space-based observations have the advantage of not being affected by atmospheric extinction, contamination and turbulence, and therefore benefit from having the entire electromagnetic range as probing domain. For instance, NASA's *James Webb Space Telescope* (*JWST*; Gardner et al. 2006) will be able to probe exo-atmospheres in the infrared (IR) wavelengths, where transmission spectroscopy from the ground is rather difficult. On the other hand, ground-based

★ E-mail: elyar.sedaghati@dlr.de (ES); hboffin@eso.org (HMJB); lcd44@cam.ac.uk (LD)

facilities benefit from telescopes with large collecting mirrors, which is essential for performing spectroscopy at high time- and spectral resolution.

ESO's FOcal Reducer and low-dispersion Spectrograph 2 (FORS2; Appenzeller et al. 1998) mounted at the Cassegrain focus of Unit Telescope 1 (UT1) of the Very Large Telescope (VLT) has been the instrument of choice to perform such observations (Bean, Miller-Ricci Kempton & Homeier 2010; Bean et al. 2011; Sedaghati et al. 2015, 2016; Lendl et al. 2016; Nikolov et al. 2016). It offers two multi-object spectroscopic modes: (1) Mask Exchange Unit (MXU, custom-designed and laser-cut masks) and (2) Multi-Object Spectroscopy (MOS, movable slitlets via 19 pairs of arms). The option of wide slits, multiple reference star selection for telluric correction in conjunction with the great light collecting power of the 8.2-m telescope, makes this instrument ideal for performing differential spectrophotometric observations, required here.

Previously, it was determined that the Longitudinal[1] Atmospheric Dispersion Corrector (LADC; Avila, Rupprecht & Beckers 1997) of the FORS2 instrument, a pair of movable prisms, introduced systematic effects in exoplanet transit light-curve observations due to the degraded antireflective coating causing differential transmission through the optics (Boffin et al. 2015). This problem was subsequently ratified by the upgrade of the LADC unit and the improvements were initially highlighted by Sedaghati et al. (2015). In this study, we present results from observations of WASP-80, a dwarf star with a transiting gas giant, that were taken prior to the aforementioned upgrade. Therefore, we will consider possible implications of the systematic effects introduced by the degraded LADC unit in the following analysis.

WASP-80b is a gas giant transiting a cool, possibly late K-type 11.88 V magnitude dwarf, with a mass of $0.554 \pm 0.035\ M_{\rm jup}$ and radius of $0.952 \pm 0.026\ R_{\rm jup}$, orbiting its host star with a 3.068 d period (Triaud et al. 2013). It is one of only a handful of gas giants orbiting a late-type dwarf host (e.g. WASP-43b, Kepler-45b, HAT-P-54b, HATS-6b; Hellier et al. 2011; Johnson et al. 2012; Bakos et al. 2015; Hartman et al. 2015) and has a day-side temperature within the T-dwarf range (Triaud et al. 2015). These authors also found a transmission spectrum indistinguishable from a flat line and no evidence of active region crossing by the planet (Triaud et al. 2013; Mancini et al. 2014), despite the stellar spectral analysis indicating high levels of activity (Mancini et al. 2014).

In this work, we present a red transmission spectrum of this planet from light curves that are somewhat compromised by systematic effects. We will study the role of telluric and instrumental effects in introducing such discrepancies in the light curves, before consideration of any astrophysical phenomena.

2 DATA ANALYSIS

2.1 Observations

A single transit of WASP-80b was observed using Antu, the 8.2-m UT1 of the VLT with the FORS2 instrument on 2013 June 16, with the data taken as part of the programme 091.C-0377(C) (PI: Gillon), before the LADC upgrade. The programme itself comprised four transit observations, two of which were not performed due to bad weather, while the light curves from the fourth transit suffered from severe systematic effects and are subsequently not used for the analysis in this work. The instrument has a 6.8×6.8 arcmin^2 field of view and is equipped with two detectors, where the red-optimized MIT set was utilized for the observations. The instrument was used in the MXU mode, which means that a custom-designed mask with 10-arcsec-wide slits positioned on the target and comparison stars was placed in the light path. This essentially acts as a blocking mask to free the CCD for recording of the simultaneous spectra. The 600z grism (with the order sorter filter OG590) was used as the dispersing element, yielding a spectral range of ∼0.73–1.05 μm, although the exact wavelength coverage for each target is dependent on the horizontal location of its slit on the CCD.

The entire science observational sequence lasted ∼4.87 h, with the first frame taken at 05:17 UT and the last taken at 10:04 UT. The complete transit lasted ∼2.26 h, with first contact at 06:17 UT and the last one at 8:32 UT. The LADC was left in park position during the observing sequence, with the two prisms fixed at their minimal separation distance of 30 mm. The standard 100 kHz readout mode was used, which together with exposure time of 25 s (apart from the first seven frames where adjustments were made in order to reach the optimal value), yielded 277 exposures, 130 of which were during the transit. The conditions were clear throughout the night and the seeing varied between 0.97 and 2.35 arcsec. The field started at airmass of 1.24, rose to 1.08 and the last frame was taken at airmass 1.45. A copy of the mask was created for the purpose of wavelength calibration, with narrow 1 arcsec slits centred on the science slits. Bias, flat-field and arc-lamp (for the purpose of wavelength calibration) images were taken, as part of the routine daytime calibration sequences, before and after the observations.

2.2 Data reduction

We used our previously written reduction pipeline based on PYRAF (Sedaghati et al. 2016), which is optimized to the science goals of transmission spectroscopy. In addition to the standard steps of overscan and bias shape subtraction, spectral flat-fielding and wavelength calibration, sky background subtraction and cosmic ray contamination removal, the pipeline also includes steps for optimizing the size of the extraction box used to obtain the one-dimensional stellar spectra, performed independently for each star. We also experiment with the optimal extraction algorithm (Horne 1986) and check to see if this in any way improves the quality of the extracted spectra, which was not the case. Once the wavelength calibrated spectra are obtained, the pipeline makes corrections to the dispersion solution calculated for each target. This is first done for all the spectra of each star through optimization of the cross-correlation function, and then the spectra of the stars are further corrected with respect to each other to ensure a consistent solution across all apertures. This is a necessary and important step due to the low resolution of the spectra. An example set of these wavelength calibrated and corrected spectra is shown in Fig. 1.

2.3 Broad-band light curves and systematic effects

To obtain the broad-band light curves, we integrate the series of spectra for each star within the largest possible common domain (shown as the grey area in Fig. 1), which are shown in Fig. 2(a). At first glance, we observe an airmass-dependent trend for all the targets, as well as the clear transit signal of WASP-80b. Initially, we correct all the light curves for both of these factors, the results of which are shown in Fig. 2(b). These values are later on used to search for possible physical variants responsible for some of the systematic trends in the final differential transit light curve. We also produce differential transit light curves of WASP-80 with respect to

[1] Or linear as both adjectives are used in the definition of the LADC.

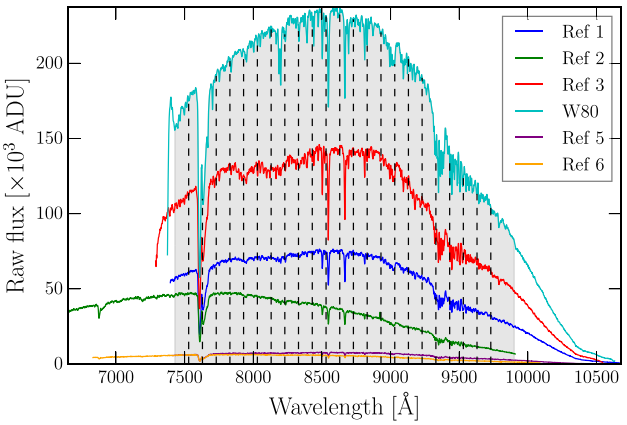

Figure 1. Wavelength calibrated and corrected spectra of all the stars observed with the MXU. The grey area shows the wavelength domain used to obtain all the broad-band light curves. The dashed lines show the boundaries of the spectrophotometric channels, used for integration of WASP-80 and reference stars.

all the observed comparison stars shown in Fig. 2(c). This shows a transit light curve that is very precise and its deviations from a transit model are mostly due to systematic trends. Most significantly, we observe an almost V-shape transit, which could be interpreted as crossing of a stellar spot by the exoplanet, as was observed for WASP-52b (Kirk et al. 2016). However, this claim cannot be made until all possible sources of correlated noise in the data have been considered.

2.3.1 *Instrumental effects*

Prior to the upgrade of the FORS2 instrument, where the LADC prisms (Boffin et al. 2015) were replaced, inhomogeneities in the degraded antireflective coating of the old unit were causing differential transmission through the telescope optics. This would then manifest itself as systematic flux variations in the differential light curves. We now take a closer look at this effect.

Boffin, Moehler & Freudling (2016) presented the improvement in the transmission of light through the optical elements of FORS2 by comparing a stack of flat-field images from before and after the LADC exchange. For our analysis of the systematic trends attributed to the old degraded LADC (used for the observations here), we use their stacked flat-field image taken with the R_SPECIAL+76 filter, shown in Fig. 3. The individual twilight flat-fields used to construct this frame were taken approximately a year after our observations. To this effect, the exact initial position of the field of view relative to the LADC configuration, inferred through observation of flat-field inhomogeneities, is not precisely known. Therefore, we can only try to estimate this position from possible trends in the light curves. In Fig. 3, we plot the observed stars at this estimated starting position and trace the path of each star through the entire observing sequence, where every 10th exposure is shown with a dot.

To obtain the possible starting point of the field of view relative to the LADC set-up, we rotate the configuration shown in Fig. 3 for 360° at 1° steps to cover all possible initial positions. If the LADC deficiencies are the cause of systematic trends in the light curve, then at the true path of the field there will be a spike in the calculated correlation between the light curve of each star (the ones that

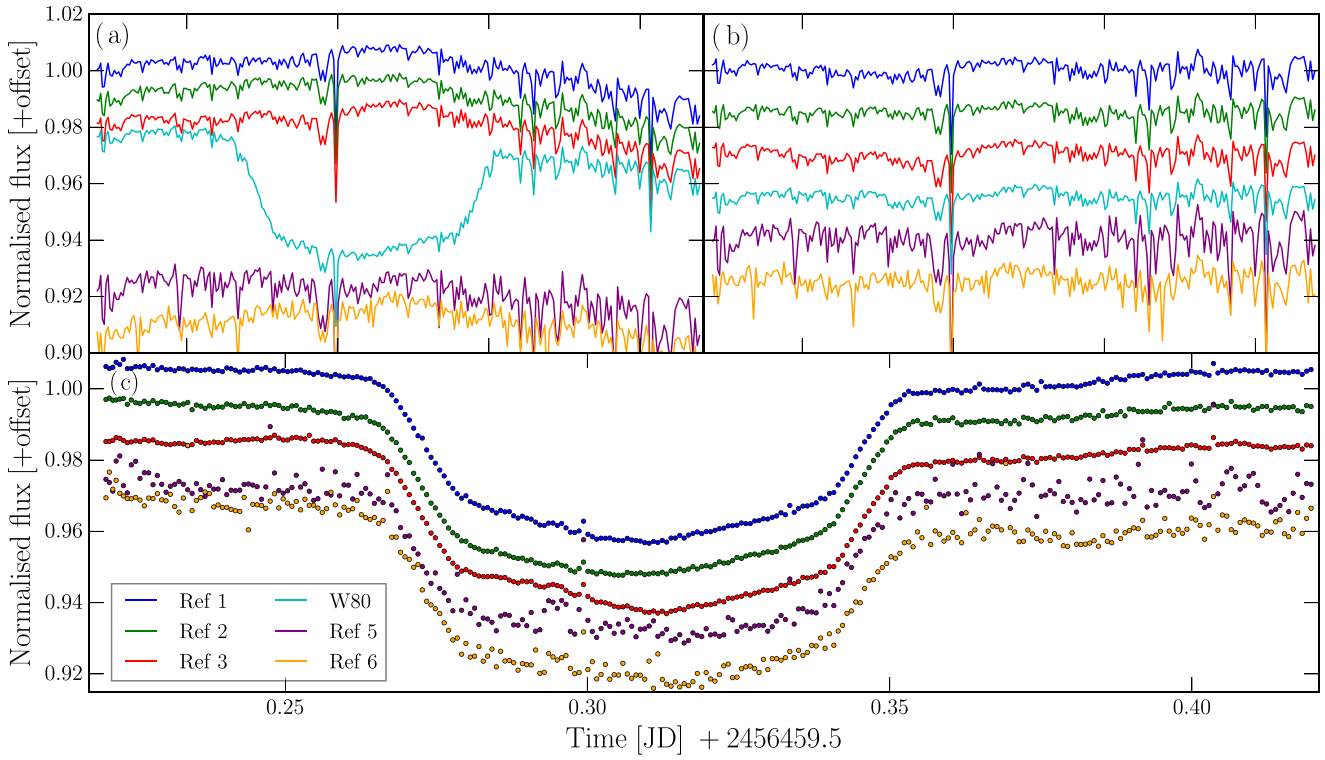

Figure 2. (a) Raw broad-band light curves, normalized to out of transit level and shifted for visual aid. (b) Broad-band light curves corrected for airmass. The transit has been removed from the WASP-80 data. These data are used to check for correlations with other physical parameters besides the airmass. (c) Differential transit light curves again normalized to the out of transit flux level and shifted for clarity. The colours correspond to the raw light curves. These data are not corrected for the airmass-dependent variations, as these will be part of the analytical transit model.

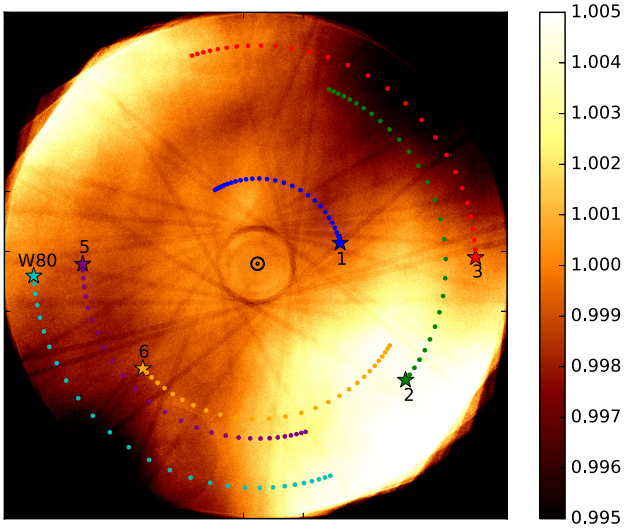

Figure 3. Studying the systematic effects due to the old degraded LADC prisms from the stacked flat-field image. The colour bar on the right shows the scale of the effect (i.e. between −0.5 per cent and +0.5 per cent). The plotted stars are the six observed targets at the starting position that optimizes the correlation with the light-curve residuals, calculated from Fig. 4. The dots represent the position of the star in every 10th frame. The colours are consistent with all the light-curve plots and additionally each star has been labelled corresponding to the aperture number, used consistently throughout the paper.

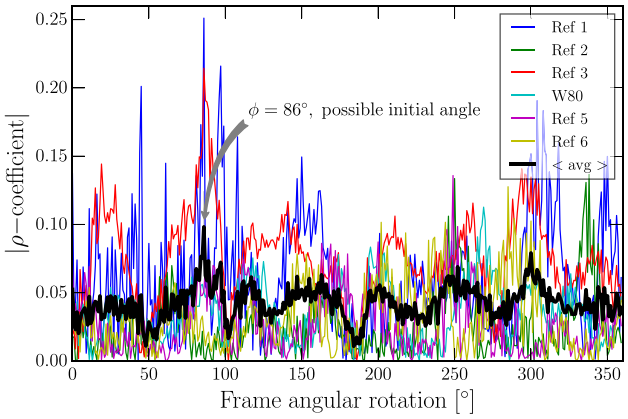

Figure 4. Determination of LADC deficiencies and light-curve systematic trends. The initial set-up shown in Fig. 3 is rotated, and the correlation between the flat-field value along each path with the corresponding light curve is calculated. The thick black line represents the mean correlation value for all the stars. A lack of strong correlation indicates that the degraded LADC is not a significant cause of systematic trends in the light curves.

are corrected for airmass and transit, ref. Fig 2b) and the flat-field value along the path taken by the star, shown in Fig. 3 and read in Figs 5(a) and (b). This calculated correlation as a function of field rotation angle is shown in Fig. 4, where the indicated peak at 86° starting angle could point to a possible relative orientation of the LADC at the beginning of the observing sequence.[2] As a measure

[2] It must be noted that this value is 3° offset from what is calculated based on the orientation of the stacked flat-field image.

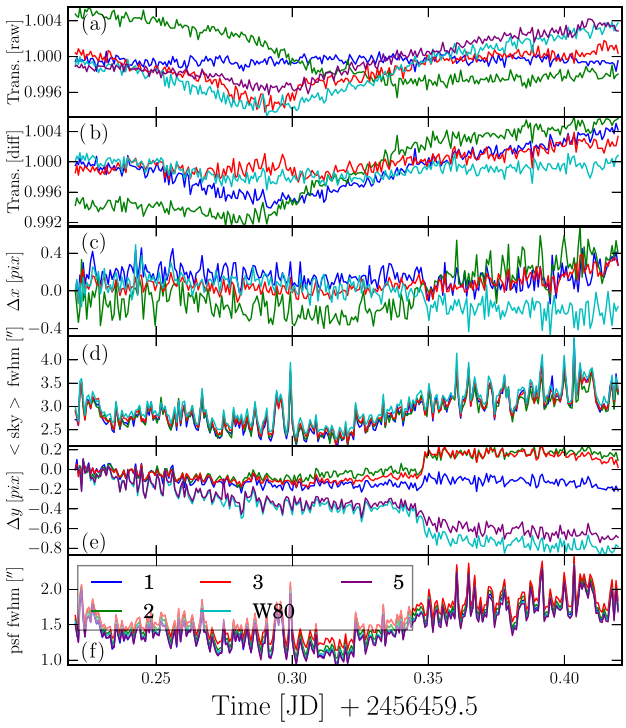

Figure 5. Measurement of physical variants that could possibly introduce systematic trends in the light curves. (a) Shows the measurement of normalized flat-field flux along the (most likely) path of the individual stars, and (b) represents the same measurements but relative to the values of WASP-80's path. (c) Shows the measurement of spectral shift in the dispersion direction relative to the first observation calculated by measuring the centres of multiple telluric absorption features across the entire spectrum, and (d) is the average FWHM values of those fitted Gaussian profiles, which is dependent on seeing conditions. (e) Indicates the drift of spectra along the physical axis relative to the first frame, calculated by again fitting multiple Gaussian functions along the physical axis of the two dimensional spectra, and (f) shows the variations of FWHM values of those fitted profiles. These variations are identical in shape to what was measured along the dispersion axis as expected, and are used as a direct measure of seeing condition variations. These parameters have not been calculated for reference star 6 due to its very low spectral S/N.

of correlation, we simply choose the *Pearson's correlation coefficient*, ρ, defined as the ratio of the covariance of the two variables (cov(x, y)) to the product of their respective standard deviations (σ_x, σ_y).

In order to study the impact of the LADC inhomogeneities on the measured light curves, we read the normalized flat-field value along the path of each star, for this given starting position, which is shown in Fig. 5(a). We use the normalized flat-field, as its variations are a direct indication of the problems caused by the degraded LADC coating. Additionally, since we are also interested in the correction of the differential transit light curves, as a second-order correction, we also calculate the ratio of these readings to the values read along the path of WASP-80. This is shown in Fig. 5(b). The calculated correlation between the light-curve residuals and the flat-field variations due to the degraded LADC is rather weak, which means that the LADC is not a major contributor to the systematic trends. However, it must be noted that the flat-field images used to construct the composite image in Fig. 3 were taken more than a year after the epoch of the observations analysed in this work. Therefore,

our conclusion about the impact of the LADC deformities is rather tentative.

A further possible cause of correlated noise is the spatial stability of the instrument. We characterize the positioning of stellar spectra on the detectors along two axes, spatial and spectral (Δy and Δx). The former variation is measured by taking the mean of the mid-points of several fitted Gaussian profiles to the two-dimensional images across the entire frame in the spatial direction, which are plotted relative to the initial frame in Fig. 5(e). We measure the latter in a similar way, but instead fit several telluric absorption features in the one-dimensional spectra, shown in Fig. 5(c). Studying the relations between both of these variables indicated no significant correlation with the flux variations, which is perhaps due to the stability of the instrument and the data reduction procedure accounting for any remaining residual effects.

2.3.2 *Telluric effects*

In addition to the instrumental effects mentioned previously, telluric conditions also play a significant role in introducing time-correlated noise into the measured time-series data. Namely, variations in the measure of atmospheric seeing, due to turbulence, cause changes in the stellar point spread function (PSF) along both the dispersion and the physical axes. We measure the former as the full width at half-maximum (FWHM) of Gaussian profile fits to several telluric absorption lines in the one-dimensional spectra, variations of which are shown in Fig. 5(d) and denoted as '<sky> FWHM'. This is essentially the convolution of the instrumental profile and the true stellar profile, and therefore a measure of variations in the stellar PSF given the instrument response is constant. The FWHM of the PSF along the physical axis is also measured through recording the characteristics of several Gaussian function fits to various columns (orthogonal to the dispersion axis) of the two-dimensional spectra. These are shown in Fig. 5(f), as 'PSF FWHM' in units of arcseconds, which is another approach to measuring the seeing variations.

We compare the variations of seeing measured separately for each star (from the PSF FWHM) to the normalized flux after the correction for the airmass trend. For WASP-80, additionally, the transit feature is also removed for these calculations, in order to maintain a constant degree of freedom in all correlation plots. Such relations are plotted in Fig. 6, where the comparison stars 5 and 6 have not been included due to their significantly low signal-to-noise ratio (S/N). This will be the case for the remainder of our analysis.

For the measure of correlation, we again use Pearson's parameter described briefly earlier, the calculated values for which are given in each panel. Additionally, we calculate the 1σ, 2σ and 3σ confidence intervals, shown as different shades of grey for visualization purposes. The levels of correlation between individual flux variations and atmospheric seeing are consistent across all the stars and point to a *moderate* association between the two parameters. The relation between each pair of parameters is calculated using an *orthogonal least squares* approach (Isobe et al. 1990), using the ODR package from PYTHON's SCIPY (Jones et al. 2001). This is preferred to the standard linear regression approach due to the present uncertainties in determining 'PSF FWHM'. We use the gradients of these relationships, $\alpha_{\rm FWHM}$ given in Fig. 6, to transform the measured seeing values to flux variations for each star, which in turn will be used as an input of our systematic model, to be described shortly.

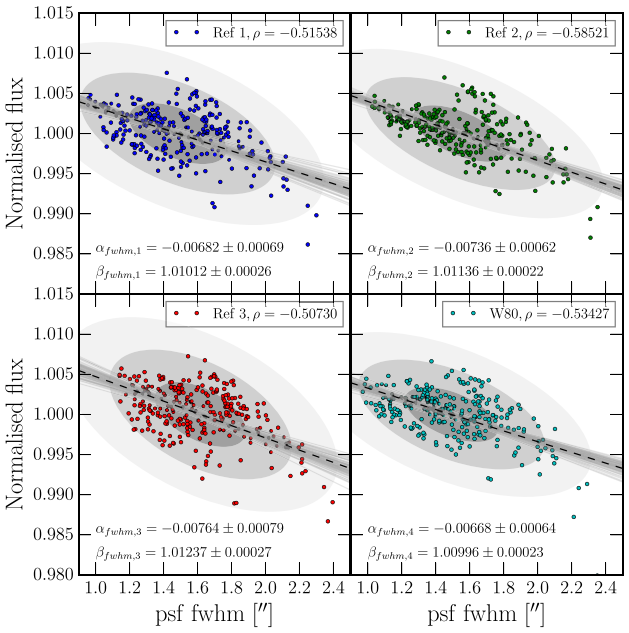

Figure 6. Correlation of seeing variations and the raw stellar light curves, for the four brightest targets observed. The Pearson's correlation coefficient, ρ, which shows a consistent and moderate correlation, has been given for each star. This correlation is further demonstrated through the 1σ, 2σ and 3σ ellipsoids drawn with different shades of grey. In order to associate the seeing values with flux variations, we fit the mean-centred data using an orthogonal linear regression model (Isobe et al. 1990) shown as black dashed line, whose parameters are given for each target.

We choose this approach instead of constructing a correction model to avoid the introduction of biases in our parameter determination and error estimation.

2.4 Light-curve models

We model the transit light curves with the implementation of the analytic solution of Mandel & Agol (2002) as the mean function. Additionally, we estimate the correlated noise as a Gaussian process (GP), which provides a model-independent stochastic method for the inclusion of the systematic component into our model (Rasmussen & Williams 2006). The application of GPs to modelling exoplanet transit light curves and transmission spectroscopy was introduced by Gibson et al. (2012a). The strength of this approach in accounting for systematic trends was highlighted in the detection of hazes in the atmosphere of the exoplanet HD 189733b, where auxiliary information from the *Hubble Space Telescope* (*HST*) were used to train the GP model (Gibson et al. 2012b). Subsequently, we use their GEAPEA and INFER modules[3] for the definition of our GP and the implementation of Bayesian inference.

In the Bayesian framework, we write the likelihood function, $\mathcal{L}$, as a matrix equation in order to introduce off-diagonal elements to the covariance,

$$\log \mathcal{L}\left(\boldsymbol{r}|\mathbf{X},\theta,\phi\right) = -\frac{1}{2}\left(\boldsymbol{r}^{\rm T}\boldsymbol{\Sigma}^{-1}\boldsymbol{r} + \log|\boldsymbol{\Sigma}| + N\log 2\pi\right), \qquad (1)$$

where $\boldsymbol{r}(= f_i - M_i)$ is the residual vector with M being the transit model, $\mathbf{X}$ is the $N \times K$ input parameter matrix (K being the number of

[3] Written in PYTHON programming language and available freely from the following repository: https://github.com/nealegibson.

inputs and N being the number of data points or flux measurements), θ and ϕ are collections of noise and transit model parameters, respectively, and $\mathbf{\Sigma}$ represents the covariance matrix. Ideally, we would like to make every element of the covariance matrix a free parameter in our model, but the size of the matrix ($N \times N$) makes this rather impractical. Hence, we 'model' those elements using a covariance function, more commonly referred to as the *kernel*. With the aid of this kernel, the covariance matrix is written as $\Sigma_{ij} = k(x_i, x_j, \theta) + \delta_{ij}\sigma^2$, x being an input of the kernel, δ the Kronecker delta and σ^2 the variance term, the last two of which ensure the addition of Poisson or white noise to the diagonal of the covariance matrix.

For the kernel, we use the squared exponential (SE)[4] kernel, which for a multidimensional parameter space (K), in its additive form, is written as

$$k_{\rm SE}(x_i, x_j, \theta) = \zeta \exp\left[-\sum_{\alpha=1}^{K} \eta_\alpha \left(x_{\alpha,i} - x_{\alpha,j}\right)^2\right], \quad (2)$$

where ζ is the maximum covariance and η_α are inverse scale parameters for all the input vectors $\boldsymbol{x}$ (essentially the columns of the $\mathbf{X}$ matrix). This parameter determines the length of the 'wiggles' in the function. We choose this form for the kernel, as it is the de facto default form for GPs as it is infinitely differentiable and easy to integrate against most functions.

Finally, in the definition of the analytical transit function, we use the quadratic limb darkening (Kopal 1950) law to describe the centre to limb variations of brightness across the stellar disc. We made this choice after the comparison of the Bayesian information criterion (BIC; Schwarz 1978) values for models of higher complexity, such as the three parameter (Sing et al. 2009) or the non-linear Claret (2000) laws.

2.4.1 Broad-band

We model the best two broad-band differential transit light curves shown in Fig. 2(c), which are produced by using the comparison stars 1 and 2 (top two), as the other light curves are either too noisy or suffer from large systematic effects. These light curves are obtained by the integration of the relevant spectra within the domain that is shaded in grey in Fig. 1. In addition to the transit function, we also include a quadratic term (as a function of parallactic angle) in the description of the analytical transit model, to account for the telescope-rotation-dependent effects in the differential light curves.

To find the maximum posterior solution, $\mathcal{P}$, we need to optimize the Bayesian relation,

$$\log \mathcal{P}\left(\theta, \phi | \boldsymbol{f}, \mathbf{X}\right) = \log \mathcal{L}\left(\boldsymbol{r} | \mathbf{X}, \theta, \phi\right) + \log P\left(\theta, \phi\right), \quad (3)$$

which is true up to a constant term, where the final term on the right-hand side of the equation is the prior probability assumed for the parameters of the complete model. We generally use uninformative priors for the transit parameters, with the exception of the linear and quadratic limb darkening coefficients, ($c_{1,2}$), the orbital period, P, and the eccentricity, e, according to

$$P(\phi) = \begin{cases} \mathcal{N}(3.06785234, 0) & \text{for} \quad \phi \in [P], \\ \mathcal{N}(0, 0) & \text{for} \quad \phi \in [e], \\ 0 & \text{if} \quad c_1 + c_2 > 1, \\ 1 & \text{otherwise}, \end{cases} \quad (4)$$

which fixes the period and eccentricity of the orbit to what has previously been determined by Triaud et al. (2015), and also ensures positive brightness across the stellar disc. For the noise model parameters, we set the following prior probability distributions:

$$P(\theta) = \begin{cases} \Gamma(1, 1) & \text{for} \quad \theta \in [\zeta, (\eta_1, \ldots, \eta_K)], \\ 0 & \text{if} \quad \sigma_{\rm w} < 0, \\ 1 & \text{otherwise} \end{cases} \quad (5)$$

to ensure positive values for all the parameters, as well as using a gamma distribution[5] with shape and scale parameters both set to unity, $\Gamma(1, 1)$, to encourage their values towards zero if the inputs that they represent are truly irrelevant in explaining the data (Gibson et al. 2012a).

For the starting values of the fitted parameters, we use the Nelder–Mead simplex algorithm (Nelder & Mead 1965) to find an initial set of optimal solutions for the transit and noise parameters. To find the maximum posterior solution, we optimize the log posterior given in equation (3). We obtain these parameter posterior distributions by using the Markov chain Monte Carlo (MCMC) method to explore the joint posterior probability distribution of our multivariate models (Collier Cameron et al. 2007; Winn et al. 2008; Gibson et al. 2012a). We run four independent MCMC simulations with 100 walkers, of 100 000 iterations each. Once the chains are computed, we extract the marginalized posteriors for the free parameters to check for mutual convergence and for possible correlations among any pairs of parameters. The transit parameters that are fitted for are mid-transit time (T_0), scaled semimajor axis ($a/R_\star$), relative planetary radius ($R_{\rm p}/R_\star$), impact parameter (b), limb darkening coefficients (c_1 and c_2) and the three coefficients of the baseline model. This model is a second-order polynomial of the parallactic angle, q, whose complexity is chosen using again the BIC selection rule. This baseline model was initially chosen as a quadratic in time, which would describe low frequency variations due to the colour difference between the target and the comparison star. However, this approach results in out of transit flux fit that is worse than using the parallactic angle, and additionally leads to an overestimation of planetary radius as compared to previous results from photometry in our wavelength region. In addition to these, we also fit for the noise model parameters (ζ, $[\eta_1, \ldots, \eta_K]$, σ^2).

In order to decide what input parameters to include in the description of the GP model, as well as which of the two final broad-band light curves suffer less from systematic effects, we model both of these broad-band data series with our previously described model using up to three input parameters for the kernel. We did not find any evidence of correlation with any other optical state parameters to justify their initial inclusion into our model. To compare the fitted models, we calculate their BIC values that include a penalty term for addition of complexity to a model. These calculated values are given in Table 1, where their comparison indicates that our systematic model is best able to describe the broad-band light curve relative to the comparison star 1, when *time*, *seeing* and the *LADC inhomogeneity* are all used to model the covariance matrix. However, it must be noted that there is some evidence against this model relative to the case that does not include the LADC variations (ΔBIC ≤ 6), but we choose to include this final parameter due to the small increase in the reduced chi-squared statistic (χ^2_ν). The correlations and posterior distributions of the parameters of this noise model are given in Fig. 7. From these posterior probability

[4] Also known as the radial basis function.

[5] The probability density function for a gamma $\Gamma(k, \theta)$ distribution of a variable x is given by $f(x, k, \theta) = x^{k-1}\exp(-x/\theta)/\theta^k$.

Table 1. Statistical comparison of our systematic noise model for various inputs, as well as the choice of reference star. The highlighted value indicates the final choice of our data and model set-up.

	Ref 1		Ref 2	
GP input parameters, η_i	χ^2_ν	BIC	χ^2_ν	BIC
t	1.85	559	1.63	504
t, PSF FWHM	0.99	335	1.35	430
t, $F_{\rm LADC}$	1.72	546	1.65	513
t, PSF FWHM, $F_{\rm LADC}$	1.00	**341**	1.41	451

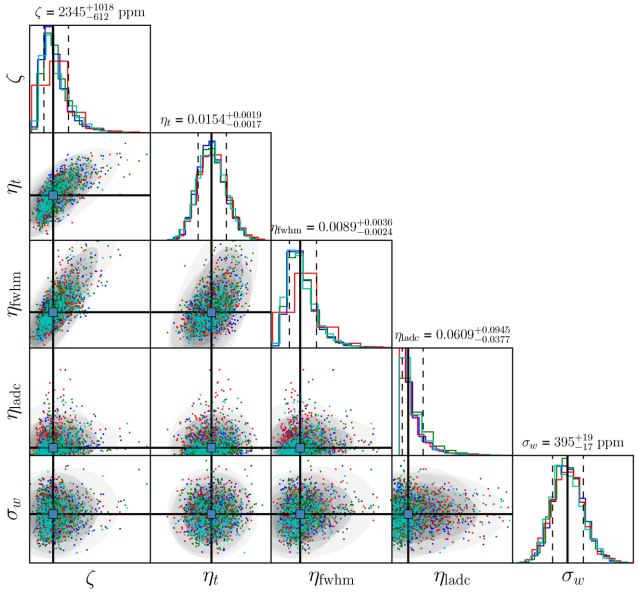

Figure 7. Correlation plots for the noise model parameters, as well as their posterior distributions, shown for the broad-band transit light of WASP-80b obtained relative to reference star 1. The four colours correspond to the four independent MCMC simulations, each of 100 000 length. For the scatter plots, we choose a random subset from each chain. The final quoted parameter values are plotted as blue squares and their values, together with their associated errors, are given on top of each relevant posterior plot.

distributions we infer that our noise model input parameters are significantly relevant in describing the data, as the inverse length scale values, η_i, for all the inputs are $>3\sigma$ away from 0, with the exception of $\eta_{\rm LADC}(\sim 2\sigma)$.

The best-fitting noise model and the corresponding transit function are given in Fig. 8 (as red and blue lines, respectively), for the broad-band light curve obtained relative to reference star 1, as discussed previously. The inferred transit and noise model parameters from this fit are given in Table 2, together with their 1σ uncertainties. Our inferred transit parameters are in statistical agreement with those values reported by previous studies, covering a similar wavelength domain as our FORS2 observations (Triaud et al. 2013, 2015; Fukui et al. 2014; Mancini et al. 2014). We particularly use those values obtained by Mancini et al. (2014) as a benchmark due to their high precision light curves and the common wavelength coverage of their photometric light curves with our observations, namely Sloan i' and z'.

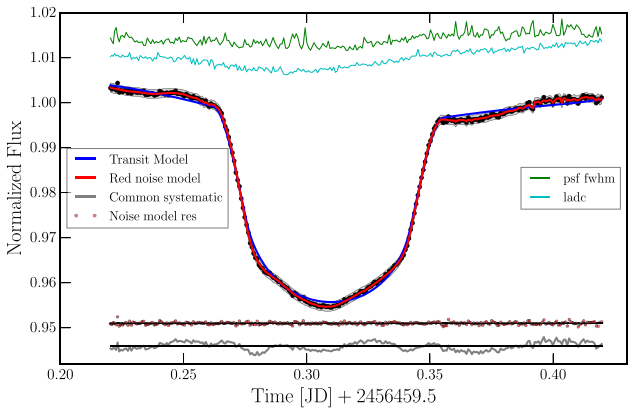

Figure 8. Broad-band transit light curve of WASP-80b. The blue line is the best-fitting transit model and the red line is our systematic model with three inputs and the dark and grey areas are the 1σ and 3σ confidences of that model, respectively. The residuals of this model are shown as red dots below the light curve, shifted for clarity. The grey line represents the common mode correction, which is essentially the residual of the transit model. The green and cyan lines at the top of the plot are the inputs of the covariance kernel, i.e. the PSF FWHM and the differential LADC discrepancy, respectively.

Table 2. The inferred transit parameters of WASP-80b from the analysis of MCMC simulations.

Transit parameter	Value
Mid-transit, T_0, (JD) +245 6459	$0.808\,79 \pm 7.3 \times 10^{-5}$
Barycentric corrected T_0 ($\rm BJD_{TDB}$)	2456 459.809 578
Scaled semimajor axis, $a/R_\star$	12.0647 ± 0.0099
Relative planetary radius, $R_{\rm p}/R_\star$	$0.173\,86 \pm 0.000\,30$
Impact parameter, b	0.2325 ± 0.0087
Linear LD coefficient, c_1	0.491 ± 0.238
Quadratic LD coefficient, c_2	0.485 ± 0.198
Noise parameter	
Maximum covariance, ζ (ppm)	2345^{+1018}_{-612}
Time inverse scale parameter, η_t	0.0140 ± 0.0018
FWHM inverse scale parameter, $\eta_{\rm FWHM}$	$0.0089^{+0.0036}_{-0.0024}$
LADC inverse scale parameter, $\eta_{\rm LADC}$	$0.0609^{+0.0945}_{-0.0377}$
White noise, σ (ppm)	395 ± 18
Derived parameter	
Planet radius, $R_{\rm p}$ ($R_{\rm jup}$)	$0.99^a \pm 0.03$
Orbital inclination, i (°)	88.90 ± 0.06

Note. [a]Calculated using the stellar radius of $0.586 \pm 0.018\,{\rm R}_\odot$ from Triaud et al. (2015).

2.5 Transmission spectrum

2.5.1 Unocculted spots

The presence of active regions on the stellar surface facing the observer, be it spots or faculae, has a differential impact upon our spectroscopic light curves as it is a chromatic effect (Csizmadia et al. 2013). Generally, this differential effect is more prominent in the near-ultraviolet (UV) wavelength domain, where the difference between the spectral density functions of the photosphere and the spot is more notable. Regardless, we do still estimate possible spot-induced radius variations as a function of wavelength, to put any atmospheric interpretations into context. Defining the dimming of the star, $1 - f$, as the flux ratio of the star at an active phase (larger

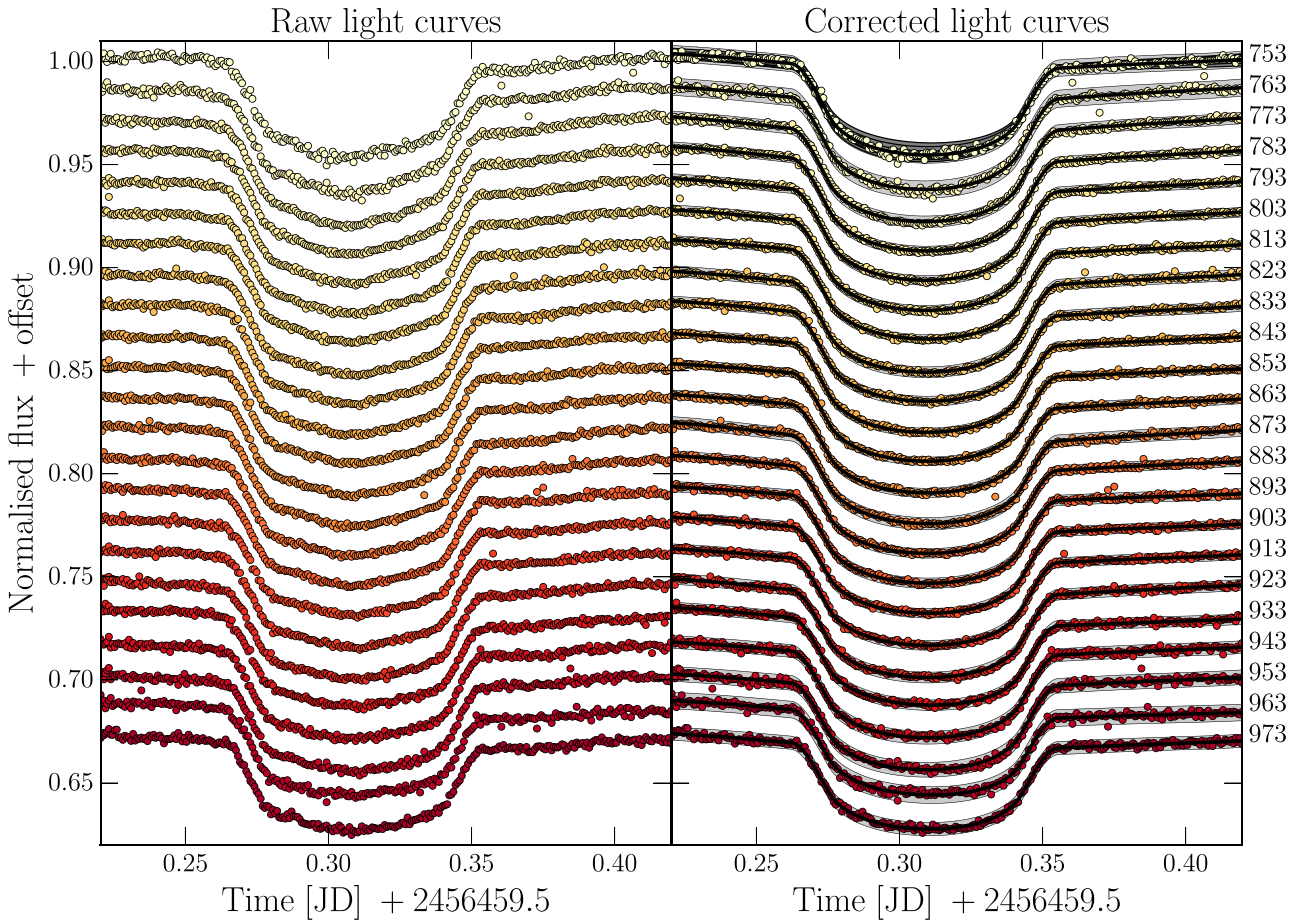

Figure 9. Spectrophotometric light curves of WASP-80b transit, obtained through narrow-band integration of spectra from the FORS2+600z grism, normalized to out of transit flux and shifted for clarity. The left-hand panel shows the raw differential light curves, and the right-hand panel presents the same light curves corrected for the common mode of systematics. The central wavelength of each channel is given to the right of each light curve, with bin size of 100 Å. Our best-fitting transit model for each channel is given as a solid black line, with the 3σ confidence of each fit shaded as light grey.

number of spots) to a relatively quiet phase, one estimates the spot filling factor, α, from the relation

$$\alpha = \frac{1-f}{1-\left(\frac{T_\bullet}{T_\star}\right)^4} = \frac{1-f}{1-\beta^4}, \quad (6)$$

where $T_\star$ is the stellar photospheric temperature, $T_\bullet$ is the spot temperature and β is the fractional temperature difference of the spot and the surrounding photosphere. Here, we have taken the bolometric approximation to Planck's law. Sarr & Neff (1990) obtain spot temperatures $\sim$750 $\pm$ 150 K below the photospheric temperature, from excess absorption in the TiO bands of two K-dwarf stars, values that are further validated by Afram & Berdyugina (2015). With the stellar photosphere at 4143 $\pm$ 93 K, and assuming a 10–20 per cent filling factor (Andersen & Korhonen 2015), we estimate a 5–11 per cent flux dimming for the star.

Based on the above estimates, to correct for the presence of unocculted spots, we simulate light curves for each spectroscopic channel, using the parameter value obtained from that particular bin. In addition, we include a spot on the stellar Southern hemisphere (assuming the transit chord is in the north), with the above physical characteristics. For each channel, only the spot contrast is adjusted, as it is the only wavelength-dependent parameter. Other spot parameters include two positional arguments and a further size argument, parametrized as spot radius. We then model these simulated light curves with our previous model that does not include a spot.

From these simulations, we obtain an average of 33 $\pm$ 8 ppm discrepancy among the values of the relative planetary radii. Therefore, we conclude that the wavelength dependence of the planetary radius is unaffected by unocculted stellar spots. We correct our eventual transmission spectrum for the presence of unocculted spots, although such correction terms are much smaller than the derived error bars of the relative planetary radii.

2.5.2 *Spectral light curves*

To obtain the wavelength-dependent variations of the planetary radius, i.e. the *transmission spectrum*, the spectra are integrated within smaller, 100 Å, bins, which are shown as dashed lines in Fig. 1. This bandwidth determines the resolution of the final transmission spectrum and is chosen through a statistical analysis of stellar spectra (Sedaghati et al. 2016). This bandwidth is similar to most previous transmission spectroscopy studies performed with the FORS2 instrument (Bean et al. 2011; Lendl et al. 2016; Sedaghati et al. 2016; Gibson et al. 2017) and those initial raw so-called spectrophotometric light curves are shown in the left-hand panel of Fig. 9. As one looks for relative variations of transit depth in transmission

spectroscopy, these spectral light curves are corrected for the common mode systematics that are present across all the channels (e.g. Lendl et al. 2016; Nikolov et al. 2016; Gibson et al. 2017). The common mode systematic correction is obtained through the division of broad-band or white light curve by the analytical transit model that includes the baseline model as a quadratic function of the parallactic angle and no correlated noise component. This correction sequence is shown as the grey line at the bottom of Fig. 8. Subsequently, the spectral light curves are divided by this common correction term and modelled with the same systematic noise model as was done for the white light curve. The corrected spectral light curves, together with the associated correlated noise models, are shown in the right-hand panel of Fig. 9.

In modelling the spectral channels we set strict, informative priors on the values of model parameters that are wavelength independent ($T_0, a/R_\star, b$), as well as the three coefficients of the baseline model. Since the limb darkening of the star is a chromatic aspect, the two coefficients of the law describing the centre to limb intensity variations are taken as free parameters in modelling the narrow-band light curves, with prior probabilities same as the broad-band case. One would also expect that seeing- and LADC-dependent systematics to be wavelength independent, which are removed by the common mode correction approach. To confirm this, we allow their respective inverse scale parameters ($\eta_{\rm FWHM}$ and $\eta_{\rm LADC}$) to be free in our analysis, and check whether their posterior distributions approach zero for each channels, which in fact was the case for all light curves. This procedure also ensures that uncertainties from any residual systematics are fully accounted for and their contributions to the final parameter error estimation are correctly propagated. The transmission spectrum obtained from this modelling process is given together with results from previous studies (Fukui et al. 2014; Mancini et al. 2014; Triaud et al. 2015) in panel (a) of Fig. 10, and separately in panel (b). And finally, the wavelength-dependent parameters obtained from modelling the spectrophotometric light curves are given in Table 3.

Additionally we produce light curves from very narrow (30 Å) integration bins around the potassium doublet absorption region (0.766 and 0.770 μm) for possible detection of K in the atmosphere of WASP-80b. We modelled these light curves with the same approach as was done for the 100 Å spectroscopic light curves, the results from which are shown in Fig. 10(c).

3 DISCUSSION

To interpret our observational results, we compare the transmission spectrum from the previous section to a variety of forward atmospheric models that explore a wide range of the parameter space, limited by abundance files provided by the atmospheric modelling code. For this purpose, we use the open source, publicly available EXO-TRANSMIT[6] code (Kempton et al. 2017) to model the planet size variations as a function of wavelength, using the opacity information provided (Freedman, Marley & Lodders 2008; Freedman et al. 2014; Lupu et al. 2014). It must be stressed that we do not fit these spectra to the data and simply overplot them for comparison. Triaud et al. (2015) measured the brightness temperature of WASP-80b as ∼900 K from *Spitzer* photometry of occultations, with the equilibrium temperature calculated as 825 ± 19 K. Consequently, we calculated theoretical spectra for 700, 800 and 900 K equilibrium temperature *T*–*P* profiles, where a comparison of the reduced chi-squared statistic, χ^2_ν, as measured with the combined transmission spectrum (cf. Fig. 10a) suggests a significantly better fit for equilibrium temperature of 800 K as compared to 700 K, and marginally better with respect to 900 K models. This result is in agreement with the estimated equilibrium temperature of the exo-atmosphere. Therefore, from here on, we only plot models calculated with the 800 K equilibrium temperature *T*–*P* profile, and quote statistics based on this assumption.

Comparison to theoretically calculated models indicates a solar or subsolar (1 or 0.1) metallicity for the atmospheric composition of this planet, with larger values (5–1000×) yielding significantly larger χ^2_ν statistics. Furthermore, for all the models evaluated, we consider the case where condensation and rain out of molecules occurs. Again the comparison significantly suggests no evidence for rain out and therefore we compute the spectra with only gas phase chemistry accounted for. The complete transmission spectrum (Fig. 10a) rules out the presence of absorption from H_2O, CO or NH_4 in the atmosphere, all of which have been included in the green dashed and solid red models, and removed from the other two. We rule out their presence at $\gg 5\sigma$ significance, calculated through the bootstrap of transmission spectrum values and their associated errors (the estimated $\chi^2_{\rm r}$ distributions are shown in the left-hand panel of Fig. 11). This result is achieved mainly through the precise photometry of *Spitzer* in the IR and Gamma-Ray Burst Optical/Near-Infrared Detector (GROND) in the near-IR (NIR). Additionally, our analysis gives marginal preference to models without a Rayleigh scattering signature, although this conclusion is not statistically significant ($\sim 2\sigma$). As mentioned earlier, our results also point to an atmosphere with subsolar metallicity, although the exact level of it would need to be determined more precisely with retrieval models, once more spectroscopic data have been obtained over a larger wavelength range – a work that is outside the scope of this paper. We note that Triaud et al. (2015) find a metallicity for WASP-80b's atmosphere of $-0.13^{+0.15}_{-0.17}$, definitively leaving the possibility of subsolar metallicity.

The bluest part of the transmission spectrum is clearly dominated by the wings of the potassium line. To investigate this further, we produce spectroscopic light curves using narrower, 30 Å, bins around the strong potassium doublet at ∼0.786 μm. The results from analysis of these light curves are given in Fig. 10(c), where comparison to atmospheric models with and without potassium included confirms the presence of this alkali metal at very high significance ($\gg 5\sigma$), in the upper atmosphere of WASP-80b, as was also previously done with FORS2 for the planet WASP-17b (Sedaghati et al. 2016). This detection is again made through an estimation of the $\chi^2_{\rm r}$ statistics from the bootstrap of the residuals, the results for which are shown in the right-hand panel of Fig. 11. High-resolution spectroscopy of this target during and out of transit (e.g. Wyttenbach et al. 2015) will provide an alternative method for validation of this detection.

4 CONCLUSIONS

We report a ground-based red transmission spectrum of the exoplanet WASP-80b with the FORS2 instrument at ESO's VLT. The instrument was used in the MXU mode to obtain simultaneous spectra of the target and the comparison stars with the 600z grism, covering a common wavelength domain of ∼0.75–1.05 μm. We successfully model the transit light curve with a GP model with optical state parameters, such as seeing and the LADC inhomogeneities, as inputs. These parameters are selected carefully through the

[6] Available at the following repository: https://github.com/elizakempton/Exo_Transmit.

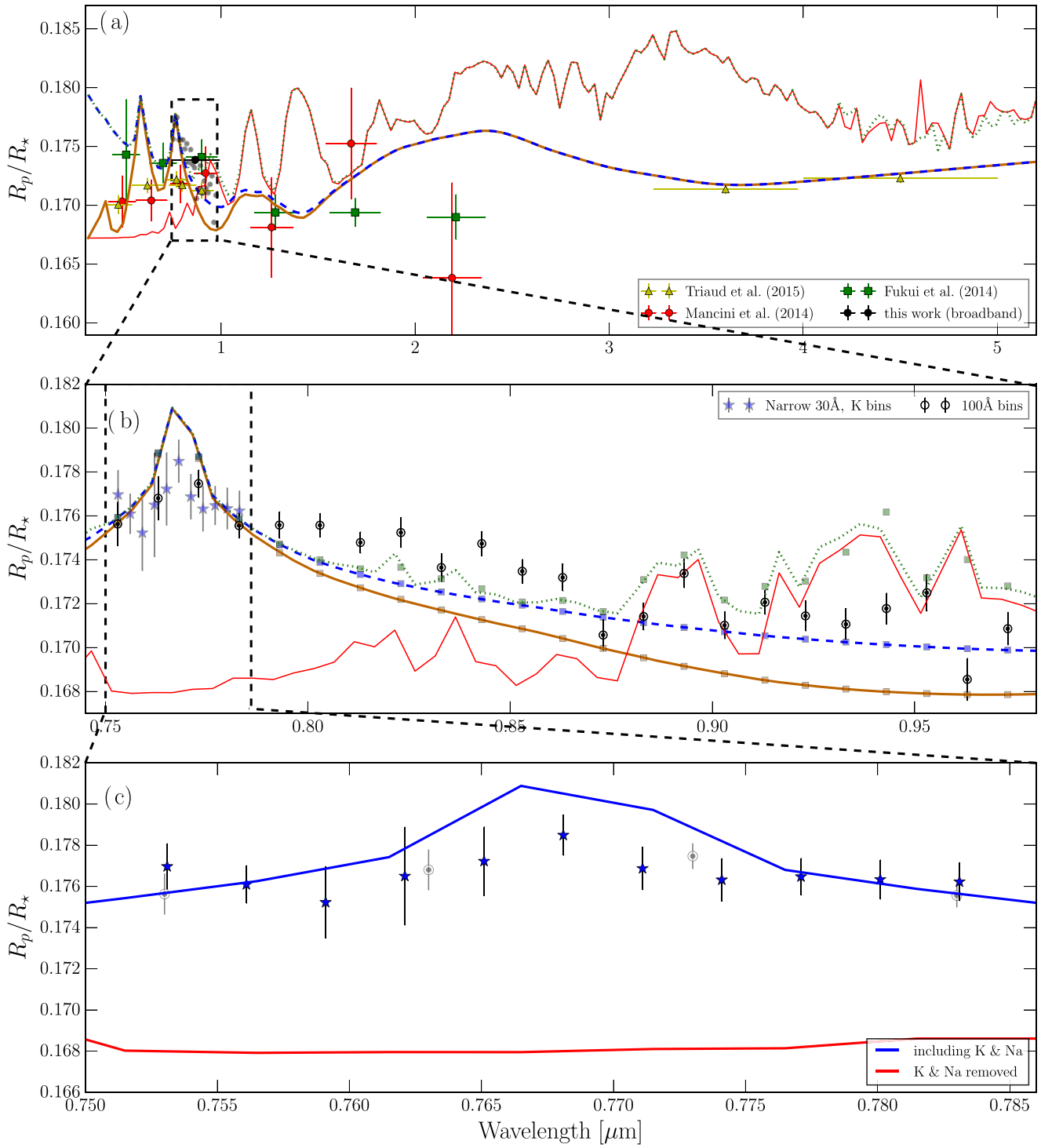

Figure 10. (a) Broad-band transmission spectrum of WASP-80b stitched together from previous studies of this planet, as well as the broad-band and spectroscopic points from our analysis. The four overplotted atmospheric models are produced with the EXO-TRANSMIT code, at 800 K equilibrium temperature, 0.1× solar metallicity. The green dotted model includes the three molecules, H_2O, CO and CH_4, as well as H, He, Na and K, and the red without K and Na. The blue dashed and brown solid lines are the same as the previous models, but with the molecular species removed, where in the brown model Rayleigh scattering has additionally been switched off. (b) A zoom into the region, where our transmission spectrum of WASP-80b is obtained with the 600z grism of FORS2, produced with bins of 100 Å width. The plotted models are the same as above. (c) A further zoom into the region of absorption from the potassium line core and the wings. The presence of potassium in the upper atmosphere is detected using the results from very narrow (30 Å) bins, where confirmation is made through a comparison with models that include potassium (solid blue, same as the dashed blue in the above plots) and one that excludes it (solid red).

Table 3. Transmission spectrum and the two limb darkening coefficients from modelling the spectral light curves.

Band (nm)	$R_p/R_\star$	c_1	c_2
748–758	0.175 63 ± 0.001 00	0.528 ± 0.266	0.434 ± 0.287
758–768	0.176 80 ± 0.000 99	0.538 ± 0.258	0.438 ± 0.280
768–778	0.177 47 ± 0.000 63	0.521 ± 0.352	0.430 ± 0.297
778–788	0.175 56 ± 0.000 57	0.550 ± 0.213	0.442 ± 0.231
788–798	0.175 58 ± 0.000 60	0.542 ± 0.221	0.442 ± 0.260
798–808	0.175 57 ± 0.000 54	0.520 ± 0.361	0.430 ± 0.030
808–818	0.174 79 ± 0.000 48	0.520 ± 0.377	0.430 ± 0.029
818–828	0.175 24 ± 0.000 68	0.522 ± 0.233	0.430 ± 0.275
828–838	0.173 65 ± 0.000 63	0.525 ± 0.232	0.435 ± 0.270
838–848	0.174 74 ± 0.000 56	0.527 ± 0.217	0.431 ± 0.274
848–858	0.173 48 ± 0.000 55	0.522 ± 0.218	0.433 ± 0.283
858–868	0.173 19 ± 0.000 62	0.522 ± 0.225	0.431 ± 0.274
868–878	0.170 57 ± 0.000 70	0.520 ± 0.311	0.430 ± 0.315
878–888	0.171 41 ± 0.000 61	0.525 ± 0.219	0.435 ± 0.276
888–898	0.173 38 ± 0.000 66	0.519 ± 0.236	0.430 ± 0.281
898–908	0.171 02 ± 0.000 62	0.516 ± 0.236	0.432 ± 0.276
908–918	0.172 07 ± 0.000 55	0.520 ± 0.030	0.430 ± 0.304
918–928	0.171 44 ± 0.000 69	0.512 ± 0.245	0.428 ± 0.271
928–938	0.171 07 ± 0.000 70	0.501 ± 0.235	0.420 ± 0.280
938–948	0.171 78 ± 0.000 71	0.520 ± 0.165	0.430 ± 0.338
948–958	0.172 50 ± 0.000 83	0.520 ± 0.290	0.430 ± 0.315
958–968	0.168 55 ± 0.000 96	0.520 ± 0.294	0.430 ± 0.302
968–978	0.170 86 ± 0.000 74	0.520 ± 0.308	0.430 ± 0.296

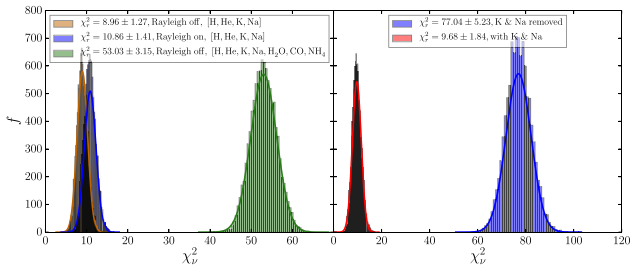

Figure 11. Left: χ^2_r distributions for three of the atmospheric models shown in Fig. 10(a), measured together with the data from broad-band photometry. This analysis significantly rules out additional absorption in the IR due to molecular species such as H_2O, CO or CH_4, and gives marginal preference to those that do not include a Rayleigh scattering signature. Right: same analysis, but performed for the two atmospheric models in Fig. 10(c), where we significantly ($\gg 5\sigma$) detect the presence of potassium in the atmosphere of WASP-80b.

analysis of their correlations with the light-curve residuals. We apply the standard common mode systematic correction to 'clean' the spectroscopic light curves, which are modelled with the same method as the broad-band approach and different prior probabilities of some parameters. Subsequently, the transmission spectrum is plotted, which describes the colour-dependent variations of the planetary radius, as is expected for an extended atmosphere. An initial analysis of our results together with previously obtained transmission spectra of this planet, points to an equilibrium temperature in agreement with the value determined by Triaud et al. (2015), as well as a subsolar metallicity. Furthermore, we rule out the presence of heavier molecules that lead to additional absorption in the IR, at high significance. However, a word of caution here is that the analysis is based on only a few data points in the IR domain and more observations will be required to validate this conclusion. The analysis of our transmission spectrum obtained with FORS2, points to excess absorption in the core and the extended pressure-broadened wing of the potassium doublet. Further analysis of this pressure broadening of the wings will result in an estimation of the cloudiness index for this planet, as proposed by Heng (2016). The presence of potassium in the atmosphere of WASP-80b is detected through the modelling of additional narrow-band (30 Å) transit light curves, where models including potassium lead to significantly ($\gg 5\sigma$) better fit statistics, as compared to those models where potassium is removed. Further observations with other grisms of this instrument will be required to extend the wavelength coverage of the spectrum and enable comparison with more complex atmospheric models. Only then, one could statistically search the atmospheric parameter space, using retrieval methods (Madhusudhan & Seager 2009), to infer a more detailed structure of this exo-atmosphere.

We conclude that the potential of exo-atmospheric observations from ground-based facilities is encouraging, once the sources of correlated noise are carefully analysed. In other words, it is imperative to understand the instrument that is collecting the light, as it was recently and very elegantly demonstrated by Deming & Seager (2017), and to try to exhaust the search for possible sources of correlated noise. This is generally more often the case for observations made from space observatories where systematic noise dominates, but nevertheless should also closely be considered when a claim of atmospheric detection from the ground is made. It must be stressed that our detections are only made possible through the use of an instrument-dependent baseline model and a thorough analysis of the sources of systematic noise in the light curves. Finally, FORS2 is the leading instrument in the world for performing such observations (Bean et al. 2010, 2011; Sedaghati et al. 2015, 2016; Lendl et al. 2016; Nikolov et al. 2016; Gibson et al. 2017), especially after the recent upgrade of the atmospheric dispersion corrector prisms, which has reduced this aforementioned systematic noise in the transit light curves significantly.

ACKNOWLEDGEMENTS

All the data, together with the calibration files, are publicly available and can be downloaded from ESO's science archive, under the programme ID 091.C-0377(C). We also acknowledge the use of several PYTHON modules, such as NUMPY, MATPLOTLIB, SCIPY, ASTROPY, PYFITS, PYASTRONOMY, as well as those mentioned in the text. ES would like to acknowledge funding and support from ESO under the studentship programme. LD acknowledges support from the Gruber Foundation Fellowship. MG is an F.R.S.-FNRS research associate. SC thanks the Hungarian National Research, Development and Innovation Office, for the NKFIH-OTKA K113117 grant.

REFERENCES

Afram N., Berdyugina S. V., 2015, A&A, 576, A34
Andersen J. M., Korhonen H., 2015, MNRAS, 448, 3053
Appenzeller I. et al., 1998, Messenger, 94, 1
Avila G., Rupprecht G., Beckers J. M., 1997, in Ardeberg A. L., ed., Proc. SPIE Vol. 2871, Optical Telescopes of Today and Tomorrow. SPIE, Bellingham, p. 1135
Bakos G. Á. et al., 2015, AJ, 149, 149
Bean J. L., Miller-Ricci Kempton E., Homeier D., 2010, Nature, 468, 669
Bean J. L. et al., 2011, ApJ, 743, 92
Benneke B., Seager S., 2012, ApJ, 753, 100
Boffin H. et al., 2015, Messenger, 159, 6
Boffin H., Moehler S., Freudling W., 2016, Messenger, 163, 10
Campbell B., Walker G. A. H., Yang S., 1988, ApJ, 331, 902
Claret A., 2000, A&A, 363, 1081

Collier Cameron A. et al., 2007, MNRAS, 380, 1230
Csizmadia S., Pasternacki T., Dreyer C., Cabrera J., Erikson A., Rauer H., 2013, A&A, 549, A9
Deming D., Seager S., 2017, JGRE, 122, 53
Deming D. et al., 2013, ApJ, 774, 95
Dorn C., Khan A., Heng K., Connolly J. A., Alibert Y., Benz W., Tackley P., 2015, A&A, 577, A83
Ehrenreich D., Hébrard G., Des Etangs A. L., Sing D. K., Désert J.-M., Bouchy F., Ferlet R., Vidal-Madjar A., 2007, ApJ, 668, L179
Freedman R. S., Marley M. S., Lodders K., 2008, ApJS, 174, 504
Freedman R. S., Lustig-Yaeger J., Fortney J. J., Lupu R. E., Marley M. S., Lodders K., 2014, ApJS, 214, 25
Fukui A. et al., 2014, ApJ, 790, 108
Gardner J. P. et al., 2006, Space Sci. Rev., 123, 485
Gibson N. P., Aigrain S., Roberts S., Evans T. M., Osborne M., Pont F., 2012a, MNRAS, 419, 2683
Gibson N. P. et al., 2012b, MNRAS, 422, 753
Gibson N. P., Aigrain S., Barstow J. K., Evans T. M., Fletcher L. N., Irwin P. G. J., 2013, MNRAS, 428, 3680
Gibson N. P., Nikolov N., Sing D. K., Barstow J. K., Evans T. M., Kataria T., Wilson P. A., 2017, MNRAS, 467, 4591
Hartman J. D. et al., 2015, AJ, 149, 166
Hellier C. et al., 2011, A&A, 535, L7
Heng K., 2016, ApJ, 826, L16
Horne K., 1986, PASP, 98, 609
Isobe T., Feigelson E. D., Akritas M. G., Babu G. J., 1990, ApJ, 364, 104
Johnson J. A. et al., 2012, AJ, 143, 111
Jones E. et al., 2001, SciPy: Open Source Scientific Tools for Python, http://www.scipy.org/
Kaltenegger L., Traub W. A., 2009, ApJ, 698, 519
Kempton E. M.-R., Lupu R. E., Owusu-Asare A., Slough P., Cale B., 2017, PASP, 129, 044402
Kirk J., Wheatley P. J., Louden T., Littlefair S. P., Copperwheat C. M., Armstrong D. J., Marsh T. R., Dhillon V. S., 2016, MNRAS, 463, 2922
Knutson H. A. et al., 2014, ApJ, 794, 155
Kopal Z., 1950, Harvard College Obser. Circular, 454, 1
Lendl M. et al., 2016, A&A, 587, A67
Lupu R. E. et al., 2014, ApJ, 784, 27
Madhusudhan N., Seager S., 2009, ApJ, 707, 24
Mallonn M., Strassmeier K. G., 2016, A&A, 590, A100
Mancini L. et al., 2014, A&A, 562, A126
Mandel K., Agol E., 2002, ApJ, 580, L171
Mayor M., Queloz D., 1995, Nature, 378, 355
Mordasini C., Alibert Y., Klahr H., Henning T., 2012a, A&A, 547, A111
Mordasini C., Alibert Y., Georgy C., Dittkrist K.-M., Klahr H., Henning T., 2012b, A&A, 547, A112
Narita N. et al., 2005, PASJ, 57, 471
Nelder J. A., Mead R., 1965, Comput. J., 7, 308
Nikolov N., Sing D. K., Gibson N. P., Fortney J. J., Evans T. M., Barstow J. K., Kataria T., Wilson P. A., 2016, ApJ, 832, 191
Rasmussen C. E., Williams C. K., 2006, Gaussian Processes for Machine Learning. The MIT Press, Cambridge, MA
Sarr S. H., Neff J. E., 1990, in Wallerstein G., ed., ASP Conf. Ser. Vol. 9, Cool Stars, Stellar Systems, and the Sun. Astron. Soc. Pac., San Francisco, p. 171
Schwarz G., 1978, Ann. Stat., 6, 461
Seager S., Sasselov D. D., 2000, ApJ, 537, 916
Sedaghati E., Boffin H. M. J., Csizmadia S., Gibson N., Kabath P., Mallonn M., Van den Ancker M. E., 2015, A&A, 576, L11
Sedaghati E. et al., 2016, A&A, 596, A47
Sing D. K., Désert J.-M., Lecavelier Des Etangs A., Ballester G. E., Vidal-Madjar A., Parmentier V., Hebrard G., Henry G. W., 2009, A&A, 505, 891
Sing D. K. et al., 2011, MNRAS, 416, 1443
Sing D. K. et al., 2016, Nature, 529, 59
Snellen I., de Kok R., Le Poole R., Brogi M., Birkby J., 2013, ApJ, 764, 182
Stevenson K. B., Bean J. L., Seifahrt A., Désert J.-M., Madhusudhan N., Bergmann M., Kreidberg L., Homeier D., 2014, AJ, 147, 161
Triaud A. H. M. J. et al., 2013, A&A, 551, A80
Triaud A. H. M. J. et al., 2015, MNRAS, 450, 2279
Wakeford H. et al., 2013, MNRAS, 435, 3481
Winn J. N. et al., 2008, ApJ, 683, 1076
Wolszczan A., Frail D. A., 1992, Nature, 355, 145
Wyttenbach A., Ehrenreich D., Lovis C., Udry S., Pepe F., 2015, A&A, 577, A62

This paper has been typeset from a TEX/LATEX file prepared by the author.

A&A 576, L11 (2015)
DOI: 10.1051/0004-6361/201525822

Astronomy & Astrophysics

L E

Regaining the FORS: optical ground-based transmission spectroscopy of the exoplanet WASP-19b with VLT+FORS2⋆

E. Sedaghati[1,2], H. M. J. Boffin[1], Sz. Csizmadia[2], N. Gibson[3], P. Kabath[4], M. Mallonn[5], and M. E. Van den Ancker[3]

[1] ESO, Alonso de Córdova 3107, Casilla 19001, Santiago 19, Chile
e-mail: [esedagha;hboffin]@eso.org
[2] Institut für Planetenforschung, Deutsches Zentrum für Luft- und Raumfahrt, Rutherfordstr. 2, 12489 Berlin, Germany
[3] ESO, Karl-Schwarzschild-str. 2, 85748 Garching, Germany
[4] Astronomical Institute ASCR, Fričova 298, 25165 Ondřejov, Czech Republic
[5] Leibniz-Institut für Astrophysik Potsdam, An der Sternwarte 16, 14482 Potsdam, Germany

Received 5 February 2015 / Accepted 12 March 2015

ABSTRACT

In the past few years, the study of exoplanets has evolved from being pure discovery, then being more exploratory in nature and finally becoming very quantitative. In particular, transmission spectroscopy now allows the study of exoplanetary atmospheres. Such studies rely heavily on space-based or large ground-based facilities, because one needs to perform time-resolved, high signal-to-noise spectroscopy. The very recent exchange of the prisms of the FORS2 atmospheric diffraction corrector on ESO's Very Large Telescope should allow us to reach higher data quality than was ever possible before. With FORS2, we have obtained the first optical ground-based transmission spectrum of WASP-19b, with 20 nm resolution in the 550–830 nm range. For this planet, the data set represents the highest resolution transmission spectrum obtained to date. We detect large deviations from planetary atmospheric models in the transmission spectrum redwards of 790 nm, indicating either additional sources of opacity not included in the current atmospheric models for WASP-19b or additional, unexplored sources of systematics. Nonetheless, this work shows the new potential of FORS2 for studying the atmospheres of exoplanets in greater detail than has been possible so far.

Key words. planets and satellites: atmospheres – techniques: spectroscopic – instrumentation: spectrographs – stars: individual: WASP-19

1. Introduction

Transiting exoplanets provide a wealth of information for studying planetary atmospheres in detail, particularly via spectroscopy. During a planetary transit, some of the stellar light passes through the limb of the planetary disc, where the presence of an atmosphere allows it to be indirectly inferred. When observed at different wavelengths, the transit depth, which is directly linked to the apparent planetary radius, may vary, providing constraints on the scale height of the atmosphere, the chemical composition, and the existence of cloud layers (Seager & Sasselov 1998, 2000; Brown 2001; Burrows 2014). Such measurements require extremely precise relative photometry in as many wavebands as possible and as such can only be done using space telescopes or large ground-based facilities.

The FOcal Reducer and low-dispersion Spectrograph (FORS2) attached to the 8.2-m Unit Telescope 1, is one of the workhorse instruments of ESO's Very Large Telescope (Appenzeller et al. 1998). Using its capability to perform multi-object spectroscopy, Bean et al. (2010) show the potential of FORS2 in producing transmission spectra for exoplanets even in the mini-Neptune and super-Earth regimes. They obtained the transmission spectrum of GJ1214b between wavelengths of 780 and 1000 nm, showing that the lack of features in this spectrum rules out cloud-free atmospheres composed primarily of hydrogen. Except for this pioneering result, all further attempts to use FORS2 for exoplanet transit studies have apparently failed, however, most likely becuase of the systematics introduced by the degradation of the antireflective coating of the prisms of the longitudinal atmospheric dispersion corrector (LADC; Berta et al. 2011; see also Moehler et al. 2010). A project was therefore started at ESO Paranal to make use of the available decommissioned twin instrument FORS1 (Boffin et al. 2015). The FORS2 LADC prisms were replaced by their FORS1 counterparts, which had their coating removed. This resulted in a transmission gain of 0.05 mag in the red to 0.1 mag in the blue, most likely because the uncoating of the LADC largely eliminates the contribution of scattered light from the previously damaged antireflective coating. As a further test of the improvement provided by the prism exchange, we also observed a transit of the exoplanet WASP-19b (Hebb et al. 2010). WASP-19 is a 12.3 mag G8V star, that hosts a hot Jupiter with a mass of 1.17 Jupiter masses (M_J) and an orbital period of 0.789 days, making it the Jupiter-like planet with the shortest orbital period known and one of the most irradiated hot-Jupiters discovered to date. Owing to its short orbital period, and subsequently brief transit duration of ∼1h30, WASP-19b was an ideal target for assessing the impact of the prisms' exchange on the FORS2 performance.

2. Observations

We observed WASP-19 between 2014 November 16 05:16 UT and 08:49 UT with FORS2, under thin cirrus, in multi-object

⋆ Appendix A is available in electronic form at http://www.aanda.org

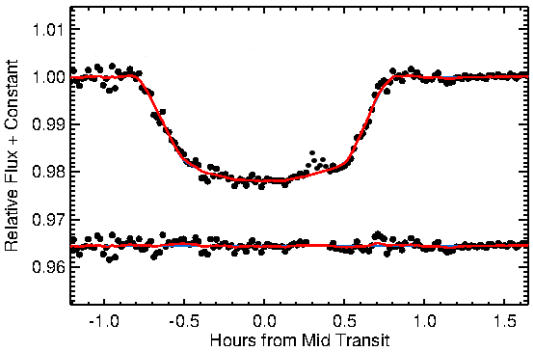

Fig. 1. Normalised, detrended broadband light curve of WASP-19 compared with the best fit obtained with the red noise model included (red line). The residuals of the light curve compared to the models are also shown. In the residual plot, the possible spot-affected data points are removed, because they are given zero weight.

spectroscopic mode (MXU), using a mask with slits 30″ long and 10″ wide placed on WASP-19, as well as on six reference stars. Data were binned (2 × 2), yielding a scale of 0.25″ per pixel. Grism 600RI (with the order sorter filter GG435) was used, leading to a wavelength coverage[1] of about 550 to 830 nm. Our observations covered a full transit, while the object moved from airmass 2.5 to 1.2, with the seeing varying between 0.8″ and 2.2″. The high airmass at the start, in combination with the cirrus, is most likely the cause of the larger scatter in the light curve prior to ingress (Fig. 1). Using the MIT CCD, time series of the target and reference stars were obtained using 30 s exposures until 08:18 UT[2]. The LADC was left in park position during the whole observing sequence, with the two prisms fixed at their minimal separation (30 mm). In total, we had 155 useful exposures, 85 of which were taken in transit. The typical signal-to-noise ratio of WASP-19 on one spectrum was about 300 at the central wavelength.

The data were reduced using IRAF, and one-dimensional spectra of the target and reference stars were extracted. Examples of such spectra are shown in Fig. A.2. Stars in apertures 1 and 2 were not considered further in the analysis, since their wavelength coverages were either too red or too blue compared to WASP-19. For the remaining five comparison stars, we constructed differential white (or broadband, hence collapsing all the spectral channels into one) light curves of WASP-19 with respect to each of these, as well as all possible combinations, and measured the out-of-transit intrinsic scatter. It was found that using only the reference Star 7 provided the most accurate light curve, regardless of the detrending process employed, and this is what is then used in the rest of this paper. We conjecture that this is due to the low counts for Stars 4 and 5, and the significant colour difference with Star 6, which leads to differential atmospheric diffraction. Because our observations span a wide range of airmasses and there is clearly a difference in spectral type between our comparison star and WASP-19, we expect to see some smooth variation, owing to the colour term. This is then corrected via the atmospheric extinction function (from Bouguer's law), given by

$$F_{\rm obs} = F_0 \exp\Big[(k_1 + k_2 c)X\Big], \quad (1)$$

where k_1 and $k_2(\lambda)$ are the first- and second-order atmospheric extinction coefficients, respectively, c is the stellar $(B-V)$ colour index, and X the airmass. This detrending process is shown for some of the spectrophotometric channels in Fig. A.3, with the final broadband and spectroscopic light curves shown in Figs. 1 and A.6, respectively. The post-egress, out-of-transit residuals in this light curve are 760 μmag. This value (close to 579 μmag estimated from photon noise following the formalism of Gillon et al. 2006) and the fact that a single extinction function is sufficient to model, in large part, the correlated noise is a clear indication that the systematics that affected similar FORS2 observations in the past have been significantly reduced, so this instrument is now ready for detailed study of transiting exoplanets[3]. This is what we do now.

3. Results

3.1. Broadband light curve

The normalised and detrended broadband light curve, obtained by integrating the spectra from 550 to 830 nm, was modelled using the Transit Analysis Package (TAP) from Gazak et al. (2012), which is based on the formalism of Mandel & Agol (2002), as well as from Carter & Winn (2009) for the wavelet-based treatment of the correlated (red) noise. The package is built on a Monte Carlo Markov chain (MCMC) code utilising a Metropolis-Hastings algorithm within a Gibbs sampler. The code has the ability to compute multiple MCMC chains in a single iteration and extend the chains until convergence is apparent. Eventually, a Gelman-Rubin statistic (Ford 2006) was used to test for non-convergence by checking the likelihood that multiple chains have reached the same parameter space. Once the state of convergence was reached, Bayesian inference is performed to quote the median solutions and the 1σ confidence levels. Parallel to this modelling process, we fitted the data again with another code, written by one of us (SzCs), using a combination of a genetic algorithm (performing a harmony search that finds a good local or a global minimum-like solution) and simulated annealing that refines this solution and performs the error estimation. The agreement in the planetary parameters is further testament to the reliability of our conclusions.

As part of our analysis, we tested the broadband and the individual spectrophotometric light curves for levels of correlated noise with the formalism described by Pont et al. (2006, see Fig. A.4), where the maximum deviation from the white noise model is 65 μmag. Based on Eqs. (5) and (6) of Gillon et al. (2006), we also estimated a red noise level of $\sigma_{\rm r}$ = 169 μmag. This prompted us to model and analyse this correlated noise using the wavelet decomposition method mentioned above, implemented in TAP. For a complete description of wavelet mathematics applied to astronomical data see Carter & Winn (2009). Strictly speaking, however, this method can underestimate the level of correlated noise present in the data if the systematics are not time-correlated with a power spectra $\sim 1/f^{\gamma}$. Using a more general approach, such as a Gaussian process (GP) model introduced in Gibson et al. (2012), many alternative models of time-correlated noise can be explored, as can the effects of systematics that are not stationary in time, i.e. systematics that are functions of auxiliary parameters, such as the seeing and position of the star on the CCD. Gibson et al. (2013) compare wavelet and Gaussian process (GP) methods, showing that GPs provide more conservative estimates of the uncertainties even for purely

[1] The exact wavelength coverage depends on the position of the star on the CCD, so it varies from one star to the next. The values mentioned are the actual ones, which we use in our analysis.

[2] Beyond this point, the exposure time was reduced to 20 s owing to the risk of saturation, but these data could not be used.

[3] Strictly speaking, however, other, possibly longer lasting transit observations are required to prove this point.

Table 1. Planetary parameters derived from modelling the broadband light curve of the WASP-19b transit.

Parameter	Value
Scaled semi-major axis, $a/R_\star$	$3.656\ ^{+0.086}_{-0.097}$
Scaled planetary radius, $R_p/R_\star$	$0.1416^{+0.0019}_{-0.0018}$
Inclination, i	$80.36^\circ\ ^{+0.76}_{-0.81}$
Linear LD coefficient, γ_1	$0.391\ ^{+0.092}_{-0.096}$
Quadratic LD coefficient, γ_2	$0.225\ ^{+0.052}_{-0.050}$
Mid-transit, T_c + 2 456 977 JD	$0.77722 \pm 1.3 \times 10^{-4}$
Uncorrelated (white) noise, σ_w	697 ± 65 μmag

time-correlated, stationary noise. However, these effects are only marginally present in our data (as shown in Fig. A.4). The modelling process is done with zero weight given to seven data points deemed to have been affected by the planet crossing a stellar spot (see Sect. 3.3). The results of our modelling are shown in Fig. 1, and the derived parameters are given in Table 1. In the modelling process, all the physical parameters are assumed to be free, apart from the period, eccentricity, and the argument of periapsis (fixed to 0.7888399 days, 0° and 90°, respectively), which cannot be determined from our single transit observations.

The values we derive are in good agreement with what was found by others. As far as the fractional planetary radius is concerned, our value agrees with Mancini et al. (2013), Tregloan-Reed et al. (2013), and Huitson et al. (2013). We can thus be confident that our FORS2 observations are useful and not affected by systematics that cannot be corrected. Because WASP-19b is so close to its host star, orbiting at only 1.2 times the Roche tidal radius, the planet is most likely tidally deformed, and the radius we derived is likely to be underestimated by a few percentage points (Leconte et al. 2011).

3.2. Transmission spectrum

We have produced spectrophotometric light curves from 550 to 830 nm, with mostly 20 nm bandwidth at 10 nm intervals – i.e. 27 light curves – and modelled them in the same manner as before, shown in Fig. A.6, while we fixed all the parameters that do not depend on wavelength to the white light curve solutions. As a result, only the relative planetary radii and the linear limb darkening coefficients are kept free. This process, also implies overlapping transmission spectrum points. Since the quadratic term is not well defined from the light curves, we assume the theoretical values, similar to that of the white light solution, as a Gaussian prior, allowing the parameter to vary under a Gaussian penalty error. The width of this distribution is taken as slightly larger than theoretically expected variations for this parameter within the given wavelength range. Furthermore, both correlated and uncorrelated noise components, along with a further airmass correction function (having two parameters), are also simultaneously modelled for all individual channels.

The limb darkening coefficients were found to vary in a consistent manner as a function of wavelength when compared to theoretically calculated values (Claret & Bloemen 2011), shown in Fig. A.7. The planetary radii obtained are shown as a function of wavelength in Figs. 2 and A.1 and compared with previous values from the literature and to models of planetary atmospheres (Burrows et al. 2010; Howe & Burrows 2012).

The modelled uncorrelated noise is 900 ± 50 μmag for all the spectroscopic channels. Since the noise in the data is predominantly white, the MCMC algorithm is not able to constrain the red noise, σ_r, for the various binned light curves, so we do not quote the determined value. The dominance of the uncorrelated

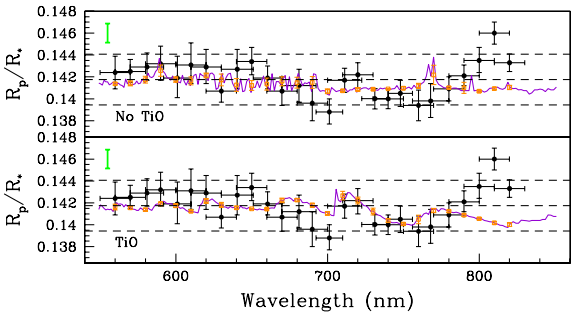

Fig. 2. Transmission spectrum of WASP-19b as measured with FORS2 (black dots, with error bars) compared to two models of planetary atmospheres, one with no TiO (*top panel*) and one with a solar abundance of TiO (*bottom panel*), from Burrows et al. (2010) and Howe & Burrows (2012). We also estimated the mean value of the models in bin sizes of 20 nm (orange open squares). The dashed lines represent the weighted mean plus or minus three scale heights. Because of the overlapping spectral bins, only alternate pairs of transmission spectrum points contain unique information. The heavy, green bar on the left side shows the maximum error associated with unocculted spots.

noise is a testament to the minimal impact of the systematics upon our observations. It is also important to note that since the noise components, as well as the detrending functions, are modelled using the MCMC code, their uncertainties have been fully accounted for when quoting our final error budget estimations. Furthermore, the uncertainties in coefficient determination of the atmospheric extinction function used initially to correct the slow trend in the light curves have also been propagated into our error values. We are therefore confident that the relative error bars for our planetary radii values are realistic and comprehensive. The numerical results from the above modelling processes are shown in Table A.1.

From Fig. A.1, we see that our measurements are those with the highest spectral resolution[4] obtained for WASP-19b in the optical. They clearly agree with the values determined with HST by Huitson et al. (2013). In Fig. 2, we compare our values with two models from Burrows et al. (2010) and Howe & Burrows (2012), which were also used by Huitson et al. (2013), after having assumed solar metallicity for chemical mixing ratios and opacities, as well as local chemical equilibrium. Our measurements redwards of 790 nm do not seem to fit any of the models and deviate from them at more than 5σ. Below 790 nm, our data is compatible, within 2σ with no variation in the planetary radius, and we can unfortunately not distinguish between the atmospheric models with and without TiO. HST observations from Huitson et al. (2013) favoured models lacking any TiO abundance, based on their low-resolution spectra covering the range 290−1030 nm. They rule out the presence of TiO features in the atmosphere, but additional WFC3 transmission spectroscopy in the infrared shows absorption feats owing to the presence of water. Similarly, Mancini et al. (2013) present ground-based, multi-colour, broadband photometric measurements of the transmission spectrum of WASP-19b, from which they determined the transmission spectrum over the 370−2350 nm wavelength range, concluding that there is no evidence for strong optical absorbers.

3.3. Spotting a spot

Our broadband light curve, as well as our spectral light curves (Figs. 1 and A.6), shows a clear in–transit substructure, between

[4] It must be stressed that only alternate pairs of data points contain unique information, so we only claim to produce a transmission spectrum at a resolution of 20 nm.

0.3 and 0.4 h after mid-transit. This is possibly the signature of a spot (or group of spots) crossing by the transiting planet (Silva 2003; Pont et al. 2007; Rabus et al. 2009) – such events have already been seen in the photometric light curves of WASP-19 by Tregloan-Reed et al. (2013) and Mancini et al. (2013). We used their code, PRISM+GEMC, to model this spot and present the results in Table A.2 and Fig. A.5. The modelling with the spot provides very similar values for the planetary transit parameters, and we have checked that this modelling does not change our conclusions concerning the transmission spectrum. We note that the latitude of the spot we find is not very different from what was seen by Tregloan-Reed et al. (2013) and Mancini et al. (2013), although ours is slightly larger but shows a very different contrast: while Tregloan-Reed et al. (2013) find a relatively bright spot with a contrast of 0.76−0.78, and Mancini et al. (2013) have values between 0.35 and 0.64, depending on the colour, we find a rather dark spot with fairly high contrast of 0.30. However, a word of caution is necessary here, since this feature could also be due to a sudden variation in seeing or systematics seen in all the reference stars at the same time. As a check, we used the average of the spot contrast values, modelled from the light curves, for the first and last four channels (blue to red) to estimate the spot temperature difference between the extremes of our transmission spectrum. The variation is significant at the 4σ level, although the actual change is four times smaller than found by Mancini et al. (2013) between the r' and i' bands, and we are thus left without any conclusion. We explored further avenues for causes of this feature, but the list of possibilities is by definition non-exhaustive owing to the nature of systematics.

Besides the impact of spot occultation, there are other uncertainties introduced in the derived parameters, by possible presence of unocculted spots. Activity monitoring of the host star is required to quantify and rule out the impact of such events, before any significant claim about an atmospheric detection can be made. This, however, is an effect that is much more crucial to consider when dealing with multiple transits at large epoch separations. Since we are only dealing with relative radius variations, the only concern for us is the wavelength dependence of the spot contrast and its impact on the determinability of the out-of-transit baseline. Assuming a wavelength-dependent variation from blue to red of spot contrast and temperature (∼100 K) similar to those found by Mancini et al. (2013) and an average spot size of 15° (from this work and others), we estimate an upper limit uncertainty of 0.0017 in the determinability of the baseline (see Fig. 2). This alone cannot explain the feature towards the red in the spectrum. The reader is referred to Csizmadia et al. (2013) for further details on the unocculted spot impact.

4. Conclusions

We have shown that following the prisms exchange of the LADC, FORS2 is now a competitive instrument for studying transiting planets using its multi-object spectroscopy mode. We observed one transit of WASP-19b as it passed in front of its host star and were able to model it. We thereby obtained the first ground-based, optical transmission spectrum of this planet, one of high resolution. Although the precision with which the planetary radii are determined needs to be improved by ∼50% to distinguish between existing atmospheric models with and without TiO, we did detect clear significant variations in the deduced planetary radius at wavelengths redwards of 790 nm, which have so far not been explained by models. However, we still refrain from making any definitive conclusions here, because unexplored sources of systematics could also be responsible for these deviations. Finally, our observations possibly indicate the presence of a dark spot on WASP-19.

Although we have limited ourselves to spectral bins of 20 nm wide, because we obtained our data under thin clouds, in a wide range of airmass and could finally only use one reference star, our analysis indicates that in good weather conditions and provided several reference stars are available, one can still improve upon the precision of the measurements and perhaps also use smaller bins for transmission spectroscopy. Such data could allow distinguishing between competing planetary atmosphere models. In addition, these data could reveal additional information about the spectral signature of the atmospheric feature we are detecting longwards of 790 nm. We can thus only encourage readers to consider applying for FORS2 telescope time.

Acknowledgements. It is a pleasure to thank Guillaume Blanchard for his analysis of the feasibility of the prisms exchange and his precise and prompt work in uncoating the FORS1 LADC prims. Staff at Paranal were very efficient in making the exchange. We are very indebted to A. Burrows and J. Fortney for providing the results of their atmospheric models, and to C. Huitson for serving as an intermediary. We acknowledge the use of the publicly available PRISM+GEMC and TAP codes. P.K. also acknowledges funding from MŠMT ČR, project LG14013, as well as Sz. Cs. the funding of the Hungarian OTKA Grant K113117. The observations of WASP-19b were obtained during technical time to check the exchanged prisms of the FORS2 LADC and are publicly available from the ESO Science Archive under Programme ID 60.A-9203(F).

References

Appenzeller, I., Fricke, K., Fürtig, W., et al. 1998, The Messenger, 94, 1
Bean, J. L., Miller-Ricci Kempton, E., & Homeier, D. 2010, Nature, 468, 669
Berta, Z. K., Charbonneau, D., Bean, J., et al. 2011, ApJ, 736, 12
Boffin, H. M. J., Blanchard, G., Sedaghati, E., et al. 2015, ESO Messenger [arXiv:1502.03172]
Brown, T. 2001, ApJ, 553, 1006
Burrows, A. S. 2014, Nature, 513, 345
Burrows, A. S., Rauscher, E., Spiegel, D. S., Menou K. 2010, ApJ, 719, 341
Carter, J. A., & Winn, J. N. 2009, ApJ, 704, 51
Claret, A., & Bloemen, S. 2011, A&A, 529, A75
Csizmadia, Sz., Pasternacki, T., Dreyer, C., et al. 2013, A&A, 549, A9
Ford, E. B. 2006, ApJ, 642, 505
Gazak, Z., Johnson, J., Tonry, J., et al. 2012, Adv. Astron., 2012, 697967
Gibson, N. P., Aigrain, S., Roberts, S., et al. 2012, MNRAS, 419, 2683
Gibson, N. P., Aigrain, S., Barstow, J. K., et al. 2013, MNRAS, 428, 3680
Gillon, M., Pont, F., Moutou, C., et al. 2006, A&A, 459, 249
Hebb, L., Collier-Cameron, A., Triaud, A. H. M. J., et al. 2010, ApJ, 708, 224
Huitson, C. M., Sing, D. K., Pont, F., et al. 2013, MNRAS, 434, 3252
Howe, A. R., & Burrows, A. S. 2012, ApJ, 756, 176
Leconte, J., Lai, D., & Chabrier, G. 2011, A&A, 528, A41
Lendl, M., Gillon, M., Queloz, D., et al. 2013, A&A, 552, A2
Mancini, L., Ciceri, S., Chen, G. 2013, MNRAS, 436, 2
Mandel, K., & Agol, E. 2002, ApJ, 580, L171
Moehler, S., Freudling, W., Møller, P., et al. 2010, PASP, 122, 93
Pont, F., Zucker, S., & Queloz, D. 2006, MNRAS, 373, 231
Pont, F., Gilliland, R. L., Moutou, C., et al. 2007, A&A, 476, 1347
Rabus, M., Alonso, R., Belmonte, J. A., et al. 2009, A&A, 494, 391
Seager, S., & Sasselov, D. D. 1998, ApJ, 502, 157
Seager, S., & Sasselov, D. D. 2000, ApJ, 537, 916
Silva, A. V. R. 2003, ApJ, 585, L147
Tregloan-Reed, J., Southworth, J., & Tappert, C. 2013, MNRAS, 428, 3671

Pages 5 to 7 are available in the electronic edition of the journal at http://www.aanda.org

Appendix A: Additional tables and figures

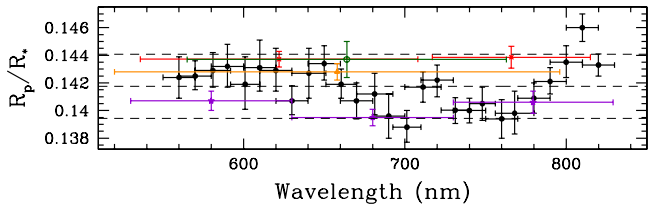

Fig. A.1. Transmission spectrum of WASP-19b based on our FORS2 observations (black, filled dots), compared to values from Huitson et al. (2013, violet filled stars) (obtained spectroscopically), Mancini et al. (2013, red squares), Lendl et al. (2013, green open circle), and Tregloan-Reed et al. (2013, orange open triangle) (from photometry). The vertical bars represent the errors in the fractional radius determination, while the horizontal bars are the FWHM of the passbands used. We note the high spectral resolution of the FORS2 data, compared to what was available until now. The dashed lines represent the weighted mean plus or minus three scale heights.

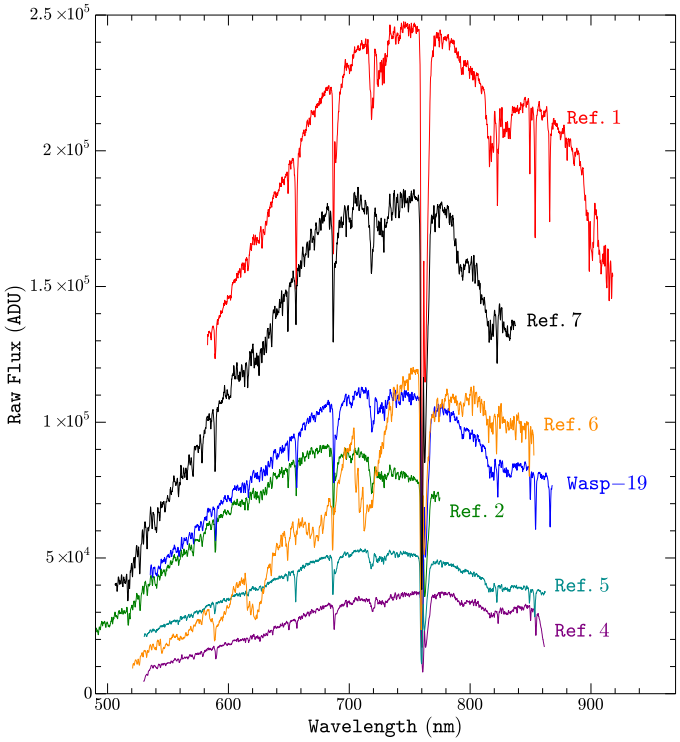

Fig. A.2. Examples of the one-dimensional extracted spectra of the target and reference stars. The target star with the transiting planet, WASP-19, is shown in blue, while the target in aperture 7, which we use as comparison star, is shown in black.

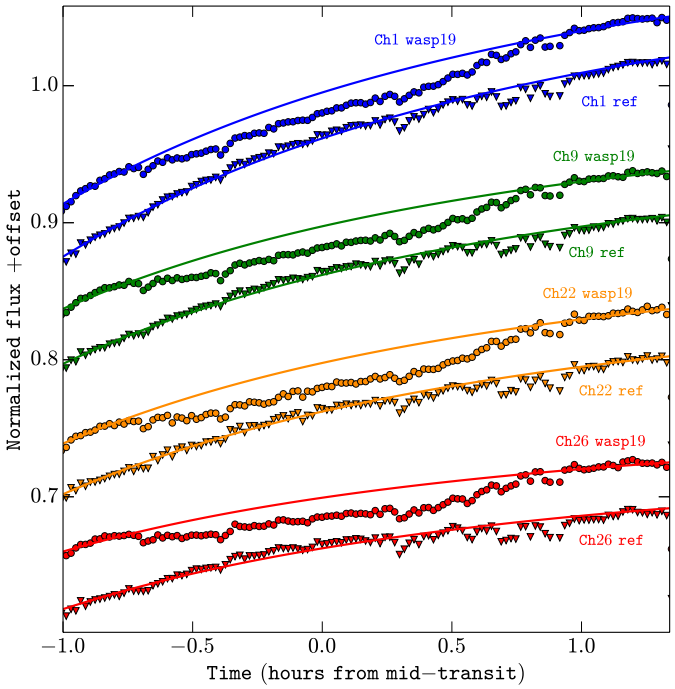

Fig. A.3. Raw light curves for four of the spectroscopic channels. The plots with circles are the light curves for WASP-19 and the triangles represent the reference star in aperture 7. The extinction functions (Eq. (1)), used for the purpose of detrending these raw light curves, are also shown as solid lines. An offset has been added to the light curves for clarity.

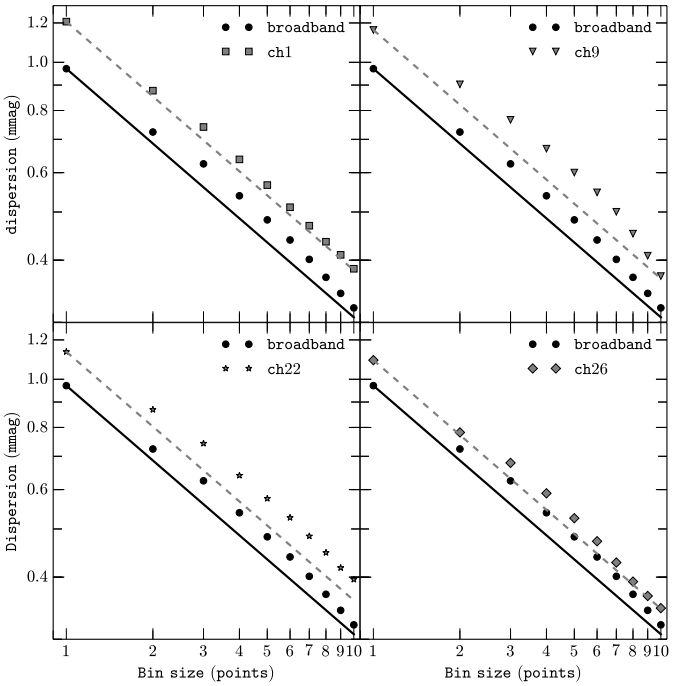

Fig. A.4. Red noise impact, where standard deviation is calculated as a function of bin size, shown for the broadband and 4 spectrophotometric channels (separate panels) for sliding bins. Solid and dashed lines represent the $\sigma/\sqrt{n}$ relation, as expected from uncorrelated (white) noise. Deviation from this model, apparent as a straight line on the log−log plots, is evidence of minimal correlated (red) noise in our data. Using wavelets to model the red noise in all the channels ensured that the impact of this correlated noise is accounted for.

Table A.1. All the determined planetary transit parameters for the modelling process of the spectrophotmetric channels for the transit of WASP-19b.

Channel[a] (nm)	$R_p/R_\star$	Linear LD coefficient γ_1	Quadratic LD coefficient γ_2
560 ± 10	$0.1424^{+0.0015}_{-0.0015}$	$0.424^{+0.065}_{-0.069}$	$0.228^{+0.052}_{-0.053}$
570 ± 10	$0.1425^{+0.0010}_{-0.0011}$	$0.440^{+0.060}_{-0.062}$	$0.225^{+0.053}_{-0.053}$
581 ± 11	$0.1429^{+0.0012}_{-0.0013}$	$0.421^{+0.063}_{-0.067}$	$0.230^{+0.050}_{-0.052}$
590 ± 10	$0.1432^{+0.0015}_{-0.0016}$	$0.406^{+0.066}_{-0.072}$	$0.227^{+0.052}_{-0.053}$
601 ± 9	$0.1419^{+0.0018}_{-0.0020}$	$0.409^{+0.073}_{-0.083}$	$0.221^{+0.054}_{-0.051}$
610 ± 10	$0.1431^{+0.0017}_{-0.0020}$	$0.415^{+0.072}_{-0.082}$	$0.221^{+0.053}_{-0.050}$
620 ± 10	$0.1429^{+0.0015}_{-0.0016}$	$0.420^{+0.065}_{-0.072}$	$0.221^{+0.054}_{-0.052}$
630 ± 10	$0.1407^{+0.0010}_{-0.0011}$	$0.420^{+0.059}_{-0.063}$	$0.222^{+0.052}_{-0.052}$
640.5 ± 10.5	$0.1427^{+0.0018}_{-0.0018}$	$0.365^{+0.074}_{-0.087}$	$0.225^{+0.052}_{-0.051}$
650 ± 10	$0.1434^{+0.0012}_{-0.0013}$	$0.366^{+0.064}_{-0.071}$	$0.225^{+0.053}_{-0.052}$
660.5 ± 9.5	$0.1419^{+0.0010}_{-0.0011}$	$0.384^{+0.060}_{-0.064}$	$0.222^{+0.053}_{-0.052}$
670 ± 10	$0.1407^{+0.0013}_{-0.0013}$	$0.385^{+0.065}_{-0.070}$	$0.223^{+0.054}_{-0.052}$
681.25 ± 11.2	$0.1412^{+0.0015}_{-0.0015}$	$0.385^{+0.067}_{-0.074}$	$0.223^{+0.055}_{-0.051}$
690 ± 10	$0.1396^{+0.0016}_{-0.0016}$	$0.387^{+0.069}_{-0.074}$	$0.225^{+0.053}_{-0.053}$
701.25 ± 8.75	$0.1388^{+0.0011}_{-0.0012}$	$0.401^{+0.060}_{-0.066}$	$0.222^{+0.051}_{-0.051}$
711.25 ± 11.25	$0.1417^{+0.0011}_{-0.0011}$	$0.387^{+0.061}_{-0.065}$	$0.221^{+0.054}_{-0.051}$
720 ± 10	$0.1422^{+0.0012}_{-0.0011}$	$0.379^{+0.062}_{-0.065}$	$0.225^{+0.052}_{-0.054}$
731.25 ± 8.75	$0.14002^{+0.00095}_{-0.0009}$	$0.405^{+0.059}_{-0.061}$	$0.229^{+0.052}_{-0.053}$
740 ± 10	$0.1400^{+0.0009}_{-0.0009}$	$0.414^{+0.058}_{-0.059}$	$0.227^{+0.053}_{-0.052}$
748 ± 8	$0.1405^{+0.0012}_{-0.0012}$	$0.364^{+0.063}_{-0.069}$	$0.222^{+0.051}_{-0.051}$
760 ± 10	$0.1394^{+0.0014}_{-0.0014}$	$0.351^{+0.068}_{-0.075}$	$0.227^{+0.051}_{-0.053}$
768 ± 12	$0.1398^{+0.0015}_{-0.0016}$	$0.350^{+0.071}_{-0.082}$	$0.224^{+0.052}_{-0.052}$
780 ± 10	$0.1409^{+0.0011}_{-0.0011}$	$0.363^{+0.060}_{-0.066}$	$0.223^{+0.051}_{-0.051}$
790 ± 10	$0.1421^{+0.0009}_{-0.0010}$	$0.368^{+0.057}_{-0.061}$	$0.224^{+0.052}_{-0.052}$
800 ± 10	$0.1435^{+0.0011}_{-0.0012}$	$0.371^{+0.060}_{-0.065}$	$0.225^{+0.051}_{-0.054}$
810 ± 10	$0.1460^{+0.0010}_{-0.0010}$	$0.368^{+0.059}_{-0.062}$	$0.229^{+0.052}_{-0.053}$
820 ± 10	$0.1433^{+0.0008}_{-0.0008}$	$0.371^{+0.056}_{-0.058}$	$0.227^{+0.052}_{-0.053}$

Notes. All other non-wavelength-dependent parameters are fixed to the broadband light curve model solution, values for which are given in Table 1. [a] The central wavelength and the width of some channels had to be adjusted slightly to avoid having integration limits that intersect with any telluric lines. Such an event could cause artificial trends in the light curve, due to uncertainties in the wavelength calibration.

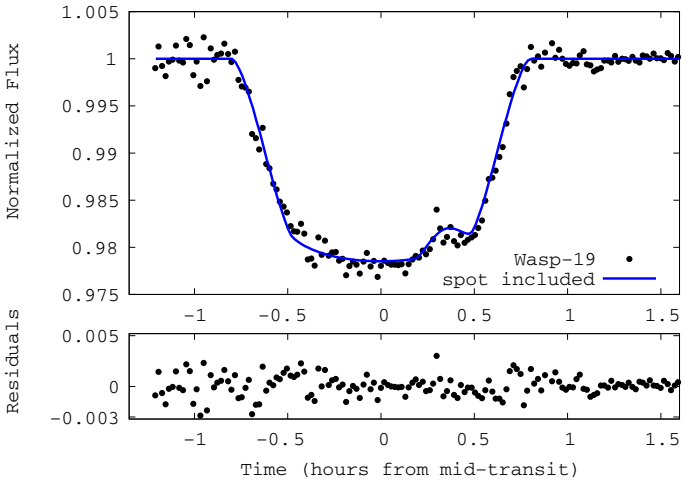

Fig. A.5. Broadband (white) light curve modelled with the GEMC+PRISM code for the purpose of stellar spot characterization, values for which are shown in Table A.2.

Table A.2. Planetary radius and the spot properties derived from modelling the broadband light curve of WASP-19b transit, where the occultation of a stellar spot is also included.

Parameter	Value
Scaled planetary radius, $R_p/R_\star$	0.1395 ± 0.0021
Longitude of the spot centre (degrees)	25.78 ± 0.52
Latitude of the spot centre (degrees)	78.33 ± 1.03
Angular size of the spot (degrees)	20.6 ± 0.4
Spot contrast	0.296 ± 0.006

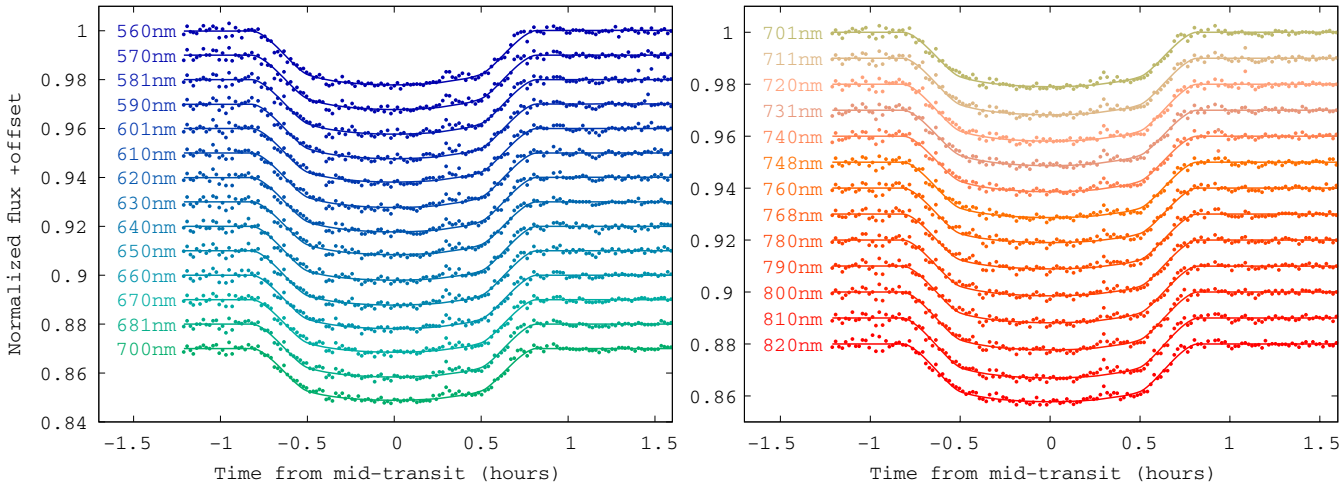

Fig. A.6. Band-integrated spectrophotometric light curves for the transit of WASP-19b. The central wavelength for each channel is indicated on the left-hand side of each plot, where the integration width is mostly 20 nm. The modelled light curves for each channel are shown as solid lines.

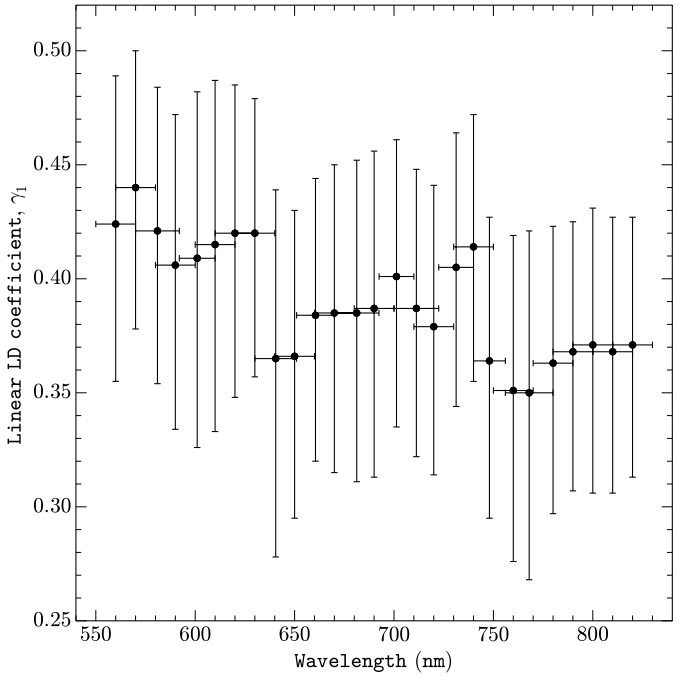

Fig. A.7. Variation in the linear limb darkening coefficient of the quadratic law, with wavelength, for the spectrophotometric channels. The values were allowed to vary between 0 and 1, as dictated by theory, for all the individual channels. The variations and the general trend agree with theoretical values calculated for photometric filters in our chosen range, from Claret & Bloemen (2011).

A&A 596, A47 (2016)
DOI: 10.1051/0004-6361/201629090

Astronomy & Astrophysics

Potassium detection in the clear atmosphere of a hot-Jupiter

FORS2 transmission spectroscopy of WASP-17b⋆

E. Sedaghati[1,2,3], H. M. J. Boffin[1,4], T. Jeřabková[5,6], A. García Muñoz[3], J. L. Grenfell[2,3], A. Smette[1], V. D. Ivanov[1,4], Sz. Csizmadia[2], J. Cabrera[2], P. Kabath[6], M. Rocchetto[7], and H. Rauer[2,3]

[1] European Southern Observatory, Alonso de Córdova 3107, Casilla 19001, Santiago, Chile
e-mail: [esedagha; hboffin]@eso.org]
[2] Institut für Planetenforschung, Deutsches Zentrum für Luft- und Raumfahrt, Rutherfordstr. 2, 12489 Berlin, Germany
[3] Zentrum für Astronomie und Astrophysik, Technische Universität Berlin, Hardenbergstraβe 36, 10623 Berlin, Germany
[4] European Southern Observatory, Karl-Schwarzschild-Str. 2, 85748 Garching bei München, Germany
[5] Astronomical Institute, Charles University in Prague, Vholešovičkách 2, 180 00 Praha 8, Czech Republic
[6] Astronomical Institute ASCR, Fričova 298, 251 65 Ondřejov, Czech Republic
[7] Department of Physics & Astronomy, University College London, Gower Street, London, WC1E 6BT, UK

Received 10 June 2016 / Accepted 14 September 2016

ABSTRACT

We present FORS2 (attached to ESO's Very Large Telescope) observations of the exoplanet WASP-17b during its primary transit, for the purpose of differential spectrophotometry analysis. We use the instrument in its Mask eXchange Unit (MXU) mode to simultaneously obtain low resolution spectra of the planet hosting star, as well as several reference stars in the field of view. The integration of these spectra within broadband and smaller 100 Å bins provides us with "white" and spectrophotometric light curves, from 5700 to 8000 Å. Through modelling the white light curve, we obtain refined bulk and transit parameters of the planet, as well as wavelength-dependent variations of the planetary radius from smaller spectral bins through which the transmission spectrum is obtained. The inference of transit parameters, as well as the noise statistics, is performed using a Gaussian Process model. We achieve a typical precision in the transit depth of a few hundred parts per million from various transit light curves. From the transmission spectra we rule out a flat spectrum at $>3\sigma$ and detect marginal presence of the pressure-broadened sodium wings. Furthermore, we detect the wing of the potassium absorption line in the upper atmosphere of the planet with 3σ confidence, both facts pointing to a relatively shallow temperature gradient in the atmosphere. These conclusions are mostly consistent with previous studies of this exo–atmosphere, although previous potassium measurements have been inconclusive.

Key words. planets and satellites: atmospheres – planets and satellites: individual: WASP-17b – techniques: spectroscopic – instrumentation: spectrographs – stars: individual: WASP-17 – methods: data analysis

1. Introduction

In the short number of years in which extrasolar planetary systems have been detected and studied, great progress has been made in understanding these alien worlds and characterising their intrinsic properties. Methods such as radial velocity and transit monitoring, have facilitated the measurement of bulk densities, as well as some initial approximations of the structure and atmospheric properties of extrasolar planets. We are concerned with the latter here, whereby spectroscopic observations of exoplanetary primary transits lead to setting constraints on the chemical composition and physical processes within exo-atmospheres.

Through transmission spectroscopy, we analyse the wavelength-dependent variations of the exoplanetary radius. These minute variations are caused by the presence of an optically thick atmosphere at specific wavelengths, dictated by the absorption and scattering characteristics of the gas and aerosols that are present near the planet's terminator. These wavelength-dependent opacity variations are scanned across the spectrum and used to probe chemical compositions of the planets' atmospheres (Seager & Sasselov 2000; Brown 2001). The ideal candidates for such studies are those planets with extended atmospheres, i.e. with large atmospheric scale heights, such as the so-called hot Jupiters (Seager & Sasselov 1998). The search for signatures of exo-atmospheres began as early as the time when predictions were being made. For instance Rauer et al. (2000) and Harris et al. (2000), among others, looked for spectral signatures that were due to absorption by extended atmospheres surrounding 51 Peg b and τ Boötis Ab.

Traditionally, transmission spectroscopy has been dominated by space-based facilities, because of their obvious advantage of not being affected by telluric extinction (Charbonneau et al. 2002; Ehrenreich et al. 2007; Pont et al. 2008; Gibson et al. 2012a; Deming et al. 2013; Knutson et al. 2014; Swain et al. 2014). However, large ground-based telescopes, with instruments meeting the requirements of transmission spectroscopy science goals such as the VLT/FORS (Appenzeller et al. 1998), Gemini/GMOS (Hook et al. 2004) or *Magellan*/IMACS (Bigelow et al. 1998) have been the most effective and have also been able to contribute to such studies.

⋆ The data of the light curves are only available at the CDS via anonymous ftp to cdsarc.u-strasbg.fr (130.79.128.5) or via http://cdsarc.u-strasbg.fr/viz-bin/qcat?J/A+A/596/A47

Gibson et al. (2013a,b), among others have shown the capabilities of GMOS to produce transmission spectra for a number of transiting hot Jupiters. With its Multi Object Spectroscopy (MOS) and Mask eXchange Unit (MXU) modes, the FOcal Reducer and low dispersion Spectrograph (FORS2) instrument on the Unit Telescope 1 (UT1 – Antu) of ESO's Very Large Telescope (VLT) has also been a key player in producing these type of spectra. Bean et al. (2010, 2011) were able to obtain pioneering results for the GJ1214b transmission spectrum, an exoplanet in the mini Neptune regime, from the visible to near-infrared bands. However, subsequent attempts at transmission spectroscopy analysis with this instrument were mostly unsuccessful owing to systematics present in the data associated with prisms of the Longitudinal Atmospheric Dispersion Corrector (LADC). Therefore, a project was started at ESO Paranal to address these issues (Boffin et al. 2015) by removing the inhomogeniously degrading coating from the prisms of the decommissioned FORS1's LADC, replacing them with their FORS2 counterpart. The improvements were subsequently highlighted through transit observations of WASP-19b, the results of which were presented in Sedaghati et al. (2015).

An essential issue, which plagues all the aforementioned instruments, has been the role of instrumental systematics and their manifestation in the final transit light curves. As transmission spectroscopy heavily relies on the extremely precise measurement of the transit depth (a few hundreds of ppm[1] for hot Jupiters, down to a few ppm for terrestrial planets) and subsequently the relative planetary radius, the consideration of such factors is crucial when determining the correct scaled radius values, as well as pragmatic estimation of their error budgets. This fact is of paramount importance when a transmission spectrum is used together with atmospheric models in determining the physical properties of an exo-atmosphere. The time-dependent correlated noise[2] that is due to systematics is somewhat reduced through differential spectroscopy techniques employed in this work, however some effects are still expected to remain that originate from poorly understood sources. With this apparent correlated noise component in mind, we utilise a method to model and analyse transit light curves in this paper. The method is based on the Gaussian process (GP) of Gibson et al. (2012b), adapted for modelling time-correlated noise, which has been shown to provide conservative and realistic error estimations (Gibson et al. 2013b) as compared to other parametric methods such as the wavelet decomposition techniques of Carter & Winn (2009). This is an essential point to consider when detecting exoplanetary atmospheric features with transmission spectroscopy, since underestimating the precision of radius measurements can lead to the false or inaccurate characterisation of the atmosphere.

Here we report FORS2 observations of WASP-17b in MXU mode. WASP-17b (Anderson et al. 2010) is an ultra low density Jupiter-sized planet on a ~3.74 d, possibly retrograde orbit around an 11.6V magnitude F6V star. It has a mass and radius of 0.486 ± 0.032 $M_{\rm Jupiter}$ and 1.991 ± 0.081 $R_{\rm Jupiter}$ respectively (Anderson et al. 2011), making it an extremely bloated hot Jupiter at only 0.06 $\rho_{\rm Jupiter}$. This, together with an equilibrium temperature of 1771 ± 35 K (Anderson et al. 2011), mean a relatively large atmospheric scale height, making it an ideal candidate for transmission spectroscopy studies.

This paper is structured as follows. Section 2 highlights our observations and data reduction, in Sect. 3 we present detailed transit data analysis steps, in Sect. 4 we show the results of the analysis and discuss the atmospheric characteristics of WASP-17b, in Sect. 5 we briefly discuss our atmospheric results for this exoplanet, and finally in Sect. 6. a brief summary of our conclusions is presented.

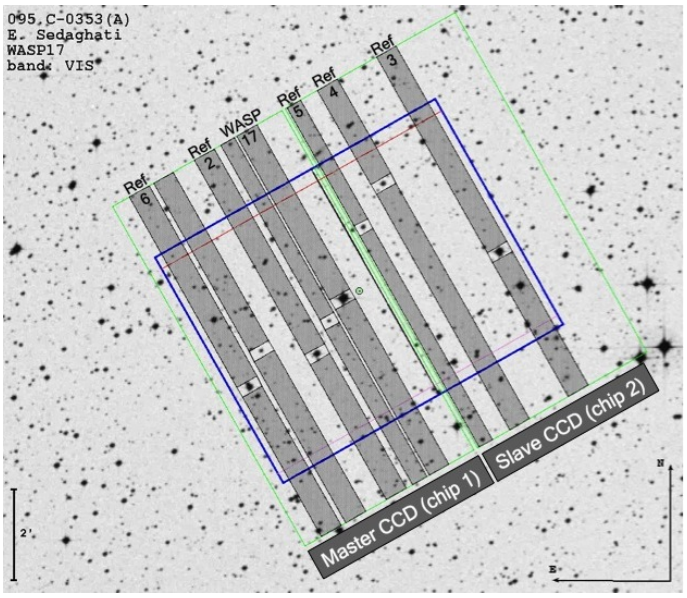

Fig. 1. 10′ × 10′ plot encompassing the FoV of FORS2 (green box) and the area covered by the 2 (2k × 4k) MIT chip mosaic (in blue). The exact design and location of the MXU slits, with the relevant target designations are also shown. The grey regions are the sections of the CCD used for recording the individual stellar spectra.

2. FORS2 observations

A single transit of WASP-17b was observed using the 8.2 m UT1 of the VLT with the FORS2 instrument on the 18 June 2015, with the data taken as part of the programme 095.C-0353(A) (PI: Sedaghati). FORS2 has a 6.8′ × 6.8′ field of view, including a detector system consisting of a mosaic of two 2k × 4k, red optimised, MIT CCDs, utilised for the observations, all of which are visible in Fig. 1. We used FORS2 in the MXU[3] mode to observe the target and a number of reference stars simultaneously for ~8.1 h, covering the 4.38 h of complete transit plus 2.3 h prior to ingress and 1.4 h post egress. Observational conditions were clear for parts of the night, with some sporadic cirrus affecting the observations in transit. The LADC was left in park position during the observing sequence, with the two prisms fixed at their minimal separation distance of 30 mm. At the start of the observations (23:20 UT), the field was at airmass of 1.48, moving through the zenith at 00:23 UT and finally settling to 2.31 for the last exposure at 07:45 UT.

The observations were performed with the 600RI grism plus the GG435 order sorter filter, covering the wavelength range[4] of ~5500 to 8300 Å. The exposure times were 35s throughout the night and the data were binned (2 × 2) yielding a scale of 0.25″ per pixel. We used the non-standard 200kHz readout mode, enabling us to spend more time on target for a fixed cadence (~70 s), owing to the reduced readout time and lower gain

[1] Parts per million.
[2] Sometimes also referred to as "red" or systematic noise.
[3] This means that a custom-designed mask is used instead of the movable arms (MOS).
[4] Note that the exact wavelength coverage for the various stars in the slits varies slightly, depending on their positions on the CCD.

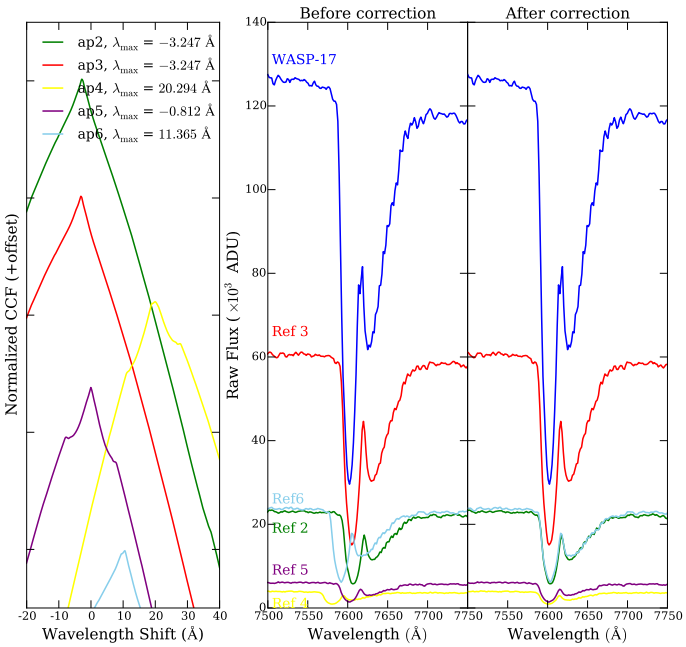

Fig. 2. *Left*: cross-correlation functions, calculated for the wavelength solutions of all reference stars, with respect to the target. The maximising wavelength at each instance, presented in the figure, is then added to each wavelength solution for the correction of the spectra. *Right*: a zoom into the telluric O_2 absorption region of the spectra, before and after the wavelength correction procedure.

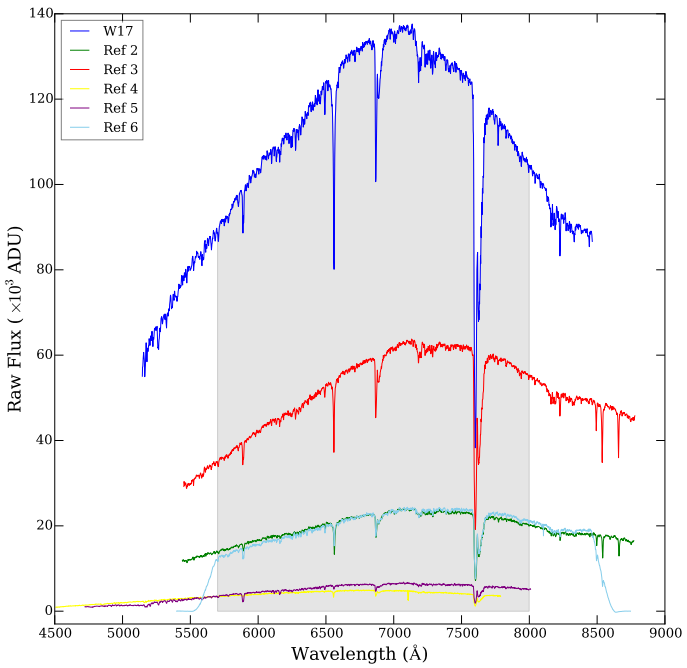

Fig. 3. Wavelength-corrected raw spectra of the target and reference stars, where the numbers are consistent with those in Fig. 1. The grey shaded region represents the integration limits for the broadband light curve production.

of this mode. This procedure resulted in 477 exposures, with some time lost to resetting the field rotator, which we ensured was performed pre-ingress. We created a customised mask with 15″ wide slits to minimise slit losses. The slits were mostly 30″ long, with the exception of two to avoid overlapping dispersion profiles. The mask set up on the sky is shown in Fig. 1. A copy of the mask was created for the purpose of wavelength calibration, with narrow 1″ slits centred on the science slits. Bias, flatfield and arc images were taken, as part of the routine daytime calibration sequences, before and after the observations. Details of an optimised observational strategy with FORS2 have been presented by Boffin et al. (2016).

3. Data reduction and analysis

We wrote a `PyRAF`[5] pipeline for the reduction purposes of the data, optimising it to the specific science goals of this dataset. The steps in the pipeline included the overscan and bias shape subtraction, spectral flat-fielding and wavelength calibration. Subsequently, wavelength-calibrated spectra were extracted for the target and five of the seven reference stars, while simultaneously subtracting the sky background and removing any cosmic ray contamination. We also needed to finely tune the dispersion solution found for the reference stars owing to the imperfect centering of stars on the slits. This was done by cross correlating the spectrum of each reference star with that of WASP-17, shown in Fig. 2, to find a small shift between each pair. The maximal solution was then added to the wavelength stamp of each reference star's dispersion relation. This is a rather important point to consider, since differences in wavelength solutions of various stars could cause artificial features in the spectrophotometric light curves. An example set of these extracted spectra is shown in Fig. 3. A careful analysis of the choice of reference star and its impact on the final light curve is presented in the following section.

3.1. Reference star analysis

We observed a total of eight targets through the custom designed mask, with wide slits placed on those targets. Of the seven reference stars, five were deemed bright enough for further analysis. We searched through a variety of catalogues for estimation of the spectral type of these stars, the results for which are given in Table 1. Furthermore, we also searched through a number of catalogs for variability in our reference stars. From the Catalina survey (Drake et al. 2009), the star in slit 3 shows periodicity at ∼4.4 days at an amplitude of ∼0.1 mag. However, this result is rather tentative since the object is brighter than the 13 $V_{\rm mag}$ saturation limit given by the survey. Additionally, the duration of our observations is considerably shorter than the variability period and therefore any possible intrinsic variation should be insignificant for our purposes.

We first integrate the individual spectra for the largest possible common wavelength domain of all six targets to produce the raw broadband light curves shown in Fig. 4a, normalised to the mean flux and shifted for clarity. We then produce differential light curves by simply dividing the normalised WASP-17 light curve by all the individual reference stars (Fig. 4b), as well as all possible multiple-star combinations. The final comparison star is created through the combination of all reference stars, excluding reference star 4, since its inclusion results in a transit light curve with larger systematics, as well as reducing the possible wavelength domain available for integration of spectra. We also experimented with a composite comparison star that was obtained using a weighted mean of all the individual reference stars using

[5] This is a product of the Space Telescope Science Institute (STScI), for running `IRAF` tasks based on the `Python` scripting language.

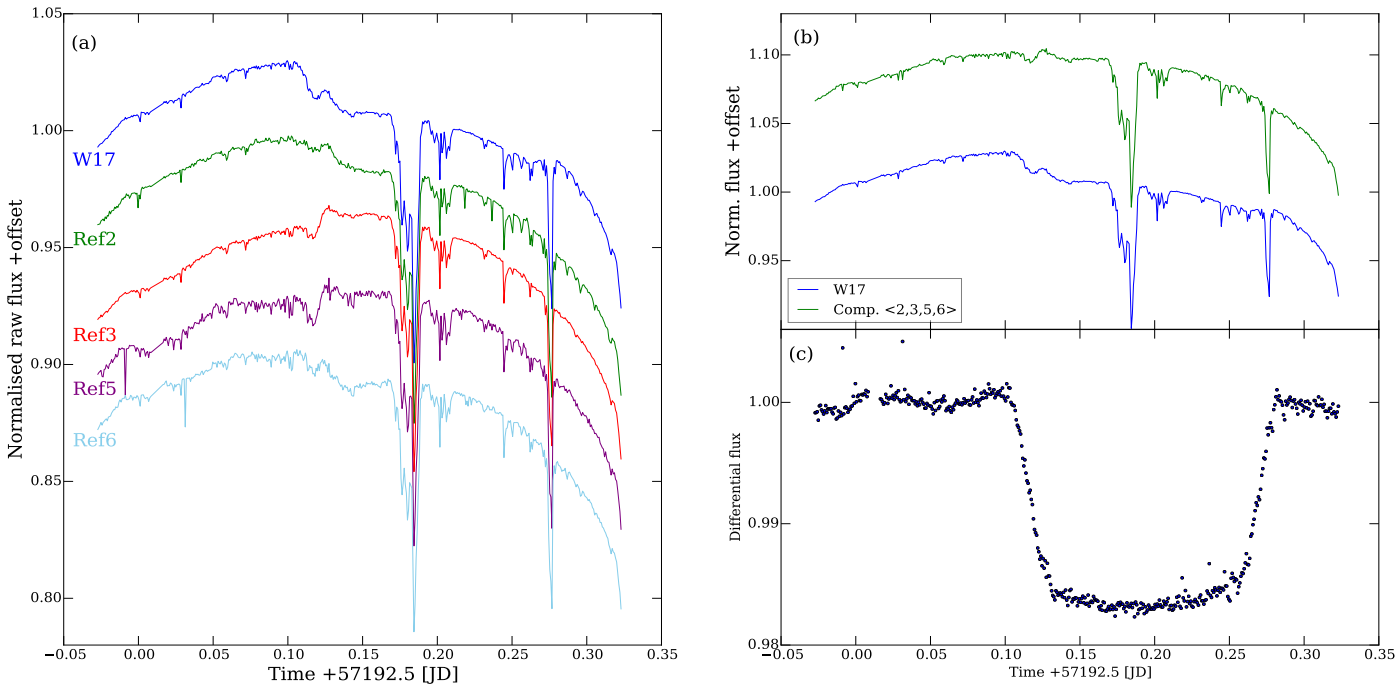

Fig. 4. **a)** Raw time-series light curves of the six stars observed and analysed with the custom designed mask, shown in Fig. 1. **b)** Raw light curves for WASP-17 and the composite comparison star made from the combination of all reference stars, excluding reference 4. **c)** Normalised transit light curve for WASP-17b obtained through division of the two plots above and normalised to out-of-transit flux mean. Light curves in panels **a)** and **b)** have been shifted for clarity.

Table 1. Spectral characterisation of the stars observed.

Star	UCAC4 ID[a]	R_{mag}[b]	$J-K$[c]	Spectral type
W17	310-085339	11.31	0.29 ± 0.06	F5.5−G8.0
Ref 2	310-085352	13.26	0.29 ± 0.05	F7.5−G8.0
Ref 3	310-085281	12.26	0.37 ± 0.06	G4.0−K1.0
Ref 4	310-085328	14.9	0.42 ± 0.07	G9.0−K3.0
Ref 5	310-085333	14.82	0.66 ± 0.06	K5.0−K7.0
Ref 6	310-085382	12.7	0.42 ± 0.04	G9.0−K2.0

Notes. [(a)] The stellar catalogue IDs are given using references from The fourth US naval observatory CCD astrograph catalog (UCAC4; Zacharias et al. 2013). [(b)] R magnitudes are obtained from the UCAC2 catalogue (Zacharias et al. 2004). [(c)] J and K magnitude are obtained from the UCAC3 catalogue (Zacharias et al. 2010). These magnitude differences are converted to spectral type by using estimates from Table 2 of Ducati et al. (2001), assuming all the stars are main sequence.

the signal to noise ratio (S/N) of individual transit light curves as the weights. However, this did not have any impact on the final transit light curve. Hence, we create the final comparison using the arithmetic mean of the chosen reference stars (2, 3, 5, and 6).

3.2. Spectral statistical analysis

To obtain the wavelength dependency of planetary radius, we need to produce spectrophotometric light curves. This is done by integrating the obtained spectra within arbitrarily positioned filters of widths that are based on the quality of the light curves produced. Typically, transmission spectra produced with FORS2 have resolutions of 200 Å (Bean et al. 2010; Sedaghati et al. 2015), with the exception of a few studies (e.g. Bean et al. 2011; Lendl et al. 2016) that produced spectra with 100 Å bands. The

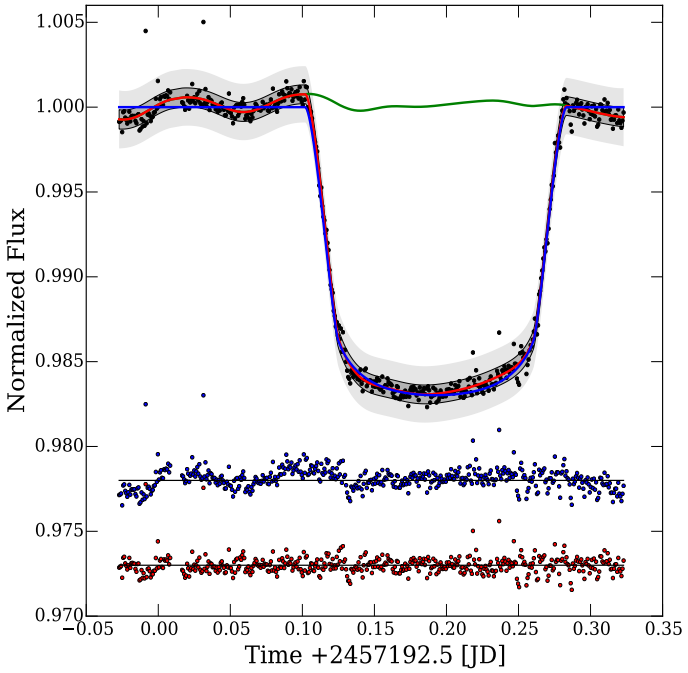

Fig. 5. Broadband (white) light curve for the transit of WASP-17b, fitted with a GP model described in Sect. 3.3. The best fitting transit light curve is shown in blue with the GP mean model given as solid red line. The residuals of both models are shown at the bottom, where they are shifted for clarity and their colours correspond to the models that they represent. The dark and light grey regions represent the 1 and 3σ predictions of the GP model, respectively. The green line shows the systematics model without the transit function.

precisions of differential and detrended light curves are calculated for a range of bandwidths, measured across the entire

wavelength domain. This is done by calculating the dispersion of the normalised $\boldsymbol{f}_{\rm oot}$ for light curves produced at a central wavelength $\lambda_{\rm c}$ and bandwidths[6] $\delta\lambda$ in the range of 20−300 Å. This process is performed for the entire wavelength range, for $\lambda_{\rm c}$ values spaced at 50 Å. Subsequently, to interpolate the results in between these steps, we apply a Gaussian convolution filter for a smoothed continuous dispersion map[7]. This is essentially similar to the mean filter, but having a different kernel, an application for which is given by Buades et al. (2005) for image denoising. The results from such statistical analysis of light curve precision across the entire spectrum is shown in Fig. 6.

It is quite evident, that in certain regions, a rather large bandwidth is required to obtain a precise light curve. This is due to the presence of telluric absorption features that reduce the signal-to-noise ratio in the produced light curve significantly. Based on this analysis and taking into account the contours of Fig. 6, we choose 100 Å as the bandwidth to be used for the production of the spectrophotometric light curves. This value is chosen to provide us with high-resolution transmission spectral points that are simultaneously precise enough for comparison with atmospheric models.

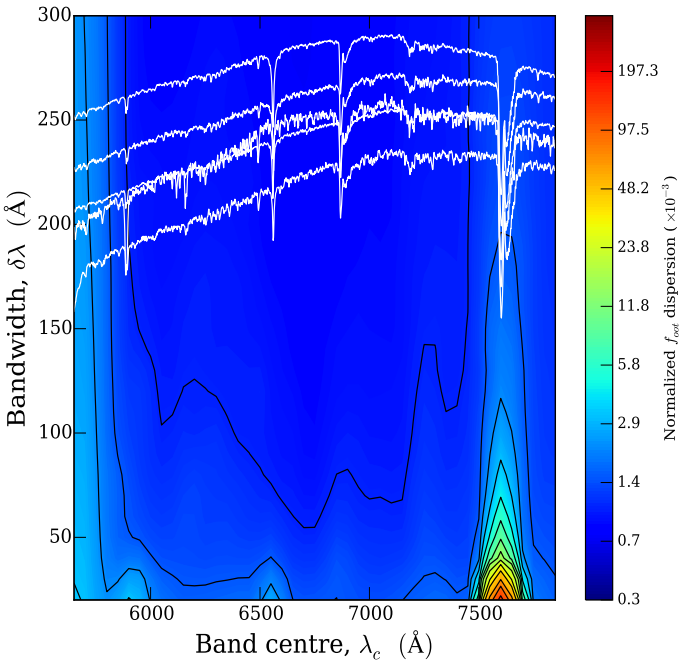

Fig. 6. Analysis of light curve precision across the entire wavelength domain, with the spectra of WASP-17 and all reference stars superimposed at the top. Clearly, the regions containing telluric absorption features, require larger bandwidths to produce reasonable spectrophotometric light curves, for instance the O_2(A) absorption region at approximately 7600 Å.

3.3. Transit light curve fitting

Once the final normalised broadband and spectrophotometric light curves are produced (see Figs. 4, 5 and 7), we first infer all the transit parameters, as well as the noise characteristics of the broadband light curve. Subsequently, the same procedure is repeated for the spectrophotometric light curves with only the wavelength-dependent transit parameters and noise components inferred, while others are fixed to the white light curve solution, since it represents the light curve with the highest S/N, and hence the most accurate solutions.

We fit all the light curves using a Gaussian process (GP) model, whose application to modelling systematics in time-series data was introduced by Gibson et al. (2012b). To determine the GP model, we made use of their `GeePea` module, as well as the `Infer` module to implement Bayesian inference routines[8].

A GP is essentially a non-parametric approach to regression analysis that does not necessarily make any assumptions about the data, nor does it impose a deterministic model on the data[9]. It is simply a collection of random variables, any finite subset of which has a joint Gaussian distribution (Gibson et al. 2012b). In this framework, each light curve is modelled as a GP of the analytical transit function, following the formalism of Mandel & Agol (2002), and the covariance matrix representing the noise characteristics of the data:

$$f(t, \boldsymbol{\phi}, \boldsymbol{\theta}) \sim \mathcal{GP}\left[T(t, \boldsymbol{\phi}), \boldsymbol{\Sigma}(t, \boldsymbol{\theta})\right] \quad (1)$$

with f being the flux measurements and t the time of each observation. Here T is the analytical transit model that is a function of t and the transit parameters $\boldsymbol{\phi}$. In addition, $\boldsymbol{\Sigma}$ represents the covariance matrix, whose kernel has time as its only input, with parameters $\boldsymbol{\theta}$ also known as the hyperparameters. We also extracted as many physical variants, also known as the optical state parameters, as available, to search for any correlations between them and the residuals of a transit model fit to the data. However, owing to the lack of any correlation none of this information was used in describing the GP model. Some of the extracted data are shown in Fig. 8.

The covariance matrix in Eq. (1) is given by

$$\Sigma_{ij} = k(t_i, t_j, \boldsymbol{\theta}) + \delta_{ij}\sigma_w^2 = \zeta^2 \exp\left(-\frac{(t_i - t_j)^2}{2l^2}\right) + \delta_{ij}\sigma_w^2 \quad (2)$$

where ζ is the output scale describing the GP's variance, l is the length scale that determines how smooth the function is, δ is the Kronecker delta ensuring the addition of white noise to the diagonal of the covariance matrix and σ_w is that Poisson noise. For the covariance function or the kernel, $k(t_i, t_j, \boldsymbol{\theta})$, we have chosen the squared exponential (SE) kernel (e.g. Wilson & Adams 2013) owing to the smoothness of the function over the parameters. We emphasise that although selecting a kernel is analogous to choosing a predetermined parametric model, it allows for a much more flexible treatment of noise than any parametric form, as well as being intrinsically Bayesian.

We also define priors for all the hyperparameters of the noise model, ensuring that their values are positive, and together with the mean transit function parameters, optimise them with a Nelder-Mead simplex algorithm (Glaudell et al. 1965). To obtain the posterior joint probability distributions, these are multiplied by the marginal likelihoods of producing the joint posterior probability distribution. In other words,

$$\ln P(\boldsymbol{\phi}, \boldsymbol{\theta}|\boldsymbol{x}) = \ln P(\boldsymbol{\phi}, \boldsymbol{\theta}) + \ln P(\boldsymbol{x}|\boldsymbol{\phi}, \boldsymbol{\theta}). \quad (3)$$

[6] We start at 20 Å minimum bandwidth, since below this integration size the algorithm that detects the transit locations automatically, runs into difficulty, due to the low S/N in the light curve. Furthermore, for practical purposes, the calculations are performed with steps in bandwidth of 10 Å to reduce computation time.

[7] Namely, this is done to obtain a continuous distribution of dispersion across the $\lambda_{\rm c}$ vs. $\delta\lambda$ parameter space, with a two-dimensional Gaussian filter of $\sigma = 1$ for the kernel in both dimensions.

[8] The modules used are available at the following repository: `https://github.com/nealegibson`

[9] This fact is essential in capturing the true impact of instrumental systematics in inferring the transit parameters.

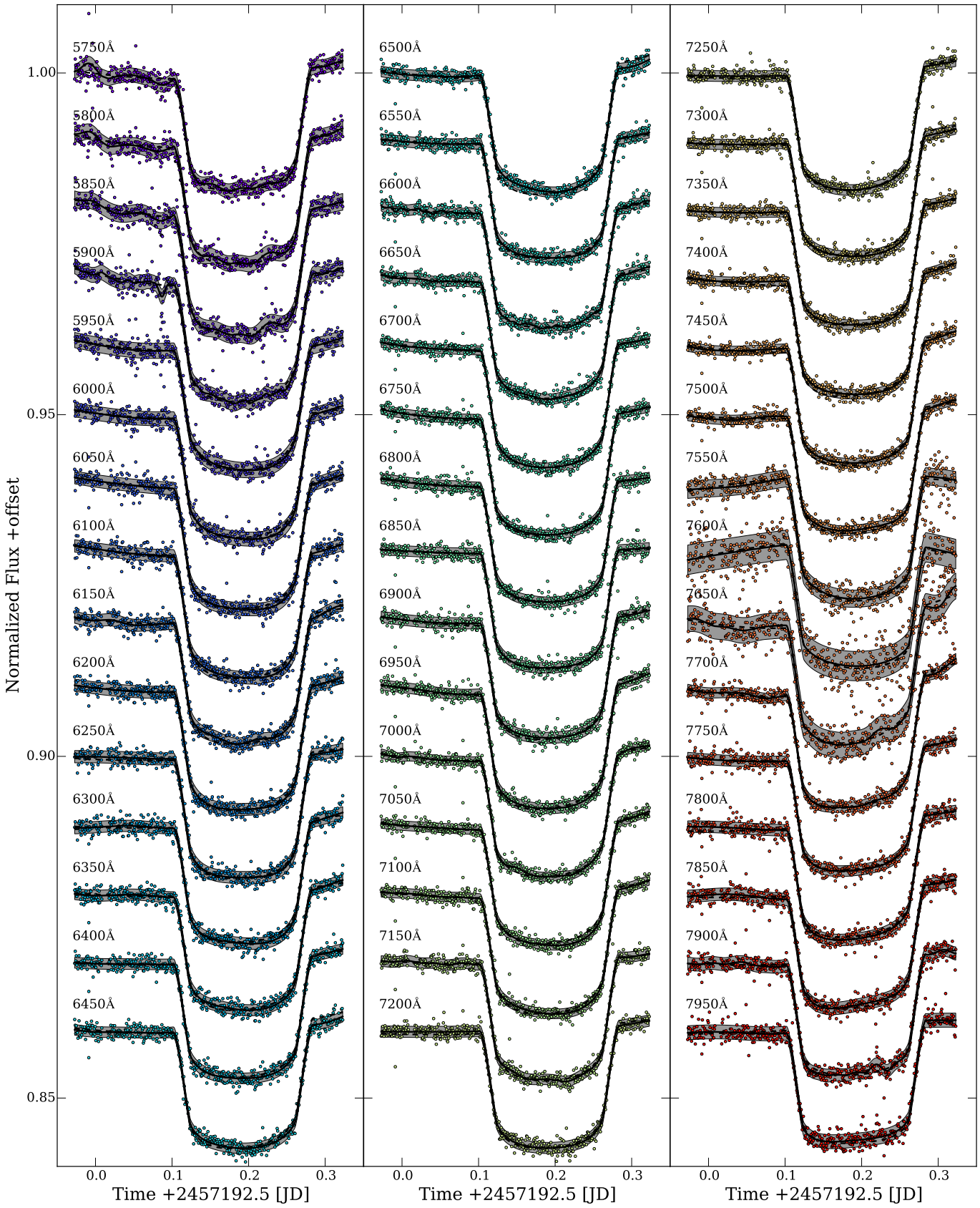

Fig. 7. Spectrophotometric light curves for the transit of WASP-17b, produced with bins of 100 Å width after the common mode correction (CMC), shifted for clarity. The solid black line for each plot is the best-fit transit systematics model and the grey areas are the 1σ representations of those solutions. The dashed lines represent transit models derived with the optimised parameters of each light curve. The central wavelength of each channel used to produce the light curve is given next to each plot. The light curves excluded from transmission spectroscopy have been included here for completeness.

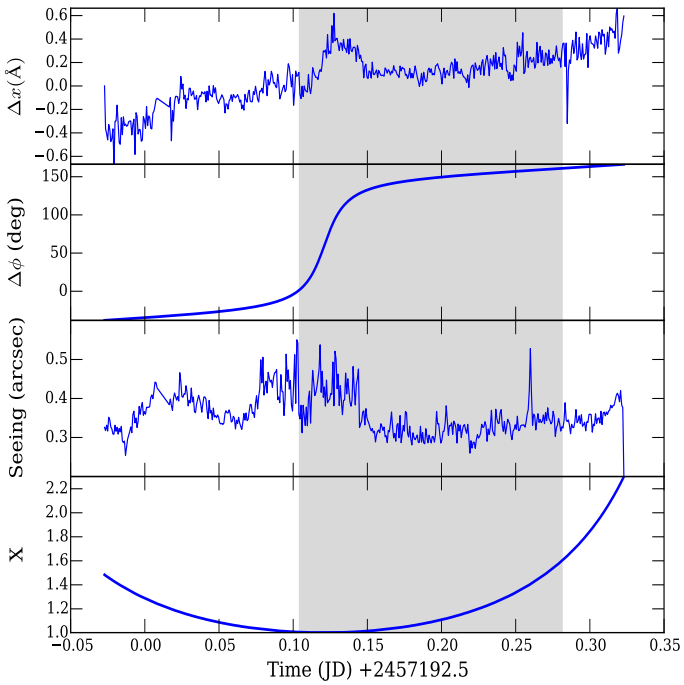

Fig. 8. Some of the optical state parameters extracted from the data. *From the top*, Δx is the spectral drift relative to the first exposure, calculated using cross-correlation of the raw spectra, $\Delta\phi$ is the instrument rotation angle, seeing is measured as the product of full width half maximum from the Gaussian profile along the spatial axis and the pixel scale in arcsec and X is the airmass. These parameters are extracted to check for any possible correlation with the systematics in the light curve. The grey shaded region shows the duration of transit.

We then use Monte Carlo Markov Chains (MCMC) to explore this posterior distribution and produce the final marginal probabilities for each of the parameters (for both the transit and the noise models). Essentially, we just assume uniform, uninformative priors for all the parameters with few restrictions, i.e. the impact parameter[10] and GP hyperparameters are positive and the sum of the two limb darkening coefficients of the quadratic law are less than unity to ensure positive brightness across the entire stellar surface. For all the light curves we ran four MCMC chains with 100 walkers of 100 000 iterations. Once the chains are computed, we extract the marginalised posteriors for the free parameters to check convergence and any correlations. Examples of these correlation plots and posterior probability distributions are shown in Fig. 9 for the broadband and one spectrophotometric light curve.

4. Results

4.1. Broadband light curve models

We first model the broadband or white light curve, which is the integral of fluxes for the largest possible common wavelength domain of the target and the comparison, namely from 5700 to 8000 Å, as shown in Fig. 5 and modelled with the quadratic limb darkening law (Kopal 1950). To ensure that the choice of limb-darkening law does not have a significant impact upon the inference of transit parameters, we initially model the white light curve using both the quadratic $I_{\rm quad}(\mu)$ and the non-linear law $I_{\rm nl}(\mu)$ (Claret 2000), also known as the four-parameter law, given by

$$\frac{I_{\rm quad}(\mu)}{I(1)} = 1 - \sum_{i=1}^{2} c_i (1-\mu)^i \quad (4)$$

$$\frac{I_{\rm nl}(\mu)}{I(1)} = 1 - \sum_{i=1}^{4} l_i \left(1 - \mu^{i/2}\right) \quad (5)$$

respectively, where μ (=cos θ) is the cosine of the angle between the observer and the normal to the stellar surface. These formulations have as particular cases, the linear law (Schwarzschild 1906, $c_2 = 0$ in the quadratic law) and the three-parameter law (Sing et al. 2009, $l_1 = 0$ in the non-linear law). To initially examine the impact of the chosen limb-darkening law on the inferred planetary radius, we model the broadband light curve with the aforementioned laws, taking a variety of approaches for coefficient determination. Beyond the quadratic law, no improvement is made to the fit when using a more complex law and there are no significant changes in the inferred transit parameters. Furthermore, high levels of correlation exist between the fitted parameters of those laws. This together with the added unjustified complexity means that the quadratic law is chosen to model the radial intensity variations across the stellar disk.

In our modelling process, both coefficients of the quadratic limb-darkening law are fitted for in the white and spectral channels, since the stellar intensity profile is expected to be colour-dependent. To determine these coefficients, we impose some informative priors. The first of these restrictions is that the sum of their values is less than unity to ensure a positive value for the stellar surface intensity across the entire disk. Initially, we calculate coefficient values for all channels using the `PyLDTk`[11] package (Parviainen & Aigrain 2015), which uses the stellar atmosphere tables of Husser et al. (2013) generated with the `PHOENIX` code. We initially use these values to construct Gaussian priors for the inference of the coefficient values from the MCMC analysis, using the calculated values as the mean and twice the error as the standard deviation. However, this approach is rather restrictive and leads to systematic errors in the final fit. Hence, we use these calculated values to construct a global and less informative prior given by

$$\ln P(c_1, c_2) = \begin{cases} -\infty & \text{if } (c_1 + c_2 > 1), \\ -\infty & \text{if } (c_1 < 0 \vee c_1 > 1), \\ -\infty & \text{if } (c_2 < -1 \vee c_2 > 1), \\ 0 & \text{otherwise.} \end{cases}$$

The optimised parameters and the noise characteristics from fitting the broadband light curve, with the above-mentioned setup, are given in Table 2. Through the combination of multiple reference stars, the colour-dependent slope in the white light curve dispears, and hence we do not include a polynomial fit of the $f_{\rm oot}$ points. This, however, is not the case for the narrowband channels. These inferred planetary transit parameters from the MCMC analysis are consistent with those reported previously (Anderson et al. 2010, 2011; Southworth et al. 2012; Bento et al. 2014).

4.2. Transmission spectrum

Once the system parameters are determined from the analysis of the broadband light curve, we model the spectrophotometric light curves in the same way, but with the non-wavelength

[10] This is due to the degeneracy with the system scale.

[11] Available from `https://github.com/hpparvi/ldtk`

Table 2. Parameters from the MCMC analysis of the broadband light curve, given for the fully marginalised Gaussian process noise model.

Parameter (inferred)	Value
Mid-transit, T_c (JD) +2 400 000	57 192.69266 ± 0.00028
T_c, Heliocentric corr. (HJD)	57 192.69798 ± 0.00028
Period, P (days)	3.735438[a] (fixed)
Scaled semi-major axis, $a/R_\star$	7.025 ± 0.146
Relative planetary radius, $R_p/R_\star$	0.12345 ± 0.00109
Impact parameter, b	0.361 ± 0.069
Linear LD coefficient, c_1	0.167 ± 0.136
Quadratic LD coefficient, c_2	0.356 ± 0.249
f_{oot}	1.0 (fixed)
T_{grad}	0.0 (fixed)
GP max. covariance, ζ (ppm)	545 ± 259
Length scale, l	0.019 ± 0.009
White noise, σ_w (ppm)	545 ± 19
Eccentricity, e	0.0 (fixed)
Argument of periapsis, ω (°)	90.0 (fixed)
Parameter (derived)	**Value**
Semi-major axis, a (AU)	0.0513 ± 0.00290
Inclination, i	$87.06^{\circ}\ ^{+0.61}_{-0.63}$
$M_\star$ ($M_\odot$)	1.306 ± 0.026[a]
$R_\star$ ($R_\odot$)	1.572 ± 0.056[a]
M_p (M_J)	0.486 ± 0.032[a]
R_p (R_J)	1.747 ± 0.078
ρ_p (g cm^{-3})	0.121 ± 0.024 (0.091 ρ_J)
g_p (m s^{-2})	3.948 ± 0.612

Notes. [(a)] Value from Anderson et al. (2011).

dependent parameters fixed to the best solution from the white light curve, which is given in Table 2. Since this light curve represents the time-series flux measurements with the highest S/N, its solutions are the most trust-worthy. In modelling the spectroscopic light curves, we fit for the scaled planetary radius ($R_p/R_\star$), both coefficients of the limb-darkening law, c_1 and c_2, as well as the three quantities that describe the noise statistics of each data set, ζ, l and σ_w, as explained above. In addition to those, in the modelling of spectrophotometric light curves, we also simultaneously fit for three coefficients of a second order polynomial, which approximates long-term trends in the differential flux. Such variations are due to larger colour differences between the target and the comparison in smaller bins as compared to the broadband bin, where such effects are not apparent. This effect is a function of airmass and spectral type described well with a polynomial of second order, which can be seen in some of the light curves in Fig. 7. An example of the correlation plots for the free parameters of one spectral light curve is shown in the upper panel of Fig. 9.

As well as this approach, we also correct the spectrophotometric light curves for a common mode of the systematic noise that is shared across all the spectral channels. This is done by dividing all the spectrophotometric light curves by the residuals of best-fit transit model to the broadband light curve, shown as the blue data points at the bottom of Fig. 5. This residual data is simply obtained by the division of the transit data by the analytical model (blue solid line in the top figure of the same plot). Subsequently, we model these light curves again with the same procedure, where the red noise is modelled as a GP owing to any residual systematic noise after this *common mode correction* (CMC). These light curves together with the transit and GP noise models are shown in Fig. 7.

The variations of relative planetary radii as a function of channel central wavelength, λ_c, are derived from this modelling process, which represents the transmission spectrum of WASP-17b. A set of results from modelling of both data sets (initial and CMC), including relative radii and limb-darkening coefficients, are tabulated in Table 3. The transmission spectrum is shown in Fig. 10 for the two employed procedures.

One possible feature of these spectra is the indication of enhanced absorption in the exoplanetary atmosphere in the range of 7650–7800 Å, which is possibly due to a combination of the telluric O_2(A) lines and the Potassium doublet (7665 Å and 7699 Å) in the exoplanet's atmosphere. This point will be discussed further in Sect. 4.3. To look for possible optical absorbers in the atmosphere of WASP-17b, we also produce narrow band light curves with 50 Å integration bins around Sodium and Potassium absorption regions, which are shown in Fig. 11.

4.3. Atmospheric models

We compare the derived transmission spectra of Fig. 10 to especially adapted theoretical atmospheric spectral models also shown in the same figure. These models are calculated with the assumption of isothermal profile using the equilibrium temperature of WASP-17b, as well as full heat redistribution and zero albedo. The only spectroscopically active gases present in the model atmosphere are H_2O, Na, and K, with volume mixing ratios of 1×10^{-3}, 2.96×10^{-6}, and 2.4×10^{-7}, the latter two being solar values that assume H_2/He bulk abundances and the water mixing ratio being somewhat arbitrary. These mixing ratios are assumed as being independent of altitude. We take the specific gravity to be non-constant and varying with altitude, since this probably would be significant for a puffy and low density planet like WASP-17b. Furthermore, we assume that the aerosol density decays with altitude using a scale height similar to that of the gas. To explore the impact of aerosol density, we have scaled the reference aerosol profile (×1), by factors of 0, 10, 100, and 1000, which are all shown in Fig. 10, superimposed onto the derived transmission spectra. In these cases, the aerosol optical thickness of 1 at 0.8 micron is reached at pressure levels of ~7, 1, 0.15, and 0.03 bars, respectively. This aerosol optical thickness is assumed to follow a Rayleigh-type law with a wavelength dependence of λ^{-4}. This law is valid when the size parameter x ($=2\pi r_{eff}/\lambda$; where r_{eff} is a measure of the particle radius) is quite small and the imaginary part of the refractive index is also small. For instance, silicates, perovskite, and silica have small imaginary parts for their refractive indices. This is a hard-coded assumption of the model, but is anyway consistent with the Rayleigh slope that is seen in numerous exoplanets. WASP-17b has a rather puffy composition, hence one would expect that small particles are easily kept aloft in the atmosphere. Given the very unconstrained nature of the problem, we think that the treatment used here is judicious. Finally, given the fact that the extinction coefficient decays exponentially with altitude, and the pressure levels at which maximal optical thickness is reached (i.e. $\tau = 1$), one reconstructs the aerosol extinction coefficient needed in the models[12]. These theoretical atmospheric models are updated versions from García Muñoz et al. (2012).

[12] Note that the aerosol densities and cross-sections are degenerate since only their product is required in transmission calculations.

Table 3. Results from modelling spectrophotometric light curves produced with 100 Å integration bins, for both data sets.

Band	Spectrophotometric LC set					
Centre	RAW			CMC		
[Å]	$R_p/R_\star$	c_1	c_2	$R_p/R_\star$	c_1	c_2
5750	0.1207 ± 0.0023	0.0866 ± 0.3687	0.5760 ± 0.6236	0.1212 ± 0.0022	0.0921 ± 0.0604	0.5687 ± 0.1396
5800	0.1222 ± 0.0032	0.0902 ± 0.1368	0.5799 ± 0.2794	0.1229 ± 0.0038	0.0953 ± 0.0630	0.5805 ± 0.1485
5850	0.1248 ± 0.0018	0.0880 ± 0.1404	0.6034 ± 0.2849	0.1223 ± 0.0020	0.0833 ± 0.0605	0.5959 ± 0.1419
5900	0.1214 ± 0.0023	0.1415 ± 0.1136	0.5714 ± 0.2347	0.1210 ± 0.0011	0.1436 ± 0.0753	0.5685 ± 0.1666
5950	0.1234 ± 0.0032	0.2407 ± 0.1366	0.4574 ± 0.2537	0.1226 ± 0.0014	0.2300 ± 0.0855	0.4552 ± 0.1636
6000	0.1239 ± 0.0014	0.1706 ± 0.0846	0.4926 ± 0.1748	0.1235 ± 0.0013	0.1679 ± 0.0722	0.4825 ± 0.1373
6050	0.1246 ± 0.0014	0.1195 ± 0.0665	0.5695 ± 0.1387	0.1242 ± 0.0011	0.1173 ± 0.0613	0.5533 ± 0.1213
6100	0.1249 ± 0.0015	0.1511 ± 0.0833	0.4923 ± 0.1803	0.1247 ± 0.0014	0.1529 ± 0.0760	0.4878 ± 0.1544
6150	0.1255 ± 0.0028	0.1618 ± 0.1428	0.5370 ± 0.2924	0.1250 ± 0.0022	0.1539 ± 0.0836	0.5249 ± 0.1644
6200	0.1237 ± 0.0020	0.1195 ± 0.0590	0.6025 ± 0.1184	0.1236 ± 0.0008	0.1018 ± 0.0557	0.5837 ± 0.1114
6250	0.1260 ± 0.0033	0.1030 ± 0.1534	0.6200 ± 0.2926	0.1246 ± 0.0012	0.0736 ± 0.0472	0.5971 ± 0.1029
6300	0.1239 ± 0.0021	0.0944 ± 0.0639	0.6260 ± 0.1266	0.1229 ± 0.0013	0.0784 ± 0.0480	0.6074 ± 0.1017
6350	0.1218 ± 0.0015	0.1252 ± 0.0657	0.5344 ± 0.1347	0.1219 ± 0.0004	0.1314 ± 0.0625	0.5205 ± 0.1243
6400	0.1235 ± 0.0015	0.1463 ± 0.0663	0.4382 ± 0.1358	0.1228 ± 0.0011	0.1424 ± 0.0616	0.4168 ± 0.1272
6450	0.1240 ± 0.0017	0.1813 ± 0.0897	0.3792 ± 0.1746	0.1244 ± 0.0023	0.1767 ± 0.0821	0.3679 ± 0.1587
6500	0.1228 ± 0.0017	0.1932 ± 0.0940	0.3895 ± 0.1896	0.1243 ± 0.0024	0.1874 ± 0.0893	0.3776 ± 0.1579
6600	0.1225 ± 0.0015	0.1168 ± 0.0552	0.4415 ± 0.1206	0.1229 ± 0.0006	0.1067 ± 0.0508	0.4298 ± 0.1094
6650	0.1227 ± 0.0015	0.1600 ± 0.0593	0.4636 ± 0.1274	0.1229 ± 0.0011	0.1589 ± 0.0703	0.4542 ± 0.1478
6700	0.1227 ± 0.0011	0.2447 ± 0.0866	0.3224 ± 0.1793	0.1230 ± 0.0008	0.2325 ± 0.0645	0.3166 ± 0.1363
6750	0.1225 ± 0.0011	0.1929 ± 0.0707	0.3577 ± 0.1430	0.1223 ± 0.0009	0.1913 ± 0.0609	0.3463 ± 0.1212
6800	0.1228 ± 0.0018	0.1136 ± 0.1253	0.4925 ± 0.2640	0.1224 ± 0.0006	0.1083 ± 0.0488	0.4858 ± 0.1047
6850	0.1224 ± 0.0013	0.1323 ± 0.1089	0.4441 ± 0.2315	0.1224 ± 0.0006	0.1284 ± 0.0490	0.4453 ± 0.1030
6900	0.1226 ± 0.0015	0.1553 ± 0.0876	0.4365 ± 0.1818	0.1224 ± 0.0010	0.1530 ± 0.0624	0.4320 ± 0.1255
6950	0.1236 ± 0.0021	0.1792 ± 0.0937	0.4279 ± 0.1759	0.1226 ± 0.0013	0.1730 ± 0.0728	0.4104 ± 0.1383
7000	0.1225 ± 0.0014	0.2107 ± 0.0926	0.3906 ± 0.1845	0.1230 ± 0.0011	0.2049 ± 0.0846	0.3826 ± 0.1751
7050	0.1225 ± 0.0015	0.1615 ± 0.0776	0.5082 ± 0.1579	0.1217 ± 0.0012	0.1498 ± 0.0638	0.4881 ± 0.1244
7100	0.1230 ± 0.0012	0.1782 ± 0.0843	0.4435 ± 0.1782	0.1232 ± 0.0014	0.1830 ± 0.0839	0.4398 ± 0.1704
7150	0.1233 ± 0.0012	0.2003 ± 0.0837	0.3785 ± 0.1791	0.1238 ± 0.0009	0.1963 ± 0.0735	0.3733 ± 0.1527
7200	0.1241 ± 0.0018	0.1881 ± 0.0879	0.3795 ± 0.1697	0.1238 ± 0.0011	0.1774 ± 0.0674	0.3754 ± 0.1308
7250	0.1232 ± 0.0012	0.2840 ± 0.0928	0.1941 ± 0.1906	0.1232 ± 0.0010	0.2777 ± 0.0662	0.1884 ± 0.1334
7300	0.1230 ± 0.0019	0.2174 ± 0.0878	0.3023 ± 0.1639	0.1223 ± 0.0010	0.2045 ± 0.0626	0.2919 ± 0.1247
7350	0.1222 ± 0.0013	0.1704 ± 0.0809	0.4045 ± 0.1555	0.1225 ± 0.0004	0.1567 ± 0.0549	0.3862 ± 0.1014
7400	0.1225 ± 0.0016	0.1314 ± 0.0922	0.4483 ± 0.1680	0.1222 ± 0.0006	0.1132 ± 0.0468	0.4338 ± 0.0899
7450	0.1222 ± 0.0017	0.2164 ± 0.0996	0.3218 ± 0.1787	0.1233 ± 0.0004	0.1995 ± 0.0640	0.3082 ± 0.1105
7500	0.1222 ± 0.0018	0.1780 ± 0.0511	0.3904 ± 0.1049	0.1240 ± 0.0015	0.1652 ± 0.0797	0.3758 ± 0.1461
7700	0.1267 ± 0.0037	0.1024 ± 0.1140	0.4673 ± 0.1980	0.1244 ± 0.0009	0.1015 ± 0.0831	0.4703 ± 0.1635
7750	0.1237 ± 0.0025	0.0691 ± 0.0975	0.5359 ± 0.1698	0.1231 ± 0.0006	0.0680 ± 0.0396	0.5373 ± 0.0822
7800	0.1227 ± 0.0025	0.1053 ± 0.0932	0.4935 ± 0.1570	0.1225 ± 0.0011	0.1004 ± 0.0621	0.4931 ± 0.1110
7850	0.1253 ± 0.0036	0.1225 ± 0.1267	0.4833 ± 0.2386	0.1222 ± 0.0017	0.1229 ± 0.0765	0.4814 ± 0.1331
7900	0.1227 ± 0.0025	0.1632 ± 0.0769	0.3366 ± 0.1724	0.1227 ± 0.0017	0.1591 ± 0.0918	0.3217 ± 0.1978
7950	0.1305 ± 0.0035	0.1006 ± 0.1259	0.3853 ± 0.2108	0.1245 ± 0.0018	0.0832 ± 0.0587	0.3697 ± 0.1072

Notes. The corresponding CMC light curves are given in Figs. 7. The three transit parameters, taken as free during the MCMC analysis, namely the relative planetary radius ($R_p/R_\star$) and the two coefficients of the quadratic limb darkening law (c_1 and c_2) are shown. Other free components for each channel were the 3 coefficients of the polynomial fit, as well as the 3 noise model parameters.

The plotted theoretical models have been shifted vertically to match the visible size of the planet and scaled by ~1.6 scale heights, a value which has been obtained through minimization of χ^2 statistics using least squares with transmission spectrum data points.

We calculate χ^2 and significance statistics using the CMC spectrum of Fig. 10 to establish whether one can discriminate between a clear or cloudy and opaque atmosphere. To do this, the synthetic spectra are compared to a flat spectrum with a one scale-height tolerance. We calculate a reduced χ^2_r value of ~1.19 for a flat spectrum, compared to ~1.07–1.11 for the various atmospheric models. Hence, we rule out a flat spectrum at $>3\sigma$, with the ΔBIC ($\gg$10)[13] value providing further, *very strong* evidence against it. Details of the statistical analysis of the individual models are given in Table 4. From this analysis, we conclude that our transmission spectrum significantly rules out a flat spectrum and suggests an atmosphere clear of large cloud particles for WASP-17b, with the possible presence of smaller

[13] Bayesian Information Criterion (Schwarz 1978).

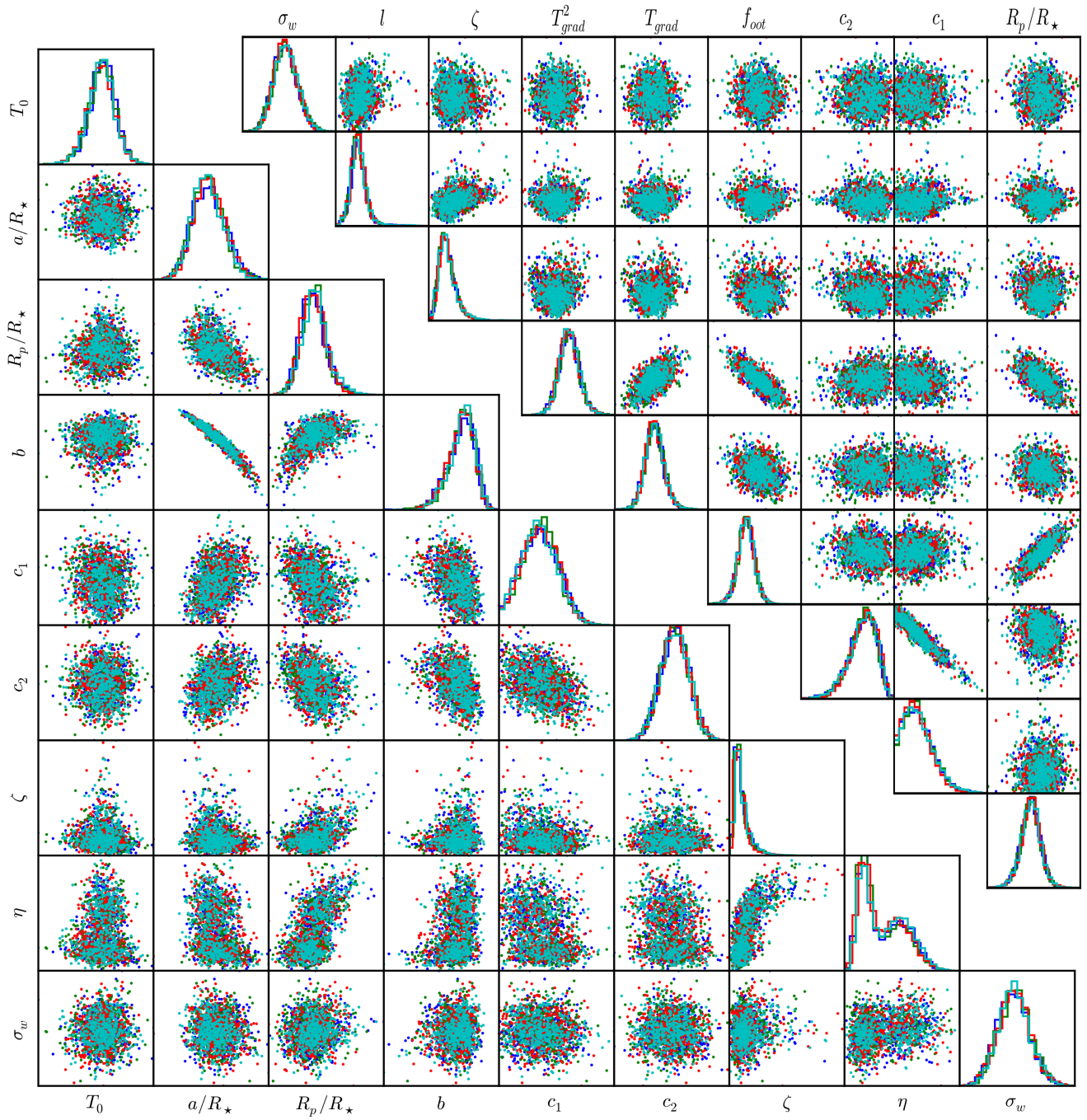

Fig. 9. Parameter correlations for the broadband (*bottom left*) and a spectrophotometric (*top right*) light curve from the MCMC analysis, for the quadratic limb-darkening law. The well-documented degeneracy between the impact parameter, b, and the scaled semi-major axis, $a/R_\star$ is also quite evident. The derived posterior probability distribution for each parameter is also given at the end of each column. The four different colours represent samples from the independent MCMC chains.

scattering particles, since there is marginally a better agreement of data with the models of increased aerosol density.

Following the recipe of Nascimbeni et al. (2013) and Mallonn & Strassmeier (2016), we estimate the mean molecular weight of the atmosphere using a fitted Rayleigh slope, from the relation

$$\mathrm{H} = \frac{1}{\alpha}\frac{\mathrm{d}R_\mathrm{p}}{\mathrm{dln}\lambda} = \frac{k_\mathrm{B}T_\mathrm{eq}}{\mu_m g_\mathrm{p}} \quad (6)$$

where H is the scale height of the atmosphere, $\alpha = -4$ for Rayleigh scattering, k_B is the Boltzman's constant, T_eq the exo-atmosphere's equilibrium temperature, μ_m is the mean molecular weight of that atmosphere and g_p is the planetary surface gravity. We estimate the Rayleigh scattering slope using the CMC transmission spectrum. Owing to larger uncertainties at either extreme of the spectrum, as well as telluric effects and possible absorption by exoatmospheric gases, we only include data points from 6100 to 7500 Å for the calculations. The slope is subsequently obtained through a weighted least squares fitting method, giving the best-fit value of

$$\frac{\mathrm{d}R_\mathrm{p}}{\mathrm{dln}\lambda} = (-0.00664 \pm 0.00233) \times R_\star. \quad (7)$$

Using the stellar radius value from Anderson et al. (2011), we obtain a mean molecular weight, μ_g, of 2.05 ± 0.79 atomic

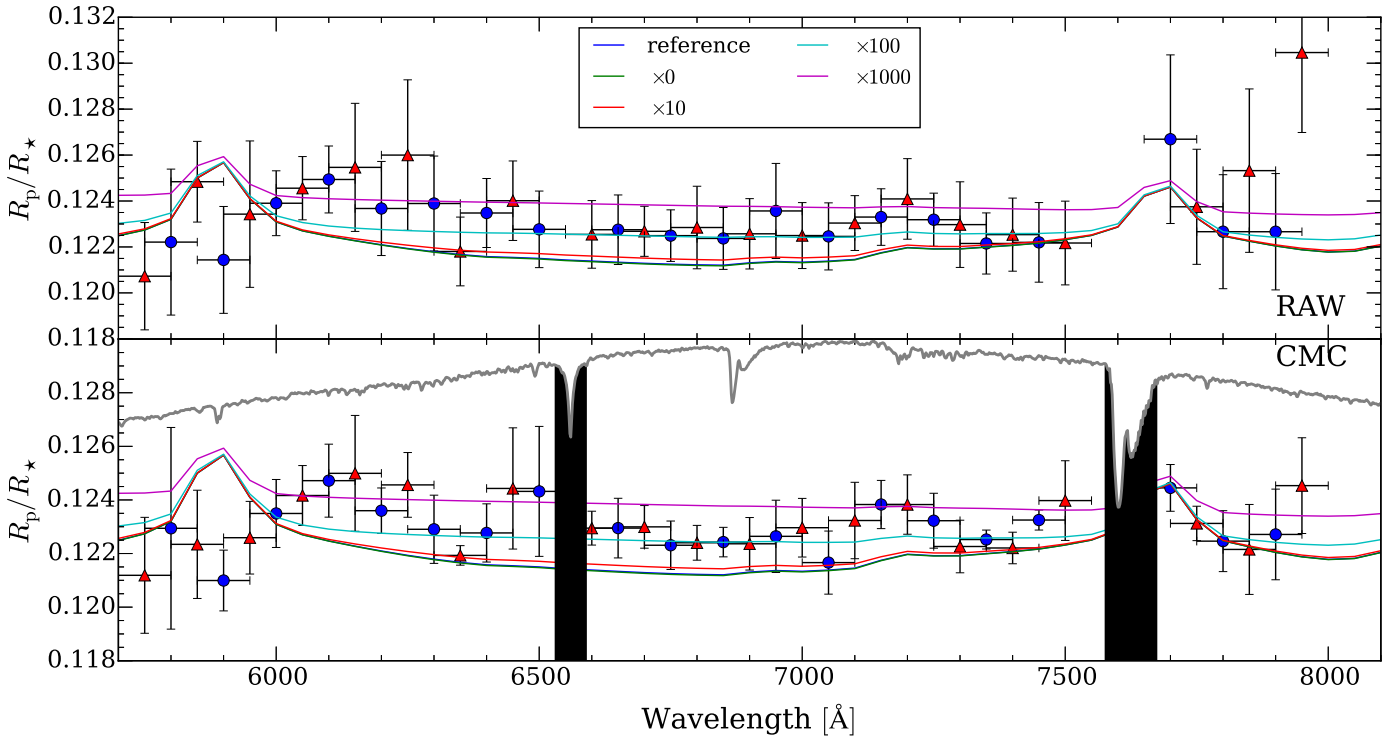

Fig. 10. Transmission spectrum of WASP-17b produced from both without (*top*) and with (*bottom*) the CMC of the spectrophotometric light curves. Blue circles and red triangles are the results from light curves made with 100 Å bins, plotted as two separate sets to show transmission spectra with unique data points. Furthermore, synthetic transmission models for the reference aerosol profile scaled by factors of 0, 10, 100 and a 1000 are also overplotted. These models are binned within 100 Å channels to match the data. In the CMC plot, an example of a WASP-17 spectrum is overplotted in grey. Two regions of telluric absorption have been shaded black, where we avoid reporting results due to the low S/N. We emphasise that the models are not fitted to the data and simply just overplotted. Hence, we do not try the retrieval approach since the wavelength coverage of the spectrum is too limited for this approach.

Table 4. Calculated statistics for the various models overplotted with the data.

	100 Å		
Atmospheric model	χ^2_r	ΔBIC	A_H
Flat	1.19	–	–
Reference aerosol (×0)	1.07	157	0.47
×0	1.07	157	0.46
×10	1.07	157	0.52
×100	1.07	157	0.82
×1000	1.11	155	1.15

Notes. A_H is the optimised number of scale heights.

mass unit (a.m.u.) for Bond albedo of 0, and 1.88 ± 0.73 a.m.u. for $\alpha_B = 0.3$, which has been shown to be a reasonable upper limit for hot gas giants (Spiegel et al. 2010; Esteves et al. 2013). These values are generally consistent with a mostly H_2 dominated atmosphere, but owing to the large uncertainties in determination of Rayleigh scattering slope, they could also point to the presence of H or He. However, a lack of H-α absorption in the transmission spectra somewhat rules out the former.

We also perform a similar analysis for the additional spectra created around the sodium and potassium absorption lines with narrower bins of 50 Å, shown in Fig. 11 to determine the significance of any possible detection. Wood et al. (2011) detect an increases in transit depth of 1.46%, 0.55%, and 0.49% for 0.75 Å, 1.5 Å, and 3 Å bin, respectively. However, they report no significant detection for bins of 4 Å and higher. Hence our non-detection of increased absorption in the Na core with the 50 Å bin is consistent with their results. Similar conclusions were also made by Zhou et al. (2012), where transit depth increase of 0.58% was detected in the Na core using a 1.5 Å bin. Taking only the points around the sodium line in Fig. 11 into consideration, we calculate a marginal improvement (~1σ) to a fit, when a flat spectrum is compared to a model with sodium absorption included. Presence of pressure broadening would point to a rather shallow temperature gradient, although more precise measurements of the planetary radius at higher resolution are required to confirm this result. More recently, Sing et al. (2015) also detected increased absorption in the sodium core using the Space Telescope Imaging Spectrograph (STIS) instrument onboard the *Hubble* Space Telescope (HST), using a narrow bin. Using very small integration bins placed on the core of the absorption line only probes the lower atmosphere (Wood et al. 2011), as opposed to larger bins where the diminished signal could be due to the presence of silicate and iron clouds increasing the opacity (Fortney et al. 2003). The absence of sodium from high altitudes can be explained for equilibrium temperatures below ~1000 K, where atomic Na is lost to the formation of various compounds and rained out of the upper atmosphere (Burrows et al. 2000), but this is not the case for WASP-17b. Lavvas et al. (2014) provide yet more possible explanations for

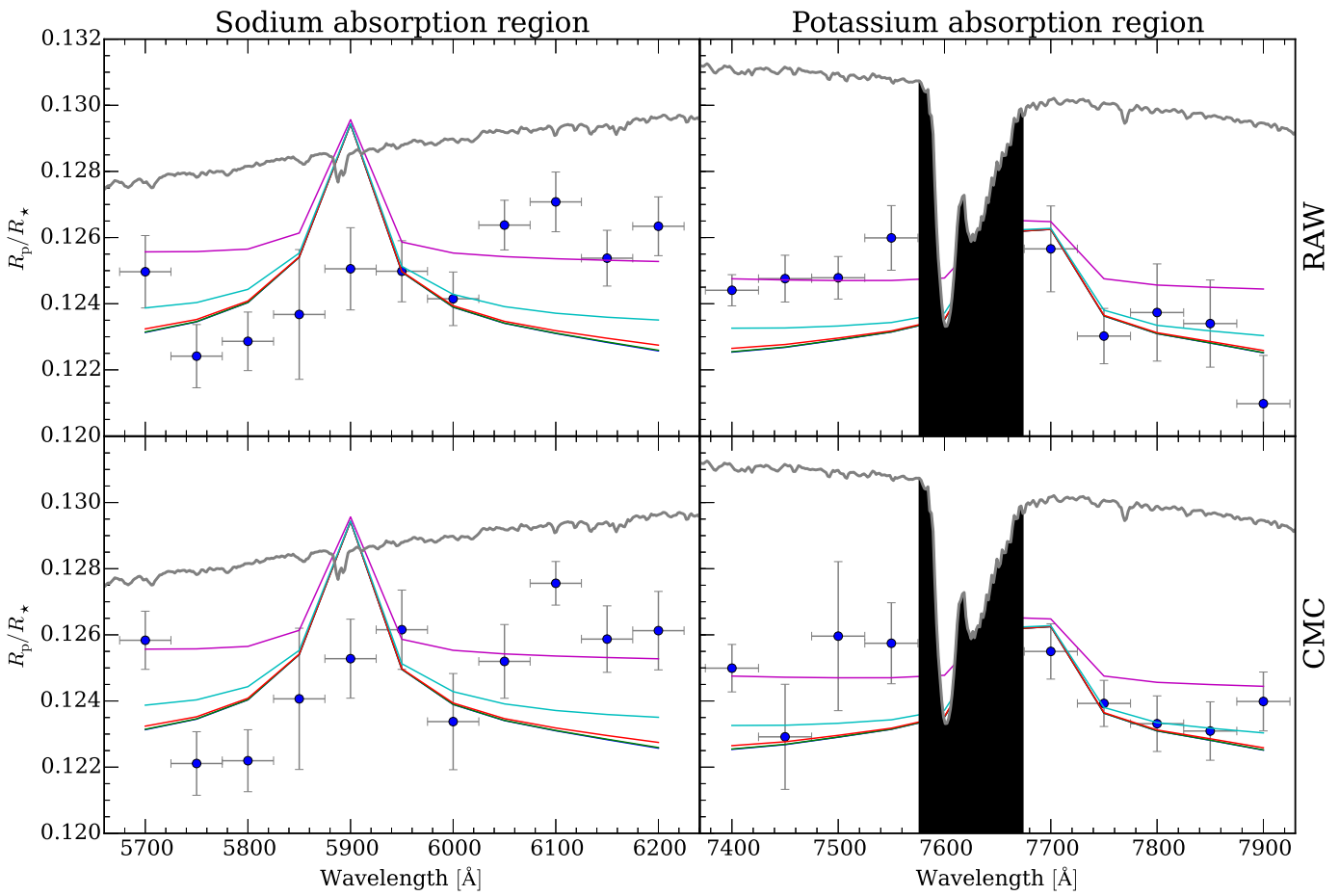

Fig. 11. Transmission spectrum reproduced with 50 Å-wide bins, as compared to Fig. 10, for domains where the possible presence of optical absorbers, such as sodium (*left column*) and potassium (*right column*), would result in an increased planetary radius. The theoretical atmospheric models are also overplotted in addition to the inferred radii, and their colours correspond to those in Fig. 10, which have again been binned to the resolution of the spectrum and plotted for 1.6 scale heights, as was performed for the overall spectrum. It must be noted that these models have not been fitted to the data points and the transmission spectrum data have not been used as a priori for the production of the model atmospheres. The black shaded region in the right column highlights the region where telluric absorption as a result of the O_2 (A) lines introduces significant systematics in the light curves produced in this region.

the presence and/or absence of Na and K in giant exoplanet atmospheres.

Similarly we also search for potassium absorption in the atmosphere of WASP-17b, obtaining and analyzing light curves using 50 Å integration bins. Unfortunately, the majority of the potassium doublet core falls on top of the telluric O_2 (A) absorption lines, as shown in the right column of Fig. 11, which introduce large systematics for light curves obtained in this region. Hence, we avoid producing and analyzing transit light curves in this domain where the signal is diminished by the Earth's atmosphere. However, since the potassium core falls close to the red edge of the telluric forbidden region, we are able to probe and detect the red wing of the pressure-broadened line. Using the data points redwards of the telluric absorption in Fig. 11, we find a 3σ improvement to the fit when a flat spectrum is compared to the atmospheric models including potassium. To date only one previous work has looked at this domain of the spectrum (Sing et al. 2015), where the narrow bin placed at the core of the potassium line is inconclusive in determining its presence or absence. Given that potassium is present in the atmosphere of WASP-17b, the pressure broadening of its wings would be consistent with what we observe for the sodium line.

Charbonneau et al. (2002) first report detection of Na in HD 209458b. Subsequent studies suggested that the Na absorption was weaker than estimated by theory (Seager & Sasselov 2000) and that the potassium signal was lacking (Snellen et al. 2008) for this planet. Four factors have been suggested that could influence the spectral bands of the alkali metals, Na and K: (i) an elemental abundance different from the commonly assumed solar value; (ii) masking by atmospheric hazes; (iii) in situ photochemical reactions; and/or (iv) condensation, e.g. on the planetary night side.

Lavvas et al. (2014) review processes affecting Na and K signals in hot Jupiter atmospheres and apply a photochemical model including in situ Na and K reactions. Regarding the effect of elemental abundances, they suggested values up to 6× lower than the solar value for Na and K, for example, for HD209458, based on stellar metallicity measurements. Regarding the masking of spectral bands, they note that it is difficult to mask only the sodium line (and not the potassium line) since sodium is a strong absorber; this could however be achieved in the presence of certain hazes although the size distribution of the haze particles would have to be consistent with the observed Rayleigh slope. With regards to in situ photochemistry, two important species that are formed are: XH (formed via: X+H_2) and XOH (formed

via X+H_2O) (where X=Na, K). Both XH and XOH can then undergo thermal decomposition to re-generate the alkali metal atoms (X). Uncertainties in the photochemistry include, for instance, reactions of potassium (e.g. here the three-body combination rates are not well known and one usually assumes the same coefficients as for sodium); also at hot-Jupiter temperatures, excited states could become important, the photochemical responses of which are not well-defined. Lavvas et al. (2014) conclude that the uncertainties in photochemistry however, are small compared with the potential effect of masking by hazes. Regarding condensation of alkali metals on the night-side, more work is required on, for example, the 3D transport mechanisms across the terminator.

5. Conclusions

We have presented the transmission spectrum of the hot Jupiter, WASP-17b, using the FORS2 instrument at ESO's VLT, in its multi-object spectroscopy mode. Using a combination of light from multiple comparison stars, we obtained the broadband differential transit light curve of this planet, whereby the bulk orbital and physical parameters were derived.

From the broadband light curve, we obtained refined non-wavelength-dependent transit parameters, which are consistent with previous analyses (Anderson et al. 2011; Southworth et al. 2012; Bento et al. 2014). Through detailed study of parameter inference and correlations, we modelled all the obtained light curves using the quadratic limb-darkening law for the host star.

Spectrophotometric light curves are analysed as independent GP noise models together with an analytical transit function, where strict, delta-function, priors for non-wavelength-dependent parameters were assumed, based on the broadband solution. We explored the posterior distribution for the remaining free parameters, these being the scaled radius, the two coefficients of the limb darkening law, noise model parameters and three coefficients of a second order polynomial, which describes the colour-dependent out-of-transit flux variations, to quote the best-fit solutions as a function of channel wavelength. We take a non-parametric approach to modelling the time-correlated noise in the data, with time taken as the only input of our GP model (Gibson et al. 2012b) in calculation of the covariance matrix. This procedure was performed on two sets of light curves, where for the second set (CMC), we applied what is known as the common mode correction by removing the systematic noise common to all the wavelength channels.

Through a comparison of transmission spectra (produced from both sets of light curves) with synthetic atmospheric models, we rule out a cloudy makeup of WASP-17b's upper atmosphere with high significance (>3σ). From fitting a Rayleigh scattering slope, we estimate an atmosphere with a mean molecular weight consistent with the prevalence of H_2. Further observations with the 600B grism of FORS2, extending the spectrum towards the ultraviolet, will be required to confirm and quantify this aspect of the exo-atmosphere with higher precision.

Additionally, we looked closer at the possibility of enhanced absorption towards the two main optical absorbers, sodium, and potassium. We do not detect a significant variation of the planetary radius at the sodium core with a 50 Å bin, consistent with previous conclusions of Wood et al. (2011) and Zhou et al. (2012). Owing to the low significance levels, we are not able to confirm nor rule out the presence of the pressure-broadened wings of the sodium absorption line. Further, higher precision and resolution observations will be required to confirm this feature. Similar conclusions are made for potassium, although we were not able to probe the absorption in the core of the line owing to the telluric O_2 feature. However, we do confirm the presence of the pressure–broadened wing of the potassium line with 3σ significance, which amounts to a significant detection.

Ultimately, our observations and analysis highlight the importance and capability of ground-based facilities in detecting and characterising exoplanetary atmospheres. FORS2 will play an important role in those efforts, providing the wider community with an essential outlet for follow-up of fascinating current and future targets.

Acknowledgements. We would like to thank the referee, Suzanne Aigrain, for great suggestions that hugely improved the quality of our analysis and conclusions. The science data together with all the calibration frames can be downloaded under the ESO archive number 095.C-0353(A). We would also like to thank Aurélien Wyttenbach for useful discussions. E.S. would like to acknowledge funding and support on this work from the ESO studentship programme. Part of the data analysis for this project was completed within the exoplanet atmosphere programme funded through the DAAD (project Nr. DAAD-2015-08). Some work by T.J. was funded through the MŠMT grant LG14013. M.R. is supported by STFC (ST/K502406/1) and the ERC project Exolights (617119). Sz. Cs. thanks the Hungarian OTKA for the Grant K113117.

References

Anderson, D. R., Hellier, C., Gillon, M., et al. 2010, ApJ, 709, 159
Anderson, D. R., Smith, A. M. S., Lanotte, A. A., et al. 2011, MNRAS, 416, 2108
Appenzeller, I., Fricke, K., Fürtig, W., et al. 1998, The Messenger, 94, 1
Bean, J. L., Kempton, E. M. R., & Homeier, D. 2010, Nature, 468, 669
Bean, J. L., Désert, J. M., Kabath, P., et al. 2011, ApJ, 743, 92
Bento, J., Wheatley, P. J., Copperwheat, C. M., et al. 2014, MNRAS, 437, 1511
Bigelow, B. C., Dressler, A. M., Shectman, S. A., & Harland W. 1998, Optical Astronomical Instrumentation, Proc. SPIE, 3355, 225
Boffin, H., Blanchard, G., Gonzalez, O., et al. 2015, The Messenger, 159, 6
Boffin, H. M., Sedaghati, E., Blanchard, G., et al. 2016, SPIE, 2016, 9908
Brown, T. M. 2001, ApJ, 553, 1006
Buades, A., Coll, B., & Morel, J. M. 2005, CVPR 2005, Conf. IEEE Comput. Soc., 2, 60
Burrows, A., Marley, M. S., & Sharp, C. M. 2000, ApJ, 531, 438
Carter, J. A., & Winn, J. N. 2009, ApJ, 704, 51
Charbonneau, D., Brown, T. M., Noyes, R. W., & Gilliland, R. L. 2002, ApJ, 568, 377
Claret, A. 2000, A&A, 363, 1081
Deming, D., Wilkins, A., McCullough, P., et al. 2013, ApJ, 774, 95
Drake, A. J., Djorgovski, S. G., Mahabal, A., et al. 2009, ApJ, 696, 870
Ducati, J. R., Bevilacqua, C. M., Rembold, S. B., & Ribeiro, D. 2001, ApJ, 558, 309
Ehrenreich, D., Hébrard, G., Des Etangs, A. L., et al. 2007, ApJ, 668, L179
Esteves, L. J., De Mooij, E. J. W., & Jayawardhana, R. 2013, ApJ, 772, 51
Fortney, J. J., Sudarsky, D., Hubeny, I., et al. 2003, ApJ, 589, 615
García Muñoz, A., Osorio, M. Z., Barrena, R., et al. 2012, ApJ, 755, 103
Gibson, N. P., Aigrain, S., Pont, F., et al. 2012a, MNRAS, 422, 753
Gibson, N. P., Aigrain, S., Roberts, S., et al. 2012b, MNRAS, 419, 2683
Gibson, N. P., Aigrain, S., Barstow, J. K., et al. 2013a, MNRAS, 436, 2974
Gibson, N. P., Aigrain, S., Barstow, J. K., et al. 2013b, MNRAS, 428, 3680
Glaudell, R., Garcia, R. T., & Garcia, J. B. 1965, Comput. J., 7, 308
Harris, A. W., Rauer, H., & Collier Cameron, A. 2000, Contributed Talk in Disks, Planetesimals, and Planets, ASP Conf. Proc. 219, 454
Hook, I., Jørgensen, I., Allington-Smith, J. R., et al. 2004, PASP, 116, 425
Husser, T. O., Wende-von Berg, S., Dreizler, S., et al. 2013, A&A, 553, A6
Knutson, H. A., Dragomir, D., Kreidberg, L., et al. 2014, ApJ, 794, 155
Kopal, Z. 1950, Harvard College Observatory Circular 454, 1
Lavvas, P., Koskinen, T., & Yelle, R. V. 2014, ApJ, 796, 15
Lendl, M., Delrez, L., Gillon, M., et al. 2016, A&A, 587, A67
Mallonn, M., & Strassmeier, K. G. 2016, A&A, 590, A100
Mandel, K., & Agol, E. 2002, ApJ, 580, L171
Nascimbeni, V., Piotto, G., Pagano, I., et al. 2013, A&A, 559, A32

Parviainen, H., & Aigrain, S. 2015, MNRAS, 453, 3821
Pont, F., Knutson, H., Gilliland, R. L., Moutou, C., & Charbonneau, D. 2008, MNRAS, 385, 109
Rauer, H., Bockelée-Morvan, D., Coustenis, A., Guillot, T., & Schneider, J. 2000, A&A, 355, 573
Schwarz, G. 1978, The annals of statistics, 6, 461
Seager, S., & Sasselov, D. D. 1998, ApJ, 502, L157
Seager, S., & Sasselov, D. D. 2000, ApJ, 537, 916
Sedaghati, E., Boffin, H. M. J., Csizmadia, S., et al. 2015, A&A, 576, L11
Schwarzschild, K. 1906, Nachrichten von der Königlichen Gesellschaft der Wissenschaften zu Göttingen: Mathematisch-Physikalische Klasse, 43
Sing, D. K., Désert, J.-M., Lecavelier Des Etangs, A., et al. 2009, A&A, 505, 891
Sing, D. K., Fortney, J. J., Nikolov, N., et al. 2015, Nature, 529, 59
Snellen, I. A. G., Albrecht, S., de Mooij, E. J. W., & Le Poole, R. S. 2008, A&A, 487, 357
Southworth, J., Hinse, T. C., Dominik, M., et al. 2012, MNRAS, 426, 1338
Spiegel, D. S., Burrows, A., Ibgui, L., & Milsom, J. A. 2010, ApJ, 709, 149
Swain, M. R., Line, M. R., & Deroo, P. 2014, ApJ, 784, 133
Wilson, A. G., & Adams, R. P. 2013, Proc. 30th Int. Conf. Machine Learning, JMLR: W&CP, 28
Wood, P. L., Maxted, P. F., Smalley, B., & Iro, N. 2011, MNRAS, 412, 2376
Zacharias, N., Urban, S. E., Zacharias, M. I., et al. 2004, AJ, 127, 3043
Zacharias, N., Finch, C., Girard, T., et al. 2010, AJ, 139, 2184
Zacharias, N., Finch, C. T., Girard, T. M., et al. 2013, AJ, 145, 44
Zhou, G., & Bayliss, D. D. R. 2012, MNRAS, 426, 2483